THE UNIVERSITY of EDINBURGH

| | |
|---|---|
| **Title** | Galactic spheroid structure from subluminous stars |
| **Author** | Digby, Andrew |
| **Qualification** | PhD |
| **Year** | 2003 |



**Digitisation Notes:**

- Pages 82, 198 missing from original

# Galactic Spheroid Structure from Subluminous Stars

ANDREW DIGBY

Institute for Astronomy

School of Physics


A thesis submitted to the University of Edinburgh

for the degree of Doctor of Philosophy

April 2003

## Declaration

This thesis describes work carried out at the University of Edinburgh between October 1999 and April 2003. No part of this thesis has been submitted for any other degree or professional qualification, and all the work contained within is my own, unless specifically stated.

Chapter 4 forms the basis for a paper accepted for publication in the Montly Notices of the Royal Astronomical Society, written with co-authors N. C. Hambly, J. A. Cooke, I. N. Reid and R. D. Cannon.

Andrew Digby
Edinburgh,
April 2003.

## Acknowledgements

This thesis wouldn't have been written without the help of many people to whom I am indebted and who deserve special thanks and mention.

At the ROE my supervisors John Cooke and Nigel Hambly have provided a huge amount of patient guidance, and an admirable, if misplaced, level of faith in my abilities. Russell Cannon and Neill Reid have also given much invaluable time and advice. John Humphreys of the BBC deserves mention for an early bracing introduction to the media's attitude to science.

My family have contributed enormously, and I wouldn't have been able to put off getting a real job for a further three and a half years without their encouragement and financial support. The effect on my thesis of Daisy the stress-relieving cow, and of all the holidays, should also not be underestimated.

My time in Edinburgh wouldn't have been anywhere near as enjoyable without the other postgrads and postdocs with whom I've shared my time here. Thanks especially to Rachel, for the good friendship and the holidays, and to all those who have been a great bunch at work, down the pub, and on the footie pitch. And I'm really grateful to Olivia, for making it all so much easier.

## Abstract

Galactic halo subdwarfs and white dwarfs are locally very scarce and many of their characteristics are hence poorly understood. As the most common members of the spheroid, however, they are crucial to the understanding of our own and other galaxies, able to yield key information about the shape, formation, chemical history and dark matter of the spheroid, as well as providing clues about the processes of stellar evolution.

Wide-field photographic data spanning observations taken over long time baselines, such as those available from the SuperCOSMOS Sky Survey (SSS), are unparalleled in their ability to identify large numbers of these dwarf spheroid stars through their large space motions. However, the "Achilles Heel" of photographic astronomy in studies such as this is poor photometry: a problem which can now be circumvented - whilst retaining the astrometric information of the photographic data - with the advent of large-scale, deep CCD surveys with accurate photometry such as the Sloan Digital Sky Survey (SDSS). In this thesis I show that the combination of these two types of dataset brings vast numbers of locally-rare dwarf spheroid stars into the observational reach of astronomers, yielding reliable samples many times larger than have previously been available solely from photographic data.

Using SSS data coupled with the SDSS archive I identify a sample of $\sim$2600 candidate subdwarfs through strict selection criteria. This forms one of the largest and most reliable samples of subdwarfs known, and enables accurate determination of luminosity functions along many different lines of sight. I derive the subdwarf luminosity function with unprecedented accuracy to $M_V \lesssim 12.5$, finding good agreement with recent local estimates but discrepancy with results for the more distant spheroid. This provides further evidence that the inner and outer parts of the stellar halo cannot be described by a single density distribution. I also use the data to show that the form of the inner spheroid density profile within distances of 2.5 kpc is closely matched by a power law with an index of $\alpha = -3.15 \pm 0.3$. Whilst this study is unable to provide further constraints on Galactic structure at present, development of these methods

and results have the potential to yield much more information on the formation and evolution of the Galaxy.

# Contents

# List of Figures

# List of Tables

# Chapter 1

# Introduction

Small, faint stars dominate the Galaxy. Low luminosity dwarfs, fainter and less massive than the Sun, are by far the most common type of star, and, despite their small size, account for at least half of the total stellar mass. If we are to develop a good comprehension of the structure and evolution of the Milky Way, we clearly need to understand more fully the nature of these stars and their individual characteristics.

Subdwarfs are dwarf stars from the Galactic stellar halo, or spheroid [1]. As members of this old population they are metal-poor, and are named due to their "subluminous" appearance on colour-magnitude diagrams, below (at fainter absolute magnitudes) the more metal-rich disc dwarfs. In fact, subdwarfs have brighter luminosities than their higher-metallicity counterparts of the same mass as a result of their lower opacities and higher effective temperatures, but appear below the disc main sequence on a colour-magnitude diagram by virtue of their bluer colours. Subdwarfs are amongst the most ancient Galactic stars, many almost as old as the Galaxy itself. Their orbits and evolution have changed little over Gigayears, and so the distribution and kinematics and other properties of this population of otherwise unremarkable objects - the most common in the spheroid - can yield a wealth of clues about our Galaxy and its constituent stars.

[1] A distinction is made between the stellar halo, or spheroid, and the dark matter halo, which as the dominant contributor to the Galactic potential is responsible for the flat Galactic rotation curve, and whose major constituents are currently unknown. See Evans (2002) for a review of Galactic baryonic dark matter possibilities.

The number densities of subdwarfs and their distributions of masses and luminosities can impart crucial information as to the nature of the spheroid and to the theories of stellar formation and evolution. The subdwarf mass distribution can also be used to estimate the expected number of substellar objects and stellar remnants in the spheroid, and their contribution to Galactic dark matter. The subdwarf mass function can also inform how star formation varies with environment and epoch, and can provide insight into cluster evolution. Searching subdwarf samples for indications of kinematic substructure ("streams") can help describe the very processes that formed the Galaxy.

Yet the understanding of these types of stars has implications for our comprehension of astronomy beyond the limits of the Milky Way. The stellar mass function is relevant to external clusters and galaxies, the Galactic dark matter problem could also be applicable to extra-Galactic astronomy, and understanding the processes of galaxy formation has important implications for cosmological theories. An improved understanding of the dwarf stars in the stellar halo of our Galaxy therefore has ramifications for many diverse areas of astronomy.

In order to study these stars they of course need to be found in significant numbers, and although they are one of the most common stellar members of the Galaxy, subdwarfs are locally very rare, comprising only $\sim$0.2% of all stars in the solar neighbourhood. This local scarcity, combined with their low intrinsic luminosities, has meant that until very recently samples of the fainter, cooler subdwarfs have been very small and mostly confined to the immediate solar neighbourhood, and hence little has been discovered about the population as a whole.

Due to the relatively high heliocentric velocities of spheroid stars, proper motion studies have proved the most effective at their identification over wide areas. With a large areal coverage and long time baselines providing accurate measures of space motions, photographic plate material has been used extensively for the proper motion surveys. Indeed, with the advent of accurate measuring machines offering precise astrometry, photographic plates have been used extensively and effectively for over thirty years to study the stellar populations of the Galaxy (eg. Murray 1986).

The inability of photographs to provide accurate magnitudes and colours, and the relative shallowness of the observations, has meant that the last decade has seen a substantial decrease

in the use of photographic astronomy. The far superior photometric accuracy of CCDs mounted on larger telescopes has meant that these have become the observing tool of choice, and photographic observations have now all but ceased. However, photographic astronomy has time on its side, and the huge archives of observations spanning the last fifty years, scanned to high precision by measuring machines such as SuperCOSMOS, offer currently unrivalled resources with which to study the motion of stars in the Galaxy. CCDs simply have not been in use for long enough to provide large-scale measures of motions with comparable accuracies.

The continuing importance of photographic plate material has been enhanced by the advent of wide-field, deep surveys with accurate CCD photometry, such as the Sloan Digital Sky Survey. As shown in this thesis, combining the precise photometry of these CCD programmes with the historical positional information offered by the plate archives has brought many more stars from the spheroid populations within the observational reach of astronomers. Applying these methods over vast regions of sky is proving very effective at finding significant numbers of subdwarfs and white dwarfs, opening the potential for detailed investigations into the nature of these populations. These far larger samples will enhance our understanding of not only the structure and formation and stellar evolution of our own Galaxy, but also of the wider Universe.

## Thesis structure

The principal intention of the research described in this thesis has been to derive an accurate estimate of the luminosity function of subdwarfs from the Galactic spheroid. Whilst I use the derived luminosity function to estimate the density structure of the spheroid, many of the avenues of research leading from this result with which to probe the structure and evolution of the Galaxy remain currently untapped, largely due to time constraints. However, I demonstrate how large, reliable samples of stars from the spheroid populations can be obtained through the combination of survey datasets. These data, in conjunction with the results I present here, offer an excellent platform from which to progress to more extensive Galactic structure studies.

Since the ultimate aim of this area of astronomy is to provide insight into the formation of the Galaxy, I first present a brief review of the history and present status of this research (Chapter 1), and describe the types of surveys used to investigate Galactic structure. This work focusses on using subdwarfs for this purpose, so I explain how the luminosity and mass func-

tions of these stars can be used to investigate many diverse aspects of Galactic astronomy, and outline some recent results in this field. As tracers of the spheroid stellar population, subdwarfs can also be used to search for additional evidence of the recently-discovered kinematic substructure in this component. I briefly discuss these findings of halo "streams" and the implications they may have for galaxy formation theories, and propose how subdwarfs can be used to further this research (Chapter 2).

The methods used to select a subdwarf sample from a series of photographic plates obtained by Andrew Murray are then detailed (Chapter 3, the "Murray programme"), but it is shown how these data are insufficient for this purpose. The progression to a combined dataset from the Sloan Digital and SuperCOSMOS Sky Surveys is described in Chapter 4, where the luminosity function results and their use in constraining the spheroid density distribution are presented. Finally, a summary of this research and suggestions for progressions of the study are given (Chapter 5). Chapter 4 forms the basis of a paper accepted for publication in MNRAS (Digby et al. 2003).

# Chapter 2

# Background and motivation

In recent years, large and highly sensitive telescopes and detectors have enabled astronomers to peer back to the early universe, and observe galaxies in the first stages of formation at high redshifts. Much effort has been devoted to deep surveys of these objects, and yet whilst their study is important, our own Galaxy and its neighbours offer a far more direct probe of the processes of galactic formation and structure. Analysis of the "fundamental plane" of galaxies have shown that the Milky Way and the galaxies of the local group appear typical of most of the galaxies in the Universe (Gilmore, Wyse, & Norris 2002), so we are presented locally with an ideal sample which which to test theories of galaxy evolution. Low mass stars in the Galaxy have lifetimes of a Hubble age or greater, so their present characteristics provide a fossil record of the environment in which they formed in the early years of the Galaxy. So although the Galaxy has evolved in the Gigayears since its creation, the kinematics and chemical composition of its older stellar populations hide a wealth of information of galaxy formation and evolution comparable to any offered from deep cosmological surveys. The detailed study of external galaxies is in its infancy, yet whilst investigations into how the Milky Way formed have been ongoing for many decades, there is still no definitive consensus on how it evolved, or even of its current structure. I first discuss the theories of the history of the Galaxy, and then the tests of its evolution and structure that are possible with low mass stars of the Galactic spheroid.

## 2.1 Formation of the Galaxy

### 2.1.1 The ELS formation model

The first comprehensive model of the formation of the Galaxy was that of Eggen, Lynden-Bell & Sandage (1962, hereafter ELS) . They obtained UV excesses[1], radial velocities and proper motions for a large sample of nearby stars, most of which were selected by proper motion. They found that as the metallicity of the stars in their sample *decreased*, then:

- the orbital eccentricity, e, *increased*
- the energies of vertical oscillation, $E_z$, *increased*
- the vertical angular momentum, $L_z$ *decreased*

The variables $e$ and $L_z$ are 'adiabatic invariants', so their values change slowly if the potential also changes slowly. From the gradients in $e$ and $L_z$ with metallicity that they found, Eggen et al. (1962) deduced that either:

*(i)* The potential of the Milky Way has changed rapidly in its history — ie. the Galaxy has undergone a violent disruption, or

*(ii)* Most low-metal stars can't have formed in a rotationally-supported disc, and must have formed on highly-radial orbits with large $e$.

From these conclusions ELS constructed a formation model for the Galaxy. In their interpretation, the Galaxy started out monolithically, as a metal-poor, near-spherical density fluctuation, which due to instabilities underwent free-fall collapse. As the protogalaxy collapsed gas condensations were created, and star formation was initiated in these clumps. At this stage the oldest stars and globular clusters present today were formed, with their kinematics reflecting that of the infalling gas in which they were created, and their metal abundances reflecting its

[1] $\delta(U-B)$: the difference between the $(U-B)$ colour of a star and that of the Hyades Main Sequence (MS) at the star's $(B-V)$ value, and hence a measure of metallicity

chemical composition. This explains the observation of ELS that the oldest stars tend to be metal-poor and on highly-eccentric orbits.

As the collapse continued, the rotational velocity and centrifugal acceleration in the protogalaxy increased in order to conserve angular momentum. Supernovae increased the metallicity of the infalling interstellar medium (ISM), and a rotationally-supported disc formed in the now metal-rich cloud. ELS estimated that the first star formation occurred about 10 Gyr ago, and from the ranges of stellar orbits observed concluded that the protogalaxy collapsed by at least a factor of 10 in the radial direction and 25 in the Z-direction (see Figure 2.1 for a description of Galactic coordinates.) Estimating the rate of the collapse was a key part of their model, and an aspect that was to cause significant debate over years to come. They postulated that early infalling material must have had $U \gg V$ in order to produce the highly-elliptical orbits of old halo stars seen today. They therefore argued that the collapse took place on a timescale faster than the Galactic rotation of $\sim 2 \times 10^8$ years, which corresponds to a free-fall collapse without pressure support. They substantiated this estimate of the timescale by pointing out that it was consistent with the coeval nature of all the halo globular clusters that had accurate photometry at the time, and that if pressure support from hot gas had slowed the collapse then it also would have prevented the formation of stars.

### 2.1.2 Problems with the ELS model

The formation model proposed by Eggen et al. (1962) had significant impact, and was to remain influential for many years. However, later researchers analysed the elements of the scenario with improved data and techniques as they became available, and began to find discrepancies with the ELS Galaxy formation theory.

Isobe (1974) introduced an evolving gravitational potential into the dynamical arguments, and found some conflict with the timescale of the ELS model which questioned whether a collapse could be responsible at all. He argued that the ELS timescale was not long enough to create the smooth correlation between kinematics and metallicity that had been established, and that it could not explain the presence of low-eccentricity, low-metallicity stars. On the other hand, a slower contraction model could also not explain these types of stars, nor the high-$e$,

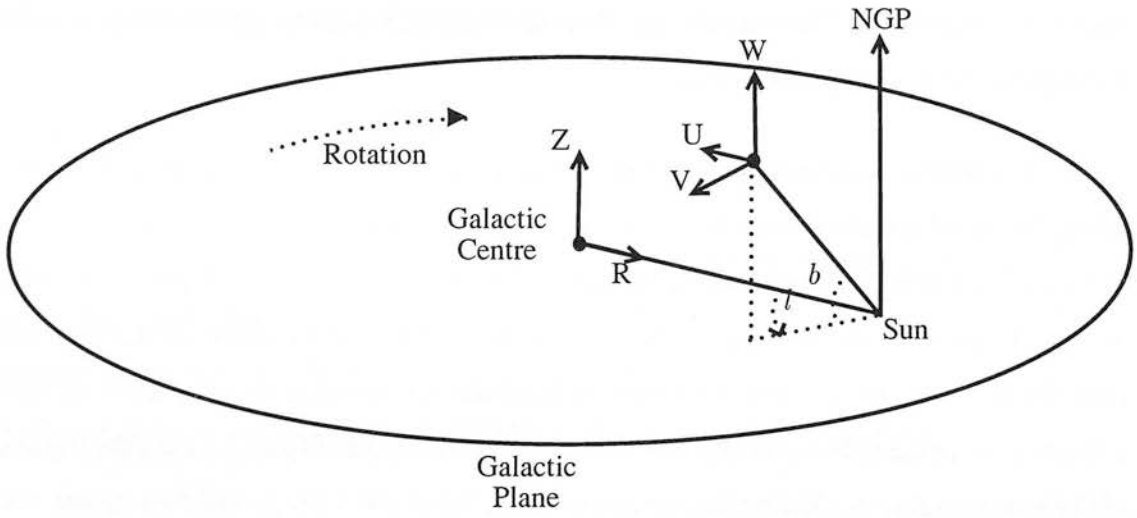


*Figure 2.1: The Galactic coordinate system, describing cylindrical coordinates $(R, Z)$, Galactic longitude and latitude $(l, b)$ and the Galactic velocity triad $(U, V, W)$ which are in the directions of the Galactic centre, direction of rotation and North Galactic Pole respectively.*

low-metallicity stars which strongly suggest a more rapid collapse.

Saio & Yoshii (1979) found more low-metal, low-$e$ stars among their sample of RR Lyrae and dwarfs, which contradicted the model of ELS, and had been missed from their study due to proper motion bias. They also found further evidence for retrograde ($V < 0$) motion in halo stars, first purported by Larson (1969) and inexplicable by a freefall collapse. They proposed a much slower collapse timescale of 2-3 Gyr, accounted for by random motions of gas clouds, whose inelastic collisions supported the collapse.

The most influential work, however, came from the landmark papers of Searle (1977) and Searle & Zinn (1977 hereafter SZ). From their studies of Galactic globular clusters, they found:

*(i)* No metallicity spread among the stars of most clusters.

*(ii)* No radial abundance gradient among the clusters in the outer halo

*(iii)* A difference in horizontal branch (HB) morphology between inner and outer halo globulars that is only explicable by an age difference, with the outer clusters younger than the

inner ones.

These findings cast significant doubt on the validity of the ELS model. Point (i) contradicts ELS since freefalling material is unlikely to be well-mixed. The second result of no radial abundance gradient, although not directly contrary to ELS's model — indeed, a *slow* collapse would be expected to produce such a result — was still only found for the outer globulars, and can be explained by a collapse timescale that is still significantly longer than freefall. The age spread of the globulars was proposed by SZ to be as much as 3 Gyr, which clearly is at odds with ELS's timescale. Searle (1977) also found that the metallicity of halo globulars had a large spread, which further contradicts the ELS freefall collapse model.

### 2.1.3 The Searle and Zinn (SZ) model

As a result of the difficulties the ELS model had in explaining their findings, Searle & Zinn (1977) put forward an alternative model of Galactic formation. Focussing on the halo, they postulated that rather than forming from an ordered collapse, the Galaxy was created from the chaotic mergers of large ($10^8\ M_\odot$) protogalactic clouds, or "fragments". These fragments disrupted each other as they collided, raising the temperature of the whole system and slowing the collapse, and scattering field stars and globular clusters throughout the halo. This formation scenario can explain the wide spread of metallicities and a lack of abundance gradient in the spheroid, since the fragments would have their own star formation histories and different metallicity distributions arising from their independent evolution.

This formation scenario is consistent with the suspected age difference between the inner and outer halo also found by SZ, whereby younger globulars tend to be found at greater Galactocentric radii (but see §2.1.5 for conflicting evidence.) During the mergers the density would be greater in the inner parts of the system, so the collapse and evolution would take place faster there and this is where the first stars would be formed. In the outer halo, on the other hand, the density would be lower and hence the star formation rates would be slower.

In the light of the evidence presented by SZ for a more chaotic and prolonged formation of the halo, it was clear that there were several problems with the ELS model of formation. In

addition to the contrary discoveries of SZ, the freefall collapse model was unable to provide an explanation for the presence of retrograde halo stars, first found by Larson (1969). This counter-rotating component has an opposite angular momentum vector to the disc and inner regions, and so therefore cannot have formed from the same ordered collapse.

Additionally, the ELS model was unable to account for the low-$e$, low-metallicity stars being discovered (eg. Saio & Yoshii 1979), since according to their picture of collapse, the oldest, and hence most metal-poor, stars were formed early on in the collapse and hence on highly radial (high-$e$) orbits.

The calculation of the controversial timescale of the ELS collapse was also suspect too, since their upper limit of the radial collapse timescale being of the order of the Galactic rotation period was based on the 200 Myr estimates of the *present* period at the Solar Circle. This is possibly far different from the rotation timescale at the stage of initial collapse, as emphasised later by Sandage himself (Sandage 1990), and pointed out earlier by Isobe (1974).

So the general view during the 1970s and 1980s was one of diminishing support for the ELS model of formation of the Galaxy, and increasing confidence for the alternative first proposed by SZ. This was consistent with the picture in extra-galactic research too, with the recognition of galaxy mergers and interactions and the principle of hierarchical growth gaining acceptance (eg. Toomre 1977, Tinsley & Larson 1979).

### 2.1.4 Further support for the SZ model and evidence against ELS

In the two decades since Searle and Zinn first proposed their formation model, further observational and analytic evidence has supported many aspects of their interpretation.

*Kinematic halo substructure*

If the Galaxy is formed by the merging and/or accretion of substructures, then there should remain signatures in the halo of these fragments, since the high velocities and low densities of its constituent stars means that the halo is not fully dynamically relaxed and well-mixed (Helmi & White 1999).

Recently there have been many significant findings of such substructure, evident as clumps of stars in velocity space (eg Majewski, Munn & Hawley 1994, 1996, Carney et al. 1996, Helmi et al. 1999, Chiba & Beers 2000, Dinescu et al. 2002) or in the spatial domain (Majewski et al. 1999, Ivezić et al. 2000, Yanny et al. 2000, Newberg et al. 2002). One of the first detections of such "streams" was from the study of Majewski et al. (1994, 1996), who found clumping in the phase space distribution of a sample of spheroid dwarf stars. Many recent detections of streams from the Sagittarius dwarf galaxy, found by Ibata, Gilmore, & Irwin (1994) to be tidally disrupted by interaction with the Galaxy, have provided strong evidence that a significant fraction of the stellar halo originates from mergers earlier in the Galaxy's history. More details of these findings are given in §2.3.4.

Further support for substructure was provided by evidence for disc moving groups (Dehnen 1998), and the discovery of retrograde globular clusters with metallicities higher than the LMC (van den Bergh 1993). Since the metallicity of globulars is correlated with the luminosity of the parent galaxy, he was able to conclude that the Milky Way had previously undergone a merger with a galaxy larger than the LMC.

*Retrograde halo*

The earlier claims of studies such as Larson (1969) and Saio & Yoshii (1979) of a retrograde halo rotation have been supported by subsequent research, casting further doubt on the ordered freefall collapse model of Eggen et al. (1962). Whereas solar neighbourhood surveys of metal-poor stars have tended to find a prograde halo, many studies at greater distances above the Galactic plane have found retrograde motion (Reid 1990, Allen, Schuster & Poveda 1991, Schuster, Parrao & Contreras Martinez 1993, Carney et al. 1996, Kinman et al. 1996, Wilhelm et al. 1996, Majewski et al. 1996). This suggests that there are two distinct metal-poor populations, and that there is a vertical kinematic gradient in the halo.

*Distinct inner and outer halos*

The existence of distinct halo populations is not feasible with the continuous collapse model of ELS, which would be expected to produce a more uniform environment. Changes in the kinematics of the inner and outer halos have been found with several studies (Majewski 1992, Carney et al. 1996, Sommer-Larsen et al. 1997), and a dramatic discontinuity between the halo

and disc has been inferred by the presence of a rotational velocity-metallicity ($V_\phi$, [Fe/H]) relation for intermediate and high metallicity stars ([Fe/H] $\gtrsim$ -1.7), but not for very metal poor ones ([Fe/H] $\lesssim$ -1.7) (Norris 1986, Norris & Ryan 1989, Beers & Sommer-Larsen 1995, Chiba & Yoshii 1998, Chiba & Beers 2000). Additionally, evidence that the spheroid has a composite structure in terms of stellar density, with both a flattened inner component and a near-spherical outer part (eg. Sommer-Larsen & Zhen 1990, Sluis & Arnold 1998, Chiba & Beers 2000, Siegel et al. 2002), is also at odds with the uniform distribution expected from the ELS model. However, there are also difficulties in reconciling such coherent structure with the random mergers suggested by Searle & Zinn (1977).

*Other evidence*

A number of other findings have helped to cast further doubt on the ELS model and support that of SZ. A large age spread in outer halo globular clusters (Rosenberg et al. 1999) and also in field stars (Schuster & Nissen 1989, Carney et al. 1996) is inconsistent with the ELS collapse timescale, as is the observation of outer halo field HB and RR Lyrae stars younger than their inner halo counterparts (Preston, Shectman, & Beers 1991a, Lee & Carney 1999).

A lack of abundance gradient in halo field stars (Carney et al. 1990, Chiba & Yoshii 1998) is also suggestive of a more chaotic, SZ-type formation, and the finding of Chiba & Yoshii (1998) of low-$e$ stars in the outer halo refutes a rapid collapse. Perhaps as the final nail in the coffin of the ELS scenario, from a large sample of metal-poor stars selected without kinematic bias and with proper motions, radial velocities and distance estimates, Chiba & Beers (2000) find *no* evidence for an ([Fe/H], $e$) correlation, which was an important basis of the formation model proposed by ELS, and is claimed by Chiba & Beers (2000) to be purely the result of proper motion selection bias.

### 2.1.5 Problems with the SZ model

Despite all the supporting evidence for the SZ formation scenario, there have been several observed discrepancies with their model. Observations of globular clusters, the basis of the SZ model itself, have subsequently conflicted with the accretion hypothesis. The correlation of the half-light radii ($r_h$) of globular clusters increasing with Galactocentric distance ($R_{GC}$) (van

den Bergh 1995), and the fact that $r_h$ correlates even better with perigalactic distance, is inconsistent with the postulated chaotic formation of SZ. Similarly, the recognition that Fornax dSph globulars are smaller than outer halo ones in the Milky Way (van den Bergh 1994) suggests that the halo globulars were not accreted from dwarf satellites. As explained in §2.1.3, in the SZ model it is expected that outer halo clusters should have a lower average age than inner ones. It is known that clusters at larger Galactocentric distances display a more prominent "second parameter" effect, whereby there are exceptions to the trend for cluster horizontal branches (HB) to be redder with increasing metallicity (see Sarajedini, Chaboyer, & Demarque 1997, and references therein). These exceptions are due to an undetermined "second parameter", which is thought to be age (Lee, Demarque, & Zinn 1994); if so it would mean that the "second parameter" observations offer support for the SZ model. However, HB morphology is not a straightforward indication of age, and there may be factors other than age which are responsible for the "second parameter" effect. Using Hubble Space Telescope (HST) observations of three outer halo clusters to measure ages more directly from cluster main sequence stars, Richer et al. (1996) found outer halo clusters as old as those in the inner regions, and claimed that there is no net age gradient in the halo clusters. They conclude that metal-poor clusters formed throughout the entire halo at approximately the same epoch and on a short timescale — a finding at odds with the SZ galaxy formation scenario.

Indeed, increasing inconsistencies with the SZ model prompted Sandage (1990) to present a defence of his and his collaborators' original model, claiming that the SZ formation scenario was just "ELS plus noise". He claimed that the retrograde halo motions found were just due to noise in the kinematic measures, and that the low-$e$, low-metallicity stars found were not really old, but due to scatter in the age-metallicity relationship. He also claimed that many of the results of ELS had been taken out of context, and that the $Z_{max}$ of 5 kpc of their study made it more applicable to the thick disc (Gilmore & Reid 1983) rather than the halo.

A number of other conflicts have arisen with the SZ model in recent years. The discontinuity between the outer and inner halos highlighted above, whilst inconsistent with the ELS model, is not compliant with the slower accretion scenario either. The rotational lag between the outer and inner parts implies a velocity gradient between the two, and evidence for such in the thick disc and halo has been found by a number of studies (Murray 1986, Hanson 1989, Spaenhauer 1989, Majewski 1992, Chiba & Yoshii 1998, Mendéz et al. 2000, Chiba & Beers

2000). This points to a dissipative formation, not chaotic merging suggested by SZ. Further evidence for distinction between parts of the halo comes from the support for a spherical density distribution for the outer halo, and a flattened distribution for the inner part (Sommer-Larsen & Zhen 1990, Chiba & Beers 2000, Gould 2003). Such coherent, internal structures are at odds with the random mergers suggest by the fragment model.

Several observed kinematic effects also are inconsistent with the SZ model. One such is the observed dominance of high angular momentum, low-$e$ stellar orbits in the outer halo, with the velocity ellipsoid becoming more tangentially anisotropic and less radially anisotropic with increasing $R_{GC}$ (Sommer-Larsen, Flynn, Christensen 1994, Chiba & Yoshii 1998). Although these low-$e$ orbits are not compliant with the ELS model, they are also at odds with SZ. Fragments merging tend to sink to smaller radii of the system due to dynamical friction (Quinn et al.1993), and are disrupted when their mean density is exceeded by that of the surrounding mass. Dynamical friction results in more circular orbits, so the expected trend would be for low-$e$ orbits to be prevalent at smaller radii, or more tangential anisotropy at lower $R_{GC}$ — *opposite* to the observed $e$-distribution.

Further kinematic discrepancies arise with the observations of retrograde components in the upper halo. Although previous studies have found evidence for such (see §2.1.4), other studies have argued against this. Carney et al. (1996) found evidence for a retrograde halo and prograde inner regions, suggestive of a SZ-formed outer part and an ELS-type inner, but, upon reanalysis of their data (Carney 1999), found *no* evidence for a retrograde halo. This was supported by Chiba & Beers (2000) who found no evidence for retrograde motion in their large sample.

It is therefore clear that the complete picture of formation of the Galaxy is not explicable by the SZ scenario. Certainly the rapidly rotating disc did not form from such a sequence of merging systems, but is in fact more consistent with an ELS-type formation. This is suggestive that the formation may have occurred as a "hybrid" of both models.

### 2.1.6 Formation of the disc

The SZ model is largely unable to account for the formation of the disc component of the Galaxy, which is likely to have formed by settling of gas from the halo. This interstellar gas cools and sinks inwards until it forms a rotationally-supported disc, formed from initial angular momenta in the system, in which the gas clouds are on circular orbits. Further accretion of gas makes the disc gravitationally unstable, causing stars to begin to form in the most dense clouds where the cooling is more rapid and star-forming hydrogen clouds can exist. These dense clouds are on the most circular orbits, so stars forming in them create a stellar disc. This disc is fragile, and can be heated and hence thickened (the scale height and temperature are correlated) by any perturbations of the stellar orbits — by, for example, scattering by molecular clouds, the presence of spiral arms, or interaction with a merging satellite.

This process of disc formation is largely established, but it is the exact nature of evolution between the halo and disc components, and the formation of the "thick disc" that is still the matter of some debate. First discovered by Gilmore & Reid (1983), this population of old stars is metal poor, with a mean metallicity between $-0.5$ and $-0.7$, and forms a rotating disc with a vertical scale height of $\lesssim 1$ kpc (Beers & Sommer-Larsen 1995, Chiba & Beers 2000, Chen, Stoughton & Smith 2001) that is approximately double that of the thin disc (Chen et al. 2001). Although its current characteristics have been quite well determined, its origin is unclear and yet central to understanding the formation of the Galaxy.

#### Formation of the thick disc

The thickening of the thin disc by the molecular cloud scattering or from the presence of spiral arms is not sufficient to account for the formation of the thick disc (Jenkins 1992), so an alternative explanation must be found. The most likely formation scenarios fall into pre-thin disc ("top-down") or post-thin disc ("bottom-up") categories. The former suggests that the thick disc is created from a dissipative "ELS-style" collapse after the major parts of the halo have formed (Larson 1976, Burkert & Yoshii 1996), whereas the "bottom-up" theory envisages the dynamical heating of an existing "old" thin disc by a satellite merger (Quinn, Hernquist & Fullagar 1993, Walker, Hihos & Hernquist 1996, Sellwood, Nelson & Tremaine 1998). In

this merger scenario gas heated by the collision would cool and settle to form the current thin disc, whilst the stars, effectively acting as collisionless particles, would retain the kinematic energy from the merger. There is also a variant of the pre-thin disc theory which postulates that the thick disc is the first Galactic component formed in an ELS collapse, followed by the later formation of the halo from the accretion of small stellar systems (Majewski 1993).

Which of the pre- or post-thin disc formation scenarios is correct should be apparent in the current structure of the thick disc. One expected discriminator is the metallicity range of the thick disc stars: if formed through the heating of an old thin disc by a merging satellite then there is likely to be a wide spread of metallicity and many metal-poor stars, reflecting the different abundance characteristics of the two merging populations. In the alternative pre-thin disc theory, on the other hand, the gas collapsing to form the thick disc will have been enriched by halo star ejecta, and so there will be fewer metal-poor stars expected.

Similarly, in the dissipative collapse model a smooth metallicity gradient should be present in the thick disc, which would not be evident if it formed from a chaotic merger. A merger would also give rise to a discontinuity in the chemical and kinematic properties of the thin and thick discs, whereas more continuous distributions would be expected for the ELS-style collapse model. Another significant test is for evidence of thick discs in other galaxies: if the thick disc formed in the ordered "top-down" scenario then *all* spiral galaxies similar to the Milky Way will be expected to contain discs.

*Evidence for the pre-thin disc model*

Several studies have argued for a low metal-poor ([Fe/H] $\lesssim -1.0$) fraction of the thick disc, indicative of a non-merger formation. Layden (1995) and Wilhelm (1995) both find little evidence of this *metal weak thick disc* (MWTD), and more recently Chiba & Yoshii (1998) and Chiba & Beers (2000) find that $\sim$10% and $\sim$30% of stars with thick disc kinematics have abundances in the range $-1.6 \lesssim$[Fe/H]$\lesssim -1.0$. These latter studies claim that this suggests a dissipative collapse origin, supported by their finding of very few disc stars with metallicities lower than [Fe/H] $\approx -1.6$, and Chiba & Beers (2000) discovering *no* thick disc stars with [Fe/H] $\leq -2.2$. Both of these analyses also provide evidence of coherent structure in the thick disc: Chiba & Yoshii (1998) detect a small metallicity gradient (see also Carney et al. 1996,

Chen 1997, 1999) and Chiba & Beers (2000) find a kinematic gradient and a distinct kinematic break between the thick disc and halo populations. All of these results are not expected in a merger formation, and Chiba & Beers (2000) are unable to detect an increase in vertical velocity dispersion ($\sigma_W$) with decreasing metallicity, which would be the expected signature of a dynamically "hot" metal-poor protodisc that was disrupted to form the thick disc in the "bottom-up" model. Other factors and results also appear to undermine the post-thin disc scenario, with the epoch of merging strongly constrained by the age limits set by the $\sim$300 pc scale height of the present thin disc, and the existence of very metal-poor disc stars hard to explain by the merger with a metal-poor satellite (Barnes 1996).

*Support for the post-thin disc model*

On the other hand, there is a large body of evidence pointing towards a post-thin disc merger being responsible for the thick disc formation. The fraction of its stars that contribute to the metal-weak tail of the distribution is contentious, for whereas the studies listed above suggest the proportion is small, others point to a much larger value: 72% and 60% of stars with thick disc-like kinematics in the range $-1.6 \lesssim$ [Fe/H] $\lesssim -1.0$ are found by Morrison, Flynn & Freeman (1990) and Beers & Sommer-Larsen (1995) respectively. The star count analysis of a huge sample of stars from the SDSS (Chen et al. 2001) also points convincingly towards a heated disc formation scenario, from their finding that the thick disc forms a separate, distinct population to the thin disc and halo, and their respective scale height estimates of $\sim$300pc and 580-750 pc for the thin and thick discs are in accordance with the values expected from a heating mechanism.

Further abundance analyses of the thick disc favour the heating origin, with the studies of Nissen & Schuster (1991), Fuhrmann (1998), Gratton et al. (2000) and Prochaska et al. (2000) all providing compelling evidence that the star formation history of the thick disc is inconsistent with dissipational formation. Although these studies could be affected by a kinematic and abundance selection bias, they nevertheless find chemical continuities between the thick disc and halo whilst finding discontinuities between the thin and thick disc properties. These results strongly suggest a merger formation scenario.

More evidence for the "bottom-up" theory comes from observations of external edge-on

disc galaxies, which find that whilst some have thick discs, not all do (Morrison, Boroson, & Harding 1994, Morrison et al. 1997, Fry et al. 1999). This indicates that a more chaotic process is responsible for the thick disc formation than that described by a coherent collapse. Some of the most compelling evidence for a merger foundation comes from the spectroscopic survey of ~2000 F & G stars by Gilmore et al. (2002). They find that the mean rotation velocity of the thick disc a few kiloparsecs from the plane is ~100km $s^{-1}$, rather than the expected ~180km $s^{-1}$, and claim discovery of a previously unknown population of stars on orbits intermediate between the thick disc and halo, with lower rotational velocities and higher random motions than the conventional thick disc. They propose that their sample is dominated by fragments of a "shredded satellite" that merged with the disc of the Galaxy 10-12 Gyr ago. Given that such a signature is inexplicable in the dissipative collapse formation theory, and considering the arguments outlined above, the currently favoured theory for the thick disc formation is for a merger heating of an existing disc from an infalling satellite.

### 2.1.7 The "Standard Model"

Given the problems with the ELS and SZ formation models highlighted earlier, and the popular explanation for the thick disc formation, so-called **hybrid models** of Galaxy formation have become the most accepted scenarios. These distinguish between a spherical outer halo and a flattened inner halo (Gould, Flynn & Bahcall 1998, Sluis & Arnold 1998, Chen et al. 2001, Siegel et al. 2002, Chiba & Beers 2000, Gould 2003). In this theory the outer part formed from accretion of satellite galaxies and/or mergers and the inner region was most likely created by a dissipative contraction on a short timescale, à la ELS (Sandage 1990), whilst the thick disc is the result of the heating of an old thin disc by a merger. Such models provide explanation for the observed duality of density, kinematic and age distributions of the inner and outer halo field stars (Sommer-Larsen & Zhen 1990, Norris 1994, Carney et al. 1996, Sommer-Larsen et al. 1997), and can account for any age difference between the outer and inner globular clusters (Zinn 1996, Rosenberg et al. 1999).

With such a scenario whether there is a clear boundary between the outer "accreted" and inner "contracted" regions of the halo is naturally questioned. Chiba & Beers (2000) argue that their result of a continuous decrease in rotational velocity with increasing $Z_{max}$, and sim-

ilar lack of distinction in the global halo density distribution, provide evidence against such a boundary, as does the lack of accepted theoretical explanations for the existence of two distinct halo populations. Consequently they argue that the formation of both inner and outer regions occurred approximately simultaneously. This is in agreement with Chiba & Yoshii (1998), who deduce that their finding of a metallicity gradient in the MWTD indicates that the halo contraction to the thick disc occurred just shortly after the main parts of the halo were assembled. This concept that the populations of the Galaxy form continuous, rather than discrete, distributions in kinematics, age and abundance is one that is gaining acceptance (Siegel et al. 2002).

The hybrid formation scenario is also consistent with the currently favoured cold dark matter (CDM) models of growth, extending the principles of Big Bang cosmology to the formation of the Galaxy. As the protogalaxy collapses, small scale fluctuations in the CDM density attract gas and each other, and star formation begins in these clumps. The clumps merge mostly dissipationlessly, which results in a final spherical density distribution, and the independent history of each fragment creates a wide age spread and no metallicity gradient in the final system, since older, metal-poor stars and metal-rich newborn stars will be found in each clump. The large clumps then sink to the centre due to dynamical friction and dissipative merging with smaller clumps, and, with the final merger between the large fragments at the centre of the system, their constituent stars are spread throughout the inner regions, and most of the gas sinks to the centre.

This "CDM scenario" explains the observed flattened density distribution and prograde rotation of the inner halo, and possibly why its angular momentum distribution is similar to that of the bulge (Wyse & Gilmore 1992), since the bulge could have largely formed from gas released in the final mergers at the centre. It also can explain the existence of low-metallicity stars ([Fe/H] $\lesssim -1.7$) on highly radial orbits that are inconsistent with a pure accretion model, since such stars could be those formed in the final infall of the large fragments. Conversely, the dominance of low-$e$ stars in the outer halo (Sommer-Larsen et al. 1994) can similarly be explained, since torque between fragments or their mergers would transfer angular momentum outwards (Sommer-Larsen & Christensen 1989). This is due to fragments with more radial orbits being more likely to be disrupted by collisions in the denser, inner parts of the system, so they would be less likely to return to their initial orbits in the outer regions. Hence more circular orbits would be more likely to survive further out, resulting in the majority of outer

halo stars being on low-$e$ orbits.

The existence of retrograde stars and young stars (Rodgers, Harding & Sadler 1981) in the high halo can also be explained by the hybrid scenario, since such stars would be the result of later, delayed accretions. The age spread among halo field stars and globular clusters is also explicable by this model, as is the lack of metallicity gradient and ([Fe/H], $e$) relation in the halo (Chiba & Yoshii 1998).

This "standard model" of formation is therefore largely verified by observations to date, and is gaining acceptance as the most likely scenario of Galactic formation. However, problems still remain. The contradictions with the SZ model from globular cluster observations (§2.1.5) are also discrepant for the hybrid model, and much of the evidence is still somewhat uncertain. The conflicts between different studies over findings such as the existence of a retrograde halo component, the formation of the thick disc and the presence of metallicity and velocity gradients imply that such "facts" are still far from being well-determined.

It is therefore clear that despite the great advances in the theory of galactic evolution and structure made since the middle of the century, many more data and studies are required in order to attempt to resolve the discrepancies that remain between the models and observations. Given our location inside what appears to be a typical spiral galaxy, the study of stellar populations in our own Galaxy remains one of the most effective probes of the evolution of galaxies and structure in the Universe. In particular, the ancient stellar halo of the Galaxy can inform more about its history than any other component, and the chemical and kinematic analysis of its stars is one of the most important challenges facing Galactic astronomy today.

## 2.2 Galactic structure surveys

The study of the stellar populations of the Galaxy represents perhaps the most effective and direct probe of its constituent components — the spheroid, discs and bulge — and hence of its current structure and evolutionary history. In particular, in order to unlock the historical information contained in the thick disc and halo populations, studies need to employ efficient techniques of identifying their stellar members with minimal contamination from other astro-

nomical sources. Concentrating here on studies of the Galactic spheroid, surveys probing this population are divided into three main types:

*(i)* **Selected local surveys** use chemical or kinematic properties of stars in the solar neighbourhood to isolate old thick disc and spheroid stars.

*(ii)* **Tracer surveys** probe the stellar halo beyond the local contamination of the solar neighbourhood with either clusters or bright or easily-identifiable stars, acting as *tracers* of their parent population.

*(iii)* ***In situ* surveys** study complete samples of dwarfs from the spheroid in a similar way to selected surveys, but employ only stars at large distances from the Galactic plane, thus avoiding disc contamination problems.

These probes of the Galactic spheroid are now discussed in more detail, with examples and descriptions of the advantages and disadvantages of each type of survey.

### 2.2.1 Selected surveys in the solar neighbourhood

Although locally halo stars are massively outnumbered by those from the disc (by about 500:1), selected surveys can identify stars from the halo by virtue of their high velocities and/or low metallicities, both properties associated with this older population. Since spheroid stars have much higher heliocentric velocities than their disc counterparts, proper motion surveys — whereby stars are selected with a minimum cut on tangential motion — have proved the most effective at isolating spheroid members (eg. Carney et al. 1990, Dahn et al. 1995, Carney et al. 1996, Gould 2003). However, there are some complications inherent in these kinematic and metallicity selection methods:

*Thick disc contamination:* stars of the extended disc are also likely to have high velocities and low metallicities, meaning that they can cause a significant contamination of spheroid samples. When velocity criteria are used, even a very small thick disc contaminant can significantly affect the derived spheroid density estimate due to their

much greater frequency in the solar neighbourhood over that of spheroid stars (Bahcall & Casertano 1986)

*Kinematic bias:* proper motion surveys are intrinsically biased, and stars with low heliocentric velocities will not be selected. However, these affects can be largely accounted for on a statistical basis with kinematic models of the Galactic populations.

*Unaccounted-for stellar classes:* surveys selecting stars with extreme kinematics and/or metallicities can miss whole families of stars that may be important to the Galactic structure. An example of this are the metal-poor stars with low-orbital eccentricities missed by the ELS kinematic selection, but which when later found cast doubt on their Galaxy formation model (Chiba & Beers 2000).

*Population overlap:* selected surveys probe the solar neighbourhood region, where the spatial overlap of the different stellar populations is close to its maximum. The kinematic and metallicity mixing of the galactic components adds to the difficulty of selecting stars from one population whilst avoiding contamination from others. Samples are obtained by assuming that within a certain range of one parameter (eg. tangential velocity or metallicity) the stars from just one population will dominate.

Despite these intrinsic difficulties, selected surveys have been successfully probing the Galaxy for decades, and with increasingly sophisticated and realistic models of its structure, the selection effects they entail can be more effectively accounted for. Such surveys also need not only probe local regions: deep proper motion surveys such as those of Majewski (1992) and Méndez et al. (1999) are able detect stars as far as 30 kpc away.

### 2.2.2 Tracer surveys

Tracer surveys of the stellar halo avoid the mixing of the stellar populations close to the disc by only considering objects at large distances from the plane. Globular clusters or stars with high luminosities or unique colours are used to trace and infer the global properties of the spheroid. In addition, with assumed density distributions the characteristics of the thin and thick discs can be estimated by extrapolating the observed halo features. These extrapolations are prone to

error, however, since any departure from the assumed distributions can have a significant effect on the results. Using a small sample of objects to infer global characteristics of a population is also clearly susceptible to systematic errors: any variations in population parameters such as age, chemical composition, kinematics or star formation history can lead to selection biases and influence derived results. Some of the most commonly used tracers are now outlined.

**Giant stars.** Red giants can probe regions as deep as 100 kpc away due to their high intrinsic luminosities, and are selected on spectral and photometric properties. However, these stars are very rare ($\sim$1-10 per square degree to $V = 20$; Morrison et al. 2000), and samples are prone to contamination from disc K dwarfs, very metal-poor halo subdwarfs, and extragalactic objects such as compact galaxies and QSOs. The first of these can be avoided with accurate photometry or spectra and the latter with spectroscopic follow-up, but the subdwarfs present significant problems (Morrison et al. 2000).

**Globular clusters.** Globulars can be used to investigate the kinematics, metallicity and age of the spheroid, and to measure the Galactic mass distribution (eg. Zaritsky et al. 1989). There are several caveats to their employment as halo tracers, however. Systematic differences between clusters in different regions of the Galaxy create problems, with the division between disc and halo clusters complicated by those with relatively low metallicities but disc kinematics, and suspicions that outer and inner halo globulars may exhibit different parameters such as age and metallicity (see §2.1.5.) The number of well-studied clusters is also small and so the tracers are limited, but perhaps most prominent is the unsuitability of using clusters to trace the field star population. Clusters members are known to have different metallicity distributions to field stars (Laird et al. 1988), and are influenced by the effects of dynamical processes that do not affect their counterparts in less dense environments. It is therefore not generally appropriate to use clusters as tracers of field stars.

**Horizontal branch stars.** Horizontal branch (HB) stars such as RR Lyrae or blue horizontal branch (BHB) stars are effective tracers as they have high luminosities and are easily identifiable from their blue colours, or variability in the case of RR Lyraes. These latter types are effective probes of the outer halo, visible to large distances (100 kpc for an SDSS $r$ magnitude of $\sim$21; Ivezić et al. 2000), and have a well-known and small

absolute magnitude range, so their distances can easily be determined. Again, however, the rarity of these types of stars limits their usefulness as tracers, and selection effects can introduce biases. Certain lower-metallicity RR Lyraes are hard to detect, and BHB stars are also easily confused with "blue stragglers" (main sequence globular cluster stars well blueward of the turnoff point which therefore should have evolved off the main sequence.) Additionally, the relative numbers of HB stars varies with parent population parameters such as metallicity, and it is therefore argued that the entire range of HB stars (RR Lyrae, BHB and red HB stars) should be used to trace each population (Majewski 1993), even though RHB stars are much harder to detect. However, these steps to avoid selection effects are much less important in populations which do not have significant age or metallicity gradients.

**Carbon stars.** These are detectable to large distances and are easily recognised through their very red colours in the optical. They have been used recently to trace the stream of the disrupted Sagittarius dwarf galaxy in the outer halo (see §2.3.5; Ibata et al. 2001b). However, carbon stars are very rare, and it is difficult to ascertain their distances.

**Dwarf spheroid field stars.** Certain types of brighter dwarf stars from the halo can also be used as tracers of the global spheroid population. Those near the main sequence turnoff can be identified through their colours of $0.38 \lesssim (B-V) \lesssim 0.5$, whilst young main sequence blue metal-poor stars (Preston, Beers, & Shectman 1994) have $(B-V) \lesssim 0.38$ — these are the field analogues of "blue stragglers". These can both trace the spheroid to distances of 16 kpc, but are prone to contamination from thick disc stars (although this is less significant at fainter magnitudes), white dwarfs, quasars and RR Lyrae stars.

### 2.2.3 *In situ* surveys

In contrast to the selected surveys, which through kinematic or abundance selection obtain samples of dwarf spheroid stars locally, or tracer surveys which probe the outer halo with rare, bright stars, *in situ* surveys attempt to obtain complete samples of dwarf halo stars at large distances from the plane. Such surveys provide ideal probes of the outer halo, sampling the major constituent of the stellar population in regions where disc contamination is non-existent.

There are, however, obvious difficulties in detecting faint dwarf stars at such large distances, with magnitude limits significantly fainter than $V = 20$ necessary to obtain sufficiently large samples. With these constraints the number of studies employing these techniques has been limited, and those that are able to probe to such depths face complications from contamination by unresolved galaxies and quasars. Galaxies outnumber stars by an order of magnitude at $V \approx 22$ and star-galaxy separation is difficult below $V \approx 20$, especially with data with low spatial resolution such as that from Schmidt photographic plates. However, most quasars can be separated photometrically because of their unusual colours, and with high resolution observations galaxies can be efficiently identified to faint magnitudes: Gould et al. (1998) obtain a pure sample of halo subdwarfs using HST data, for which star-galaxy discrimination is reliable to $I \approx 23.8$.

### 2.2.4 This study

There are therefore several different types of survey that are used to investigate the structure of the Galactic stellar halo, and many varieties of stellar sample with which to conduct each one. Each type of survey has its inherent benefits and disadvantages, although the availability of data often dictates that which is most applicable — a large scale wide-field survey is not possible using (narrow) HST data, for example. Some surveys are restricted as probes of the stellar halo population by severe selection effects (eg. globular clusters as tracers), current observational limits (*in situ* subdwarf surveys) or by samples comprising only a tiny fraction of the total halo population (bright star tracer surveys). This latter drawback is particularly relevant in the light of discoveries of significant kinematic and spatial substructure in the outer halo (§2.3.5) — indeed, Ibata et al. (2001b) use carbon stars to probe such features. In light of these considerations, and with large amounts of digitised long time baseline photographic data available from SuperCOSMOS scans of survey plates, this thesis is concerned with a selected proper motion survey to identify and study halo subdwarf stars within a few kiloparsecs of the Sun. Although there are kinematic biases inherent in such identification techniques, strict velocity criteria can eliminate any significant contamination, and improved kinematic models of the disc and halo (eg. Chiba & Beers 2000) can compensate effectively for any selection effects. In order to study the stellar halo large samples of stars representative of the entire population are required, and subdwarfs are the best choice for such probes. With large subdwarf

samples currently unattainable beyond the discs, proper motion surveys have proved arguably the most efficient method of selecting such stars locally, and therefore provide one of the most effective techniques with which to study the inner halo, with the ultimate aim of unravelling the secrets of the structure and evolution of the Galaxy.

## 2.3 The study of subdwarfs

As the most common members of the oldest component of the Galaxy, subdwarfs are crucial for understanding its current structure and evolutionary history. Their local scarcity means that they are difficult to detect, although proper motion studies (eg. Carney et al. 1996) have provided several examples of the brighter, early-type (F-K) subdwarfs in the solar neighbourhood, yielding important information about their chemical composition, density and kinematics. However, only small samples exist of the fainter, later-type subdwarfs beyond the immediate solar neighbourhood. As a result, there are significant uncertainties surrounding the characteristics of not only the subdwarf population itself, but also of the stellar halo ("spheroid") as a whole. These include ambiguity over the shape and normalisations of the luminosity and mass functions, and poor determination of the shape, stellar content and kinematics of the spheroid at distances beyond the solar neighbourhood. Through this enhanced understanding of the spheroid the analysis of subdwarfs can yield vital clues as to the processes that formed the Galaxy, and it can also greatly improve our knowledge of stellar evolution.

### 2.3.1 The subdwarf luminosity and mass functions: motivation for study

The luminosity function is simply the spatial number density of a type of object as a function of absolute magnitude; the subdwarf luminosity function therefore describes the number of subdwarfs per unit volume per magnitude bin. Derivation of the number density of subdwarfs in the form of the luminosity function is important for a number of reasons. One of the most significant of these is the ability to transform the luminosity function into a mass function (the number of stars of each mass) by assuming a mass-magnitude relation. The form and shape of the subdwarf mass and luminosity functions have key implications for several areas of both Galactic and stellar astronomy.

**Star formation & stellar evolution**

The mass function of low-mass stars such as subdwarfs, which have lifetimes comparable to the age of the Universe, provides constraints on the star-forming conditions in the early Galaxy. Comparing the mass function of old, metal-poor subdwarfs with other types of stars allows determination of the mass function as a function of epoch and metallicity, and hence describes the conditions in which the different populations of stars formed: for example, stars forming in regions of higher temperature are expected to have higher masses. In a spectroscopic survey of subdwarfs, Hartmann & Gehren (1988) find evidence for a deficiency of low-mass, metal-poor subdwarfs, which could indicate that the initial mass function at the formation epoch of the Galaxy was biased towards higher mass stars. This would be in accordance with an explanation for the rarity of F & G disc stars with low metallicity (the "G dwarf problem", Sommer-Larsen 1991), which suggests that the halo gas was already enriched from high-mass, short-lived stars when it settled to form the disc. Stars of different masses have significantly different effects on their environments: whereas high mass stars enrich the interstellar medium (ISM) with metals through supernovae, low-mass stars lock up ISM gases for long periods. Knowledge of the relative numbers of stars in each mass range and variations of the initial mass function with different star-forming conditions is therefore crucial to developing star formation and stellar evolution theories, and can constrain the processes of the formation of the Galaxy. It is also important for comprehending events in the early universe: the great age of subdwarfs means that their mass function is important to the understanding of star and galaxy formation at high redshifts, where conditions are similar to those in the early Galaxy. The relevance of the stellar initial mass function to all areas of astronomy is a prime motivation for its study: it directly controls the chemical and luminosity evolution of the Universe, yet only in our own Galaxy can it be examined directly in a range of environments.

**Galactic baryonic dark matter**

The subdwarf mass function also has relevance to understanding the nature of "dark matter" in the Galaxy. The subdwarf mass function provides not only the number density of subdwarfs in the spheroid, but it can be extrapolated to estimate the halo densities of white dwarfs and sub-stellar objects. The mass-to-light ratio can therefore be ascertained, as can the contribu-

tion of each of these populations of objects to the baryonic dark matter content of the halo. Subdwarfs are thought to constitute only a negligible part of this dark matter (Bahcall et al. 1994, Flynn, Gould, & Bahcall 1996, Chabrier & Mera 1997, Fields, Freese & Graff 1998), but their contribution to the mass budget is important: whilst the true proportion of halo stars remains uncertain, then the amount of dark matter certainly does. Despite early signs from microlensing studies, brown dwarfs are now thought to constitute only a small amount of the missing mass (Flynn et al. 1996, Chabrier & Mera 1997, Fields et al. 1998, Chabrier & Baraffe 2000). White dwarfs, on the other hand, remain a serious candidate for contributing a major proportion of baryonic halo dark matter (see Evans 2002 for a discussion of possible halo dark matter candidates.)

Microlensing experiments indicate that a maximum of 25% (EROS; Afonso et al. 2003) to 50% (MACHO; Alcock et al. 2000) of the halo's mass may be in the form of objects with masses up to $M_{\odot}$ . White dwarfs are the only likely candidates with masses of this magnitude, so over the recent years there have been many surveys dedicated to the search for these stellar remnants in the halo (Knox, Hawkins, & Hambly 1999, Ibata et al. 1999, Oppenheimer et al. 2001, Majewski & Siegel 2002, Nelson et al. 2002).

A revision of white dwarf atmosphere models led to the recognition that these stars become *bluer* with age rather than redder as previously thought (Hansen 1999). This transformed the searches, and resulted in the first discoveries of cool, fast-moving halo white dwarfs (Hambly, Smartt, & Hodgkin 1997, Ibata et al. 2000). Speculation that a number of blue high proper motion objects in the Hubble Deep Field (HDF) could be halo white dwarfs (Ibata et al. 1999) was disproved when these were shown to be spurious detections (Richer 2002), but the debate was reignited with the discovery of a large number of local old WDs by Oppenheimer et al. (2001), a study with which I was involved.

Oppenheimer et al. (2001) claimed that 38 of the white dwarfs in their sample were halo members by virtue of their high tangential velocities. If true then this new population of cool halo white dwarfs constitutes a *lower limit* of two percent of the halo dark matter, and could provide a natural explanation for the microlensing results. This finding sparked significant debate, with claims from kinematic arguments that the white dwarfs found by Oppenheimer et al. (2001) are in fact high-velocity members of the thick disc (Reid, van Wyk et al. 2001,

Reylé, Robin & Crézé 2001, Gibson & Flynn 2001), or perhaps the debris from a "shredded" satellite galaxy (Gilmore et al. 2002). Other analyses have supported the conclusion that these are halo white dwarfs (Koopmans & Blandford 2002), or even the bright part of a large faint population (Hansen 2001). Further recent surveys also suggest that white dwarfs comprise a significant fraction of the halo mass (Goldman et al. 2002), or even all of the thick disc and halo dark matter in the solar neighbourhood (Mendéz 2002).

This debate has profound implications for many different areas of astronomy. Confirmation that white dwarfs are responsible for a non-negligible proportion of the Galaxy's dark matter would help resolve the missing mass problem; ruling them out as dark matter candidates would suggest that the unseen mass is largely non-baryonic. There are wider implications too, for the existence of a large population of ancient white dwarfs would have repercussions in star formation theory and the chemical evolution of the Galaxy, and would affect extra-galactic astronomy. Under current theories of stellar evolution these old white dwarfs would have ejected more metals into the interstellar medium than are currently observed (Gibson & Mould 1997), and would result in brighter Galaxy halos at high redshifts from their precursors (Charlot & Silk 1995), whilst also suggesting an initial mass function that is biased to higher masses. Existing theories of stellar physics also imply that the white dwarf progenitors would restrict the levels of $\gamma$-rays emitted to lower than those seen today, and a large halo white dwarf population could be inconsistent with the baryonic density of the universe derived from primordial nucleosynthesis (Freese, Fields, & Graff 2001).

Whilst the confirmation of a significant number of white dwarfs in the spheroid would have a resounding effect on these diverse fields of astronomy, the discovery of Oppenheimer et al. (2001) is also intrinsically linked to the Galactic subdwarf population. The assertion that the density of halo white dwarfs found is between 5 and 10 times the expected value (Koopmans & Blandford 2002, Oppenheimer et al. 2001) is calculated from expected spheroid white dwarf number densities derived from the subdwarf luminosity function of Gould et al. (1998). This determination is obtained from a relatively small sample ($\sim$160) of subdwarfs, so a more accurate derivation of the subdwarf luminosity function will provide a crucial reference point in the search for baryonic halo dark matter. The subdwarf mass function derived from the luminosity function therefore ideally complements microlensing observations in this research.

**Spheroid density profile**

The subdwarf luminosity function can be integrated over a magnitude interval to yield the number density of subdwarfs. If samples are taken over a wide range of lines of sight and to sufficient depth, then the variation of number density with direction can be used to accurately determine the density law governing the spheroid. It is becoming increasingly clear that the spheroid is not adequately described by simple models, with recent studies providing evidence for a two component stellar halo density, with an inner flattened part and a near-spherical outer component. Several surveys have found that an axial ratio that increases with Galactocentric radius is necessary to fit observations, whether from samples selected by proper motion (Carney et al. 1996), metallicity (Sommer-Larsen & Zhen 1990, Allen et al. 1991, Chiba & Beers 2000), stellar type (Preston et al. 1991a, Preston, Shectman, & Beers 1991b) or from star counts (Siegel et al. 2002). It is also likely that even this two-component model is not strictly sufficient, with the presence of kinematic star streams in the outer halo (see §2.3.4) possibly prohibiting these more distant regions from being described by a single, smooth density distribution (Siegel et al. 2002).

The distribution of the inner spheroid is expected to be relatively unaffected by such streams (Siegel et al. 2002, and references therein), and so the subdwarf luminosity function provides an ideal means with which to explore its density law. Indications are that a power law of the form $\rho(r) \sim r^{-3}$ and an axial ratio of $(c/a) \approx 0.6$ describe the local spheroid data (Gould et al. 1998, Sluis & Arnold 1998, Yanny et al. 2000, Ivezić et al. 2000, Chen et al. 2001, Siegel et al. 2002, Gould 2003), and this can be verified from a large subdwarf sample along many different lines of sight.

Determining the spheroid density distribution has implications for our understanding of galaxy formation and evolution. Evidence for a two component stellar halo would contradict the expectation of a uniform distribution predicted by the ELS galaxy formation model (§2.1.1), and indications of a more complex halo structure would provide evidence for kinematic and spatial substructure arising from a merger history.

**Globular cluster evolution**

As well as yielding the stellar mass function and the spheroid density profile, the subdwarf luminosity function can also enhance understanding of globular cluster evolution. Comparing the luminosity and mass functions of globular clusters with those of field stars of similar ages and metallicities can highlight evolutionary processes in the clusters. The mass-to-light ratios of globulars are low and their mass functions flatter than other old stellar systems such as bulges and elliptical galaxies, and it is thought that the evaporation of the low-mass stars in the clusters could be responsible for this (Piotto & Zoccali 1999, Kroupa 2001). This would be manifested by a field star mass function that is steeper than that for globular clusters. Obtaining luminosity and mass functions for clusters is considerably easier than for field stars, particularly with deep photometry from the HST, so accurate derivations of mass functions exist for a number of different metallicity clusters (eg. Santiago, Elson, & Gilmore 1996, Chabrier & Mera 1997). Determining a field luminosity function of sufficient accuracy to match these cluster observations would therefore significantly improve our understanding of globular cluster dynamics and evaporation and hence of the evolution of the Galactic spheroid.

**Other applications**

Knowledge of the halo stellar density from the luminosity function is useful for a wide range of astronomical applications, as described above. Indeed, these are not just restricted to Galactic astronomy, but also include extra-Galactic studies: faint spheroid stars can significantly contaminate samples in galaxy number counts and redshift surveys, for example, so an accurate determination of their expected density is also useful in this respect.

### 2.3.2 The subdwarf luminosity function: recent results

With their local rarity and intrinsic faintness making them hard to detect, there are two principal methods used to efficiently search for subdwarfs. The traditional method is to exploit the high heliocentric velocities of halo stars by imposing a minimum proper motion limit on the sample. This biases selection towards halo members, increasing the ratio of disc to halo stars from

around 500:1 for a volume-limited sample to about 4:1 for the proper motion-limited one.

The bias this selection introduces can be modelled with assumed velocity ellipsoids for the disc and halo, although there remains a significant sensitivity towards the kinematic models used. A further disadvantage of this method arises with contamination of the sample from high-velocity thick disc stars; however, imposing a strict lower tangential velocity cut-off can render this negligible.

The alternative method is to perform deep star counts, looking beyond the solar neighbourhood and Galactic discs to probe pure regions of halo stars. This approach has been made possible with the advent of sensitive telescopes such as the HST, enabling accurate star-galaxy separation at large distances where the stellar population contains only halo members. Whilst samples derived in this method have none of the contamination problems of the kinematic studies, there are disadvantages. The great distances probed mean that trigonometric parallaxes are currently unobtainable, so photometric parallaxes have to provide the sole indicator of distance and hence luminosity. Additionally, these distant samples are more prone to bias arising from unresolved binaries, and there is no opportunity to obtain follow-up spectra of the sample members.

Most studies have employed the method of proper motion selection to determine the halo luminosity function, simply because it remains the most efficient method for obtaining samples of local halo stars. Work in this field was pioneered by Schmidt (1975), who produced the first determination of the halo luminosity function and mass density. He used a sample of 126 stars with proper motions, many also with parallaxes, and applied a lower proper motion and tangential velocity cut-off to identify 17 non-white dwarf halo candidates. From this he used the $V_{max}$ method (§4.5.1) to derive a luminosity function and mass function, determining a halo mass density of $1.7 \times 10^{-4}\, M_{\odot}\mathrm{pc}^{-3}$.

With only small samples of halo stars obtainable from the observations at the time, attempts to improve Schmidt's first estimate of the density were limited. Eggen used his large proper motion catalogue to identify potential halo candidates based on the eccentricity of their orbits in the Galactic plane (Eggen 1979, 1983), and derived an estimate of the halo density ten times larger than Schmidt (1975). However, Bahcall & Casertano (1986) reanalysed the samples of

Schmidt (1975) and Eggen (1979, 1983) , and found that the more relaxed selection criteria of Eggen (1983) meant that his sample was heavily contaminated by disc stars. Reconciling the studies of Schmidt (1975) and Eggen (1979, 1983) by imposing a stricter velocity cut-off on the latter and compensating with correction factors derived from Monte Carlo simulations, Bahcall & Casertano (1986) derived a number density of $n \approx 9 \times 10^{-5}$ pc$^{-3}$ for each sample.

The next significant advance came through the growing availability of accurate trigonometric parallaxes for large numbers of stars from studies such as the USNO parallax programme (Monet et al. 1992). Dahn et al. (1995) used a subset of stars from the LHS catalogue of Luyten (1979) with USNO parallaxes where available, and applying proper motion and tangential velocity selection they obtained a sample of 114 candidate halo stars from which they derived a population II luminosity function to unprecedented accuracy. From the shallow slope of their luminosity function towards faint magnitudes they speculated that substellar objects contribute little towards the halo dark matter, and derived a number density of $1.23 \times 10^5$ kpc$^{-3}$ for the same magnitude range ($4 < M_V < 11$) as Bahcall & Casertano (1986).

Gizis & Reid (1999) offered a more refined approach to the determination of the luminosity function, using spectra of candidate halo stars to identify them as disc or halo M dwarfs using the classification scheme of Gizis (1997). Gizis & Reid (1999) used photographic data from POSS-I and POSS-II plates, applying a lower proper motion limit and tangential velocity cut-off to select candidate subdwarfs. They then used the $V_{max}$ method to derive the luminosity function of the final sample of ~50 confirmed M subdwarfs, although they only obtained an estimate in the range $11 \lesssim M_V \lesssim 12.5$.

The most recent determination of the subdwarf luminosity function uses a kinematically-defined sample nearly two magnitudes larger than from any previous study. Gould & Salim (2002) and Salim & Gould (2002a,b) have revised the New Luyten Two-Tenths (NLTT) catalogue (Luyten 1980), providing improved astrometry from Hipparcos (Perryman et al. 1997), Tycho-2 (Høg et al. 2000), Starnet (Röser 1996) and USNO-A catalogues (Monet 1996, 1998), and enhanced photometry from the Two Micron All Sky Survey (2MASS). Gould (2003) uses the method of reduced proper motion (RPM) with the revised NLTT to discriminate between the disc and halo members, identifying a huge sample of $\sim$ 4500 potential subdwarfs. He then uses a maximum-likelihood method to derive the luminosity function to unprecedented

accuracy.

The alternative to kinematic selection of the subdwarf sample is the very different approach employed by Gould et al. (1998) of using deep star counts. They used deep HST images to probe to over 40 kpc in many directions, photometrically selecting $\sim$166 candidate subdwarfs with distances greater than 8 kpc. Using maximum likelihood methods they determined estimates for the halo density power law and luminosity and mass functions from their sample.

Although the size of the samples from which the subdwarf luminosity function is determined has increased dramatically since the first estimate of Schmidt (1975), there has not been the expected overall improvement in the agreement between different studies. Figure 2.2 shows the recent results of the determination of the subdwarf luminosity function, with the kinematic studies of Bahcall & Casertano (1986), Dahn et al. (1995), Gizis & Reid (1999) and Gould (2003) shown along with the star count analysis of Gould et al. (1998). As in Gould et al. (1998), the luminosity functions of Bahcall & Casertano (1986) and Dahn et al. (1995) have been respectively scaled by 0.62 and 0.75 to reflect the use of larger completeness fractions derived from an improved determination of the halo velocity ellipsoid by Casertano, Ratnatunga, & Bahcall (1990) (CRB90).

It is evident from Figure 2.2 that the *shape* of the luminosity functions are mostly in accordance, with the peak at $M_V \approx 11$ present in all of the results. There is also little evidence for a increasing number densities towards faint magnitudes in all of the luminosity functions, confirming results from independent studies that faint subdwarfs are unlikely to make a significant contribution to the dark matter content of the Galactic halo (Bahcall et al. 1994; Flynn et al. 1996; Chabrier & Mera 1997; Fields et al. 1998).

However, although the studies to date are in fair agreement as to the shape of the luminosity function, there is clearly significant disagreement over its normalisation, and hence over the space density of halo subdwarfs. This is most striking in the range $9 \lesssim M_V \lesssim 13$, where there is as much as a factor of four difference in the derived densities. Even among the kinematic studies there is significant discrepancy, with the luminosity function from Bahcall & Casertano (1986) predicting far fewer stars than those of Dahn et al. (1995), Gizis & Reid (1999) and Gould (2003), all of which are in rough accordance. One explanation of why the

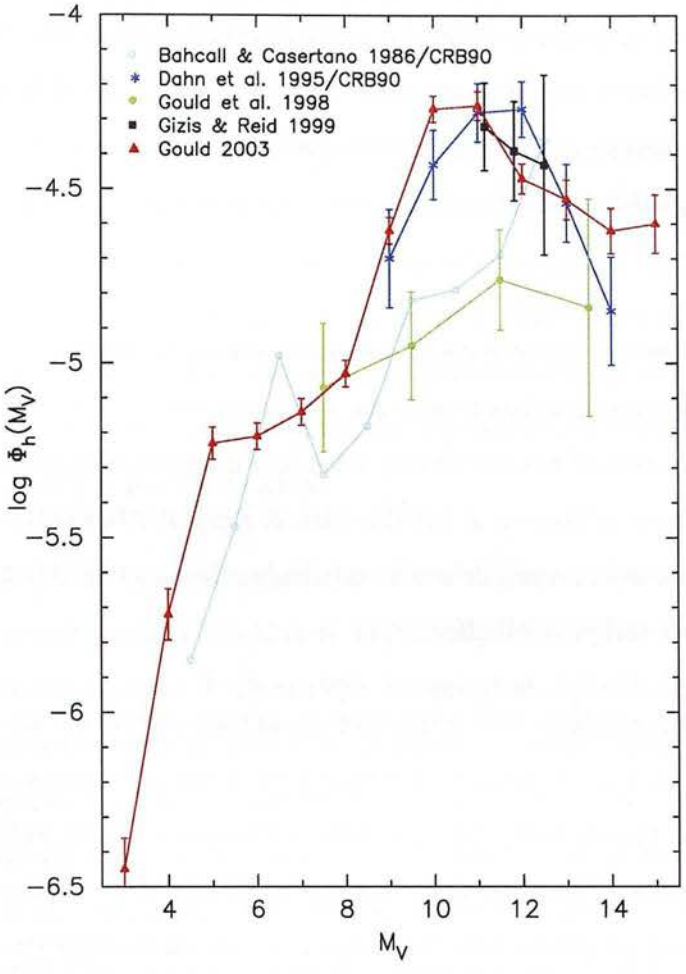


*Figure 2.2: Existing estimates of the subdwarf luminosity function, with the kinematic studies of Bahcall & Casertano (1986)/Casertano et al. (1990) (light blue) Dahn et al. (1995)/Casertano et al. (1990) (dark blue), Gizis & Reid (1999) (black) and Gould (2003) (red), and the deep starcount study of Gould et al. (1998) (green). The luminosity functions of Bahcall & Casertano (1986) and Dahn et al. (1995) have been scaled by 0.62 and 0.75 respectively, allowing for the improved estimates of halo kinematics by Casertano et al. (1990) (CRB90). With the Bahcall & Casertano (1986) result likely to be significantly underestimated due to sample incompleteness, the number density predicted by the deep HST study is many times lower than that suggested by the kinematic analyses.*

Bahcall & Casertano (1986) luminosity function suggests a lower density of subdwarfs (even with the smaller correction factor originally used by Bahcall & Casertano 1986) could be due to incompleteness of their sample towards the Galactic plane. Gizis & Reid (1999) indicate that as a result the Bahcall & Casertano (1986) luminosity function may be as much as 30% incomplete, although this only accounts for about one third of the discrepancy between their respective results.

Despite the differences between the kinematic results, by far the largest discrepancy in the luminosity function normalisations is with the star count study of Gould et al. (1998). This analysis suggests a subdwarf number density some four times lower than that derived from the local kinematic samples of Dahn et al. (1995), Gizis & Reid (1999), and Gould (2003) (Figure 2.2), and this has prompted much debate as to whether the cause of this discrepancy lies in systematic errors or a real physical effect.

Systematic effects are likely to be responsible for at least some of the inconsistencies. Even the kinematic studies rely on samples probing a large range of volumes, and the sensitivity of the completeness factors to the different halo kinematics assumed will lead to variations in the derived densities. The photometric parallaxes derived in the studies that do not have trigonometric parallax information are also subject to error, particularly since the large spread of the metallicity of halo subdwarfs relates to a large variation in absolute magnitude, and hence distance, for a given colour. The linear colour-magnitude relation (CMR) assumed by Bahcall & Casertano (1986) is a poor match to the observed sequence (Baraffe et al. 1997), and the local calibrating stars used to calibrate the CMR for the deep HST sample of Gould et al. (1998) may be biased to higher metallicities and hence partially explain the lower luminosity function derived by that study (Gizis & Reid 1999).

Contamination from non-halo stars is also likely to play a part in the observed discrepancies, with thick disc stars a particularly likely source of error. The high velocity tail of the thick disc component has a substantial overlap with the halo kinematic distribution, and so care has to be taken to exclude such stars from the sample. Even a small number of contaminant thick disc stars in the sample can significantly affect the derived number densities, since, as discussed by Bahcall & Casertano (1986), these brighter stars are biased towards larger distances and hence make a magnified contribution to the luminosity function determination.

Significant levels of contamination are unlikely with studies that use spectroscopic confirmation of sample members such as Gizis & Reid (1999) and those that impose a strict tangential velocity cut-off as in Dahn et al. (1995). However, these analyses rely heavily on the assumed velocity ellipsoids, and the assumption of Gaussian kinematics, which, if in error, would significantly alter the results. The large sample of Gould (2003) is also prone to thick disc contamination, since the candidate subdwarfs are selected simply by cuts made by eye in the reduced proper motion diagram (see §3.7.1), and it is likely that a significant number of thick disc stars exists in the sample. With no correction made for the contribution these stars make to the derived space density, it is likely that the luminosity function of Gould (2003) represents an upper limit to the true function.

Despite these possible systematic errors, the difference between the local kinematic studies and the deep star count result of Gould et al. (1998) may be due to a real effect. There are suggestions (eg. Sommer-Larsen & Zhen 1990, Preston et al. 1991a,b, Siegel et al. 2002 — see §2.3.1) that the stellar halo consists of two components: a large spherical part and a more local flattened constituent. These components are expected to have similar densities at the solar circle, but would lead to a density at a few kiloparsecs above the Galactic plane that is about half that in the solar neighbourhood. Although not sufficient to account for the entire difference between the kinematic and star count number densities (Reid & Hawley 2000, p435), it could go some way towards explaining the discrepancy, with the flattened, higher density, local subdwarf component not sampled by the deep HST data. This may also help to explain why the luminosity functions are more discordant at brighter magnitudes but agree for the faintest bins: brighter stars probe greater distances and hence are more sensitive to variations in the Galactic structure. Faint stars are sampled to much smaller distances on the other hand, and so are expected to be less affected by the halo density profile.

However, there is only provisional evidence for a two-component halo, and it is uncertain whether such structure can fully account for the discrepancies in the luminosity functions and for observed star counts (Siegel et al. 2002). It is clear therefore from the inconsistencies in the determinations of the subdwarf luminosity function to date that further investigations are required. A large sample of subdwarfs along many different lines of sight could help resolve the issue of whether the observed discrepancies are due to systematic errors in the analyses or reflect a real density variation in the structure of the halo. Confirmation of the latter would have

significant implications for the structure and evolution of the Galaxy.

### 2.3.3 The subdwarf mass function - recent results

As previously explained (§2.3.1), the mass function of low mass stars in the spheroid is important for our understanding of a wide range of astronomical topics. A better definition of this mass distribution would improve the current theories of star formation and the evolution of stars, galaxies and globular clusters, and would help determine what objects are and are not responsible for the baryonic dark matter present in the Galaxy. However, the mass function of the spheroid low-mass field stars such as subdwarfs is at present poorly-defined, for a number of reasons.

#### Deriving the mass function

In order to determine the mass function of a population or sample of stars, the individual stellar masses must be determined. These can only be directly measured in binary systems, so direct observational determination of the mass function is not possible. The most useful observable quantity is the surface brightness of stars, or the luminosity function. A mass-luminosity relationship must therefore be assumed in order to convert a luminosity function $\Phi(M) = \frac{dN}{dM}$ into a mass function $\Psi(m)$:

$$\Psi(m) = \frac{dN}{dm} = \frac{dN}{dM}\frac{dM}{dm} = \Phi(M)\frac{dM}{dm} \tag{2.1}$$

The function $\frac{dM}{dm}$ can in principle be derived from empirical data, but there are no direct observational determinations of masses for stars below solar metallicity with which to calibrate the relationship (Chabrier 2003). A theoretical mass-luminosity relation is therefore required, and a number of these have been computed for metal-poor stars in recent years (D'Antona & Mazzitelli 1996, Alexander et al. 1997, Baraffe et al. 1997).

However, there are a number of complications and caveats to the adoption of a theoretical mass-luminosity function. One of the main problems is that the mass function derived is very sensitive to the mass-magnitude relation through the use of its derivative in Equation 2.1. This

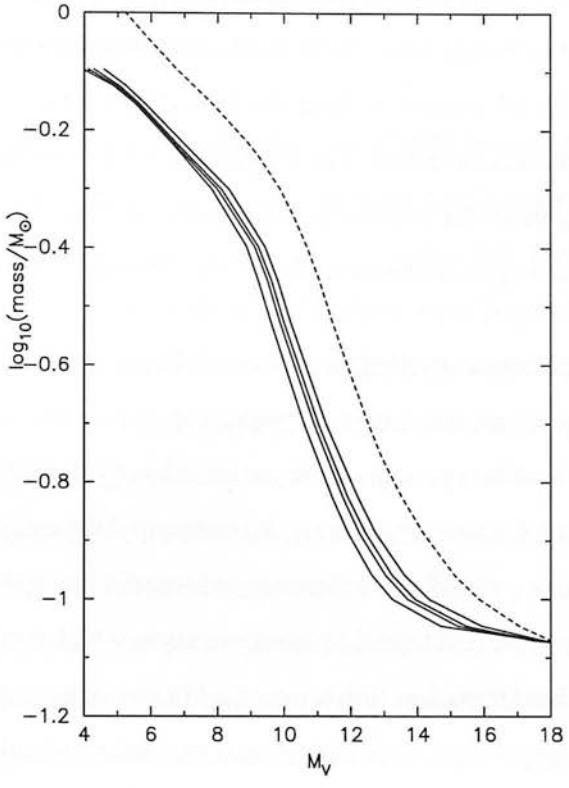


*Figure 2.3: The mass-luminosity relationships predicted by the models of Baraffe et al. (1997) (solid lines) for metallicities (from bottom to top) [m/H] = -2.0, -1.5, -1.3 and -1.0. Also shown is the solar-metallicity, 1 Gyr model of Baraffe et al. (1998) (dashed line). The metallicity dependence of the relations is clear.*

causes any errors in the models to be magnified, and the shallowness of the function close to the hydrogen-burning limit ($\approx 0.072\,M_{\odot}$) means that in these regions a small interval in mass is distributed over a large range in luminosity and so large uncertainties arise. The mass-luminosity relation can therefore introduce artefacts into the derived mass function.

The mass-luminosity relations are also correlated with metallicity, and the fact that subdwarfs span a large range in abundance means that in principle different mass-luminosity functions should be used for each metallicity interval. Subdwarf samples with accurate abundance determinations are usual too small to permit this approach, however, so a single relation corresponding to the modal subdwarf metallicity (typically [m/H] $\sim$-1.5) is adopted. This clearly compromises the accuracy of the derived masses.

Multiple stellar systems also affect mass functions derived from luminosity functions that are unable to resolve most binary stars. With most stellar populations having a large binarity fraction (at least 30% for M-dwarfs — Reid & Gizis 1997), many companion stars will be present in the sample but not detected. The distribution of the secondary mass typically increases with decreasing mass for a given primary mass (Malkov & Zinnecker 2001), so the contribution of low mass stars is underestimated in surveys that do not detect companions.

Globular clusters provide an alternative method of deriving the mass function for spheroid stars. The cluster members are more homogeneous than field stars, having very similar ages, chemical compositions and distances, and with the abundances of clusters known to high precision, the problems arising from the metallicity dependence of the mass-luminosity relation are avoided. However, there are significant difficulties inherent in this approach, not least because it still relies on use of a theoretical mass-luminosity relation, which is where many of the uncertainties in deriving the field mass function arise. In addition, extracting faint cluster stars from the background field population is problematic, and uncertainties in the cluster distance scale will affect results. Most significantly, dynamical evolution in clusters means that their derived mass functions cannot be readily applied to field stars in any case; indeed, comparison of field and cluster mass functions is used as a means to understanding cluster evolution. It is therefore unsuitable to estimate the spheroid field mass function from globular cluster luminosity functions. In light of this, and in spite of the difficulties outlined above, the spheroid mass function is at present most accurately derived from the field luminosity function and a theoretical mass-luminosity relation. Whilst the use of this relation will introduce uncertainties, comparisons between theoretical functions and observationally-derived relations show that such effects will be modest (Chabrier 2001).

**Current mass function results**

Several recent studies have derived estimates for the spheroid mass function from field star luminosity functions. Graff & Freese (1996b) used the 114 solar neighbourhood spheroid stars with trigonometric parallaxes from the sample of Dahn et al. (1995), in conjunction with the stellar models of Alexander et al. (1997), and determined a power law $dN/dm \sim m^{-\alpha}$, with $\alpha \leq 2$. Extrapolating this mass function into the brown dwarf regime ($m < 0.072\,M_{\odot}$), they

use this result to infer that brown dwarfs contribute less than 3% to the local spheroid mass density.

Chabrier & Mera (1997) also used the Dahn et al. (1995) luminosity function to derive the mass function, and compared this with that derived from the photometric luminosity function (ie. photometric parallaxes were used for distance estimates) of Richer & Fahlman (1992). Chabrier & Mera (1997) found that both mass functions were consistent with a slope of $\alpha \approx 1.7 \pm 0.2$ to $0.1 \leq m \leq 0.8\,M_{\odot}$, outside of which range they were unable to adequately constrain the function, and integrated the mass function to derive a spheroid density of $n = 1 \times 10^{-4}\,M_{\odot}pc^{-3}$. Comparing the field star mass function with those derived for several globular clusters, they found qualitative and semi-quantitative similarities, and claimed that this indicates a common origin for these stellar populations. They also compared the field star mass function predictions with star counts in the Hubble Deep Field (Flynn et al. 1996), and from the correlation between expected and observed number counts concluded that there are very few subdwarfs in the dark halo: at most just 1% of the spheroid population.

The deep HST starcount study of Gould et al. (1998) also provides a mass function estimate, using a maximum likelihood method applied to modelled and observed colour-magnitude diagrams to determine the mass function directly rather than converting the luminosity function. This approach is analogous to the method used to derive their luminosity function and avoids the metallicity-degeneracy of the mass-luminosity relations, although it still has to estimate the metallicity of each star by interpolating across a colour-magnitude diagram of stars with trigonometric parallaxes using the isochrones of the Baraffe et al. (1997) models. From their sample of 166 spheroid stars Gould et al. (1998) found that a power law mass function with $\alpha \approx -0.75$ for $0.09 < m < 0.71\,M_{\odot}$ provides the best fit to their data (with no binarity correction) and is similar to those of globular clusters of moderate to high metallicity.

Reid & Hawley (2000) formed a composite subdwarf luminosity function by combining data from Bahcall & Casertano (1986) for $M_V < 9$ and from Dahn et al. (1995) for $M_V \geq 9$. With a single mass-luminosity relation corresponding to [m/H] $= -1.5$ from Baraffe et al. (1997) they subsequently derived a subdwarf field mass function with $\alpha \sim 1.65$ and which they integrated to estimate a local spheroid density of $7.8 \times 10^{-5}\,M_{\odot}pc^{-3}$.

Chabrier (2003) used the luminosity function of Gould (2003) in conjunction with the Baraffe et al. (1997) mass-luminosity relations for [m/H] $= -1.5, -1.0$ and $-0.5$ to produce a subdwarf mass function estimate. To show the effect of the variation of different luminosity functions on the derived result, he contrasted these mass functions with one from an updated version of the luminosity function of Dahn et al. (1995) and the Baraffe et al. (1997) mass-magnitude relations (Figure 2.4.)

The subdwarf mass function results to date indicate that the spheroid mass function has a different shape to that of the disc, and is steeper in the intermediate mass ranges of $0.25 - 0.8\ M_{\odot}$. It appears that the spheroid mass function "turns over" at the hydrogen-burning limit, which implies that brown dwarfs are unlikely to contribute a significant amount to the halo mass (Graff & Freese 1996a, Chabrier & Mera 1997). Perhaps the most apparent conclusion from the studies to date is that the subdwarf mass function is poorly-defined, and that a power law is an inadequate description of the observed distribution. Significant efforts are therefore required to improve the accuracy of the spheroid mass function before it can be used to shed light on key areas of current astronomical research such as galactic and stellar formation and evolution, and the nature of Galactic dark matter.

### 2.3.4 Spheroid kinematic substructure: motivation for study

In hierarchical structure formation scenarios favoured by current cold dark matter cosmologies, galaxies form by the gravitational amplification of protogalactic "fragments" and subsequent mergers of satellite galaxies (see White 1996 and references therein). These mergers are crucial to understanding the nature of galaxies: they may be the dominant process in determining the Hubble type (Silk & Wyse 1993), and a merger creating a heated disc is presently the most popular theory explaining the origin of thick discs (Velazquez & White 1999).

Evidence for mergers in the Galaxy can therefore provide information essential to determining the theories of galaxy and structure formation. They offer tight constraints on what structures merged in the Milky Way, and when, and on early star formation in the thick disc. Knowledge of the amount of halo substructure due to mergers in the Galaxy can test cold dark matter (CDM) cosmologies and could also help to solve the "dwarf satellite problem" (Bullock,

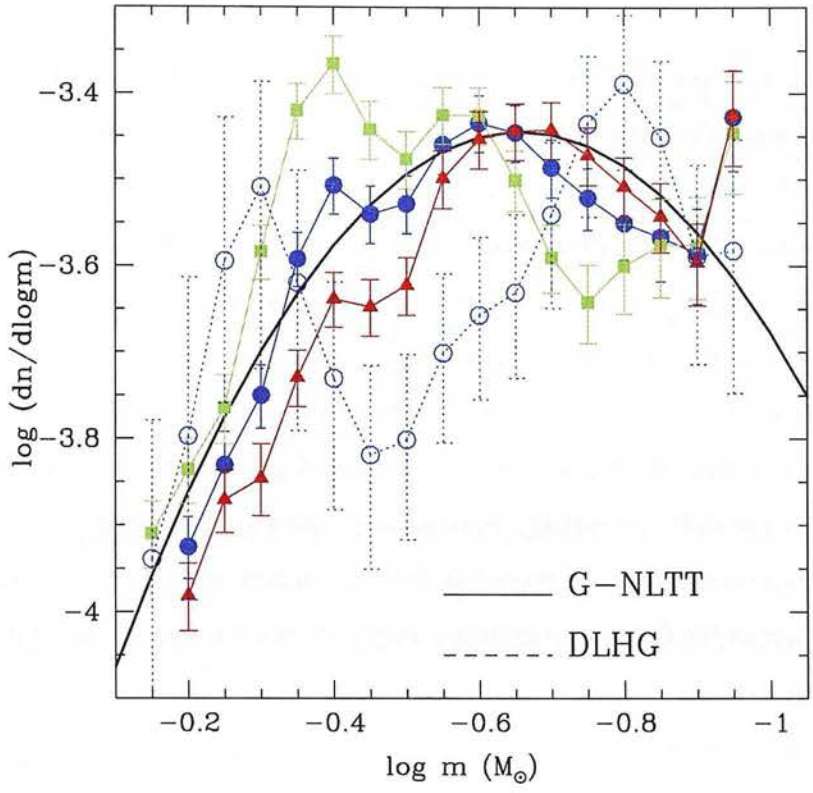


*Figure 2.4: Spheroid mass function estimates from Chabrier (2003), based on the Gould (2003) luminosity function (solid lines) and the Baraffe et al. (1997) mass-luminosity relations for [m/H] = -1.5 (red triangles), -1.0 (filled blue circles), -0.5 (green squares). The dotted line shows the mass function from the Dahn et al. (1995) luminosity function and the Baraffe et al. (1997) [m/H] = -1.0 model. Comparison of these mass functions demonstrates that whilst using different metallicity models results in only a relatively small variation in the derived mass function (since metallicity has only a limited effect on the slope of these mass-luminosity relations), using different luminosity functions has a much more pronounced effect. Accuracy of the luminosity functions is therefore central to deriving a reliable mass function estimate. The solid line shows the lognormal fit to the mass function from Chabrier (2003), from which this figure is taken.*

Kravtsov, & Weinberg 2001) — whereby CDM $N$-body simulations of galaxy formation tend to predict many more satellite galaxies than actually seen (Moore et al. 1999).

If the galaxy was formed by primordial clumps combining and the later merging of satellite galaxies, then simulations predict that although after 10 Gyr there will be little evidence in the *spatial* distribution of stars, there should be *kinematic* substructure in the halo (Lynden-Bell & Lynden-Bell 1995, Johnston, Spergel, & Hernquist 1995, Helmi & White 1999). This takes the forms of "streams" of stars in co-moving groups in the halo, coherent in velocity. CDM cosmology simulations imply that large numbers of such streams should be present, possibly sufficient to account for the entire stellar halo (Bullock et al. 2001). Simulations by Helmi & White (1999) indicate that a single, $10^8 L_\odot$ dwarf galaxy disrupted 10 Gyr ago would be evident from about 30 streams in the *local* halo today. If the entire halo were made up of swallowed satellites, then there should be 300-500 streams present locally. Searching for this fossil evidence of the Galaxy's formation history has become the subject of much attention in recent years.

### 2.3.5 Spheroid kinematic substructure: recent results

One of the first confirmed detections of spheroid substructure came from a proper motion survey of Galactic structure and kinematics towards the North Galactic Pole (Majewski 1992, Majewski et al. 1994, 1996). Evidence for a co-moving group of halo stars was found from proper motions, and radial velocity measures confirmed clumps of stars in phase space and metallicity. This provided evidence that the halo is not dynamically mixed, and that a large fraction of it may consist of such streams. This hypothesis was later supported by Helmi & White (1999), who applied numerical simulations to the Majewski et al. (1996) sample, and claimed that the clumping was part of two independent halo streams.

The most significant example of halo substructure was the discovery by Ibata et al. (1994) of the tidally-disrupted Sagittarius dwarf galaxy and its associated streams of stars. This striking example of satellite merging in the Galaxy has been the focus of many studies, with analyses of its structure (Mateo, Olszewski, & Morrison 1998), kinematics (Ibata et al. 1997) and metallicity and stellar age (Layden & Sarajedini 2000) among those conducted since its discov-

ery. The Sagittarius streams have been detected in many studies, with evidence in carbon stars samples (Ibata et al. 2001b) and the presence of a northern stream (Martínez-Delgado et al. 2001), that if associated with the Sagittarius galaxy would confirm simulations indicating that the debris from disrupted satellites could completely envelop the halo and account for a large proportion of its stellar content (Helmi et al. 1999). The great extent of the Sagittarius tidal tail is borne out by the large number of kinematic detections of its streams — for example from giant star studies (Dohm-Palmer et al. 2001, Kundu et al. 2002) and excess blue stars (Dinescu et al. 2002) (a continuation of the study of Majewski et al. 1994, 1996.) Several theoretical studies have also modelled the merging of the dwarf galaxy with the Galaxy and its predicted effect on halo substructure (Ibata & Lewis 1998, Ibata et al. 2001a, Johnston et al. 1999).

There is also increasing evidence for substructure in spatial, and not just kinematic, studies of the spheroid. Majewski et al. (1999) find clumps in colour-magnitude diagrams that are consistent with the Sagittarius stream detected in other analyses, although inconsistencies in the radial velocities of these stars indicate that they may form part of a previously undetected stream associated with the same disrupted galaxy. Large samples of A stars from the Sloan Digital Sky Survey (SDSS) (Ivezić et al. 2000, Yanny et al. 2000) also reveal remarkable spatial associations that can be explained as Sagittarius substructure (Ibata et al. 2001a,b). Newberg et al. (2002) also analysed SDSS colour-magnitude diagrams and found further Sagittarius clumps, and other substructure that could be a previously unknown disrupted satellite.

Indeed, in addition to the many detected streams from the Sagittarius dwarf galaxy, there is evidence both from simulations and observations that much of the halo is comprised of streams from absorbed satellites. From a kinematic study of the angular momenta of giant and RR Lyrae stars, Helmi et al. (1999) find streaming motions that appear to be from a single precursor structure that was disrupted during or soon after the Galaxy's formation, and that it accounts for as much as 10% of the stars in the halo outside the Sun's radius. Gilmore et al. (2002) conducted a spectroscopic study of ~2000 F and G stars close to the Galactic plane and find that their sample is dominated by stars from a satellite disrupted 10-12 Gyr ago. Although they do not find evidence for the large mergers expected in hierarchical clustering theories, they discover substructure indicative of minor mergers, and which may account for some of the structures found by Newberg et al. (2002).

**Probing the substructure with dwarf spheroid stars**

Although there is growing evidence for stellar streams in the Galactic halo, the study of kinematic substructure is still in its infancy and data from many separate surveys of different stellar types along many different lines of sight will help to determine the extent and nature of the structure. Indications of streams can be found from two-dimensional kinematic data from proper motion studies alone: indeed, one of the first identifications arose from the proper motion data of Majewski (1992), and Murray (1986) provisionally identified a co-moving group of stars from proper motions. The study of Dinescu et al. (2002) detected debris from the Sagittarius galaxy from colour and proper motion information. However, to efficiently detect streaming motions in limited samples three-dimensional velocities are required, with the simulations of Helmi & White (1999) suggesting that a velocity accuracy of $\sim$5km s$^{-1}$ is necessary in order to identify all of the expected streams in the local halo. However, the kinematic substructure can be easily discerned with a sample of several thousand stars and an accuracy of $\sim$20km s$^{-1}$(Helmi & White 1999, Morrison et al. 2000), which is within the reach of proper motion surveys with $\sigma_{\mu} \sim$ 10mas yr$^{-1}$ and $\sigma_{v_{rad}} \sim$10km s$^{-1}$ radial velocities.

Most surveys to date have used giant stars as tracers of the Galactic halo, simply because their high intrinsic luminosities means that they can be detected out to large distances. For example, the SDSS surveys (Ivezić et al. 2000, Yanny et al. 2000) use bright A stars, Ibata et al. (2001b) use carbon stars and Helmi et al. (1999) use red giants and RR Lyrae stars. The "Spaghetti" survey (Morrison et al. 2000) employs red halo giants and blue horizontal branch (BHB) stars as tracers which are visible to 100 kpc on 4m telescopes.

However, due to their short evolutionary timescales and the sharp decrease in spheroid density with radius ($\rho \propto r^{-3}$), stars such as giants and BHB stars are very rare, and are limited in the information they can impart about spheroid kinematics. On the other hand, dwarf stars are the most common stellar component of the spheroid, and are detectable in very large numbers. In addition to giant and BHB stars, Morrison et al. (2000) also use main sequence turn-off stars and blue metal-poor halo field stars, easily identifiable because of their colours, which occur with a far greater frequency than the giants. Despite their faintness meaning that they are visible only at smaller distances, dwarf stars can still be used to probe halo substructure. Simulations by Harding et al. (2001) of the "Spaghetti" survey show that a $10^7\ M_{\odot}$ satellite

galaxy that contributes 1% of the total spheroid mass can be detected from the velocities of just 100 halo turnoff stars in a 1 deg$^2$ field. This is with a magnitude limit of $V < 20$, which will probe halo turnoff stars to a maximum Galactocentric distance of $R \sim 20$ kpc.

Despite dwarf halo stars only being visible (with 4m telescopes) to within ~15-20 kpc of the Sun, they are nevertheless useful tracers of the spheroid due to their profusion (they constitute most of the stellar halo, after all) and the fact that their highly eccentric orbits mean that many sample regions far beyond the solar neighbourhood. This means, for example, that the "Spaghetti" survey turn-off stars will have apocentres up to 27 kpc from the Galactic centre, which is most of the distance to the edge of the spheroid. The ability of metal-poor solar neighbourhood stars to probe the global kinematics of the Galactic halo was first demonstrated by May & Binney (1986) and employed in later studies (Sommer-Larsen & Zhen 1990, Chiba & Beers 2000). By Jeans' Theorem — which states that for a well-mixed stellar population, the phase-space distribution function $f(\mathbf{x}, \mathbf{v})$ can be presumed to be a function only of isolating integrals of motion — it is possible to determine the phase space distribution at any given point in the spheroid by extending the orbits of solar neighbourhood halo stars to the entire halo. Thus, with a sample of $10^3 - 10^4$ local stars the phase space distribution function describing much of the spheroid can be determined.

However, this methodology will not be wholly applicable if the spheroid is not a well-mixed system. As explained above, the outer halo is expected to consist of many discrete stellar streams, and so extrapolation to global kinematic properties from local observations will be badly affected by such non-uniformities. The inner halo, on the other hand, is thought to be more well-mixed (Helmi et al. 1999, Harding et al. 2001), and Jeans' theorem extrapolation is therefore still at least approximately relevant in this region. Assuming that the inner spheroid is sufficiently mixed in phase space, dwarf spheroid stars within a few kiloparsecs of the Sun can thus be used as an effective probe of more global halo kinematics. If the well-mixed assumption is not valid then spheroid star streams should still be detectable in the solar neighbourhood. With large numbers of local metal-poor subdwarfs identified from proper motion techniques and supplemented with radial velocities (large numbers of these would be obtainable with a multi-object spectrograph), such a sample will be able to detect any halo streams that are present, and thus contribute to tests of galaxy and structure formation.

## 2.4 Future Galactic structure studies

As outlined in this introduction, whilst our understanding of much of the current structure and the evolution of our Galaxy has advanced significantly over the last few decades, there are many issues that remain unresolved. Aspects such as the history of the thick disc and the formation of the spheroid are still contentious, and much work remains to be done to improve our knowledge of these components. The progression of studies over recent years has led to the recognition (eg. Chiba & Yoshii 1998, Chiba & Beers 2000) that more *global* and representative studies of the stellar populations are required, with narrow-field pencil-beam studies liable to suffer from the effects of discontinuous structure such as clumps and streams in the spheroid. Larger samples of stars from each population with accurate proper motions and distances, together with precise multi-colour photometry (and ideally spectra), are necessary to formulate a picture of the properties of the entire stellar population of each Galactic component.

The solutions to many of the currently unanswered questions regarding Galactic structure will be provided with the advent of the astrometric satellites such as GAIA (Gilmore et al. 1998), which will measure the proper motions and provide photometry for nearly one percent of the stars in the Milky Way (and will produce radial velocity measures for a large fraction of this sample.) However, missions of this nature will not return results for many years (over a decade in the case of GAIA), so steps should be taken in the interim to work with existing data. This is made possible by new, huge wide-field surveys such as the SuperCOSMOS (SSS) and Sloan Digital Sky Surveys (SDSS), which provide data of sufficient depth and quality with which to undertake accurate, large-scale studies of Galactic structure. In this thesis I show how large samples of halo subdwarf stars are attainable from proper motion-selected subsets of these wide-field surveys. By analysing the characteristics of these populations of stars described above, such methods hence provide the potential to yield significant information about the current structure and evolutionary past of the Galaxy.

# Chapter 3

# The "Murray Programme"

## 3.1 Background

In the late 1970s and 1980s Murray and collaborators conducted a study into the use of measuring machines as a means of investigating the astrometric properties of nearby stars. In a series of papers they investigated some 15000 objects to $B \approx 18$ with a sequence of over 50 UK Schmidt plates taken during the period 1974-1977.

In their first paper (Murray & Corben 1979) they presented the results of a pilot study into using GALAXY measures for astrometry, determining the proper motion and parallax accuracies achievable. This work was continued in Murray, Argyle, & Corben (1986), when they derived positions, proper motions and parallaxes for ~6000 stars towards the South Galactic Cap (SGC), attaining accuracies of $\sigma_\pi \sim 15$mas yr$^{-1}$ and $\sigma_\mu \sim 7$mas yr$^{-1}$. Analysis of this sample was followed in Murray (1986), when maximum-likelihood techniques were used to derive a disc luminosity function and ascertain a disc scale height of 311 pc. Perhaps more significantly, evidence for a spheroid stellar stream was found from the proper motions, and from a difference between the proper motion zero point of the disc and spheroid stars in the sample, a shear in the disc was inferred.

Later the study was continued with the spectroscopic follow-up of stars in the SGC with unusual kinematics (Reid & Murray 1992). Although the data were too local for a detailed

study of the spheroid, a spheroid number density of $n \sim 4.4 \times 10^{-5}$ stars pc$^{-3}$ was derived.

The advent of CCDs and particularly the Hipparcos and Tycho missions (Perryman et al. 1997, Høg et al. 2000), with their great accuracy of proper motions, parallaxes and positions, seemed to indicate the demise of photographic astrometry in the 1990s. However, studies continued to demonstrate the importance of long time baseline photographic studies for proper motion studies (Evans 1992, Evans & Irwin 1995), especially with the use of a large number of plates taken of the same field to improve astrometric accuracy. Although unable to compete in terms of simple accuracy with the Hipparcos results, photographic material still had important potential, not least because even relatively shallow plates could reach stars more than 6 magnitudes fainter than those attainable with the $V \sim 12.5$ Hipparcos and $V \sim 11.5$ Tycho limits. Both Hipparcos and Tycho are significantly incomplete below $V \sim 10.5$, and so are unsuited to large-scale studies of dwarf stars which are fainter than this. The combined advantages of greater depth and long time baselines held by photographic data made a case for its continued use in proper motion studies, and there was a strong case for reviving the Murray study due to the increased accuracy available from the SuperCOSMOS measuring machine and vastly increased computing capabilities enabling many more stars to be analysed for proper motion and parallax in a single solution. Cooke & Reid (2000) therefore revisited the programme with a pilot investigation of astrometric plate material obtained by Murray during the period 1987-1994. They conducted an analysis of 4 of the plates from the complete dataset (see §3.2), obtaining follow-up spectroscopy of high proper motion stars and using this to derive disc and halo luminosity function estimates. The Cooke & Reid (2000) study acts as a precursor to the work in this thesis.

## 3.2 Plate data

The photographic sequence for the project initiated by Murray consists of over 250 plates taken from the period 1987-1994. There are 50-70 short (20 minute) astrometric V plates for each of three fields, and sky-limited $BVRI$ plates for photometric calibration. Details of these are given in Table 3.1. In addition to this UK Schmidt material, two Palomar Sky Survey I plates (POSS-I E & O, epoch ~1950) in field SA107 were added to provide a much longer time

baseline for enhancing proper motion accuracy.

| Field | Plate | Emulsion | Filter | Epoch | Exposure (min) |
|---|---|---|---|---|---|
| Astrometric plates | | | | | |
| SA94 | V (×52) | IIaD | GG495 | 1987-1994 | 20 |
| 87 | V (×67) | IIaD | GG495 | 1987-1994 | 20 |
| SA107 | V (×59) | IIaD | GG495 | 1987-1994 | 20 |
| Photometric plates | | | | | |
| SA94 | I13898 | IVN | RG715 | 1990.8 | 90 |
| SA94 | J13930 | IIIaJ | GG395 | 1990.8 | 80 |
| SA94 | R13420 | IIIaF | RG630 | 1990.8 | 100 |
| SA94 | V13977 | IIaD | GG495 | 1990.9 | 60 |
| 87 | I12306 | IVN | RG715 | 1987.9 | 90 |
| 87 | J13521 | IIIaJ | GG395 | 1990.0 | 70 |
| 87 | R12319 | IIIaF | RG630 | 1988.0 | 135 |
| 87 | V12311 | IIaD | GG495 | 1988.0 | 60 |
| SA107 | I15578 | IVN | RG715 | 1993.4 | 90 |
| SA107 | J14356 | IIIaJ | GG395 | 1991.4 | 75 |
| SA107 | R14344 | IIIaF | RG630 | 1991.4 | 90 |
| SA107 | V15572 | IIaD | GG495 | 1993.4 | 60 |

*Table 3.1: The astrometric and photometric plates in each of the three fields. The number in the 'Plate' column for the astrometric plates denotes the number of plates exposed and scanned per field.*

The three survey fields are described in Table 3.2, and are chosen so as to maximise the potential for kinematic analysis. All fields are approximately 90° from each other, enabling derivation of motions in three dimensions, in contrast to the original study, which in the direction of the SGC was unable to detect motion perpendicular to the Galactic plane. Additionally, Field 87 is close to the Large Magellanic Cloud, providing a good absolute reference for the proper motions.

| Field | RA | Dec | $l$ | $b$ |
|---|---|---|---|---|
| SA94 | 2h 53m | 0°12' | 175° | -50° |
| 87 | 6h 36m | -65°03' | 275° | -26° |
| SA107 | 15h 38m | -0°10' | 006° | +42° |

*Table 3.2: The J2000.0 coordinates of the three fields from the Murray programme, in each of which there are ∼60 short astrometric plates and sky-limited $UBVRI$ photometric calibration plates.*

## 3.3 SuperCOSMOS measures

The plates listed in §3.2 were scanned by SuperCOSMOS and processed by the Image Analysis Mode (IAM) software as described in Appendix A. The pixel data for each plate were also retained so as to enable inspection of the images if required during the reduction and analysis.

The plates were thresholded at $\sim 2.3\sigma_{\rm sky}$ above the background, as described in §A.1.4. However, due to features of the scanning process there is a variation in the threshold level from plate to plate, with some having a $3\sigma$ threshold. The plates are star-galaxy separated using the SuperCOSMOS classifications (§A.2.2).

## 3.4 Photometric calibration

Photometric measures are required for all stars in at least $B$ and $V$ for correcting for atmospheric refraction, and in $I$ for the separation of the sample according to reduced proper motion (see §3.7.1). However, the SuperCOSMOS instrumental isophotal magnitude is non-linear with respect to true external magnitudes, and varies from plate to plate. The non-linearities arise from the thresholding process and the limited dynamic range of the measuring machine, as well as non-linearities in the photographic characteristic curve with respect to the linear $(D, \log I)$ scale assumed (§A.1.1). It is therefore necessary to calibrate the SuperCOSMOS magnitudes with external CCD data.

In the case of SA94, CCD photometry was taken by Neill Reid for study by Cooke & Reid (2000). However, the photometry was calibrated to old COSMOS data, which had much poorer photometric measures than SuperCOSMOS, and covered an area of just $5.3° \times 5.3°$compared with the $6.25° \times 6.25°$scanned by SuperCOSMOS. This means that large areas of the plates in SA94 would have to be calibrated by extrapolating the COSMOS-calibrated data, and even the photometry of those objects near the plate centre is poor.

Unfortunately no extensive photometry of the SA94 region is published in the literature that is suitable for photographic plate calibration. However, photometry of suitable accuracy can be obtained by using an approach similar to that employed by the SuperCOSMOS Sky

Survey (Hambly et al. 2001b), whereby limited external CCD photometry is used to calibrate the SuperCOSMOS linearise profile magnitudes.

### 3.4.1 Linearised profile magnitude photometric calibration

#### Approximate profile magnitude calibration

The SuperCOSMOS *linearised profile magnitudes* are derived by linearising stellar isophotal magnitudes based on the invariance of their areal profiles as a function of magnitude: stars should have the same approximate profile shape (§A.1.5) regardless of their apparent brightness. This magnitude scale is determined by deriving a linearised transfer function between isophotal and profile magnitudes, using a method described in Bunclark & Irwin (1983). The linear profile magnitudes for stars are easier to calibrate against external data than isophotal magnitudes since they are better behaved over a wider magnitude range (Figure 3.1), allowing the magnitude calibration of a plate using only a few external standards. Although this magnitude scale is only useful for stellar objects, the photometry of galaxies is not required in this case, so this method is suited for the purposes of this study.

External CCD photometry is obtained from the Tycho Catalogue (Perryman & ESA 1997) and the Guide Star Photometric Catalogue I (Lasker et al. 1988), providing $BV$ photometry down to $V \sim 15$. Magnitudes in $RI$ are obtained using $(B-V, V-R)$ and $(B-V, V-I)$ relations derived from Landolt standards (Landolt 1992), and the photoelectric magnitudes are "naturalised" to photographic passbands using the relationships collated in (Hambly 1998) and given in Box 1.

| Photoelectric passband | Emulsion | Filter | Photographic passband |
|---|---|---|---|
| B | IIIa–J | GG395 | $B_J$ |
| V | IIa–D | GG495 | $V_{49D}$ |
| $R_C$ | IIIa–F | RG630 | $R_{63F}$ |
| $I_C$ | IV–N | RG715 | $I_N$ |

*Table 3.3: Photometric passbands defined by various emulsion/filter combinations*

Since the Tycho and GSPCI stars are relatively bright, additional, fainter photometric stan-

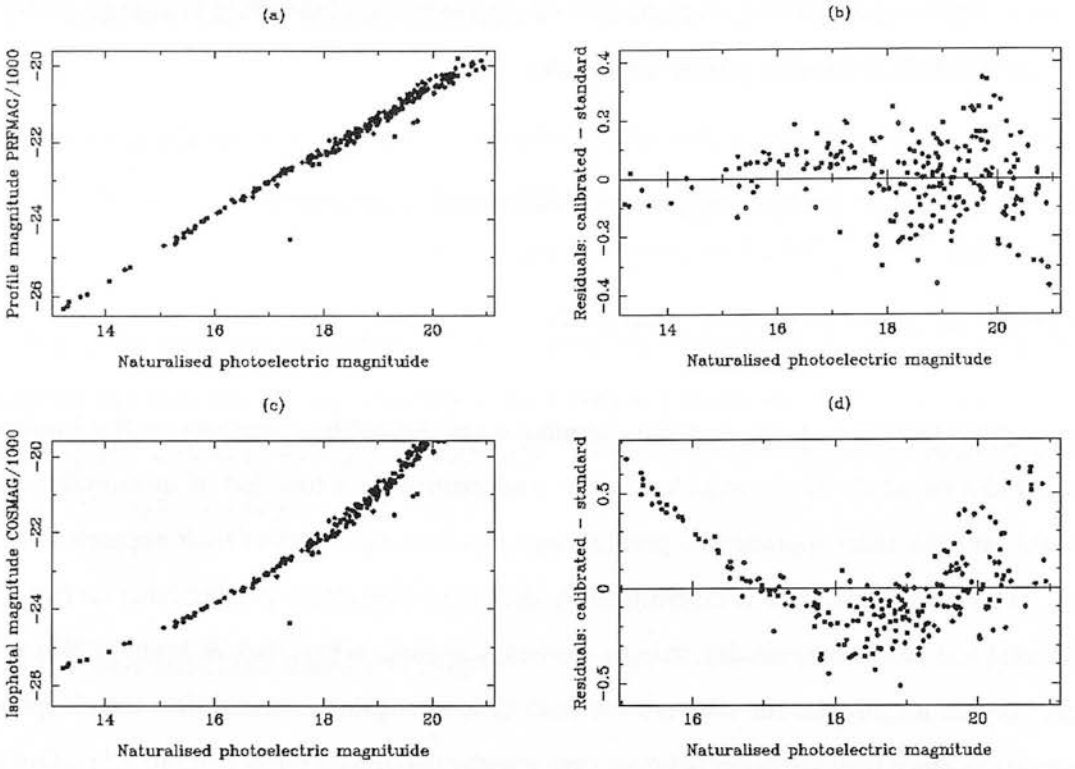


*Figure 3.1: A comparison of the linearised profile (a) and isophotal magnitudes (c) against naturalised CCD magnitudes from Hambly et al. (2001b) (their figure 5). The right panels show the residuals arising from linear least-squares fits and demonstrates the greater suitability of the profile magnitudes for calibration with CCD data. Whilst the linear profile magnitudes are linear over ∼8 mags, the isophotal scale is non-linear at the ∼0.5 mag level, and these non-linearities are non-repeatable between plates.*

dards are added from the Landolt (1992) catalogue in order to improve the calibration. The linearised profile magnitudes are then calibrated to the naturalised standard CCD magnitudes by a least-square fit, with the constraints that at a fixed point 3 mags fainter than the faintest calibrating standard the gradient is set to an appropriate mean value, and the second derivative of the fit is set to zero. The mean gradient is obtained from values published in Hambly et al. (2001b), derived by comparing each of the SSS survey plates against CCD data for the faintest 7 magnitudes in each survey. These constraints ensure that the calibration function can be extrapolated to the plate limit, and that it and its first derivative have no discontinuities. The resulting fitting function follows the true shape of the linearised stellar profile magnitude scale, which is linear over the faintest 7 mags, but is non-linear at the bright end due to the limited

$$
\begin{aligned}
B_J &= B - (0.28 \pm 0.04)(B-V); -0.1 \leq (B-V) \leq 1.6 \\
V_{49D} &= V - (0.10 \pm 0.02)(B-V); -0.1 \leq (B-V) \leq 1.6 \\
R_{63F} &= R_C - 0.013 - 0.204(R-I) + 0.1(R-I)^2 + 0.0295(R-I)^3 \\
(R-63F-I_N) &= -0.016 + 0.785(R-I) + 0.121(R-I)^2 + 0.027(R-I)^3
\end{aligned}
$$

where $(\mathrm{R}-\mathrm{I}) = 0.956(\mathrm{R_C}-\mathrm{I_C})$ and $(\mathrm{R_C}-\mathrm{I_C}) < 2.0)$.

Box 1: *Equations to "naturalise" photoelectric magnitudes to photographic passbands. From Hambly (1998).*

dynamic range of SuperCOSMOS and the photographic plates.

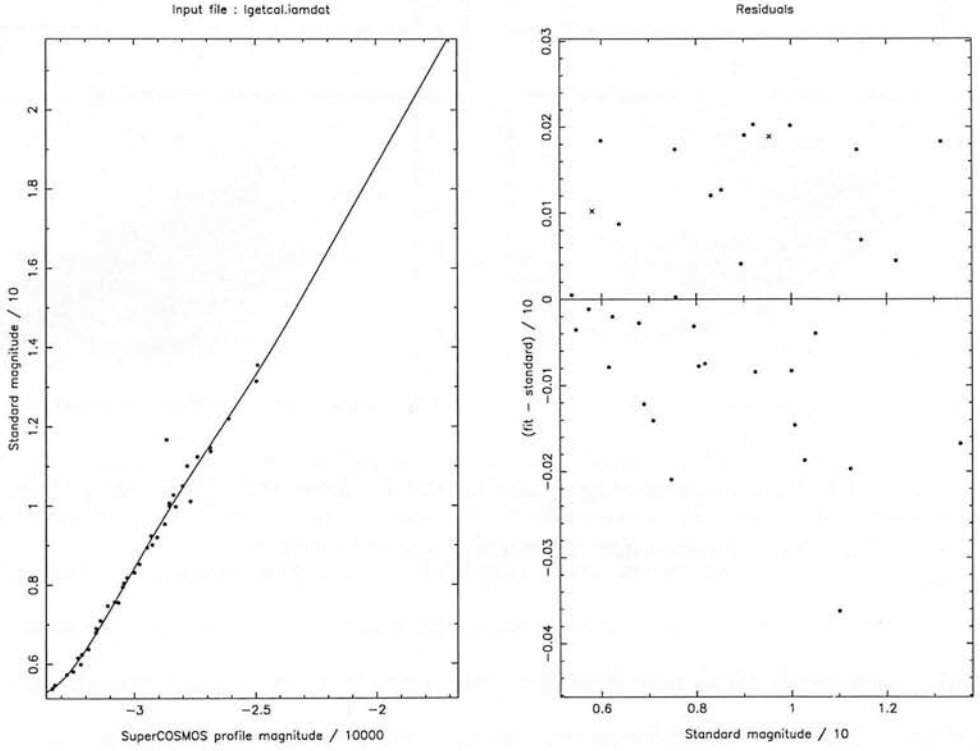


*Figure 3.2: The linearised profile magnitude calibration with external CCD data naturalised to the photographic system for I13898 in SA94. The left panel shows the result of a least-squares polynomial fit constrained to have a specified gradient at the faint end, and the right panel shows the residuals of the fit.*

The results of a typical example of this procedure in the $I$ band is shown in Figure 3.2. This process is repeated in each of $BVRI$ and the results from each calibration are combined

to create a catalogue of stars in each field with linearised $BVRI$ magnitudes. Small $\sim 10\%$ errors in the zero point of the faint magnitude calibration result from this method, which are as expected for photographic data. Colour-magnitude diagrams and colour-colour plots from the resulting calibrated magnitudes for SA94 are shown in Figures 3.3 and 3.4. There are clearly significant systematic effects present in the data, which are now addressed.

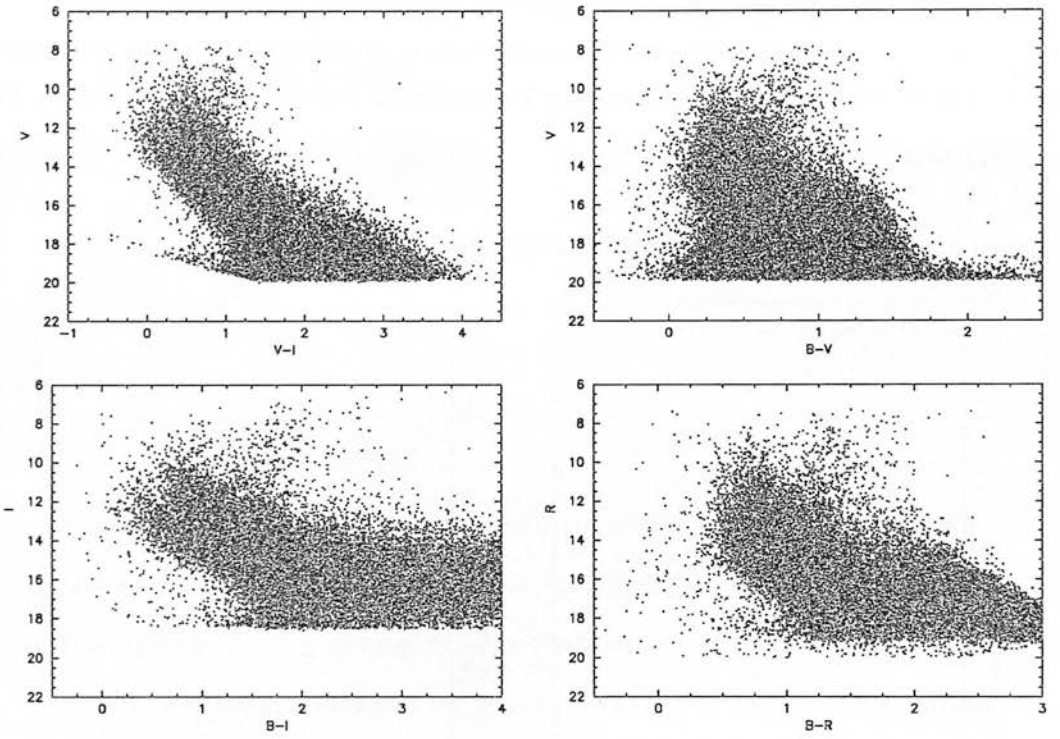


*Figure 3.3: Stellar colour-magnitude diagram for SA94 from linearised profile magnitudes* ***before*** *correction for systematic colour errors.*

### Correcting systematic photometric errors

It is clear from Figure 3.3 that the calibration function for the linearised profile magnitudes is not actually the same over the whole plate. This is particularly evident in the derived colours, and gives rise to spurious features in the colour-magnitude and colour-colour diagrams that also vary from plate to plate. For example, brighter stars tend to display systematically bluer colours and a larger scatter in the colour-magnitude diagram (Figure 3.3), and there is a poor correlation between colours and a significant spread in the two-colour diagram (Figure 3.4). These effects are due to a non-uniform response of the emulsion across the plate, and result in systematic photometric errors as a function of position and magnitude.

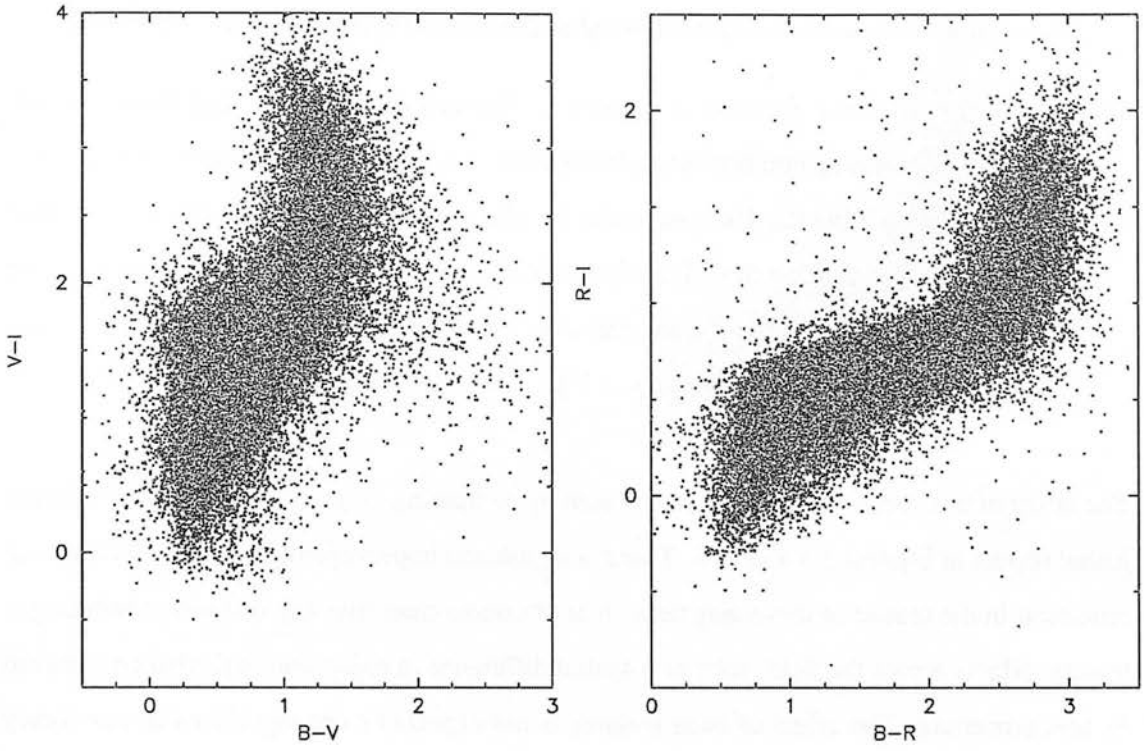


*Figure 3.4: Stellar two-colour diagram for SA94 from linearised profile magnitudes* ***before*** *correction for systematic colour errors.*

With no large numbers of external calibration stars known, the only solution is to use the stellar colour distributions to correct the data. The colour-position effects can be measured and corrected internally across each plate, but the colour-magnitude distributions must be straightened with respect to a global distribution via the median colour of the blue edge measured from many fields (see the second step below). This implies the assumption that the same population of stars is being sampled by each plate and each field, and that the colour-magnitude distributions are therefore expected to be the same for all plates. The algorithm operates in each band by measuring and correcting shifts in colour first as a function of position and then as a function of magnitude. These colour adjustments necessitate one passband being chosen as a standard against which to correct the others: the $B_J$ plates are used since there is more external photometry and calibrations tend to be more accurate at $B_J$ wavelengths. The two stages of the process are as follows:

(i) *Shifts in colour as a function of position.* These are measured by cross-correlating histograms of number-colour counts as a function of magnitude and position in 1 mag and 2cm bins. These bins are padded where data is sparse and resampled onto a grid three

times finer, and are then linearly filtered and smoothed to provide final shift values.

*(ii) Shifts in colour as a function of magnitude.* The colour-magnitude diagram is straightened by determining number-colour histograms as a function of magnitude in 1 mag bins and then calculating the 10th percentile in colour from the blue end. The data are then straightened by shifting this blue edge with respect to a fixed global value ascertained from the median blue edge of faint stars over the entire SSS dataset (0.689 for $(B_J - R)$, 1.204 for $(B_J - I)$ and 0.5 for $(B_J - V)$.)

The effect of this correction process can be seen by comparing Figures 3.3 and 3.4 with the adjusted results in Figures 3.5 and 3.6. There is significant improvement in the correlations and reduction in the scatter in these diagrams. It is of course clear that any real astronomical systematic effects across the field, such as a spatial difference in reddening, will also be removed by this procedure. The effect of such features is not expected to be significant in our survey fields with respect to the accuracy of photographic photometry, however, so these calibrations can be safely applied.

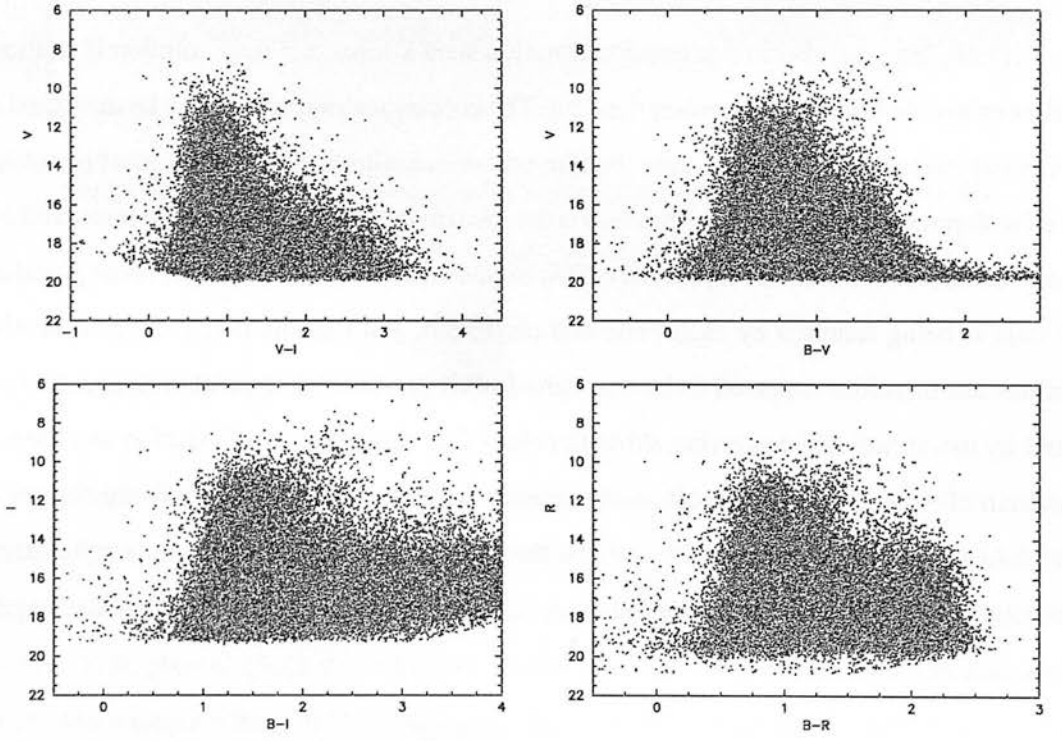


*Figure 3.5: Stellar colour-magnitude diagrams for SA94 from linearised profile magnitudes* ***after*** *correction for systematic colour errors.*

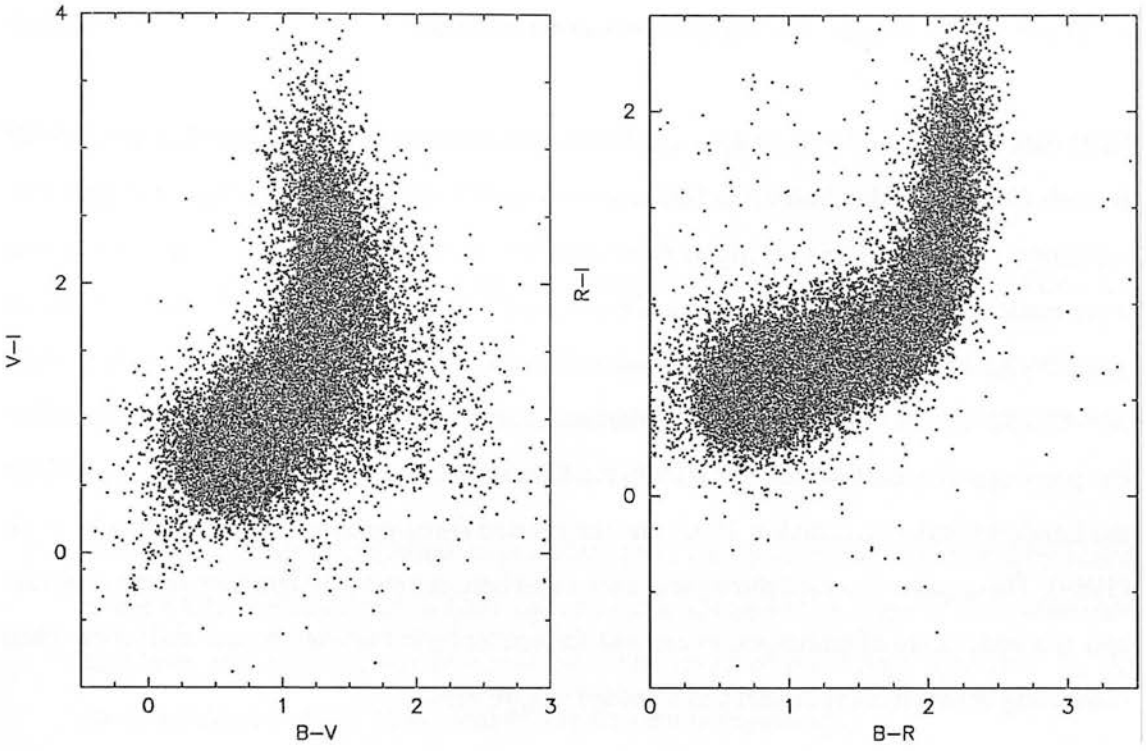


*Figure 3.6: Stellar two-colour diagrams for SA94 from linearised profile magnitudes* ***after*** *correction for systematic colour errors.*

### 3.4.2 Calibrating with large-scale CCD data

If large numbers of stars with accurate CCD photometry exist in a field then there is an alternative calibration technique to the linearised profile magnitude method described above. With calibration data extending below the plate magnitude limit, there is no need to rely on the linear extrapolation from brighter standards to fainter magnitudes, since calibration of stars close to the plate limit can be achieved using CCD observations of fiducial stars at comparable magnitudes. Using large quantities of deep CCD sequences in this way produces more reliable magnitude determinations for the more common fainter programme stars, and ones which are less likely to be affected by systematic effects than those obtained with the linearised profile magnitude method. For Field 87 and SA107 I was able to acquire calibrating CCD frames from observations at Siding Spring Observatory, which are now briefly described.

**CCD calibration sequences - observations and reductions**

CCD calibration data for Field 87 and SA107 were obtained from an observing run with Dr Russell Cannon on the Australian National University's 40" telescope at Siding Spring Observatory, Australia, over four nights from 30th March to 2nd April 2001. The observations were made using the Anglo-Australian Observatory's Wide-Field Imager (WFI), a mosaic of eight 2048×4096 pixel CCDs arranged in a 8192×8192 pixel array, producing a field of view of ∼52×52 arcmin. Several long (∼600s) and short (∼60s) exposures were made of different pointings in each field for $BVRI$ filters. Photometric standard stars were obtained from the Landolt Catalogue (Landolt 1992) and the revised E-region compilation of Menzies et al. (1989). These were observed throughout each night between every programme frame exposure and at a wide range of airmasses, to account for atmospheric fluctuations and extinction when converting between instrumental and standard magnitudes.

Reductions of the data were performed using standard IRAF procedures. The frames were bias-subtracted, linearity-corrected and flattened with twilight and dark sky flats, and the $I$-band images were defringed with a fringe map created from dark sky observations. Aperture photometry was achieved with the IRAF APPHOT package, and transformations from instrumental to standard magnitudes with PHOTCAL. Positions of the calibrating standards was obtained with the Starlink ASTROM astrometric reduction software, using fiducial stars with positions measured from the SuperCOSMOS Sky Survey. Only one CCD frame from the eight in the mosaic was used to provide calibration data for the photographic plates, since in this way difficulties mosaicing the CCD chips could be avoided whilst still ensuring that sufficient numbers of stars spread across each field were measured. Calibrated magnitudes were obtained for up to ∼1000 stars from each long exposure of the single chip, with a total of ∼2300 calibrating stars with $BVRI$ photometry acquired for Field 87 to a depth of $V \approx 20$.

**CCD calibrations method**

The observations and reductions provided several thousand stars per field, several magnitudes fainter than the astrometric plate limit, with which to calibrate the SuperCOSMOS isophotal magnitudes. The calibration method, as applied to both Field 87 and SA107, proceeds as

follows:

*(i)* From the CCD reductions a file containing the positions and $BVRI$ magnitudes of the calibration stars is created.

*(ii)* The CCD photoelectric magnitudes are "naturalised" using the relations given in Box 3.1.

*(iii)* The CCD photometry file is paired with each of the $B_J, V, R$ and $I$ photographic sky-limited photometric plates (star-galaxy separated) to create an index of pointers between each calibrating star and its corresponding SuperCOSMOS measure.

*(iv)* The SuperCOSMOS isophotal magnitudes (IAM parameter 9) are calibrated by fitting to the CCD measures with a least-squares cubic spline in the range of the calibration standards and with a linear fit elsewhere. The result of this fitting procedure for the photometric plate V12311 in Field 87 can be seen in Figure 3.7.

*(v)* Following the calibration there will be some systematic colour effects as a function of magnitude and position across the plate. These are removed and the colour-magnitude diagram "straightened" by the process described in §3.4.1. The final calibrated and straightened colour-magnitude diagrams for Field 87 are shown in Figure 3.8 and two-colour diagrams in Figure 3.9. These data appear more prone to systematic effects than the corresponding SA94 plots, but this is exacerbated by the much larger number of stars in Field 87: the final number of stars on the photometric plates with CCD-calibrated $BVRI$ photometry was $\sim$ 210 000 for Field 87, compared with $\sim$ 39 000 with linearised profile magnitudes in SA94. Additionally, most of these effects only appear at the bright and faint photometric plate limits, and would thus not affect the subdwarfs appearing on the shallower astrometric plates.

## 3.5 Astrometric plate reduction

As explained above, the $BV$ magnitudes are required in order to derive a star's astrometric parameters, and $I$ is used to plot reduced proper motion diagrams (§3.7.1). With photometric measures of each star on each of the sky-limited photometric plates obtained by the methods

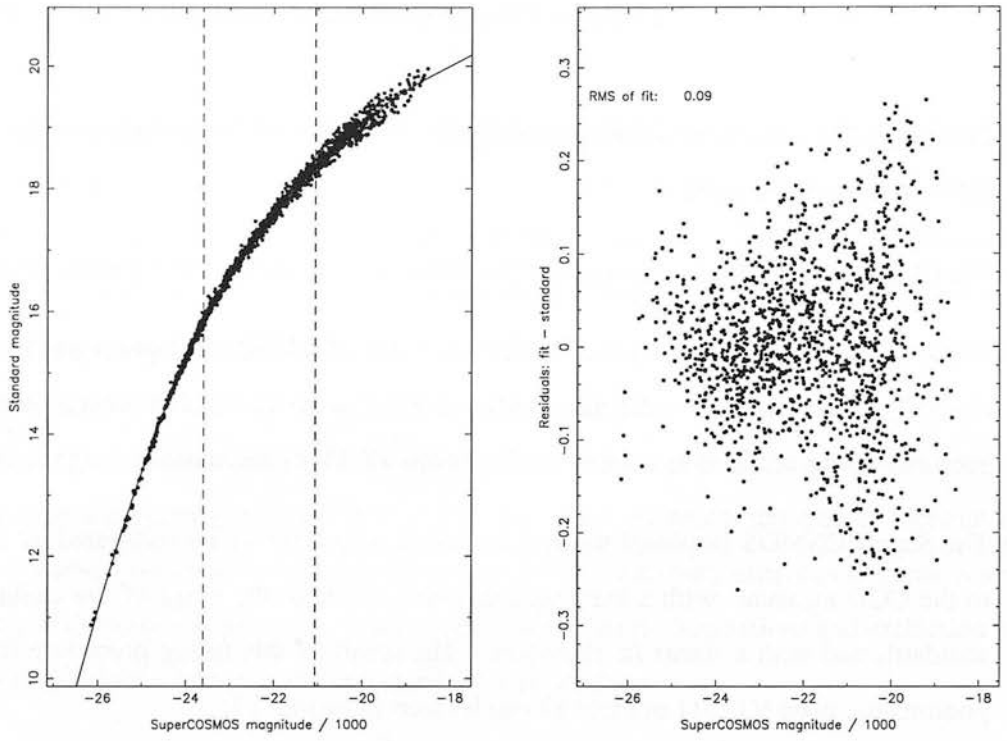


*Figure 3.7: The calibration of SuperCOSMOS isophotal magnitudes by large numbers of fiducial stars with CCD photometry, for the V photometric plate in Field 87. A least-squares cubic spline calibrating function is fitted to the data within the extent of the calibrating stars, and a linear function is applied elsewhere. The left panel shows the calibrating stars and the derived fitting function (solid line), with the knots used for the spline fit (dashed lines); the right panel displays the residuals of the calibrators about the fit.*

described in §3.4, this information can be used to reduce the short astrometric plates to solve for the position, proper motion and parallax of each star. Initially analyses were conducted for SA94, which has photometry calibrated from linearised profile magnitudes, and Field 87, which was calibrated from large-scale CCD observations. SA107, which has photometric calibrations derived from the same source as Field 87, would be reduced later. The photometric and astrometric plates for each field are described in §3.2.

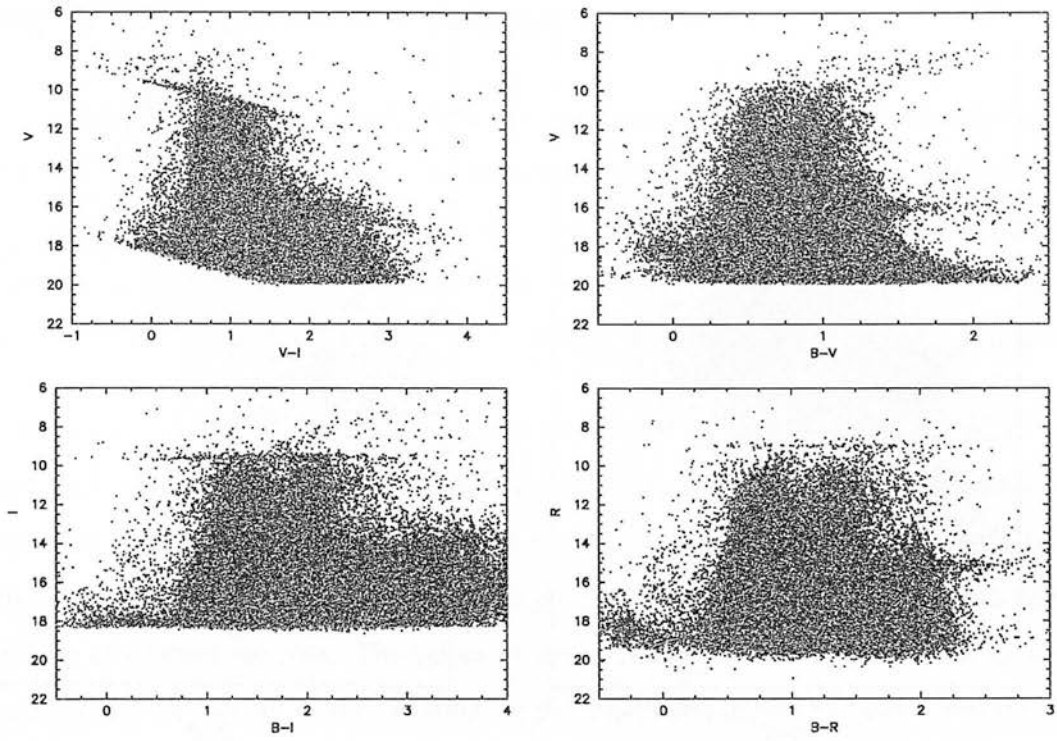


*Figure 3.8: The straightened colour-magnitude diagrams for the CCD-calibrated photometry in Field 87. Calibration was achieved with ~2200 stars with BV RI CCD photometry, with ~ 210 000 photometric reference stars in the final calibrated catalogue. Although there appear to be substantial systematic effects in comparision with the SA94 data, this is accentuated by the larger number of stars, and mainly arises at the plate limits where it will not affect the subdwarfs used in this study.*

### 3.5.1 Star-galaxy separation

Prior to any analysis the stars on each of the astrometric plates have to be identified and isolated. This is achieved using the image classification from the SuperCOSMOS image processing (§A.2.2), which is sufficiently accurate for these purposes. The classification has been shown to be >95% accurate for stars with $B_J < 21$ and >90% accurate for galaxies with 17.5< $B_J$ <21.5. Each astrometric plate is star-galaxy separated, with a declination-sorted list of the stars on each written for input into the pairing software.

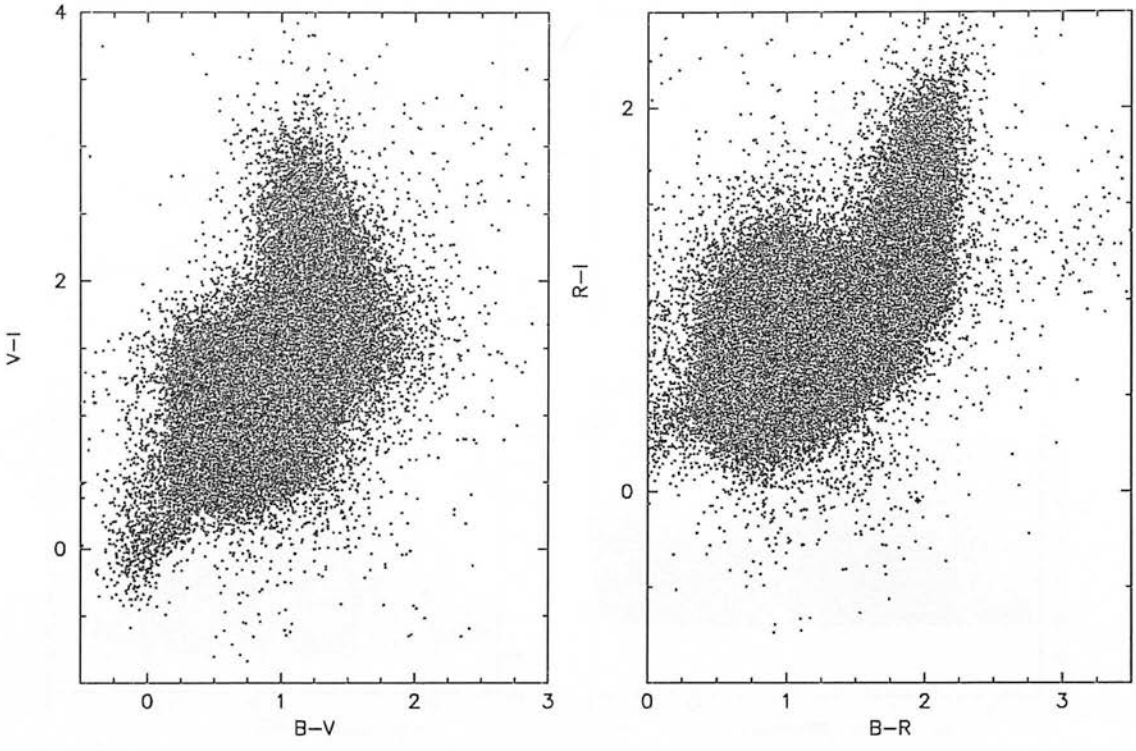


*Figure 3.9: Two-colour diagrams for the straightened CCD-calibrated photometry in Field 87.*

### 3.5.2 Pairing

Photometry in each of the four photographic passbands and astrometric measures on the majority of the short plates is a pre-requisite for all programme stars to be considered in the reduction, and SuperCOSMOS measures of astrometric reference stars are also required on each plate in the sequence. Hence the lists of stars on each plate have to be paired so as to identify those stars present on every photometric plate and on most astrometric plates; similarly a catalogue of reference stars also has to be paired with each plate to identify those with measures on every one.

These pairings are achieved through a 'master' plate, which is chosen to be of good quality (with a high, but not too high, plate threshold), and close to the middle of the plate time sequence so as to minimise the risk of very high proper motion stars being unpaired. The master plate is paired with each $(B_J, V, R, I)$ photometric plate and with each of the astrometric 'slave' plates. It is also paired with the astrometric star catalogue, which is a list of all stars from the Tycho-2 catalogue (Høg et al. 2000) that lie in the field, converted into a form

equivalent to the SuperCOSMOS IAM data files.

The pairing is done on proximity alone by a multipass algorithm, with the area on the slave plate around the position corresponding to each star on the master plate searched for a pair. The first pass searches a box close to the star, with each subsequent pass searching a larger box until a pair is found or a maximum separation is reached. The maximum pairing radius and number of passes is specified on input: a maximum of 12" and 12 passes are used in this case.

Once the master has been paired with the astrometric plates, the number of plates upon which each star appears is ascertained. Only stars which have a measure on all four photometric plates and on at least a minimum number of astrometric plates are retained for the solution. This latter constraint is included to ensure a high level of accuracy is achieved for the derived positions and proper motions. The values of the minimum number of astrometric measures necessary and the number of stars passing the pairing criteria in Field 87 and SA94 are given in Table 3.4. Note that the difference in the number of stars in each field is due to the direction of each: Field 87 is towards the higher density regions of the Galactic centre whereas SA94 is more towards the Galactic anticentre. For comparison, the SuperCOSMOS scans of the short plates in Field 87 typically include ~200 000 objects, whereas those in SA94 contain ~50 000.

| Field | No. Slave Plates | Minimum no. of measures | No. Stars with ≥min measures |
|---|---|---|---|
| Field 87 | 53 | 50 | 102 640 |
| SA94 | 44 | 42 | 20 862 |

*Table 3.4: The number of astrometric slave plates in Field 87 and SA94 and the minimum required number of slave measures* minmeas *required for a star to be included in the astrometric solution. The final column gives the number of stars passing this criterion.*

### 3.5.3 Tangent plane reduction

With a paired set of stars with photometric and a large number of astrometric plate measures, their positions at each plate epoch can be analysed to derive their positions and space motions. In order to derive celestial coordinates, proper motions and parallaxes for each object from

the plate series, the measured positions on the plate first have to be converted into tangent plane coordinates (§C.2). This transformation is determined from a set of reference stars with known celestial coordinates, that are distributed across each plate. The traditional method of calculating this transform is to compare the measured plate coordinates of the reference stars with their tangent plane coordinates (*standard coordinates*), which are derived from their celestial coordinates and knowledge of the tangential direction. This means, however, that the standard coordinates of each reference star have to be calculated individually, and the fact that the direction of the tangent point is unknown and must be approximated leads to errors in the transformation between measured and standard coordinates which must be compensated for.

The need for adopting a tangential direction and for calculation of reference star standard coordinates can be avoided with an iterative plate reduction (Murray, Tucker & Clements 1971, Murray 1983) that matches the coordinates of the reference stars (relative to any triad) with their measured plate positions to derive the matrix for directly transforming the programme object plate coordinates to tangent plane coordinates. The proper motion and parallax of each star can then be calculated using its standard coordinates on every plate in the series (§3.5.4). This method of deriving the standard coordinates is described in detail in Appendix C.

### 3.5.4 The central overlap method

With the standard coordinates of each star known for each plate epoch, these tangent plane positions can then by analysed to determine the proper motions and parallaxes of the programme objects. This is achieved by the *central overlap* method (Eichhorn & Russell 1976), which solves the conditional equations connecting the plate coordinates of the programme stars to the corresponding star constants (deviation from mean position, proper motion and parallax) and plate constants (zero point, scale and orientation). The central overlap method solves for these variables in a single least squares solution, improving the accuracy of the plate constants by using the measures of stars on all plates. Full details are given in Appendix D.

### 3.5.5 Removing position-dependent astrometric systematic errors

The software developed by Murray (Murray 1986) to perform the tangent plane reduction and central overlap method uses a linear plate model, compensating for zeropoint, scale and orientation corrections in the variation of a star's position from plate to plate (§D.1.2). Whilst this provides some description of the differences in positions between plates, there are also *non-linear* terms which can cause significant position-dependent astrometric errors across the field.

The largest of these systematic errors are manifested in the well-known "swirl patterns" that appear between measured and expected positions on Schmidt plates (Taff et al. 1992). These are largely due to the mechanical deformation of the plate when it is exposed in the telescope, being vacuum clamped to fit the curved focal plane of the Schmidt telescope. Stresses within the glass plate and the emulsion cause slight shifts in the position of each image when the plate is relaxed after exposure, and these are of the order of 1 arcsec. This affect is approximately described by a cubic radial distortion, and this "Schmidt distortion" is allowed for in the calculation of the tangent plane coordinates of the images on the plate (§C.4). However, variations in the clamping of each plate and the properties of the glass mean that this correction will not fully compensate for the mechanical deformations. In addition, there are variations between plates of the emulsion properties, since the emulsion expands during developing and slight differences in the conditions when each plate dries can lead to large scale emulsion shifts.

These effects are accounted for in the SuperCOSMOS astrometric solution that provides celestial coordinates for each object on the plate (§A.2.1). However, Murray's code does not use these coordinates, instead directly employing the plate coordinate measures for each star. The software makes no provision for the correction of the systematic positional errors other than the option to use a more sophisticated, non-linear plate model, and given that there will be different distortions and emulsion shifts for each plate, there is the potential for significant astrometric errors to affect the derived proper motions. In light of the variation of errors for each plate, I therefore introduce a correction procedure for the position-dependent astrometric errors on a plate by plate basis. The implication in applying this procedure is that there are no real systematic space motions of stars across the field, or in other words that the proper motion of each star is independent of its position on the plate. For the purposes of using proper motions

to identify subdwarfs through reduced proper motion (§3.7.1) this is a suitable procedure; if the proper motions of the subdwarfs are to be analysed for bulk streaming motions (§2.3.4) then this process may lead to real motions being scaled out.

The algorithm operates by using the mean standard coordinates of each star derived from the central overlap solution, and calculating the residual of the measure on each plate from this mean. These residuals are then used to calculate the smoothed positional systematic displacements as a function of position on the plate, which are then used to correct the positions of each star, much in the same way as the SSS procedure (§A.2.1). In more detail, the procedure is as follows:

- Each plate is divided into a 1cm (10 arcmin) grid, and the mean displacement of the stars in each bin is calculated. This grid is an optimum size to correct for the expected $\sim$30 arcmin non-linear distortions.
- These mean residuals are then smoothed across the plate, padded where there are insufficient stars, and bilinear filtered to produce the smooth systematic positional errors at each grid point.
- The systematic residual at the location of each programme star is found by bicubic interpolation inside this grid, and this residual vector is subtracted from the star's position.
- The stars, with positional systematics removed, are then re-entered into the tangent plane and central overlap solutions, resulting in positions and space motions for each star that are free from systematic Schmidt plate distortions.

Figure 3.10 shows the result of the procedure in the contrast between the systematic positional errors present after the first central overlap solution, prior to the error correction, and after the adjusted positions have been re-reduced for tangent plane and central overlap reduction. The absence of any large-scale systematics in position after the algorithm has been applied suggests the improvement this addition makes to the Murray reduction method. The systematic displacements seen in the left panel of Figure 3.10 would have otherwise been measured as real proper motions, thus causing a substantial number of objects with false proper motions to enter the high proper motion subset, leading to likely contamination of the subdwarf sample.

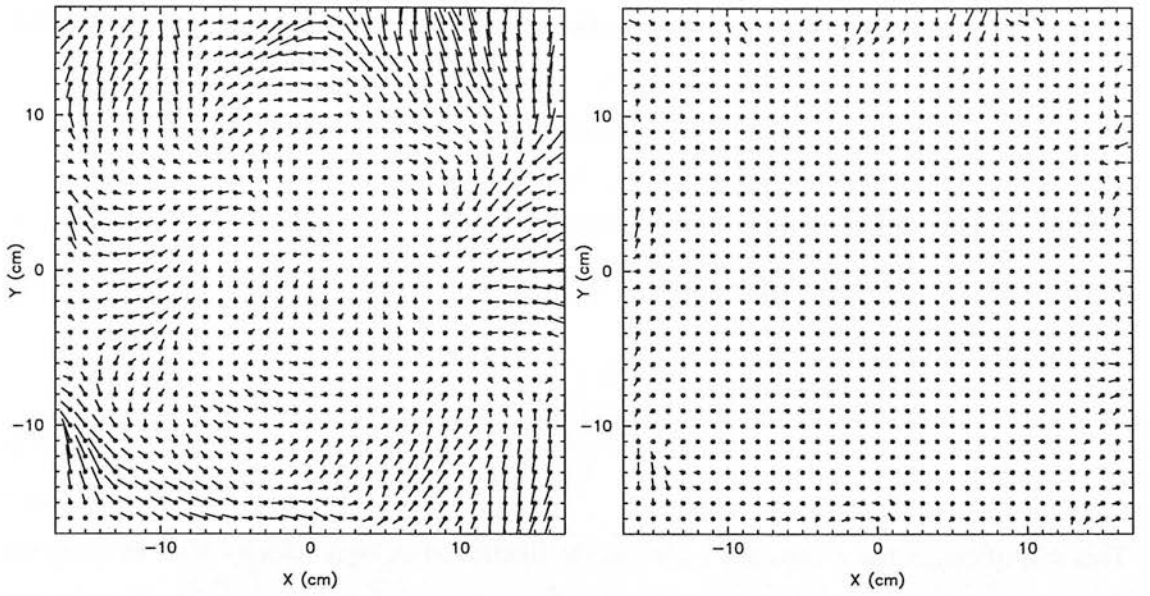


*Figure 3.10: The result of removing systematic positional errors as a function of position on plate V13781 in SA94. Each plot shows an entire plate, ∼ 32 cm or ∼6° square, and the vectors are scaled so that that one tick mark corresponds to 1 arcsecond. The left panel shows the binned and smoothed systematic errors prior to correction, and the right panel shows the errors afterwards, when no systematics errors are left at significant levels and only random errors in position present. Correcting these systematic astrometric errors makes a substantial improvement to the Murray reduction techniques by ensuring that fewer spurious proper motion contaminants enter the final subdwarf sample.*

## 3.6 The high proper motion sample

With positions, proper motions and parallaxes for all programme stars, a proper motion cut-off can be applied to the catalogue, and potential subdwarf candidates can be isolated. A lower proper motion limit is applied to the sample of paired stars for two principal reasons: to amplify the proportion of spheroid stars selected and to create a 'cleaner' proper motion sample. The proper motion selection magnifies the contribution from the higher-velocity spheroid population, since they are effectively sampled over larger volumes than the lower-velocity disc stars (Reid 1997b, Cooke & Reid 2000). Proper motion surveys are in this way one of most efficient and effective method of identifying spheroid members. The number of stars of each population

in a proper motion selected sample is proportional to the mean population tangential velocity:

$$N(\mu > \mu_{min}) \propto \rho_0 \langle V_T \rangle^3 , \tag{3.1}$$

with $\rho_0$ the local space density of the population (Hanson 1983, Reid 1984). This therefore amplifies the contribution of the higher velocity population above the ratio of the local space densities by the amount:

$$A_\mu = \left( \frac{\langle V_T^1 \rangle}{\langle V_T^2 \rangle} \right)^3 . \tag{3.2}$$

This amplification has a dramatic effect on the likelihood of high velocity stars entering the proper motion sample, and demonstrates the efficiency of proper motion selection in selecting halo stars. As seen in Cooke & Reid (2000), a halo to disc number ratio of $N_{disc}$:$N_{halo}$ = 400:1 for a volume-limited sample can be increased to $N_{disc}$:$N_{halo}$ = 5:1 for a proper motion sample.

The second effect of applying a minimum proper motion limit to the sample is to include stars with small relative errors in proper motion, avoiding those with marginal proper motions arising from errors in the positions or pairing. This results in a 'cleaner' reduced proper motion diagram (§3.7.1), and more accurate subdwarf selection.

### 3.6.1 Proper motion error

In determining the lower proper motion limit the proper motion error must first be evaluated so as to ensure that a cut of a sufficiently high number of sigma is applied, ensuring that only stars with significant motions are included in the sample. The proper motion standard deviation $\sigma_\mu$ is calculated for each field from linear regression, assuming that the measures of a star at $N$ different epochs (ie. on $N$ plates) can be fitted with a straight line model. The position $x(t)$ of a star (in one coordinate direction) at time $t$ is related to its initial position $x_0$ and proper motion $\mu$ by

$$x(t) = x_0 + \mu t \tag{3.3}$$

If a star has measures $x_i, i = 1, ..., N$ over $N$ plates, then the proper motion is determined by minimising the goodness-of-fit function with respect to $\mu$:

$$\chi^2(\mu, t) = \sum_{i=1}^{N} \left( \frac{x_i - x_0 - \mu t_i}{\sigma_i} \right)^2 \tag{3.4}$$

So

$$\frac{\partial \chi^2}{\partial \mu} = 0 \Rightarrow \mu = \frac{SS_{tx} - S_t S_x}{SS_{tt} - (S_t)^2} \tag{3.5}$$

where

$$S = \sum_{i=1}^{N} \frac{1}{\sigma_i^2},\ S_t = \sum_{i=1}^{N} \frac{t_i}{\sigma_i^2},\ S_x = \sum_{i=1}^{N} \frac{x_i}{\sigma_i^2},\ S_{tx} = \sum_{i=1}^{N} \frac{t_i x_i}{\sigma_i^2},\ S_{tt} = \sum_{i=1}^{N} \frac{t_i^2}{\sigma_i^2} \tag{3.6}$$

and $\sigma_i$ is the error in the measurement of $x_i$. Now, from Equation 3.5:

$$\frac{\partial \mu}{\partial x_i} = \frac{St_i - S_t}{\sigma_i^2 (SS_{tt} - (S_t)^2)} \tag{3.7}$$

$$\begin{aligned} \Longrightarrow \sigma_\mu^2 &= \sum_{i=1}^{N} \sigma_i^2 \left( \frac{\partial \mu}{\partial x_i} \right)^2 \\ &= \frac{S}{SS_{tt} - (S_t)^2} \end{aligned} \tag{3.8}$$

The error $\sigma_i$ of the measure of a star on each plate $i$ is unknown, but it can be assumed with sufficient accuracy that the error is the same for each plate. Therefore we can write $\sigma_i = \sigma_u$, where $\sigma_u$ is the standard deviation of unit weight measure, calculated in the central overlap solution as

$$\sigma_u^2 = \sum_{i=1}^{N_S} \sum_{j=1}^{N_P} \frac{w_{ij}(\Delta\xi_{ij}^2 + \Delta\eta_{ij}^2)}{D} \tag{3.9}$$

where $i$ is summed over the $N_S$ programme stars and $j$ over the $N_P$ plates in the solution. The $i^{th}$ star on the $j^{th}$ plate has weight $w_{ij}$ and its residuals from its mean standard coordinates are

given by $\Delta\xi_{ij}^2$ and $\Delta\eta_{ij}^2$. $D$ is the number of degrees of freedom in the solution, given by

$$D = N_{all}(N_P - N_{SC}) + N_P(N_{all} - N_{PC}) + N_L \tag{3.10}$$

where $N_{all}$ is the number of stars with measures on all plates, and $N_P$, $N_{SC} = 5$, $N_{PC} = 6$ and $N_L$ are the number of plates, star constants, plate constants and Lagrangian multipliers respectively. Equation 3.8 then simplifies to

$$\sigma_\mu^2 = \frac{N_P \sigma_u^2}{N_P \sum_{i=1}^{N_P} t_i^2 - (\sum_{i=1}^{N_P} t_i)^2} \tag{3.11}$$

The proper motion errors found in each field are

SA94: $\sigma_\mu = 7.7$ mas yr$^{-1}$

Field 87: $\sigma_\mu = 6.0$ mas yr$^{-1}$

From consideration of these limits and inspection of reduced proper motion diagrams (§3.7.1), the lower proper motion limit applied to both fields was

$$\mu_{min} = 50 \text{ mas yr}^{-1} \tag{3.12}$$

This is equivalent to at least a $7\sigma_\mu$ cut for each field, ensuring that only stars with significantly high proper motions enter the sample and that contamination from objects with spurious measures is kept to a minimum.

## 3.7 Subdwarf selection

### 3.7.1 Reduced proper motion

Although applying a lower proper motion limit produces a cleaner sample of fast-moving stars, this will consist not only of subdwarfs but also white dwarfs and high velocity members of the disc. In order to identify the candidate subdwarfs, the *reduced proper motion* of each star is

used as a discriminator. Defined as

$$H = m + 5\log\mu + 5 = M + 5\log V_T - 3.379, \tag{3.13}$$

the Hertzsprung parameter (Luyten 1925) separates high-velocity ($V_T$), low-luminosity (M) subdwarfs from the white dwarf and thin disc populations.

This effect can seen in the reduced proper motion diagram (RPMD) of $H_V$ plotted against $(V - I)$: Figure 3.11 shows the RPMDs for all stars with $\mu > \mu_{min} = 50$ mas yr$^{-1}$ in SA94 and Field 87. Stars with large residuals or with low weights from the central overlap solution are rejected from the high proper motion sample at this stage. Although there is significant scatter in the diagrams, there is some evidence for the presence of two separate sequences of stars, with the lower-luminosity, higher-motion subdwarfs to the lower left, and the bright disc stars to the upper right.

Whilst much of the scatter between the populations visible in Figure 3.11 is due to errors in the observed quantities, especially the photometry, some of the apparent merging is due to thick disc stars, which overlap both the main sequence and subdwarf populations on the diagram. These stars have relatively high velocities, and hence are responsible for the many of the objects lying between the old disc and subdwarf sequences. Separation of the thick disc stars is important when deriving subdwarf luminosity functions and number densities, however, for they have a much higher local number density than subdwarfs, and the inclusion of even a tiny proportion in the sample can result in a significant overestimation of the subdwarf density (Bahcall & Casertano 1986).

### 3.7.2 Tangential velocity cut-off

One method of selecting subdwarfs is to chose stars between given percentiles of the expected reduced proper motion distribution for subdwarfs, as described in §4.3.4. However, this method is not suitable in this case as it requires knowledge of the colour errors which are more poorly-defined for photographic data, and more importantly it makes no allowances for thick disc contamination. A technique that does allow the selection of subdwarfs whilst avoiding significant contamination by thick disc stars is to introduce tangential velocity restrictions into the

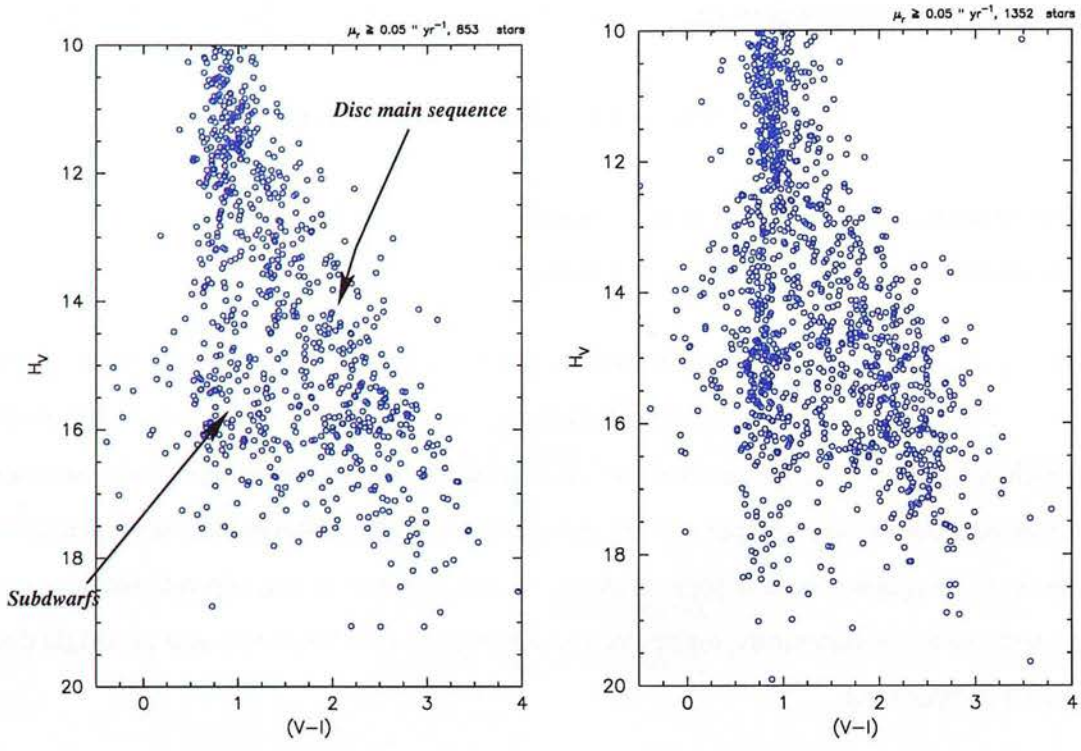


*Figure 3.11: The reduced proper motion diagrams for all stars with $\mu > 50$ mas yr$^{-1}$ in SA94 (left) and Field 87 (right), excluding those with high residuals or low weights. Although there is significant scatter and merging of the populations, the subdwarf and disc sequences are apparent to the lower left and upper right respectively.*

selection.

The tangential velocity distributions of the disc and spheroid populations for each of the survey fields can be generated either by Monte Carlo simulations or through theoretical calculations, both assuming velocity ellipsoids described by a solar motion and Gaussian dispersions. The disc kinematics adopted are from two analyses of local M dwarfs (Reid, Hawley & Gizis 1995, Hawley, Gizis & Reid 1996), and the halo ellipsoid is derived from the study of a large sample of low metallicity stars by Chiba & Beers (2000). The parameters of these ellipsoids are given in Table 3.5, and the calculations and simulations used to derive the tangential velocity distributions are described in Appendix E. Figure 3.12 shows the tangential velocity distribution calculated for SA94.

| Population | $U_\odot$ | $V_\odot$ | $W_\odot$ | $\sigma_U$ | $\sigma_V$ | $\sigma_W$ |
|---|---|---|---|---|---|---|
| Halo | -26 | -199 | -12 | 141 | 106 | 94 |
| Thin Disc | 10 | -5 | -7 | 41 | 27 | 21 |
| Thick Disc | 10 | -23 | -7 | 52 | 45 | 32 |

*Table 3.5: Adopted solar motions and velocity ellipsoids, showing the assumed disc (Reid et al. 1995; Hawley et al. 1996) and halo (Chiba & Beers 2000) stellar kinematics used in the tangential velocity simulations. All speeds are in kms$^{-1}$, and U, V, W denote the usual Galactic coordinate triad in the respective directions of the Galactic centre, direction of rotation and NGP. Note that whilst the halo radial solar motion derived by Chiba & Beers (2000), $U_\odot = -26$ km s$^{-1}$, is somewhat larger than the $-9$ km s$^{-1}$ found by Layden et al. (1996) from RR Lyrae stars, we adopt the former since it is calculated from a dataset that is more suited to our sample in terms of both metallicity and proximity to the Sun.*

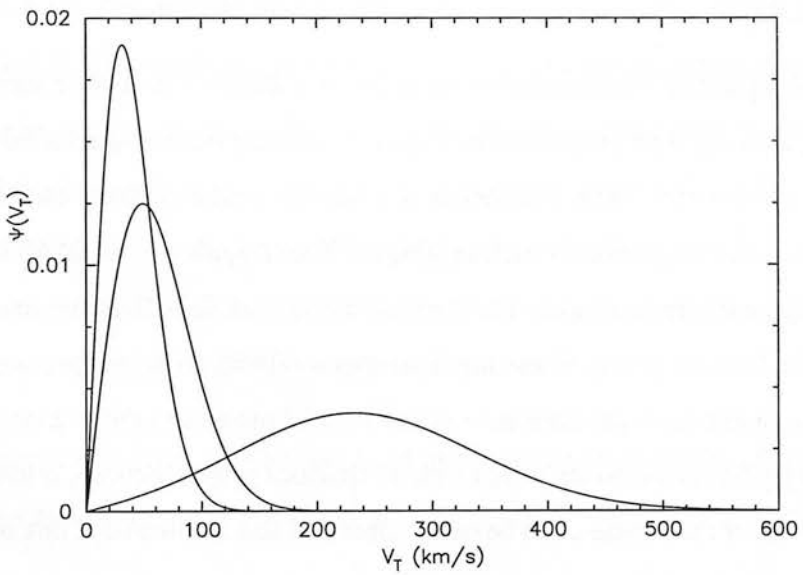


*Figure 3.12: Analytical tangential velocity distributions for the thin and thick discs and spheroid (in order of ascending velocity) in the direction of SA94.*

It is clear from Figure 3.12 that a tangential velocity constraint of $V_T > 150$ km s$^{-1}$ will exclude all but a negligible proportion of the thick disc population. Calculations show that a maximum of 0.77% and 0.6% of the thick disc population will enter a sample with these constraints in respective directions of SA94 and Field 87. This velocity cut-off will also cause the low-velocity tail of the spheroid population to also be excluded from the sample,

but the calculation results allow the subsequent correction of the derived number densities and luminosity functions (§4.5.4).

The definition of reduced proper motion (Equation 3.13) suggests that with an assumed colour-magnitude relation lines of constant $V_T$ can be plotted on the reduced proper motion diagram. A spheroid-disc separating line of $V_T = 150\text{km s}^{-1}$ can then be applied to the RPMD in order to select candidate subdwarfs from the high proper motion sample. The colour-magnitude relations from Gizis & Reid (1999) used by Cooke & Reid (2000) are also used here, with the colour-magnitude relation offset by $5 \log V_T = 150\text{km s}^{-1}$ defining the disc/halo separating line, and by the appropriate value of $\langle 5 \log V_T \rangle$ for the thin and thick disc population ridgelines. Figure 3.13 shows the RPMDs for SA94 and Field 87 with the two disc fiducial relations and the disc/halo separating line overlaid.

### 3.7.3 Selecting subdwarfs

The disc/halo separating line corresponding to $V_T = 150\text{km s}^{-1}$ is used to identify the subdwarf sample, with any high proper motion object beneath the line being selected as a candidate subdwarf or white dwarf. With a catalogue of potential subdwarfs from each field the list is "cleaned" by visual inspection of each candidate. The image's SuperCOSMOS ellipse plots from several plates in the sequence are overlaid onto SuperCOSMOS pixel data images from scans of POSS-I survey plates. These are from epoch $\sim$1950, so the proper motion of the object is clearly visible from the difference of the POSS-I image and the overlaid ellipses. Any objects that may have entered the sample due to spurious proper motions, often due to a false detection on one or more plates, can be easily identified and eliminated at this stage.

### 3.7.4 Estimating the luminosity function

An estimate of the subdwarf luminosity function can be derived from the subdwarf sample using the methods described in Reid (1997b) and Cooke & Reid (2000) and briefly outlined here. The distance distribution of a proper motion sample can be modelled with Monte Carlo methods by assuming a uniform spatial density and the Gaussian velocity dispersions given in

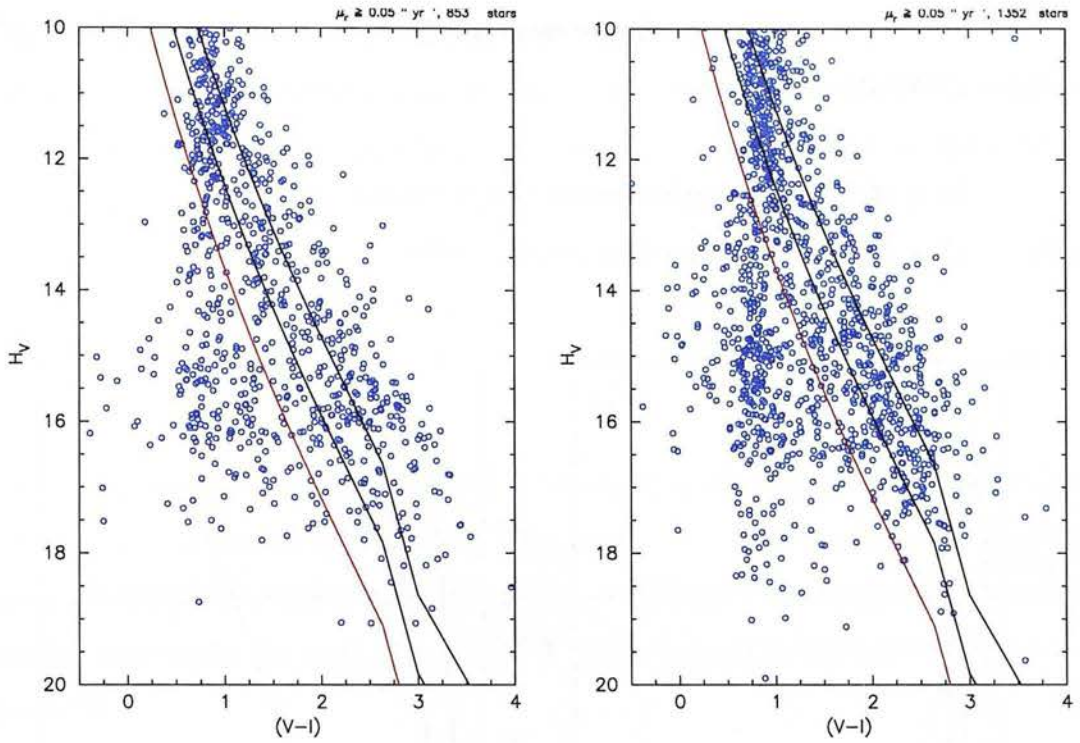


*Figure 3.13: The reduced proper motion diagrams for all stars with $\mu > 50$ mas yr$^{-1}$ in SA94 (left) and Field 87 (right), with the thin and thick disc fiducial relations (black lines) plotted by offsetting the mean colour-magnitude relations of Gizis & Reid (1999) by the appropriate value of $\langle 5 \log V_T \rangle$ from the $V_T$ distribution calculations. The red line indicates the disc/halo separating line corresponding to the spheroid star colour-magnitude relation offset by $5 \log V_T = 10.88$.*

Table 3.5 (Figure 3.14). From similar simulated distributions, Reid (1997b) finds that 80% of stars in a proper motion-limited sample with $\mu > \mu_{lim}$ will be found at distances of less than

$$d_C = \frac{\langle V_T \rangle}{\kappa \mu_{lim}} \tag{3.14}$$

where $\kappa = 4.74$. Each population therefore falls into two regimes: a proper motion-limited sample, where the distance limit is set by the velocity distribution, and a magnitude-limited sample, where the distance limit is set by the plate depth. From the cumulative distribution curve (Figure 3.14) the 80-percentile distance limits can be obtained, and hence a limiting distance modulus, $(m - M)_{lim}$, derived for each population. Entering the apparent magni-

tude depth, $m_{lim}$ of the survey, an absolute magnitude limit $M_{lim}$ can be obtained for each population, such that for

$M < M_{lim}$ the sample is proper motion-limited

and for $M > M_{lim}$ the sample is magnitude-limited

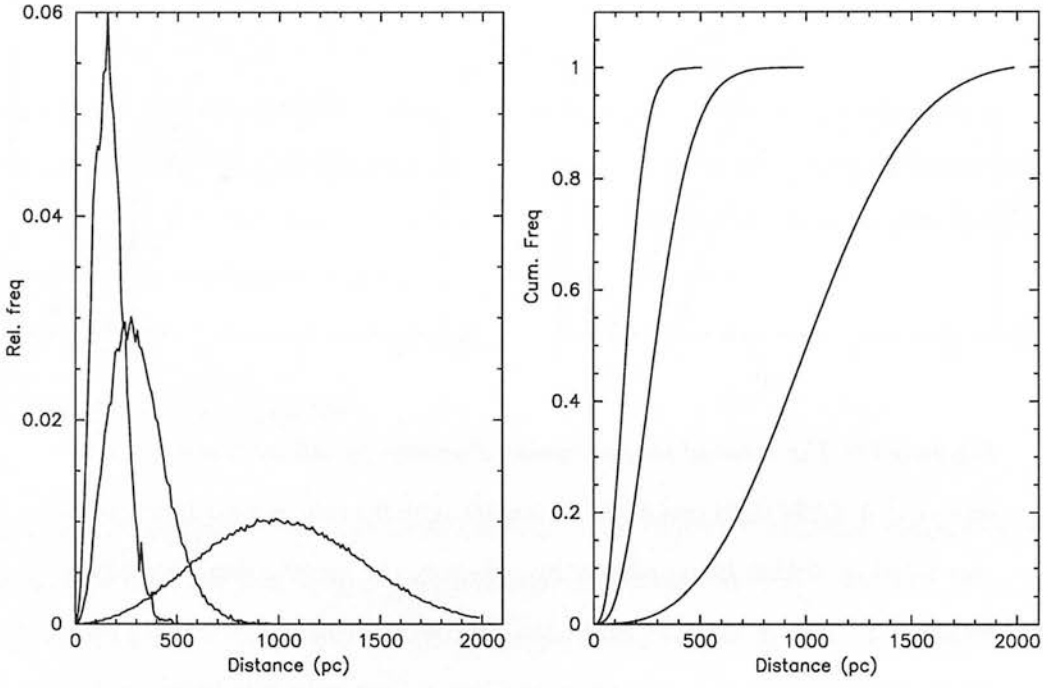


*Figure 3.14: The distance distributions (left) and cumulative distance distributions (right) generated from Monte Carlo simulations for (in order of increasing distance) the thin disc, thick disc and spheroid populations in the direction of SA94.*

The space densities and luminosity functions of each stellar population can then be derived from the simulated density distribution. The relative completeness, $f_\mu$, of a proper motion-selected sample is the fraction of stars with $\mu > \mu_{lim}$, such that

$$f_\mu = \frac{N_\mu}{N_{tot}} \tag{3.15}$$

where $N_\mu$ is the number of stars in the proper motion-limited sample, and $N_{tot}$ the actual total number of stars. Plotting $f_\mu$ cumulatively against distance gives the fraction of this subset that have $d < d_{lim}$, with the effect of fewer stars meeting the $\mu > \mu_{lim}$ criterion with increasing

distance apparent (Figure 3.15). From these distributions the proportion of each population with distances less than their respective $d_C$ that will be detected can be calculated. Thus, for a proper motion-limited sample taken from observations over a solid angle $\Omega$, the space densities can be estimated as

$$\begin{aligned} \rho &= \frac{N_{tot}}{Vol} \\ &= \frac{3}{\Omega}\frac{0.8N_\mu}{f_\mu d_C^3} \end{aligned}$$

since $0.8N_\mu$ stars lie within a distance of $d_C$. For magnitude-limited stars, the distance limit is reduced and $f_\mu$ increased. The luminosity function is then derived by performing this calculation as a function of absolute magnitude, approximated for each star from the colour-magnitude relations used to plot the population ridge lines on the reduced proper motion diagram (Figure §3.13).

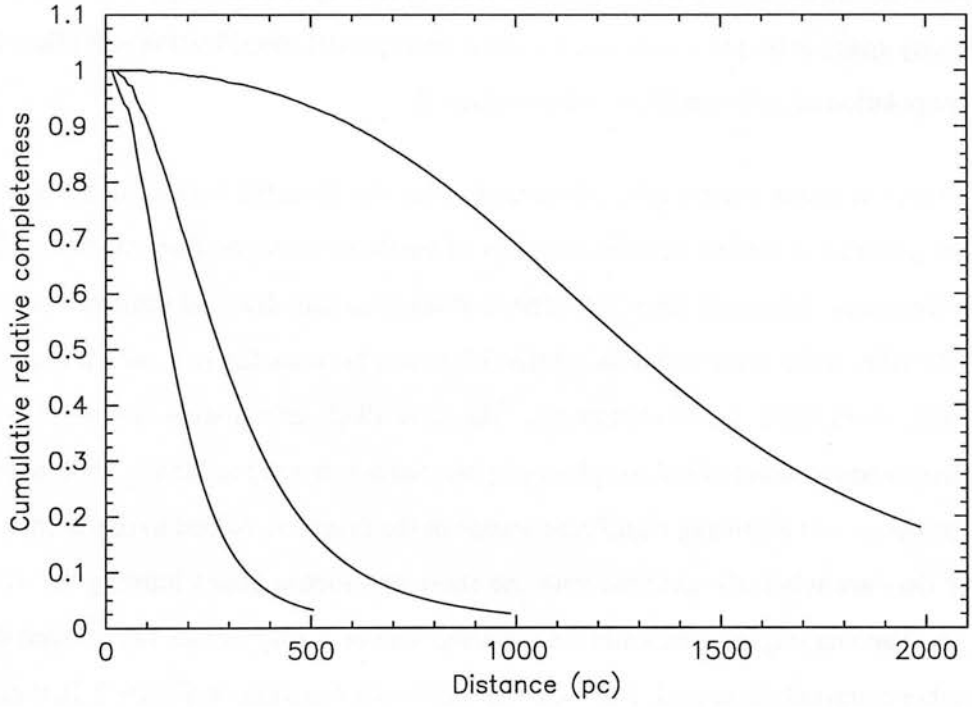


*Figure 3.15: The cumulative value of the relative completeness, $f_\mu$, of a proper motion-selected sample, showing the cumulative fraction of disc and spheroid stars expected to have $\mu > 0.05$ mas yr$^{-1}$.*

This method has been applied with some success to the proper motion sample in SA94 of Cooke & Reid (2000) to derive disc and spheroid luminosity functions. However, it is a some-

what inferior method to the $V/V_{max}$ method of Schmidt (1975) (see §4.5.1), since individual stellar distances are not known and only average densities can be derived, and there is a high sensitivity to the adopted velocity ellipsoids (Equations 3.14 and 3.16).

## 3.8 Results and discussion

With the $V_T > 150$ km s$^{-1}$ criterion applied to the high proper motion sample with $\mu > 50$ mas yr$^{-1}$ and the sample "cleaned" by visually inspection, a total of 153 and 319 candidate subdwarfs were identified in SA94 and Field 87 respectively. This provides a large sample with which to probe local spheroid properties: the methods of Cooke & Reid (2000) can be applied to derive the subdwarf luminosity function with a larger dataset than both Gould et al. (1998) and Gizis & Reid (1999), and the subdwarfs can be searched in proper motion space for potential spheroid streams. Radial velocities from follow-up spectroscopy will enable the full 3D velocity space to be probed for substructure, and spectral identification will allow the true parent population of each candidate to be confirmed.

However, it is this latter aspect which raises concern about the validity of the sample, for there are potential problems with the accuracy of subdwarf selection from the reduced proper motion diagrams. Although there is evidence of separate thin disc and subdwarf populations on the RPMDs, there is nevertheless substantial scatter between the two, which is unlikely to stem solely from thick disc contaminants. The most likely explanation is that the relatively poor photometry available from the photographic plates is mainly to blame, with large colour errors of $\sigma_{V-I} \sim 0.2$ causing significant scatter in the diagram. Added to this is the problem that the data are relatively shallow, with the short astrometric plates limiting the sample to $V \lesssim 18$. The majority of subdwarfs are expected appear at magnitudes fainter than this (see the number counts of Chen et al. 2001 and the luminosity functions in Figure 2.2), with a limit of just one magnitude fainter likely to result in a far large subdwarf sample. What is required, therefore, is deeper data with better photometry, which will enable a large and more reliable subdwarf sample to be defined. For this reason I proceed no further with the Murray plate data for identifying subdwarf samples, having optimised its use for this purpose by producing some of the best possible astrometry and photometry attainable with these photographic data.

I instead switch attention to the Sloan Digital Sky Survey (SDSS) and SuperCOSMOS Sky Surveys, which between them provide a deeper dataset with comparable proper motions yet far superior photometry.

# Chapter 4

# The Subdwarf Luminosity Function from SDSS & SSS Data

## 4.1 The data

As discussed in §3.8, the Murray plate data are not deep enough nor have sufficient photometric accuracy to allow effective identification of subdwarfs through the method of reduced proper motion. Alternative data were therefore needed to investigate the solar neighbourhood subdwarf population, and the publication of the Sloan Digital Sky Survey Early Data Release (SDSS EDR) in July 2001 proved timely. Combining the SDSS EDR data with digitised scans of earlier epoch plates from the SuperCOSMOS Sky Survey (SSS) yields a dataset with high precision photometry and astrometry and a long time baseline: one that is ideally suited to the detailed yet large scale study of stellar populations.

### 4.1.1 The Sloan Digital Sky Survey

The Sloan Digital Sky Survey is an ambitious project to map the local universe with a large scale photometric and spectroscopic survey, covering $\sim$10 000 deg$^2$ in the northern hemisphere, and a small region region ($\sim$740 deg$^2$) in the south (Figure 4.1). The principal ob-

jectives of the survey are to constrain cosmological and galaxy evolution models, but the high quality data produced by the survey has applications in virtually all areas of astronomy.

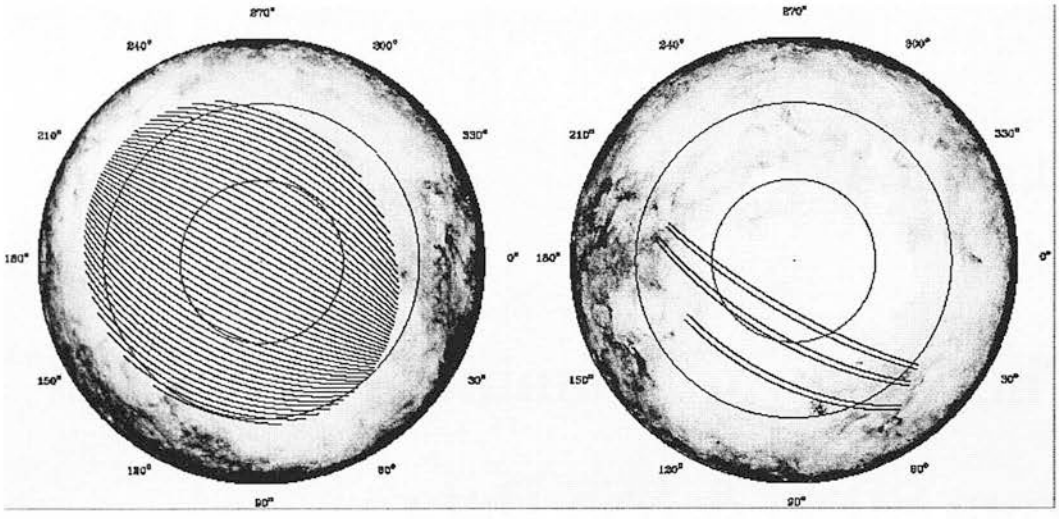

*Figure 4.1: The SDSS imaging stripes in the North (left) and South (right) Galactic hemispheres, with the circles indicating Galactic latitudes $|b|$ =30°, 60°. The grey scale indicates dust reddening, from no reddening (white) to one magnitude (black) in $(g' - r')$ colour.*

The survey is split into photometric and spectroscopic programmes. The complete survey will include high accuracy *ugriz* photometry for some $10^8$ stars and $10^8$ galaxies with a precision of 3-5%, or less than 0.02 magnitudes in $r$. The passbands, shown in Figure 4.2, are specifically designed for the survey and cover the near-UV to the near-IR wavelength range (Fukugita et al. 1996, Smith et al. 2002). The survey will probe to a limiting magnitude of $g' \approx 23$. In addition to the photometry, spectra will be obtained for a large number of objects: $\sim 10^6$ galaxies, $\sim 10^5$ quasars and $\sim 10^5$ stars.

In June 2001 the SDSS collaboration published the Early Data Release, covering three regions of sky over a total area of 462 deg$^2$ and including photometry of some 14 million objects and 54000 follow-up spectra. Table 4.1 and Figure 4.3 give the location and areas of the three EDR regions: the South Galactic Stripe (SGS), North Galactic Stripe (NGS) and the SIRTF First-Look field. The wide range in Galactic coordinates of the EDR regions makes the data ideal for this subdwarf study, and although the photometric calibrations are not final (and are thus denoted $u^*g^*r^*i^*z^*$ rather than $u'g'r'i'z'$), the photometry is still of very high quality — uniform to of order 3% in $g^*$, $r^*$ and $i^*$, and 5% in $u^*$ and $g^*$ (Stoughton et al. 2002).

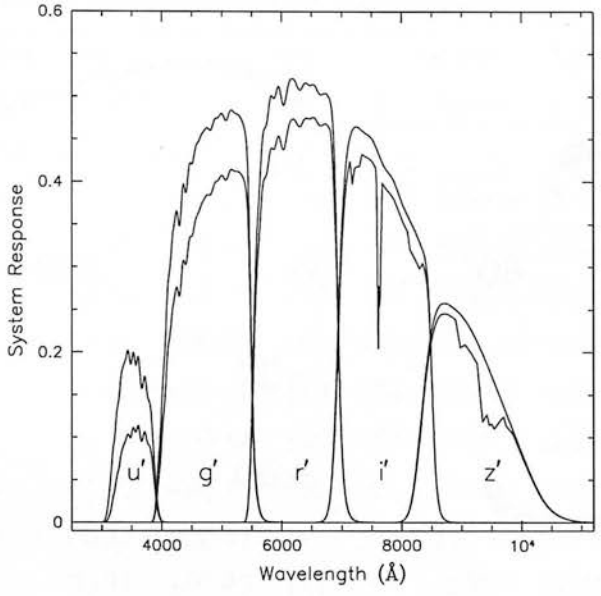


*Figure 4.2: The SDSS* ugriz *filter passbands, designed specifically for the survey and covering the near-UV to near-IR range.*

*Table 4.1: SDSS EDR regions*

| Region | RA | Dec | Area (deg$^2$) |
|---|---|---|---|
| North Galactic Stripe | 145°- 236° | 0° | 228 |
| South Galactic Stripe | 351°- 56° | 0° | 166 |
| SIRTF First-Look Field | 257° | 59° | 32 |
| | 261° | 60° | 36 |
| | | Total | 462 |

### 4.1.2 The SuperCOSMOS Sky Survey

The SuperCOSMOS Sky Survey (SSS) is a programme to digitise survey plates from the UK Schmidt Telescope (UKST), the ESO Schmidt and the Palomar Schmidt, and to make the high-precision scans publically available.

The survey is ongoing, but in May 2001 the whole of the southern sky had been scanned in two colours (blue UKJ and red UKR) and placed online, with the database 97% complete in UKI and 75% complete in ESO-R. Also added were selected regions of scans from the first Palomar Sky Survey (POSS-I), and it is these that are used in this study. With a mean epoch of $\sim$1953, the POSS-I scans are an ideal complement to the SDSS data, yielding some of the

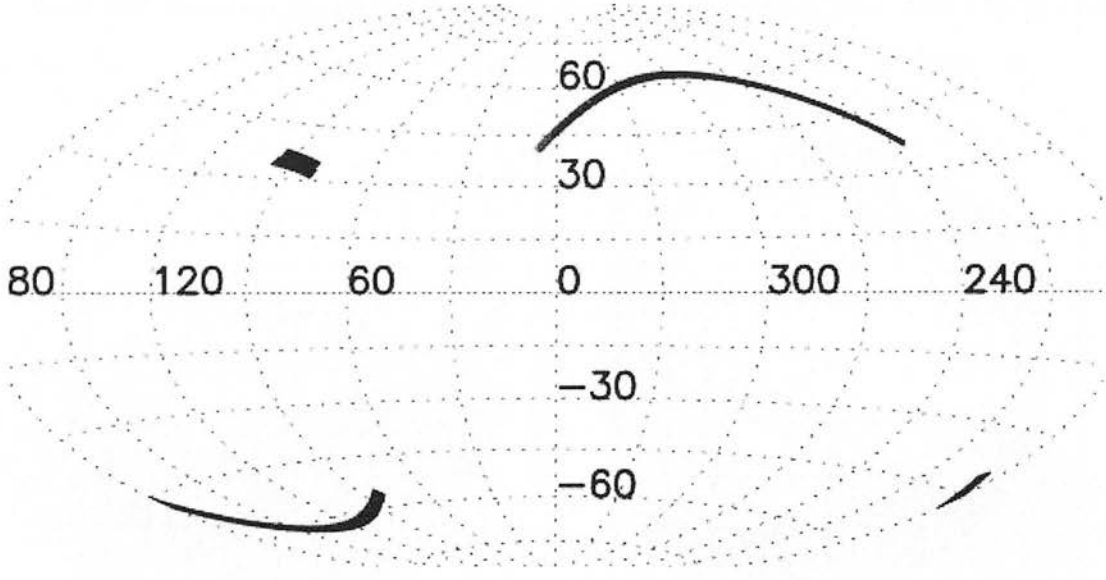


*Figure 4.3: The imaging sky coverage for the SDSS EDR, showing the south and north Galactic stripes and the SIRTF First Look Survey patch. The coordinates show Galactic longitude and latitude,* $(l, b)$.

greatest epoch differences available for large-scale data (about 45 years) and hence enabling accurate proper motions to be derived.

The POSS-I plates each cover 6.25 x 6.25°, and reach a depth of R∼20.5. There are 12 plates overlapping the SDSS EDR SGS, and 16 overlapping the NGS, with the area of overlap between the POSS-I plates and EDR stripes hereafter referred to as 'fields' and detailed in Table 4.2. Each of the SDSS stripes are ∼2.5 °wide, and so form a strip along the centre of each of the Schmidt fields. It is evident from the field areas in Table 4.2 that the SGS forms a region of constant width, whereas the NGS narrows at either end: this is a consequence of the scanning pattern in the EDR.

For the purposes of measuring proper motions the POSS-I data are selected for the first epoch (∼1950) measures and the SDSS as the second epoch (∼1998). Whilst proper motions are available from the SSS database this choice is made so as to maximise the time baseline and hence the proper motion accuracy.

These data form an ideal sample from which to select high proper motion halo stars: the

*Table 4.2: The POSS-I fields in the EDR SGS & NGS regions used in this study.*

| POSS-I | $\alpha$ | $\delta$ | | | Plate | Area |
|---|---|---|---|---|---|---|
| Field | (J2000.0) | | l | b | Epoch | ($\times 10^{-3}$ ster) |
| South Galactic Stripe | | | | | | |
| 0932 | 03 43 | +00 28 | 186 | -40 | 1954.0 | 2.66 |
| 0363 | 03 19 | +00 31 | 181 | -45 | 1951.7 | 4.60 |
| 1453 | 02 55 | +00 35 | 175 | -49 | 1955.8 | 4.61 |
| 1283 | 02 31 | +00 38 | 168 | -53 | 1954.9 | 4.59 |
| 0852 | 02 07 | +00 41 | 159 | -56 | 1953.8 | 4.61 |
| 0362 | 01 43 | +00 44 | 149 | -59 | 1951.7 | 4.64 |
| 1259 | 01 19 | +00 46 | 138 | -61 | 1954.8 | 4.61 |
| 1196 | 00 55 | +00 47 | 125 | -62 | 1954.7 | 4.58 |
| 0591 | 00 31 | +00 48 | 112 | -62 | 1952.7 | 4.59 |
| 0319 | 00 07 | +00 48 | 100 | -60 | 1951.6 | 4.60 |
| 0431 | 23 43 | +00 48 | 90 | -58 | 1951.9 | 4.64 |
| 0834 | 23 19 | +00 48 | 80 | -54 | 1953.8 | 1.81 |
| North Galactic Stripe | | | | | | |
| 0151 | 15 43 | -00 28 | 6 | 40 | 1950.5 | 1.57 |
| 1402 | 15 19 | -00 32 | 1 | 45 | 1955.3 | 3.23 |
| 1613 | 14 55 | -00 35 | 355 | 49 | 1957.3 | 3.56 |
| 1440 | 14 31 | -00 39 | 348 | 53 | 1955.4 | 3.81 |
| 1424 | 14 07 | -00 41 | 339 | 56 | 1955.4 | 4.06 |
| 0465 | 13 43 | -00 44 | 329 | 59 | 1952.1 | 4.33 |
| 1595 | 13 19 | -00 39 | 318 | 61 | 1956.3 | 4.39 |
| 1578 | 12 55 | -00 47 | 305 | 62 | 1956.2 | 4.51 |
| 1405 | 12 31 | -00 48 | 292 | 62 | 1955.3 | 4.59 |
| 1401 | 12 07 | -00 48 | 280 | 60 | 1955.3 | 4.55 |
| 0471 | 11 43 | -00 48 | 270 | 58 | 1952.1 | 4.50 |
| 1400 | 11 19 | -00 48 | 261 | 54 | 1955.3 | 4.38 |
| 1397 | 10 55 | -00 52 | 253 | 50 | 1955.3 | 4.27 |
| 0467 | 10 31 | -00 45 | 247 | 46 | 1952.1 | 4.08 |
| 0470 | 10 07 | -00 43 | 241 | 42 | 1952.1 | 3.81 |
| 1318 | 09 43 | -00 40 | 237 | 37 | 1955.0 | 2.22 |

epoch difference of $\sim$45 years enables proper motions to be determined accurately, whilst the SDSS photometry provides precise magnitudes and colours.

## 4.2 Data acquisition and astrometry

### 4.2.1 Downloading the data

The SuperCOSMOS data, comprising the IAM data and housekeeping files and images, were obtained directly from the SuperCOSMOS servers at the Royal Observatory Edinburgh; they are also available from the SSS web site (http://www-wfau.roe.ac.uk/sss/). Whilst the catalogues downloaded from the SSS contain additional object information such as proper motions and calibrated magnitudes in other bandpasses, only the basic IAM positional, quality and classification data were required.

The SDSS data were downloaded by means of the SDSS Query Tool (sdssQT), a graphical user interface allowing simple or complex queries to be submitted to the SDSS Catalogue Archive Server at Fermilab (http://archive.stsci.edu/sdss/software/#sdssQT). Queries were run for each of the Schmidt Field areas (Table 4.2), with a deliberate overlap between each field. Records were downloaded for objects in the PRIMARY database with a right ascension between the limits of the plate data (plus overlap) and with $r^* \leq 20.5$. The PRIMARY status is used to resolve multiple detections in regions where the survey scan lines overlap: one of the scan lines is assigned to have the *primary detection*. In regions with no overlap all objects are given PRIMARY status. The EDR data reduction does include deblending of objects, but this was not considered in the queries, so both BLENDED (child and parent) and unBLENDED items were downloaded. Blended objects are dealt with at a later stage through the SSS data, when parent objects as defined in the SuperCOSMOS scans are rejected during pairing (§4.2.2). Object parameters downloaded were right ascension, declination, $u^*g^*r^*i^*z^*$ petrosian and PSF magnitudes and object classification (see §4.2.3), with typically a quarter of a million objects obtained for each 6°-wide field. An example query, in the SDSS Structured Query Language (SQL), is shown in Figure 4.4.

```
SELECT
obj.ra,obj.dec,u,g,r,i,z,psfMag[0],psfMag[1],psfMag[2],psfMag[3],psfMag[4],
field.mjd[1],obj.objType,objID
FROM
sxPrimary
WHERE (RA() BETWEEN 45 AND 53 && r < 20.5)
```

*Figure 4.4: A query submitted to the SDSS Archive Catalogue Server for SGS field 0363, returning positions, magnitudes and classifications for all objects with $r^* < 20.5$ and with right ascensions between 45° and 53°.*

### 4.2.2 Pairing the catalogues

In order to combine the SDSS and SSS datasets and obtain proper motions for objects, the two catalogues were paired by an algorithm matching on proximity, to a maximum radius of 10 arcsec. With the ~45 year epoch difference between the catalogues, this corresponds to a maximum proper motion of ~220 mas yr$^{-1}$. Although this only represents ~50% of the high proper motion stars in the NLTT catalogue (Hambly et al. 2001c, figure 3), a larger radius than this would result in many spurious pairings and would necessitate additional complex pairing criteria. Integrity of the dataset and minimal contamination by false proper motion objects is more important in this application than including all very high proper motion stars.

Prior to pairing, the SDSS data was limited to $r^* \leq 20.5$ to avoid contamination from faint objects, and parent deblended objects from the SSS data were rejected on the basis of their poor centroiding. Each object in the SDSS catalogue was then paired to its closest neighbour in the SSS data on a field-by-field basis, by searching for the SSS objects whose declinations lay within a 10 arcsec tolerance level, and then selecting the closest of these. The SDSS was chosen as the master set as it reaches fainter magnitudes and is expected to contain fewer false detections. Its objects were paired in the original order as downloaded from the database; it was not necessary to prioritise the pairing sequence, since an index of items already paired ensured that each SSS object was matched only once, and to its closest SDSS counterpart rather than to a nearby neighbour which happened to appear first in the pairing process.

In a typical field there were ~250 000 objects in each of the SDSS and SSS datasets, of which typically ~50 000 were paired. These numbers include *all* objects: stars, galaxies (which

are later used to fix the proper motion zero point), quasars (used to check the zero point and estimate proper motion errors) and spurious noise detections. All detections in each dataset (except parent deblended objects in the SSS) were included at this stage so as to ensure no real objects were rejected prematurely. Noise artefacts and plate defects are likely to be responsible for the majority of the unpaired objects, with the remainder accounted for by the likes of poorly-centroided galaxies, stars and galaxies not detected in both datasets due to the slight difference in passbands, and high proper motion stars.

Despite the apparently large fraction of objects that remain unpaired, significant numbers of false pairings are unlikely, especially those due to spurious detections. With $\sim 2 \times 10^5$ objects on a $\sim 30$ deg$^2$ plate, the expected mean separation between objects is $\sim 40$ arcsec, significantly larger than the 10 arcsec maximum pairing radius. This means that the majority of objects in one dataset will be paired with their real counterpart in the other, and not a noise detection. The integrity of the pairing process is borne out by subsequent checks: the consistency of quasar proper motions with zero motion (Figure 4.7) shows that false pairings are not a significant problem for this class of objects, and the good correlation between these proper motions and those from the SSS (Figure 4.8) provides further proof of the pairing quality. Furthermore, the excellent population separation in the reduced proper motion diagram (Figure 4.11) strongly suggests minimal contamination from incorrect pairings, which if present would be evident as high proper motion clumps.

Although the pairing algorithm is shown to be unaffected by any significant amounts of false pairings, it is perhaps an area of the analysis which warrants further investigation. Matching only objects with similar magnitudes, colours and image size and shape would decrease the likelihood of mismatches, although would be difficult to implement in datasets with different photometric and astrometric measures. Such stringent criteria would also increase the likelihood of real stars being rejected, especially when combined with the problem that many variable stars would be likely to change brightness appreciably over the 45 year epoch difference. Another option would be to include data from an intermediate epoch, since this would both increase the pairing efficiency, improve the proper motion accuracy, and enable higher proper motion stars to be found. However, requiring that a star appears on all three catalogues would result in fewer stars in the final paired sample, especially since the datasets would be in different passbands and have different depths. Additionally, whilst it would be optimal to use

a third dataset at an epoch halfway between the existing two, the only suitable SuperCOSMOS data are the UKST $B_J$ plates, which in many cases date from only a few years prior to the SDSS data. Given the satisfactory reliability of the existing pairing routine and the difficulties implementing improvements to it, any such developments are left for future work.

### 4.2.3 Star-galaxy separation

Star-galaxy separation was achieved using the classifications given in the SDSS catalogue. Objects are classified either as stars or galaxies from the image shape and morphology according to the model PSF, deVaucouleurs and exponential fits to the flux of the object, and the likelihoods of the fits. The PSF magnitude is the optimal measure of stellar flux, whereas exponential or deVaucouleur models better describe the flux of a galaxy. Objects are classified as either stars or galaxies based on a criterion combining these magnitudes (Stoughton et al. 2002).

This star-galaxy separation has been shown to be at least 95% accurate for $r^* \leq 21$ (Stoughton et al. 2002), which is adequate for the purposes of this study and better than could be obtained from analysis of the photographic plate material (see §A.2.2). At this stage the galaxies are retained for use in providing an absolute zero point of proper motions.

### 4.2.4 Position-dependent astrometric errors

In order to accurately determine proper motions is it necessary to remove systematic positional errors present in the photographic plate data. These "swirl patterns" are already removed on large scales from the SSS data by a mean error map with the technique described in §A.2.1 and §3.5.5. The SSS data therefore has mean large-scale positional errors removed, but there will still be plate-to-plate effects present as well as systematic errors on smaller scales. These are dealt with by an error mapping algorithm first used by Evans & Irwin (1995) (and employed for deriving the SSS proper motions), which applies a large scale (10 arcmin or 1cm) correction to account for plate to plate systematics, and then a further one-dimensional algorithm to remove small scale (2 arcmin) errors. The procedure operates as follows:

*(i)* A two-dimensional large-scale error mapper is applied by dividing the field into an grid

of 10 arcminute squares and measuring the mean shift in the $x$ and $y$ coordinates between the two datasets from all the stars in each cell. A 3x3 linear filter is used to reduce the error function noise, and the $x$ and $y$ shift for each object in the field is interpolated from the grid point corrections. The SDSS position for each object (stars and galaxies) is then shifted with respect to the SuperCOSMOS coordinates (the orientation of this shift is immaterial) to remove large scale errors. Stars and galaxies are not treated separately at this stage so as to facilitate the proper motion zero point shift by using the galaxies as described in $(iv)$ below.

*(ii)* Small scale errors are then removed by a one-dimensional error mapper, which calculates $x$ and $y$ errors as a function of both $x$ and $y$ by evaluating the mean shift for stars in each 2 arcminute strip in both directions over the field. Median and then linear filters are applied to smooth and reduce the noise in the functions, which are then used to again shift the star and galaxy SDSS positions with respect to the SuperCOSMOS measures. This process is iterated until the mean shift in each of the $x$ and $y$ strips is less than a tolerance level (0.008 times the rms $x$ or $y$ shift.)

*(iii)* The two-dimensional error mapper is then applied again to remove any large scale shifts introduced by the one-dimensional algorithm.

*(iv)* At this point the stars have zero mean proper motion, whilst the mean galaxy displacement is non-zero, since stars dominate the number counts at these magnitudes. The galaxies are used to shift the proper motion zero point by determining a least-squares fit of the galaxy positions to find a six-coefficient linear plate model accounting for zero-point, scale and orientation. A global translation is then applied using this model to reset the galaxies to zero mean proper motion, with the SDSS measures transformed by

$$\begin{aligned} x_{SDSS} &= a + bx_{SSS} + cy_{SSS} \\ y_{SDSS} &= d + ex_{SSS} + fy_{SSS} \end{aligned}$$

where $a, b, c, d, e$ and $f$ are the plate coefficients determined from the least-squares fit to the galaxy positions.

The results of applying this error mapper can be seen in Figure 4.5, which shows a typical survey field covering a strip along the centre of the Schmidt plate that is 6.25°wide and 2.5°high. The first panel shows the field after the SSS mean large-scale distortion algorithm has been used, but before the error mapping algorithm described above has been applied, with the large scale 'swirl pattern' of the photographic data still evident. After the error mapper there are only very small residual systematic errors in position, and the remaining random errors have an rms of only ~0.3 arcsec.

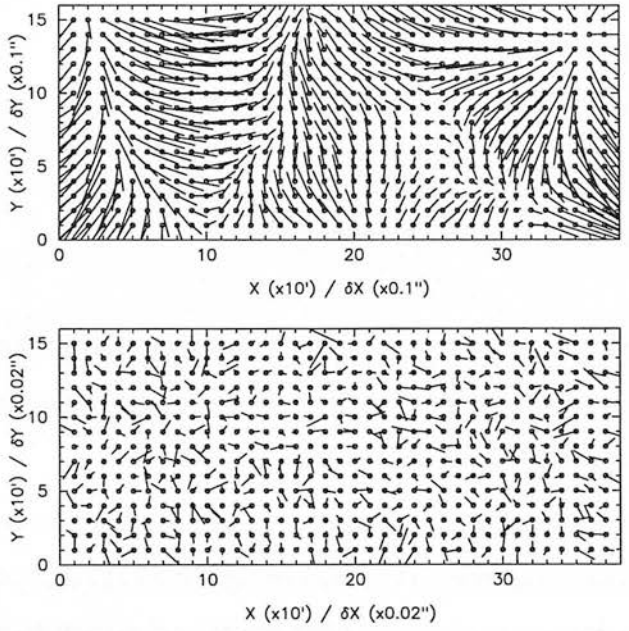


*Figure 4.5: Before and after the error mapper is applied in field 0363 in the SGS, which covers a 2.5°-high strip along the centre of the Schmidt plate. The vector "lollipops" show the relative size of the binned, smoothed and filtered positional errors at each point in the field. Note that the binning and smoothing means that these plots show systematic, not random errors, and that the scale of the errors in the bottom figure is five times smaller than that in the top figure. The vectors are scaled so that one tickmark corresponds to 0.1 arcsec in the top panel, and 0.02 arcsec in the bottom panel.*

### 4.2.5 Photometric-dependent astrometric errors

Systematic biases dependent on the magnitude and colour of targets are particularly prevalent in photographic astronomy, and could affect the selection or derived astrometric parameters of stars. However, such effects are unlikely to have a large bearing on these data. Figure 4.6 demonstrates this by showing the rms of positional errors in $x$ and $y$ for a typical plate after the error mapping has been applied. Over the range of stellar magnitudes from which the sample is selected ($15 \lesssim r^* \lesssim 19.5$) there is systematic variation in the positional errors only at the $\sim$0.1 arcsec level (corresponding to $\sim$2 mas yr$^{-1}$ for the $\sim$45 year epoch difference), which should not lead to significant systematic astrometric or selection errors.

#### Magnitude-dependent astrometric errors

Positional errors are expected to increase as a function of magnitude, but Figure 4.6 shows that brighter images have worse positional accuracy than fainter ones in these data. These effects are due to a number of possible reasons, such as:

- *Schmidt telescope distortion.* The radial distortion on Schmidt photographs means that image quality deteriorates from the plate centre, and asymmetrical images are liable to result from a misalignment of the telescope corrector plate. This effect is larger for brighter and saturated images since they have poorer centroiding, and is exacerbated by the limited dynamic range of SuperCOSMOS.

- *Measuring machine-induced errors.* One effect that could lead to magnitude-dependent astrometric errors arising from the SuperCOSMOS scanning is laser misalignment (Evans & Irwin 1995). The plate emulsion has a finite thickness ($\sim$25$\mu$m), which means that if the laser beam is not precisely vertical then bright stars, which sensitize the emulsion through its entire thickness, can have a systematic shift with respect to faint images, which only sensitize the emulsion surface.

These systematic magnitude errors cannot be corrected for in the data, since this could remove real effects present, such as that of brighter stars tending to have higher proper motions

due to their mean closer proximity to the Sun. However, as shown in Figure 4.6, their combined effect is likely to be small for the high proper motion sample: only $\lesssim$8 mas yr$^{-1}$ for a sample selected with a proper motion cut five times larger (see §4.3.1). Additionally, this systematic error applies to the error difference with magnitude across the whole $15 \lesssim r^* \lesssim 19.5$ range, whereas the subdwarf sample is dominated by stars with $r^* \gtrsim 17$ (Chen et al. 2001, Gould 2003). The more pronounced errors at $r^* \lesssim 16$ seen in Figure 4.6 are therefore unlikely to have a large effect on the derived proper motions in this study.

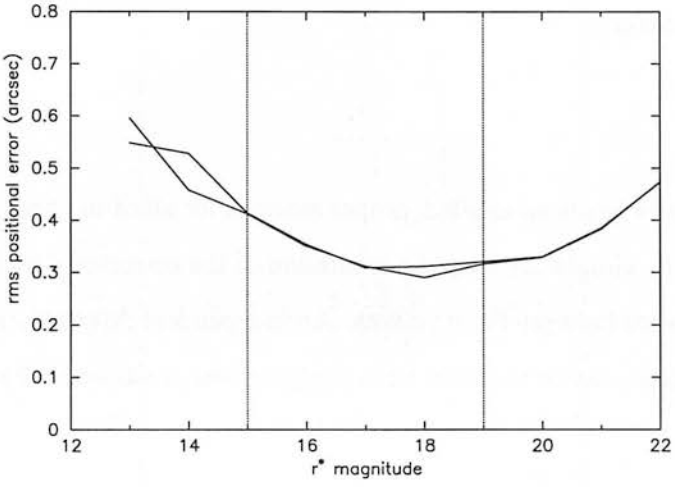


*Figure 4.6: The rms of the random positional errors in $x$ and $y$ as a function of magnitude for a typical field in the NGS, once the error mapping algorithm has been applied. In the magnitude range of interest (dashed lines) there is only variation with magnitude at the ~0.1 arcsec level (~2.2 mas yr$^{-1}$), indicating that systematic magnitude effects will not significantly affect the high proper motion sample in this study.*

**Colour-dependent astrometric errors**

Differential colour refraction, whereby stars of different colour have different atmospheric refraction, is also a common cause of such photometric-dependent astrometric errors. However, it is unlikely to have a large effect in this case, since when determining the relative difference in positions for proper motions a precise value of the *absolute* refraction value is not necessary, and also differential colour refraction is less pronounced for $V$ plates (Evans & Irwin 1995), which are used for the astrometric measures in this study. Biases arising from variations in

atmospheric effects are unlikely since all observations were taken on or near the meridian, and the telescopes used in the survey are at similar latitudes: Apache Point Observatory where the SDSS observations were made is at 32°N 46', and the Palomar Observatory is at 33°N 21'. Discrepancies in positions between the SDSS and SSS data due to differential colour refraction will also contribute only a small effect since the SDSS $r^*$ and POSS-I E passbands are very similar, centred at $\lambda \sim$6400 Å.

### 4.2.6 Proper motions

#### Quasar motions

After the error mapper has been applied, proper motions for all of the stars in the paired catalogue are obtained by simply dividing the separation of the corrected positions at each epoch by the epoch difference between the measures. An independent determination of the accuracy of these proper motions can be obtained from analysing the positions of the quasars present in the data.

The Veron and Veron 10th QSO catalogue (Veron-Cetty & Veron 2001) and the SDSS QSO catalogue (Schneider, Richards & Fan 2002) provide a large database of quasars suitable for purpose. Pairing the known quasars with the SDSS/SSS paired data on proximity yields a total of 1613 and 2754 quasars in the SGS and NGS respectively. This equates to a mean of 135 and 172 quasars per field in the SGS and NGS, which is sufficient to estimate the proper motion accuracy on a per-field basis.

Under the assumption that the quasars should exhibit zero proper motion, the median spatial discrepancy between the quasars' SDSS and SSS measures divided by their epoch difference yields the proper motion zero point for each field. This systematic offset of the proper motions is consistent with zero, as shown in Figure 4.7. The root mean square (rms) spatial difference is accordingly divided by the epoch difference to derive the rms proper motion error, $\sigma_\mu$. This error deviates significantly from field to field, with $5.0 \lesssim \sigma_\mu \lesssim 9.0$ mas yr$^{-1}$ for the SGS and $5.0 \lesssim \sigma_\mu \lesssim 10.0$ mas yr$^{-1}$ in the NGS. However, it should be noted that the true proper motion errors of the proper motion sample are liable to be less than these values, since the quasars are fainter and have poorer centroiding than the majority of subdwarfs in this study. The reason

for the large range in the derived proper motion error is unclear, although is likely to be a result of the varying quality of the photographic plates and possible systematic errors in the quasar positions, especially between the two Galactic stripes. This latter reason and the results of initial reductions led to the adoption of a global proper motion error, rather than the use of separate error estimates for each field. The proper motion error has an important application in the determination of the lower proper motion limit, as seen in §4.3.1.

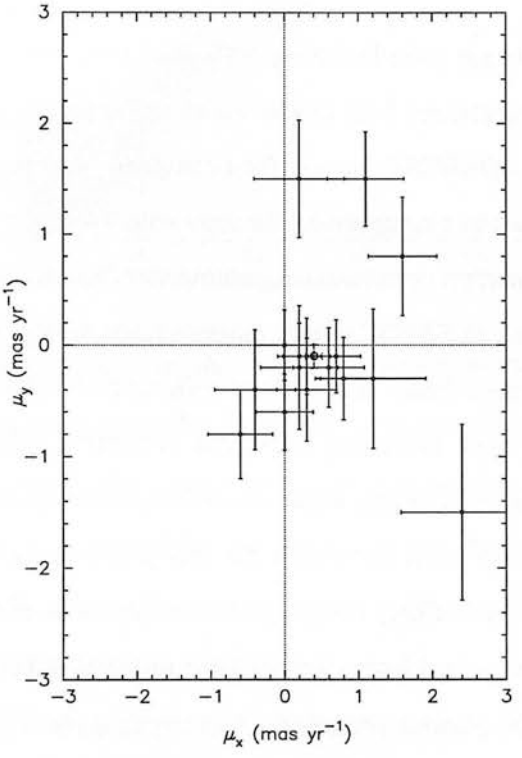


*Figure 4.7: Proper motion zero points for the NGS fields measured from quasars for the NGS fields (points) and the combined NGS dataset (open circle).*

**Comparison with SSS proper motions**

The accuracy of the derived proper motions can also be ascertained by comparison with those published in the SuperCOSMOS Sky Survey (Hambly et al. 2001c). These are measured from the $B_J$ and R plates of the survey, with systematic positional errors removed as in this study (§4.2.4) and differential colour refraction effects also accounted for. The SSS proper motions are currently derived from data at two epochs, with a median epoch difference between the $B_J$

and R plates of 15 years, although future releases will soon utilise measures from four plates where available.

To compare the proper motions derived here with the SSS results we have analysed SSS UKJ/UKR field 866, which overlaps the POSS-I fields 1440 and 1424 in the NGS. The $B_J$ and R plates in field 866 have an epoch difference of 17 years, so with good plate quality this comparison uses SSS proper motions that are likely to be of above average accuracy.

The stars in the sample are paired with the SSS data, with image quality criteria (such as restrictions on blended objects, see §4.3.1) applied as in the SDSS/SSS analysis. The proper motions derived from the SDSS/SSS data are then compared with the SSS proper motions for each star. Figure 4.8 shows this comparison for stars with $15.0 \lesssim r^* \lesssim 19.5$, along with $1\sigma$ and $2\sigma$ deviations from a perfect correlation, assuming standard deviations of 10 mas $yr^{-1}$ and 8 mas $yr^{-1}$ for the SSS and SDSS/SSS proper motions respectively. There is good correlation between the measures, with a linear correlation coefficient of $\sim$0.85 and $\sim$99% of the stars falling with the $2\sigma$ error bars, indicating negligible systematic effects. Note that there are virtually no stars that have discrepantly high SDSS/SSS proper motions compared to the SSS measures, although there are some for which the SSS proper motion estimate appears to be significantly too high. This is likely to be due to the facts that the SSS results are derived from a smaller time baseline and from photographic material at both epochs, increasing the likelihood of objects with spurious proper motions entering the SSS sample. The excellent consistency of the SDSS/SSS proper motions compared to the SSS measures for stars with high SDSS/SSS proper motions demonstrates the good reliability of the strict high proper motion sample selection in this study and suggests negligible contamination from objects with false motions.

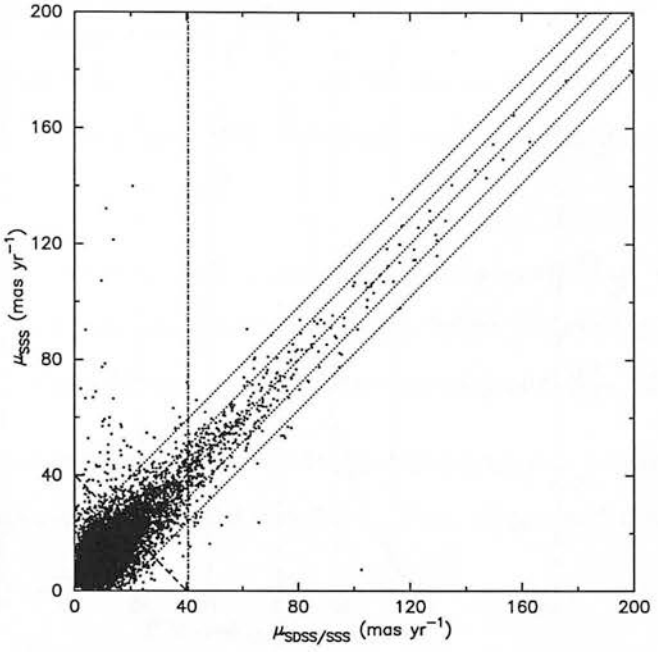


*Figure 4.8: Comparison of the proper motions derived in this study ($\mu_{SDSS/SSS}$) with those from the SuperCOSMOS Sky Survey ($\mu_{SSS}$) in NGS fields 1424 and 1440. The dotted lines show $1\sigma$ and $2\sigma$ deviations from a perfect correlation: some ~99% of stars fall within the $2\sigma$ boundaries of a perfect correlation, and the linear correlation coefficient is 0.85. The lack of stars along the $\mu_{SDSS/SSS}$ axis shows close agreement between the SDSS/SSS measures and the corresponding SSS estimates for stars with high SDSS/SSS proper motions, demonstrating the good reliability and negligible contamination of our high proper motion sample. Stars to the right of the dot-dashed line pass the high proper motion criterion, and the dashed line shows the cut along which the distribution of proper motion differences is plotted in Figure 4.9*

## 4.3 Candidate Subdwarfs

### 4.3.1 The high proper motion sample

#### Image quality criteria

Prior to the proper motion cut being applied, the data are subject to criteria to ensure that only objects with stellar and high quality images are included in the final sample. From the SSS data

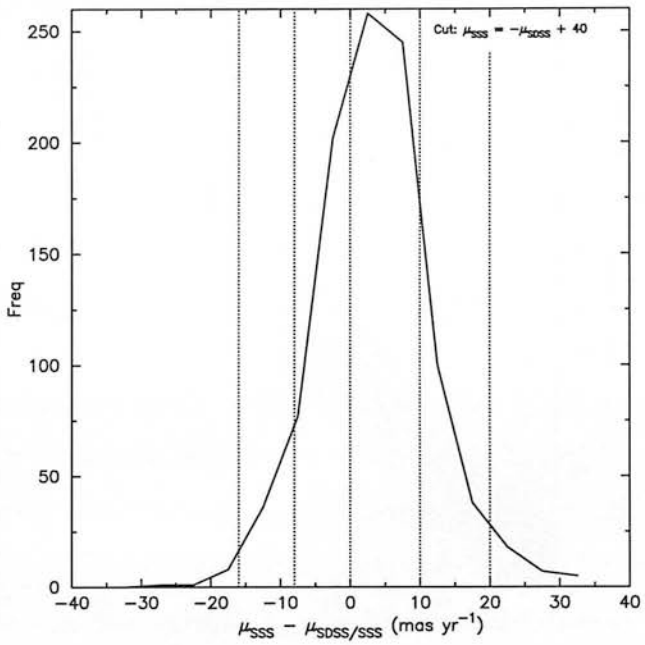


*Figure 4.9: The distribution of differences in the SSS and SDSS/SSS proper motions of stars along a 10 mas-wide cut, indicated by the dashed line in Figure 4.8. The dotted lines correspond to those in Figure 4.8, denoting a perfect correlation and the expected $1\sigma$ and $2\sigma$ deviations from it. At these low proper motions there is a tendency for the SSS values to be slightly larger than those from this study, evident by the slight zero point offset and lack of symmetry in the distribution. This latter aspect is mainly accounted for by the larger SSS proper motion error, and deviations from the expected distribution can at least in part be explained by the fact that in this region the motions are likely to be significantly affected by noise — hence the reason why only stars with much higher proper motions are included in the final sample. Nevertheless, that the distribution of the proper motion difference shows no large systematic offset and is consistent with the expected errors, even at these low proper motions, shows the good consistency between the SSS measures and those from this study.*

the following characteristics of each image are restricted (see §A.1.6 and Hambly et al. 2001a for more details):

- *Blend:* Objects appearing as blended in the SSS database are rejected.
- *Profile Classification Statistic, $\eta$:* This quantifies the 'stellarness' of an object by comparing the residuals of the areal profile of an image with that of an average stellar template. Objects with $\eta \geq 4\sigma$ are rejected.
- *Quality:* During processing the SSS data are assigned a quality flag, which is affected by circumstances such as an image being very large, bright, fragmented or close to a bright star or plate boundary. Images with a quality value of greater than 127 are rejected.
- *Ellipticity:* The ellipticity of an image is calculated from the weighted semi-minor and semi-major axes given by the SSS processing. Only objects with e $\leq$ 0.25 are included in the sample.

**Proper motion cut-off**

As in the analysis of the Murray data (§3.6), a lower proper motion limit is applied to the population of paired stars for two principal reasons. The first is that proper-motion selection amplifies the contribution from the higher-velocity halo population, and the second is to ensure a 'clean' reduced proper motion diagram and more accurate subdwarf selection by only including stars with small relative proper motion errors.

The lower proper motion limit can be applied either on a global basis, with one limit for all fields, or for each field individually, using the proper motion error estimates from the quasar positions in each field (§4.2.6). Initially this latter approach was used, but evidence of systematic differences between the proper motion accuracies derived for the SGS and NGS led to the adoption of a global proper motion minimum for the entire SGS and NGS sample. The total rms of all the quasar "proper motions" in each stripe was found to be $\sigma_\mu \approx 6.7$ mas yr$^{-1}$ for the SGS and $\sigma_\mu \approx 8.1$ mas yr$^{-1}$ for the NGS. In order to avoid the low proper motion 'tail' in each stripe the more conservative value of the NGS error was used for all fields. A $5\sigma_\mu$ cut on the proper motions was applied in defining the lower limit, so that the value used for the entire sample was:

$$\mu_{\rm min} = 40.5 \text{ mas yr}^{-1}. \tag{4.1}$$

A maximum proper motion limit is also adopted so as to ensure sample completeness. This limit is theoretically determined by the maximum pairing radius of 10 arcsec, corresponding to $\mu_{\rm max} \approx 220$ mas yr$^{-1}$. However, the actual maximum is somewhat smaller than this value due to systematic shifts in position affecting the pairing process; I therefore adopt a conservative $\mu_{\rm max} = 160$ mas yr$^{-1}$ from proper motion number counts (see §4.4.4.)

Figure 4.10 shows the relative proportions of high proper motion stars in the SGS and NGS. Although there are discrepancies at the bright and faint ends, over the magnitude range of the sample selected ($15 \lesssim r^* \lesssim 19$) the fraction of stars passing the proper motion criteria agree to within a few percent.

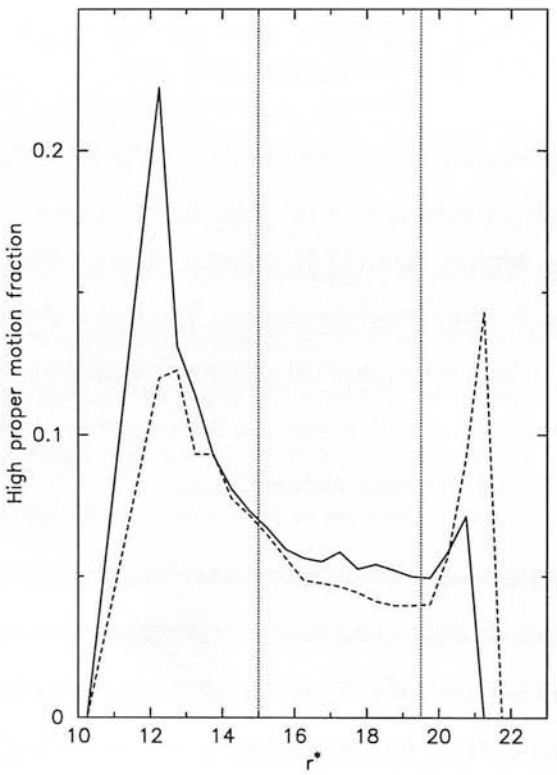


*Figure 4.10: The numbers of high proper motion stars in the SGS (solid line) and NGS (dashed line), expressed as a fraction of the total number of paired stars. For the magnitude range of the sample (between the dotted lines) the proportion in each stripe agree to within a few percent, indicating no systematic errors in the derivation of proper motions or high proper motion selection.*

### 4.3.2 Reduced proper motion selection

The method of reduced proper motion (§3.7.1, Equations 3.13 & 4.2) is used to select the high-velocity and low-luminosity subdwarfs from the high proper motion sample. The RPMDs of $H_{r*}$ against $(r^* - i^*)$ for all stars within the magnitude, proper motion and quality limits in the SGS and NGS are shown in Figure 4.11. The greater depth and more accurate photometry of the SDSS survey compared to the photographic data is apparent in the contrast with the RPMD for the Murray data (Figure 3.11). Here the white dwarfs, subdwarfs and disc main sequence stars form three clearly separate sequences.

$$H = m + 5\log\mu + 5 = M + 5\log V_T - 3.379 \tag{4.2}$$

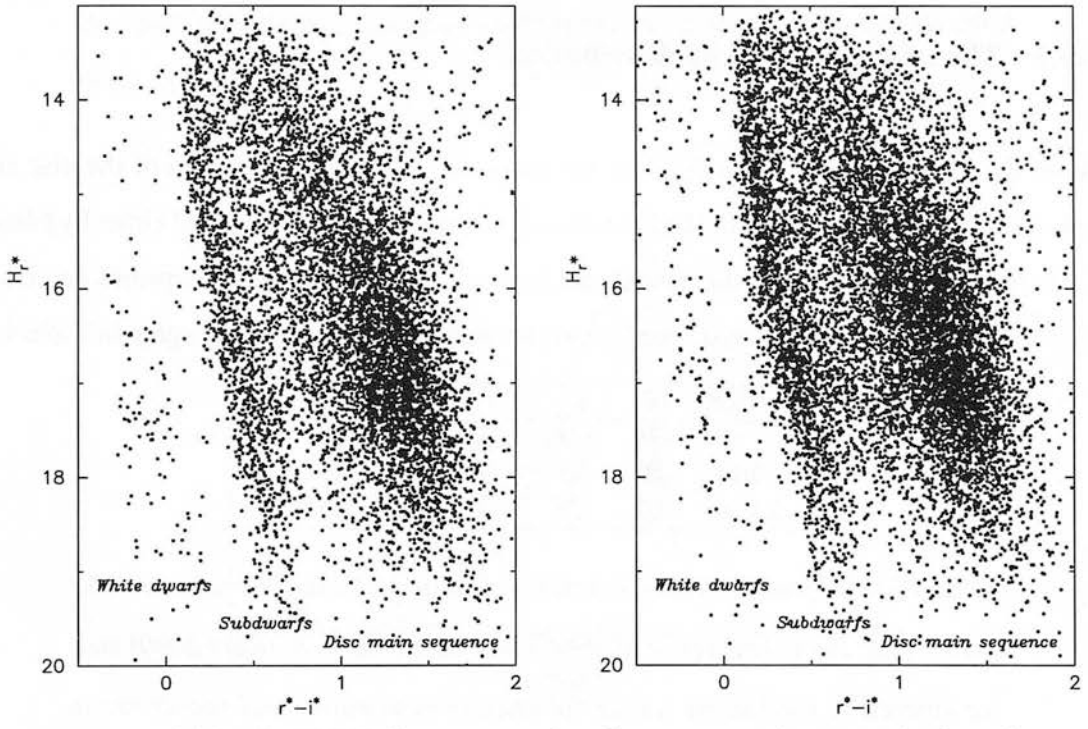


*Figure 4.11: The RPMD for stars passing the proper motion, magnitude and quality criteria in the SGS (left) and NGS (right). The three separate sequences of white dwarfs, subdwarfs and thin disc stars are clear and the subdwarf population forms a tight locus, in great contrast to the large scatter seen in the equivalent diagram from photographic data (Figure 3.11).*

Although the subdwarfs form a distinct sequence on the RPMD, a rigorous selection method is required for which any selection biases are defined and can thus be accounted for. As ex-

plained in §3.7.2, one such technique is to select stars within a percentile range of the expected reduced proper motion distribution for subdwarfs; another is to select stars between a lower and upper tangential velocity ridgeline on the RPMD. From Equation 4.2 it is apparent that derivation of the reduced proper motion distribution $\Psi(H_{r*})$ requires knowledge of the absolute magnitude distribution $\phi(M_{r*})$ and the tangential velocity distribution $\psi(V_T)$. For the method of transverse velocity selection, on the other hand, Equation 4.2 suggests that with a mean colour-magnitude relation lines of constant $V_T$ can be plotted on the RPMD: these can be used to select stars from given regions of the diagram, with a knowledge of the logarithm of the spheroid tangential velocity distribution required in order to model the selection biases. It is therefore necessary to first derive a subdwarf colour-magnitude relation and the tangential velocity distributions in each of the lines of sight.

### 4.3.3 The tangential velocity distribution

As in the Murray data analysis (§3.7.2), the tangential velocity distributions of the disc and spheroid populations for each of the fields in the SGS and NGS are generated either by Monte Carlo simulations or through theoretical calculations. The same velocity ellipsoids described by a solar motion and Gaussian dispersions are assumed, and are given here again in Table 4.3.

| Population | $U_\odot$ | $V_\odot$ | $W_\odot$ | $\sigma_U$ | $\sigma_V$ | $\sigma_W$ |
|---|---|---|---|---|---|---|
| Halo | -26 | -199 | -12 | 141 | 106 | 94 |
| Thin Disc | 10 | -5 | -7 | 41 | 27 | 21 |
| Thick Disc | 10 | -23 | -7 | 52 | 45 | 32 |

*Table 4.3: Adopted velocity ellipsoids and solar motions. The assumed disc (Reid et al. 1995; Hawley et al. 1996) and halo (Chiba & Beers 2000) stellar kinematics used in the tangential velocity simulations. All speeds are in $kms^{-1}$, and U, V, W denote the usual Galactic coordinate triad in the respective directions of the Galactic center, direction of rotation and NGP.*

The derivations of the tangential velocity distributions by theoretical calculation and by Monte Carlo simulations are given in Appendix E. Figures 4.12 and 4.13 show the theoretically-calculated $V_T$ and $5 \log V_T$ distributions towards field 0363 in the SGS; whereas Figures 4.14 and 4.15 show the corresponding results from Monte Carlo simulations.

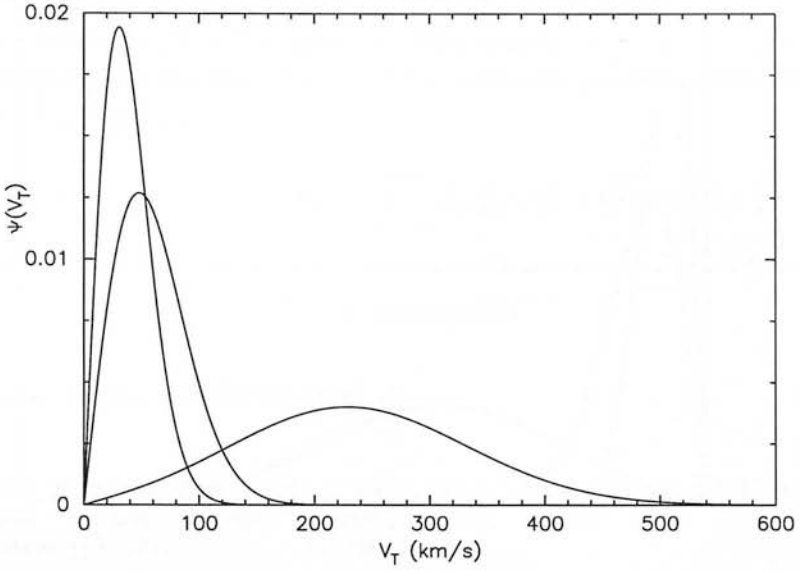


*Figure 4.12: Analytical tangential velocity distributions for the thin and thick disc and spheroid (in order of ascending velocity) in the direction of field 0363 in the SGS.*

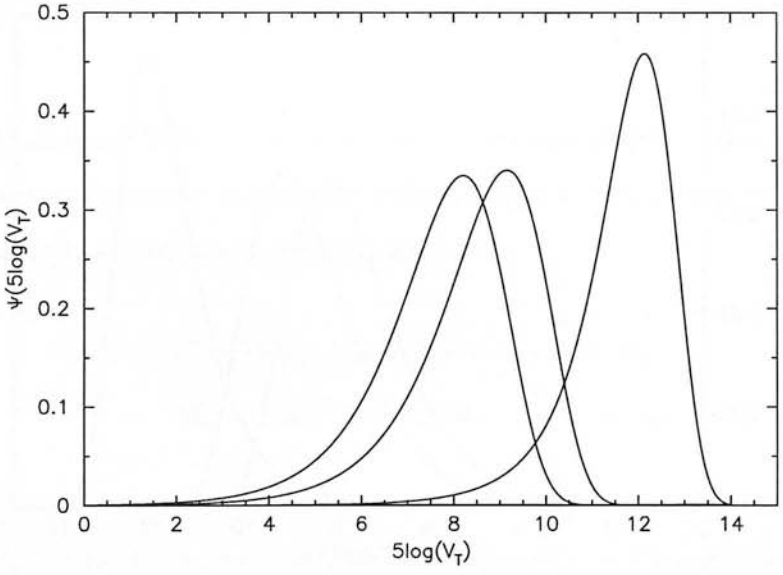


*Figure 4.13: The analytical distributions of the logarithm of the tangential velocity for the thin and thick disc and spheroid in the direction of field 0363 in the SGS.*

### 4.3.4 The reduced proper motion distribution

With knowledge of the tangential velocity distribution of the stars in each field, the reduced proper motion distribution of the disc and spheroid stars can subsequently derived by convolu-

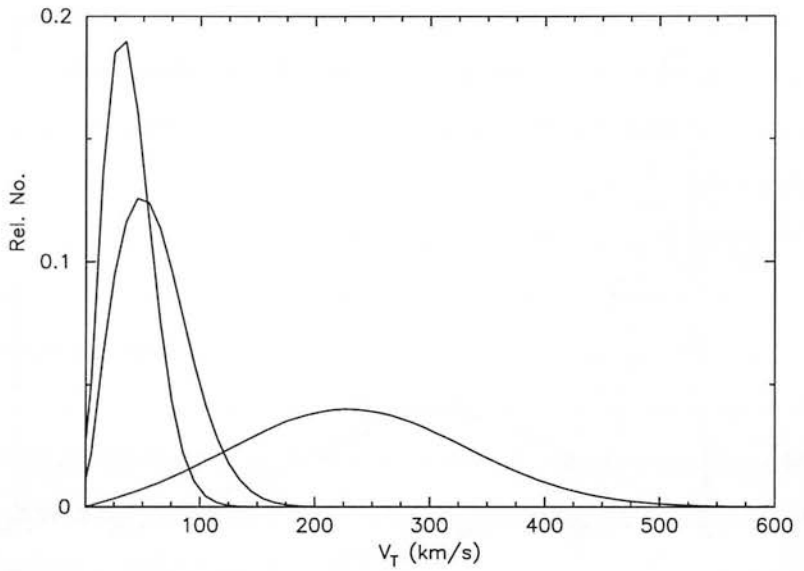


*Figure 4.14: Monte Carlo tangential velocity distributions for the thin and thick disc and spheroid in the direction of field 0363 in the SGS. These are consistent with the theoretical distributions shown in Figure 4.12*

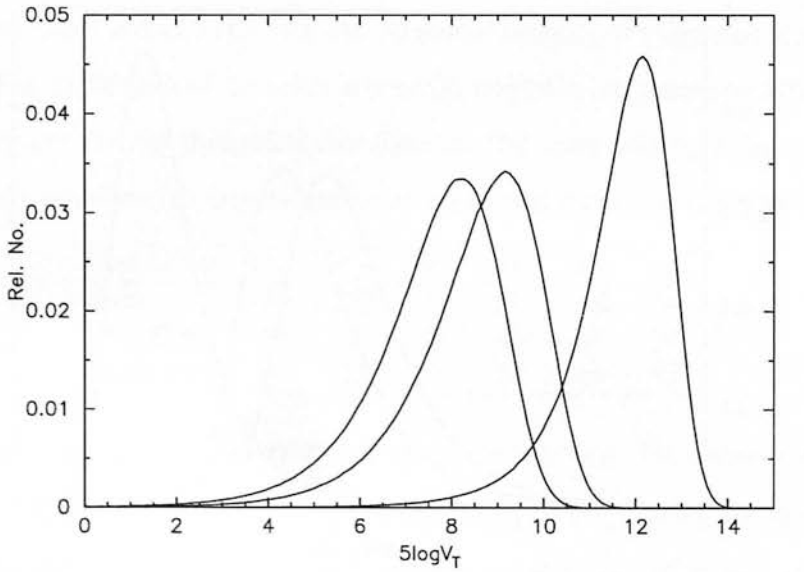


*Figure 4.15: The logaritm of Monte Carlo tangential velocity distributions for the thin and thick disc and spheroid in the direction of field 0363 in the SGS (cf. Figure 4.13.)*

tion (Box 2).

From Equation 4.2, the absolute magnitude distribution $\phi(M_{r\bullet})$ is convolved with the $5 \log V_T$ distribution (§4.3.3) and then shifted 3.38 magnitudes to bright luminosities to give

If the variable U = X + Y is the sum of the random variables X and Y with probability density functions $f_x(x)$ and $f_y(y)$ then the pdf of U is the convolution of $f_x(x)$ and $f_y(y)$:

$$f(u) = \int_{-\infty}^{\infty} f_x(x) f_y(u-x) dx = \int_{-\infty}^{\infty} f_y(y) f_x(u-y) dy = f_x * f_y$$

Box 2: Convolution

the reduced proper motion distribution $\Psi(H_{r^*})$.

The absolute magnitude distribution is taken as a Gaussian spread about the mean colour-magnitude relation (§4.3.5):

$$\phi(M_{r^*}) = \frac{1}{\sqrt{2\pi\sigma_I^2}} e^{\frac{-(M_{r^*}-\overline{M}_{r^*})^2}{2\sigma_I^2}} \tag{4.3}$$

where the intrinsic Gaussian spread used is $\sigma_I = 0.35$ mag for main sequence stars (Chiu 1980, Evans 1992).

In order to compare $\Psi(H_{r^*})$ with the observed reduced proper motions of the sample, the error functions of observed quantities of colour, magnitude and proper motion need to be convolved with $\phi(M_{r^*})$ and $\psi(5\log V_T)$ (Equation 4.4).

$$\begin{aligned} H_{r^*} &= r^* + 5\log\mu + 5 + \Delta_{r^*} + \Delta_{r^*-i^*} + \Delta_\mu \\ &= M_{r^*} + 5\log V_T - 3.379 + \Delta_{r^*} + \Delta_{r^*-i^*} + \Delta_\mu \end{aligned}$$

$$\Longrightarrow \Psi(H_{r^*}) = (\phi(M_{r^*}) * \psi(5\log V_T)) * \mathrm{erf}(r^*) * \mathrm{erf}(r^* - i^*) * \mathrm{erf}(5\log V_T) \tag{4.4}$$

*(i) Magnitude error function:* The error function of the observed $r^*$ magnitude, $\mathrm{erf}(r^*)$, is assumed to be a Gaussian with $\sigma_{r^*} = 0.033$, since the error in flux in the SDSS $r^*$ band is $\sigma_F/F \approx 3\%$ (Stoughton et al. 2002) and $\sigma_{r^*} = \frac{2.5}{\ln 10}\frac{\sigma_F}{F}$

*(ii) Colour error function:* Given that $\sigma_{i^*} = \sigma_{r^*}$ and assuming uncorrelated errors in magnitude, this gives a colour error of $\sigma_{r^*-i^*} = \sqrt{\sigma_{r^*}^2 + \sigma_{i^*}^2} = 0.047$. The assumption of uncorrelated magnitude errors is likely to lead to an overestimation of the colour error,

since the error in each band comprises a random and systematic component, and the systematic error cancels in the difference of magnitudes. However, overestimating the colour error will simply result in a wider reduced proper motion distribution and a more conservative reduced proper motion selection, so this approach is suitable for these purposes. The colour error function is a Gaussian of standard deviation $\sigma = s\sigma_{r^*-i^*}$, where $s$ is the slope of the $(\overline{H}_{r^*}, r^* - i^*)$ relation.

*(iii) Proper motion error function:* As noted in Evans (1992), a Gaussian function is not an accurate representation of the proper motion errors, since the error in $5 \log \mu$ is a function of $\mu$:

$$\sigma_{5 \log \mu} = 5 \log_{10} e \frac{\sigma_\mu}{\mu} \tag{4.5}$$

and so the proper motion distribution should be derived from the tangential velocity and density distributions. For high proper motion stars, however, a Gaussian approximation can be made as the size of the proper motion error will be relatively small — for a $5\sigma_\mu$ limit:

$$\frac{\sigma_\mu}{\mu} \leq \frac{\sigma_\mu}{\mu_{\min}} = 0.2 \tag{4.6}$$

Using this value in Equation 4.5 means that the proper motion errors will be overestimated, but as the derived error of $5 \log \mu_{lim} = 0.43$ is much smaller than the width of the $H_{r^*}$ distribution this effect is limited.

With the tangential velocity and absolute magnitude distributions given in §4.3.3 and Equation 4.3, and the error functions described above, the reduced proper motion distributions as a function of $(r^* - i^*)$ colour are calculated for subdwarfs and extreme subdwarfs in the direction of each field. Figure 4.16 shows the expected distributions for field 0363 in the SGS.

### 4.3.5 The colour-magnitude relations

A $(M_{r^*}, r^* - i^*)$ colour-magnitude relation is necessary for both techniques of subdwarf selection: for plotting lines of constant $V_T$ on the RPMD when using tangential velocity criteria,

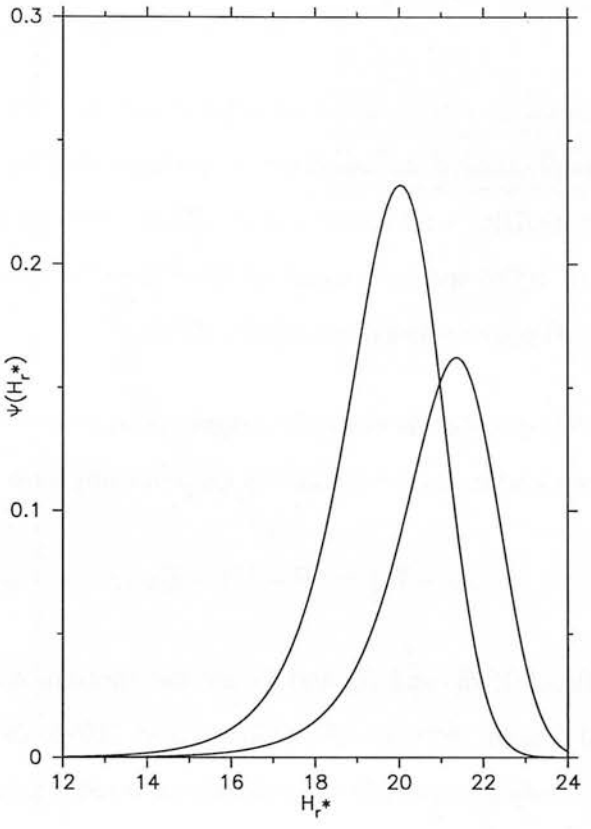


*Figure 4.16: The theoretical reduced proper motion distributions for subdwarfs (left) and extreme subdwarfs (right) at* $(r^* - i^*) = 1.0$ *in the direction of field 0363 in the SGS.*

and for the mean absolute magnitude relation $\overline{M}_{r^*}(r^* - i^*)$ in Equation 4.3.

However, obtaining a reliable colour-magnitude relation for subdwarf stars empirically is problematic, due to the existence of relatively few known subdwarfs with accurate trigonometric parallaxes. Additionally, applying a single relation to spheroid stars is prone to error due to the large range of metallicities present in the spheroid, and hence the wide spread of absolute magnitudes for a given colour. Three methods of deriving a colour-magnitude relation were investigated: from *(i)* globular clusters, *(ii)* model atmospheres and *(iii)* subdwarfs with accurate trigonometric parallaxes.

**(i) Cluster colour-magnitude relations**

An observed colour-magnitude relation for a globular cluster of known metallicity close to that expected for the sample subdwarfs can be used to estimate their luminosities. The cluster M5 has a metallicity of [Fe/H]$\approx -1.1$ (Sneden et al. 1992), a well-defined colour-magnitude relation (Sandquist et al. 1996) and an accurate distance modulus determination of $DM = (m - M)_0 = 14.5$ from Hipparcos data (Reid 1997a, 1998).

Sandquist et al. (1996) give the M5 cluster $V$ magnitude as a function of $(B - V)$ colour; extinction is allowed for by adjusting the colours by the reddening term $E_{B-V}$:

$$(B_0 - V_0) = (B - V) - E_{B-V} \tag{4.7}$$

where $E_{B-V}$ = 0.02 (Reid 1998) and $B_0$ and $V_0$ are the apparent magnitudes without extinction. The corrected fiducial sequence of Sandquist et al. (1996) therefore provides $V_0 = f(B_0 - V_0)$ and so the absolute magnitude of the cluster main sequence as a function of colour is given by

$$M_V = V_0 - 5 \log d + 5 = V_0 - DM \tag{4.8}$$

This relation is tested in Figure 4.17 against subdwarfs with accurate parallaxes and luminosities from Fukugita et al. (1996), Gizis (1997), Reid, van Wyk et al. (2001) and Smith et al. (2002). The parallax subdwarfs do not form a good fit to the cluster sequence, which may be at least in part due to problems such as age differences arising from the comparison of field and cluster stars. Additionally, the sequence only extends to $(r^* - i^*) \approx 0.3$ and so would be unsuitable for a large proportion of the subdwarf sample. Also, the cluster sequence would need to be transformed to $(M_{r^*}, r^* - i^*)$: no published $(B - V, r^* - i^*)$ relations exist, and it would be difficult to calibrate with the small number of fiducial subdwarfs in the SDSS standard star catalogue (Smith et al. 2002) due to a large difference between these colour indices. Finally, as is apparent in Figure 4.17 and as noted by Gizis (1997), the $(M_V, B - V)$ relation is a poor discriminator of metallicity, with little separation between the disk and subdwarf sequences, and the large inflection in the colour-magnitude relation at $(B - V) \approx 1.5$ means that $(B - V)$

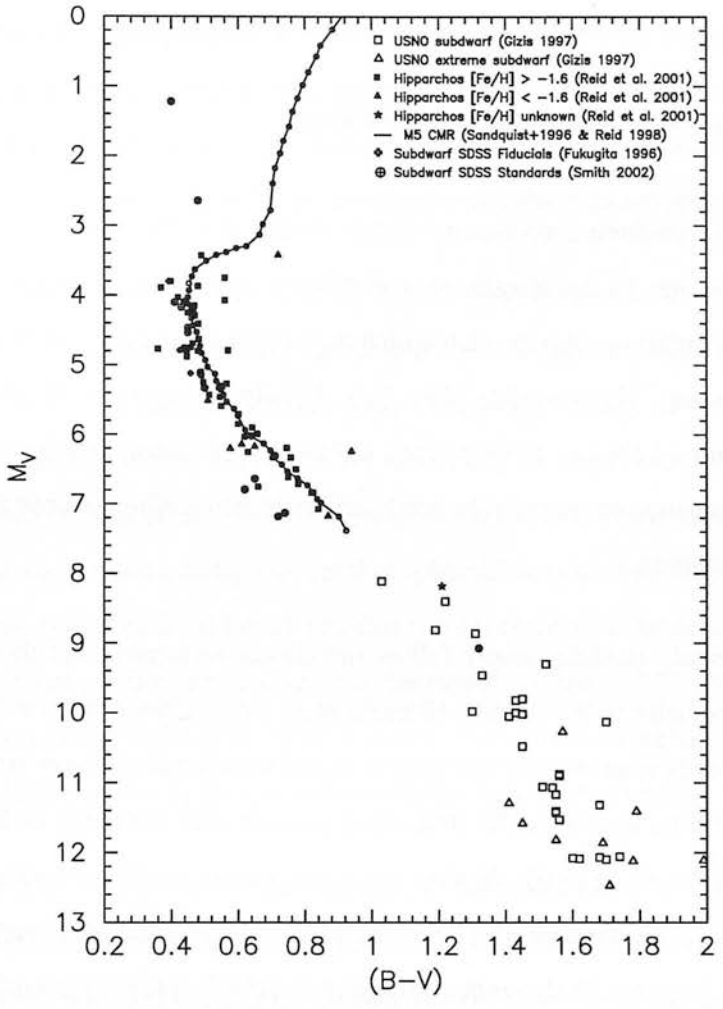


*Figure 4.17: The de-reddened colour magnitude relation (solid line) for the cluster M5 ([Fe/H] $\approx -1.1$) from Sandquist et al. (1996) plotted against subdwarfs with accurate parallaxes and luminosity determinations. The sequence is not a good fit to the parallax subdwarfs, possibly arising from age differences between cluster and field stars, and does not extend redwards enough for the candidate subdwarfs in this study. Additionally, it is clear that $(M_V, B-V)$ does not separate subdwarfs of different metallicity and that $(B-V)$ is a poor absolute magnitude indicator for these stars due to the steepness of the relation, especially at redder wavelengths.*

colours are poorly suited for estimating absolute magnitudes for M-dwarf stars. For these reasons alternative methods of deriving a colour-magnitude relation for the candidate subdwarfs

are considered.

**(ii) Model atmosphere colour-magnitude relations**

Theoretical isochrones from evolutionary stellar models provide colour magnitude relations for stars of varying metallicity. Baraffe et al. (1997) calculate models for low mass stars with metallicities from [m/H] = $-2.0$ to $-1.0$ which they claim accurately follow observations for cluster and field stars. They provide $(M_V, V-I)$ colour magnitude relations for [m/H] = $-2, -1.5, -1.3$ and $-1$ for $t = 10$ Gyr over a wide range of colour, which could be converted to $(M_{r^*}, r^*-i^*)$ and used to estimate the subdwarf luminosities of my sample given an estimate of each star's metallicity.

The Baraffe et al. models closely follow the cluster sequences and the majority of the field star data, especially in the infrared (Baraffe et al. 1997, 1998, Chabrier 2003). However, there is some disparity with the field star data at optical wavelengths, where metal-rich versions ([m/H] $\gtrsim -1.0$) of the models suffer from discrepancies with the lower end of the observed main sequence ($V - I_C \gtrsim 2.0$). Whilst lower metallicity models are expected to be less affected in this way, when matched to field star data they still yield poor reproductions of the observed colours. Figure 4.18 shows the Baraffe et al. (1997) colour-magnitude diagram (their figure 8), comparing their models with the subdwarfs with accurate parallaxes from Monet et al. (1992), Leggett (1992) and Dahn et al. (1995), and it is clear that there are differences between the models and field stars. In mitigation, the assertion that the Leggett (1992) sample is a poor representation of the spheroid is valid, since his classification relies solely upon two colour photometric selection, and his spheroid colour-magnitude sequence is uncertain. Any contamination by disc stars is curbed, however, by the fact that Baraffe et al. (1997) only consider stars from the Leggett (1992) sample with $V_T > 180$ km s$^{-1}$. Additionally, the relatively low cut-off velocity (160 km s$^{-1}$) of the Dahn et al. (1995) sample may cause it to be contaminated by thick disc stars. However, this is unlikely to account for the full extent of discrepancy of the Dahn et al. (1995) data with the models, nor their disparity with several of the Monet et al. (1992) stars.

The inconsistency between the Baraffe et al. (1997) models and field stars is further noted

by Gizis (1997), who compares the solar metallicity isochrone with nearby M-dwarfs from Reid et al. (1995) with good parallaxes. He finds that the model does not match the observed disc stars, whereas a previous generation of models (Baraffe et al. 1995) provides a good match for both low and solar metallicity stars. Baraffe and collaborators, however, believe that the newer models provide a better fit to the stellar physics and the cluster data.

Gould et al. (1998) also find fault with the Baraffe et al. (1997) models when they interpolate between the isochrones to estimate the metallicity of subdwarfs with $V_T > 260$ km s$^{-1}$ from C. Dahn (1997, unpublished.) They find a mean metallicity of $\langle [m/H] \rangle = -0.93$, which is somewhat higher than the expected metallicity of high-velocity spheroid stars of $\langle [Fe/H] \rangle \sim -1.5$ (Laird et al. 1988, Nissen & Schuster 1991). As noted in Gould et al. (1998), this is partially explained by the fact that spheroid stars tend to have lower levels of Fe than other metals, but there is still evidence that the expected abundance of spheroid stars is incorrect and/or there are inconsistencies with the models. Gizis (1997) found that the abundances of a subset of the Dahn et al. (1995) sample were in the expected range of [Fe/H] $\sim$ -1.5, providing further evidence for inaccuracies in the synthetic relations.

The Baraffe et al. (1997) models are therefore unable to fit the observed colours at redder optical wavelengths (Baraffe et al. 1997, Chabrier 2003), and exhibit possible systematic errors in metallicity when used to estimate abundances from colour-magnitude diagrams (Gizis 1997, Gould et al. 1998). These factors could significantly affect the ability of the models to provide the reliable colour-magnitude relations required here, calculating an expected absolute magnitude from each subdwarf given an observed colour and metallicity estimate. Therefore, whilst the latest theoretical model atmospheres provide good matches to most of the stellar physics and observed parameters, the possibility of systematic colour offsets, perhaps wavelength-dependent, leads me to instead employ an empirical colour-magnitude relation.

**(iii) Parallax subdwarf colour-magnitude relations**

The colour-magnitude relation from subdwarfs with accurate trigonometric parallaxes used to select subdwarfs from the reduced proper motion diagram is derived in a similar way to that of Gizis & Reid (1999). Following the classifications defined by Gizis (1997), separate relations

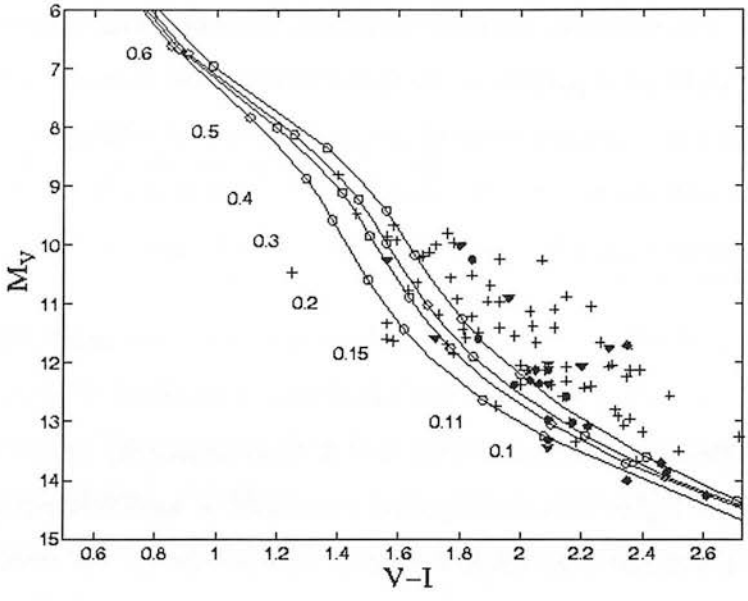


*Figure 4.18: Figure 8 from Baraffe et al. (1997), showing their model isochrones (solid lines, t = 10 Gyr) for [M/H] = -2, -1.5, -1.3, -1 (from left to right) against subdwarf field stars with good parallaxes from the studies of Monet et al. (1992) (filled circles), Dahn et al. (1995) (crosses) and Leggett (1992) (triangles). The open circles correspond to the model masses as indicated. There appears to be some significant discrepancy between the models and field star data.*

are determined for subdwarfs of low and high metallicity, with stars of [Fe/H] $\approx -1.2 \pm 0.3$ defined as subdwarfs (sd), and those with [Fe/H] $\approx -2.0 \pm 0.5$ as extreme subdwarfs (esd).

I use calibrating subdwarfs from the compilations of Gizis (1997) and Reid, van Wyk et al. (2001). Both of these studies use the spectral classification scheme described in Gizis (1997) to identify subdwarfs, and give accurate trigonometric parallaxes for their samples. These are derived from the USNO (Monet et al. 1992) and Yale (4th ed; van Altena et al. 1995) catalogues in the case of Gizis (1997), and from the Hipparcos catalogue (Perryman et al. 1997) in the case of Reid, van Wyk et al. (2001). The latter study uses only Hipparcos stars with parallax precisions of $\sigma_\pi/\pi < 0.15$, which corresponds to a Lutz-Kelker correction (Box 3) of $\Delta M_{LK} = 0.3$ mag for a uniformly-distributed sample. Gizis (1997), on the other hand, makes no such restriction or magnitude correction, since their sample selection is not well-defined. Lutz & Kelker (1973) showed that only parallaxes with $\sigma_\pi/\pi < 0.2$ are useful, so

this criteria is applied to the Gizis (1997) stars. However, no Lutz-Kelker adjustment is made to the parallax subdwarf sample used here, since the size of the absolute magnitude correction is sufficiently small considering a colour-magnitude relation is being fitted to the sample as a whole. The restriction of $\sigma_\pi/\pi < 0.2$ corresponds to a Lutz-Kelker correction of $\Delta M_{LK} < 0.51$ magnitudes for a uniform $(n = 4)$ distribution. However, the real corrections are likely to be much smaller, since selection by proper motion reduces the statistical correction (Hanson 1979) and subdwarf samples are likely to have a much flatter $(n < 4)$ parallax distribution (Reid, van Wyk et al. 2001).

> Lutz-Kelker bias is the analogue of Malmquist bias (which affects magnitude-limited surveys) for parallax-limited (ie. volume-limited) surveys. The fact that the number of stars in the survey cone increases non-linearly with distance means that errors in distance measurements (such as trigonometric parallax) cause more stars to be scattered into the sample than out of it. When selecting stars from this sample according to $\pi > \pi_{lim}$ this results in the mean distance of the sample being underestimated, and hence the mean absolute magnitude is also underestimated. This bias is a function of the accuracy of the parallaxes, so when combining parallax data statistically, such as in this case of deriving a mean colour-magnitude relation, a Lutz-Kelker correction $M_{LK}$ is usually applied to each calculated absolute magnitude such that $M_{true} = M_{obs} + \Delta M_{LK}$.

Box 3: Lutz-Kelker correction

I plot the subdwarfs with $\sigma_\pi/\pi < 0.2$ on a $M_I$, $(V - I_C)$ Hertzsprung-Russell diagram (Johnson $V$ and Cousins $I_C$), and fit a colour-magnitude relation to the sdM and esdM separately. Gizis & Reid (1999) used two linear segments to describe the colour-magnitude relation at the red end $(V - I_C \gtrsim 1.6)$ where the sd and esd sequences separate, and a single line for $(V - I_C \lesssim 1.6)$. However, linear fits in the colour-magnitude diagram are inappropriate for low mass stars since they do not accurately reflect their physical properties (Baraffe et al. 1997), and even two-segment fits as in Gizis & Reid (1999) poorly match the inflection in the subdwarf main sequence at $(V - I_C) \sim 1.5$. For these reasons I fit a cubic spline with unit weighting to the subdwarfs and extreme subdwarfs (Figure 4.19).

**Two-colour relations**

There is currently no published SDSS photometry for stars with accurate trigonometric parallaxes, so it is necessary to first derive the colour-magnitude relation in the standard Johnson/Cousins photometric systems, and then convert the colours and magnitudes to SDSS $r^*$

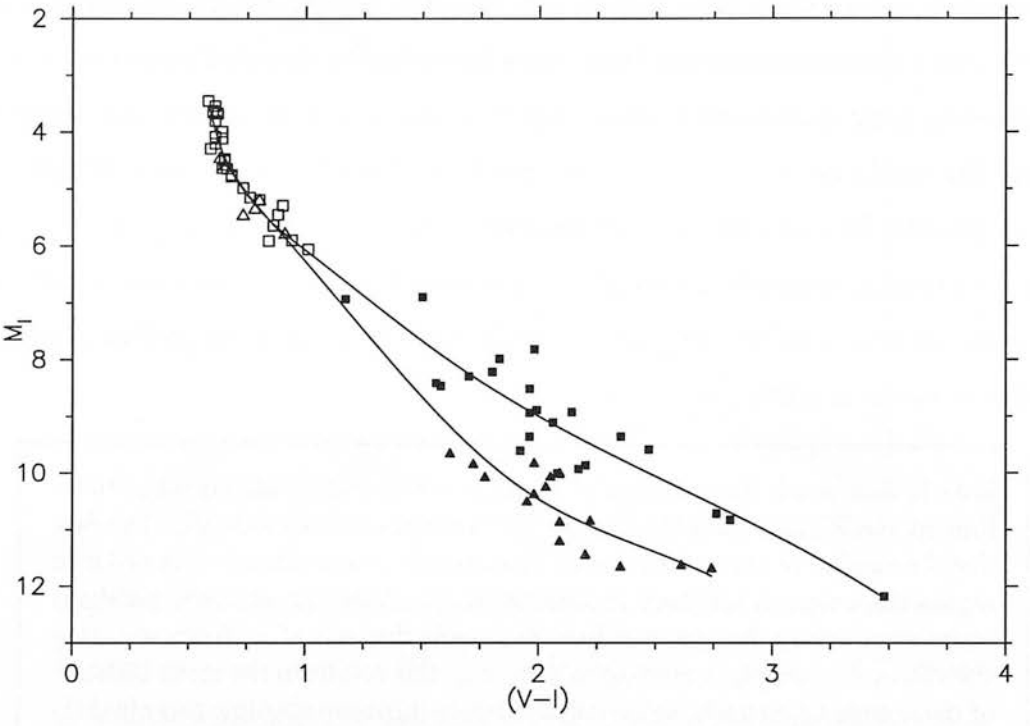


*Figure 4.19: The cubic spline colour-magnitude relation fits to the subdwarfs with accurate trigonometric parallaxes from the compilations of Gizis (1997) and Reid, van Wyk et al. (2001). Squares denote higher-metallicity subdwarfs (sd) and triangles the more metal-poor extreme subdwarfs (esd). Filled symbols are subdwarfs from Gizis (1997); open symbols represent those from Reid, van Wyk et al. (2001).*

and $(r^* - i^*)$. This is done by means of the relation

$$M_{r^*} = r^* - V + (V - I_{\rm C}) + M_I, \tag{4.9}$$

combined with two-colour relations to convert from SDSS $(r^* - i^*)$ to $(r^* - V)$ and $(V - I_{\rm C})$.

These two-colour relations should ideally be obtained from subdwarfs with accurate photometry and similar metallicities to those in my sample. However, of the subdwarfs with very accurate photometry in the SDSS Standard Star Catalogue (Smith et al. 2002), very few have published $V\,I_{\rm C}$ photometry and span only a small range in colour. I therefore fit linear two-colour relations between the Johnson/Cousins and SDSS systems for higher-metallicity disc stars instead (Smith et al. (2002) provide some colour transforms for solar metallicity stars,

but not the $(r^* - V, r^* - i^*)$ relation I require.) Despite this metallicity discrepancy, there is evidence that any consequent effect will be minor: comparing these fits with the few subdwarf stars with SDSS and $VI_C$ magnitudes suggests that the disc metallicity fits apply well to the spheroid metallicity stars. In any case, any error introduced by the two-colour relations will be insignificant compared to any errors in the $(M_I, V - I_C)$ colour-magnitude relation which is by far the dominant source of possible error. The colour-colour relations derived are

$$r^* - V = -0.889(r^* - i^*) - 0.040, \tag{4.10}$$

$$V - I_C = 2.097(r^* - i^*) + 0.429, \tag{4.11}$$

and are shown in Figure 4.20.

### 4.3.6 Selecting candidate subdwarfs

As discussed in §4.3.2, a rigorous and controlled method of selecting subdwarfs from the reduced proper motion diagram is required, with a choice of selecting between percentiles of the reduced proper motion distribution, or between specified tangential velocity limits. However, care has to be taken to avoid contamination from other stellar populations, for although the RPMD separates the subdwarfs from the thin disc stars and white dwarfs, there is some overlap with the locus of thick disc stars (Figure 4.11). Thick disc stars have a much higher local number density than subdwarfs ($\sim$ 40:1 — see §4.5.4), and the inclusion of even a tiny proportion of this population in the sample can result in a significant overestimation of the halo density (Bahcall & Casertano 1986.)

#### Reduced proper motion distribution selection

This contamination can be avoided by choosing appropriate $\Psi(H_{r^*})$ percentiles or velocity limits. For the reduced proper motion distribution selection method an upper and lower percentile can be chosen so as to encompass the subdwarf sequence on the diagram whilst considering

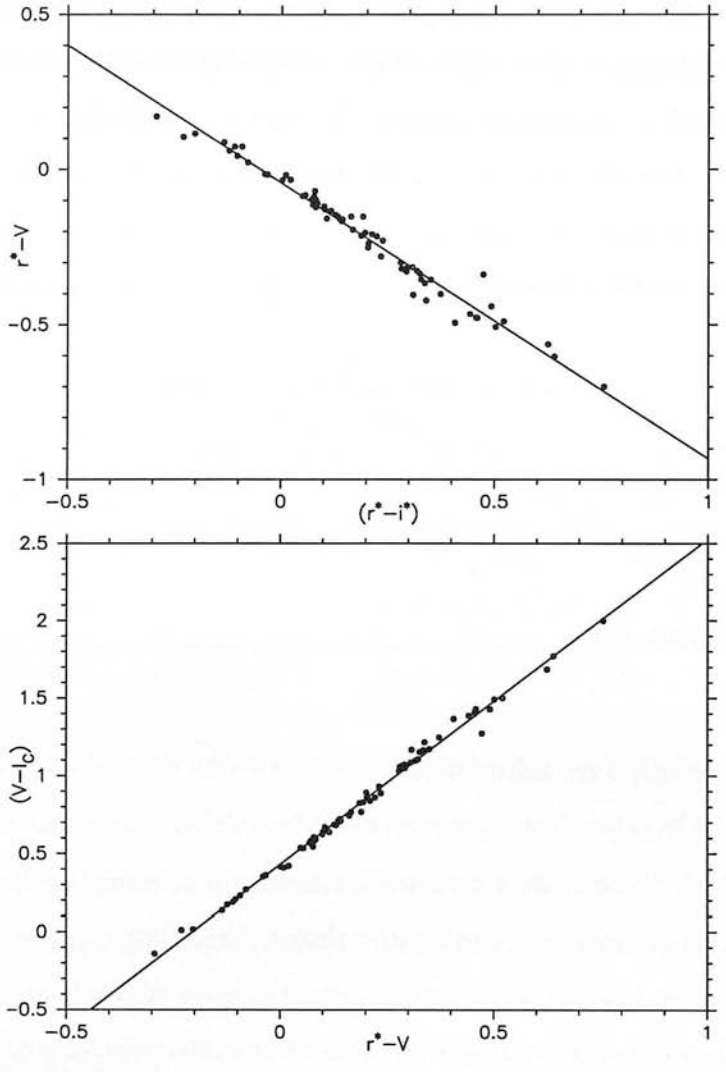


*Figure 4.20: The two colour relations between the SDSS and Johnson/Cousins systems, derived from standard stars of solar metallicity in the SDSS Standard Star Catalogue (Smith et al. 2002). I am unable to derive transforms of appropriate metallicity due to the very small number of subdwarfs with published accurate SDSS and $V I_C$ photometry and the small range in colour these few stars span. However, it appears that any systematic errors introduced by using the higher-metallicity relation will be small, and negligible compared to any errors arising from the parallax subdwarf fitting.*

the effective tangential velocity of each percentile, estimated from

$$V_T = 10^{0.2(H_{r^*} - \overline{M}_{r^*} + 3.379)} \tag{4.12}$$

where $\overline{M}_{r^*}$ is the absolute magnitude from the mean colour-magnitude relation. To demonstrate this, Table 4.4 gives the mean values of $V_T$ corresponding to the $\Psi(H_{r^*})$ percentiles for subdwarfs and extreme subdwarfs. The lower percentile can be selected so that the corresponding $\overline{V_T}$ allows few thick disc stars to enter the sample, as determined by the tangential velocity distribution described in §4.3.3.

| $\Psi(H_{r^*})$ | $\langle V_T \rangle$ (km s$^{-1}$) | |
|---|---|---|
| % | sd | esd |
| 0.10 | 100 | 98 |
| 0.20 | 137 | 136 |
| 0.30 | 167 | 166 |
| 0.40 | 195 | 194 |
| 0.50 | 223 | 222 |
| 0.60 | 253 | 253 |
| 0.70 | 288 | 289 |
| 0.80 | 332 | 336 |
| 0.90 | 402 | 409 |

*Table 4.4: The mean effective tangential velocities corresponding to percentiles in the reduced proper motion distribution $\Psi(H_{r^*})$ for the subdwarf and extreme subdwarf sequences in SGS field 0363.*

**Tangential velocity selection**

The technique of selecting candidate subdwarfs from the RPMD by applying tangential velocity cuts in conjunction with a mean colour-magnitude relation allows direct use of the $V_T$ and $5 \log V_T$ distributions from §4.3.3. From the velocity distribution shown in Figure 4.12 and inspection of the RPMD, appropriate velocity limits can be selected so as to maximise the likelihood of subdwarfs entering the sample whilst minimising thick disc star contamination. This direct applicability of the tangential velocity distributions is one of the main reasons why the tangential velocity cut-off method is used in preference to selecting between $\Psi(H_{r^*})$ percentiles. This method is far easier to implement, avoiding the lengthy convolution calculations required in deriving $\Psi(H_{r^*})$, and requires no knowledge or assumption of the colour, magnitude and proper motion errors (cf. §4.3.4). Additionally, calculating the selection effects that correct the derived luminosity function for the proportion of the spheroid recovered ("discovery fraction") and allowing for the thick disc contamination (§4.5.4) is considerably more simple and accurate when using tangential velocity criteria.

*Choice of $V_T$ limits*

When imposing a tangential velocity cut-off it is necessary to minimise the number of contaminant objects entering the sample whilst also attempting to maximise the fraction of objects under study. It is evident from the spheroid and thick disc tangential velocity distributions (Figures 4.12 and 4.14) that a limit of $V_T > 200$ km s$^{-1}$ will exclude all but a negligible amount of the thick disc population whilst still allowing the selection of a large proportion of spheroid stars. Indeed, the kinematic calculations and simulations show that for all of the SGS and NGS fields a maximum of just 0.04% of the thick disc population will be included in the sample with limits of 200 km s$^{-1}$ $< V_T <$ 500 km s$^{-1}$ (Table 4.5.) The upper limit of $V_T < 500$ km s$^{-1}$ is chosen from inspection of the RPMDs to prevent the inclusion of white dwarfs.

Note that the thick disc contamination estimate quoted here is based on direct calculations from the expected velocity distributions, and is unrelated to the colour-magnitude relation assumed. When displaying the effect of the velocity cuts and selecting stars from the reduced proper motion diagram, a colour-magnitude relation needs to be adopted that is appropriate to the metallicity of stars under investigation. Hence the halo subdwarf colour-magnitude relation is used to apply tangential velocity selection lines for subdwarfs on the RPMD (Figure 4.21), and is not suitable for displaying the expected locus of thick disc stars with the same velocities. However, the thick disc $V_T = 200$ km s$^{-1}$ limit will appear at *lower* $H_{r^*}$ than the equivalent subdwarf velocity cut, since higher metallicity dwarfs have a tendency to have brighter absolute magnitudes at a given colour (Figure 4.19). Therefore any thick disc stars entering the subdwarf sample are liable to have tangential velocities *higher* than 200 km s$^{-1}$, and so the thick disc contamination levels in Table 4.5 will be slightly overestimated. However, since the strict selection criteria employed here mean that the inclusion of thick disc stars has little bearing on the derived luminosity function (§4.5.4), the effect of this overestimation is negligible.

**Selecting subdwarfs**

Candidate subdwarfs are identified by using the mean colour-magnitude relations for subdwarfs and extreme subdwarfs (§4.3.5) to plot lines corresponding to $V_T = 200$ km s$^{-1}$ and $V_T = 500$ km s$^{-1}$ on the reduced proper motion diagram. Any star lying within the union of the subd-

SGS

| Field | $\chi_h(\%)$ | $\chi_{td}(\%)$ |
|---|---|---|
| 0932 | 61.15 | 0.01 |
| 0363 | 62.56 | 0.01 |
| 1453 | 63.57 | 0.01 |
| 1283 | 64.16 | 0.02 |
| 0852 | 64.39 | 0.02 |
| 0362 | 64.27 | 0.02 |
| 1259 | 63.85 | 0.03 |
| 1196 | 63.13 | 0.03 |
| 0591 | 62.13 | 0.04 |
| 0319 | 60.85 | 0.04 |
| 0431 | 59.31 | 0.04 |
| 0834 | 57.50 | 0.04 |

NGS

| Field | $\chi_h(\%)$ | $\chi_{td}(\%)$ |
|---|---|---|
| 0151 | 61.15 | 0.01 |
| 1402 | 62.56 | 0.01 |
| 1613 | 63.57 | 0.01 |
| 1440 | 64.16 | 0.02 |
| 1424 | 64.39 | 0.02 |
| 0465 | 64.27 | 0.02 |
| 1595 | 63.87 | 0.03 |
| 1578 | 63.13 | 0.03 |
| 1405 | 62.12 | 0.04 |
| 1401 | 60.85 | 0.04 |
| 0471 | 59.31 | 0.04 |
| 1400 | 57.50 | 0.04 |
| 1397 | 55.42 | 0.03 |
| 0467 | 53.26 | 0.03 |
| 0470 | 50.94 | 0.03 |
| 1318 | 48.62 | 0.03 |

*Table 4.5: The proportion of the spheroid ($\chi_h$) and thick disc ($\chi_{td}$) populations that will be recovered with tangential velocity selection criteria 200 km $s^{-1}$ $< V_T <$ 500 km $s^{-1}$, calculated from the the derived velocity distributions assuming the population kinematics given in Table 4.3.*

warf and extreme subdwarf locii defined by these ridgelines (ie. between the sd 200 km $s^{-1}$ and esd 500 km $s^{-1}$ boundaries) is considered to be a subdwarf candidate. Figure 4.21 shows the RPMD for the high proper motion stars in NGS field 0465 with the 200 km $s^{-1}$ and 500 km $s^{-1}$ ridgelines for subdwarfs and extreme subdwarfs superimposed. These limits clearly are a good match for the observed subdwarf sequence, including the majority of the population whilst avoiding the thick disc locus between the subdwarfs and main sequence disc stars. The subdwarf selection is done on a field by field basis to account for the varying kinematics between fields and the differing plate magnitude limits. The numbers of high proper motion stars and candidate subdwarfs passing all selection criteria (including estimated metallicity constraints described in §4.4.1) are listed in Table 4.6. Although the numbers of subdwarfs shown are only representative of the proportion of the halo included due to the kinematic selection criteria, this can be corrected for by estimating from the $V_T$ distributions (§4.3.3) the fractions of halo and thick disc stars that are expected to be recovered.

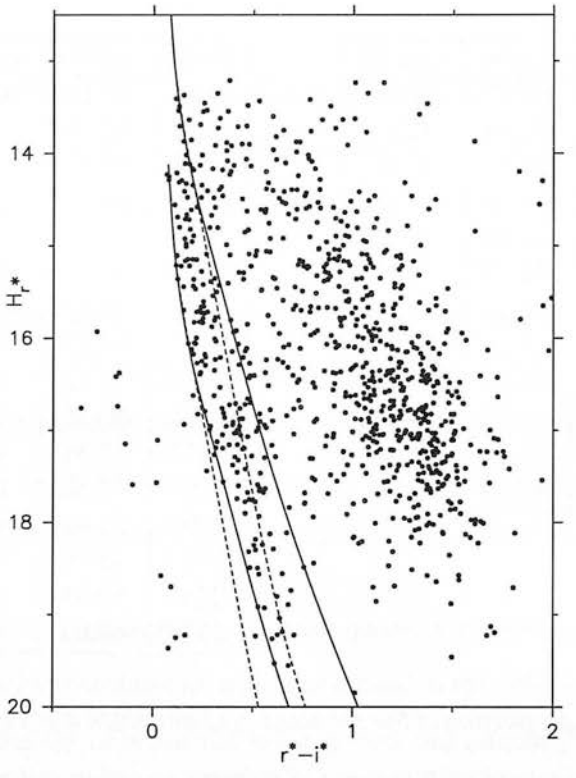


*Figure 4.21: The RPMD for high proper motion stars in field 0465, with the subdwarf (sd & esd) selection lines corresponding to $V_T$ = 200 and 500 km $s^{-1}$ overlaid. These ridgelines clearly provide a good match to the subdwarf main sequence whilst avoiding significant contamination from thick disc stars and white dwarfs.*

## 4.4 Metallicities and photometric parallaxes

### 4.4.1 Estimating metallicities

The division of the subdwarf colour-magnitude relation into two metallicity ranges is clearly a poor approximation (§4.3.5), and one that is unsuitable for use in obtaining photometric parallaxes of the candidate stars. With no abundance estimate of the sample, the spread of nearly two magnitudes in luminosity between metal-rich and metal-poor subdwarfs at $(V - I_C) \approx 2$ could lead to significant errors in the distance estimates. A more robust method which accounts for the absolute magnitude-metallicity degeneracy is required.

SGS

| Field | $N_{hpm}$ | $N_{sd}$ |
|---|---|---|
| 0932 | 296 | 15 |
| 0363 | 757 | 68 |
| 1453 | 703 | 81 |
| 1283 | 747 | 85 |
| 0852 | 709 | 80 |
| 0362 | 814 | 91 |
| 1259 | 804 | 89 |
| 1196 | 790 | 107 |
| 0591 | 875 | 96 |
| 0319 | 864 | 84 |
| 0431 | 847 | 90 |
| 0834 | 320 | 32 |
| Total: | 8526 | 918 |

NGS

| Field | $N_{hpm}$ | $N_{sd}$ |
|---|---|---|
| 0151 | 256 | 44 |
| 1402 | 703 | 143 |
| 1613 | 700 | 125 |
| 1440 | 814 | 145 |
| 1424 | 866 | 145 |
| 0465 | 910 | 164 |
| 1595 | 853 | 130 |
| 1578 | 802 | 128 |
| 1405 | 947 | 125 |
| 1401 | 1005 | 125 |
| 0471 | 947 | 111 |
| 1400 | 813 | 89 |
| 1397 | 704 | 69 |
| 0467 | 762 | 76 |
| 0470 | 600 | 56 |
| 1318 | 282 | 21 |
| Total: | 11964 | 1696 |

*Table 4.6: The numbers of high proper motion stars ($N_{hpm}$) and subdwarfs ($N_{sd}$) passing all magnitude, proper motion, quality and metallicity selection criteria for each field.*

The highly accurate five-band photometry of the SDSS is ideally suited for estimating metallicities from colours. The photometric precision is sufficient to clearly separate stars of differing metallicities when plotted in metallicity-sensitive colours such as $(u^* - g^*)$ and $(g^* - r^*)$ (Figure 4.22). All five photometric bands are used to match observed colours to model atmosphere grids in order to derive a metallicity estimate for each subdwarf candidate.

The model atmospheres of Lenz et al. (1998) use Kurucz ATLAS9 models (Kurucz 1993) to give grids of synthetic SDSS colours $(u^* - g^*)$, $(g^* - r^*)$, $(r^* - i^*)$, $(i^* - z^*)$ for stars with effective temperatures from 3500K to 40000K and with metallicities [m/H] = +1.0, 0.0, -1.0, -2.0, -5.0 and $\log g$ = 4.0 and 4.5.

Observations and atmospheric models indicate that main sequence subdwarfs typically

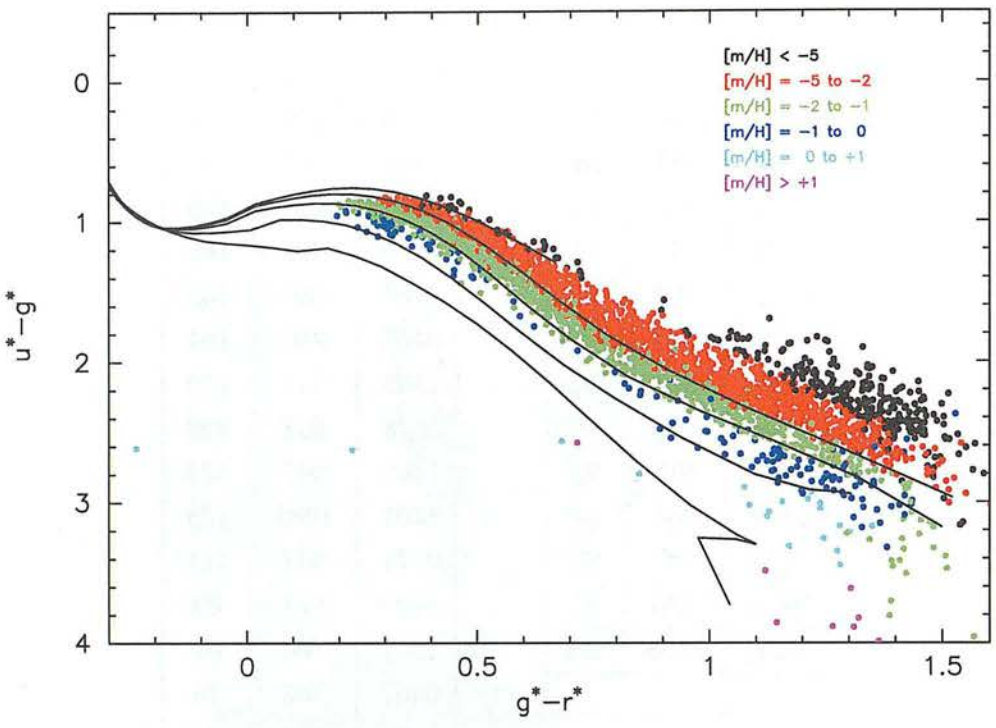


*Figure 4.22: Two-colour diagram for all candidate subdwarfs in the SGS and NGS, colour-coded according to estimated metallicity. Overlaid are the synthetic atmosphere predictions of Lenz et al. (1998) for models with [m/H] = +1.0, 0.0, -1.0, -2.0 and -5.0 (from bottom to top). The accurate photometry of the SDSS is clearly well capable of providing good metallicity estimates.*

have surface gravities in the range $\log g \approx 4.5 - 5.0$ (Axer, Fuhrmann, & Gehren 1995, Fulbright 2000, Cox 2000), with $\log g$ increasing for cooler and fainter stars and $\log g \approx 4.2$ typical of a subdwarf at the main sequence turnoff (Axer, Fuhrmann, & Gehren 1994). Since the sample in this study will be dominated by main sequence subdwarfs, I therefore adopt $\log g = 4.5$ as the most appropriate surface gravity parameter from the Lenz et al. (1998) models.

The method of estimating metallicity and temperature by interpolating between the atmosphere grids to match the observed colours proceeds as follows:

(i) *Estimate temperature:* For each metallicity I interpolate between the given temperatures to find expected values for each of the four colours at 10K intervals. Interpolation is

performed by a least squares cubic polynomial if within the penultimate grid points, or a linear fit otherwise. For each subdwarf candidate the best-fit temperature for each metallicity is then determined by finding the temperature grid point with the closest least-squares fit to the observed colours. This is done by minimising the quantity

$$\Delta_{colour} = \Delta^2_{u^*-g^*} + \Delta^2_{g^*-r^*} + \Delta^2_{r^*-i^*} + \Delta^2_{i^*-z^*} \tag{4.13}$$

for [m/H] = +1.0, 0.0, -1.0, -2.0, -5.0, where $\Delta_{u^*-g^*} = (u^* - g^*)_* - (u^* - g^*)_{grid}$ is the colour difference between the subdwarf colour and the colour of each temperature grid point.

*(ii) Estimate metallicity:* With a temperature estimate at each metallicity for each candidate, a finer grid is obtained by interpolating between the five metallicity grid points to derive an estimated colour for 0.1 dex metallicity intervals. The best-fit metallicity for each star is then found by minimising

$$\Delta_{[m/H]} = \Delta^2_{u^*-g^*} + \Delta^2_{g^*-r^*} + \Delta^2_{r^*-i^*} + \Delta^2_{i^*-z^*} \tag{4.14}$$

where $\Delta_{u^*-g^*}$ is the difference of the observed colour with each point in the metallicity grid.

*(iii) Reject high residual fits:* Subdwarfs with poor fits to the metallicity/ temperature model grid are eliminated from the candidate sample by rejecting all stars with $\Delta_{[m/H]} > 20\sigma_\Delta$, where $\sigma_\Delta$ is the rms residual of the final metallicity grid fits. This leads to ~3% of candidates being rejected, although their highly unusual colours means that most of these objects will not be subdwarfs.

It is clear from inspection of the metallicities derived that there is a zero point error in the estimates: the sample medians of $[\widetilde{m/H}] \sim -2.3$ for the SGS and $[\widetilde{m/H}] \sim -2.5$ for the NGS are considerably lower than [Fe/H] $\sim -1.5$ expected for spheroid stars (Laird et al. 1988, Nissen & Schuster 1991). There are a number of likely contributing causes of this: one is that the [m/H] $= -5.0$ model only extends blueward of $(g^* - r^*) \approx 0.7$, and so the metallicities of subdwarfs redder than this have to be extrapolated from the [m/H]$\geq -2.0$ models. Even subdwarfs with $(g^* - r^*) \lesssim 0.7$ rely on interpolation between the [m/H]$= -5.0$ and $-2.0$

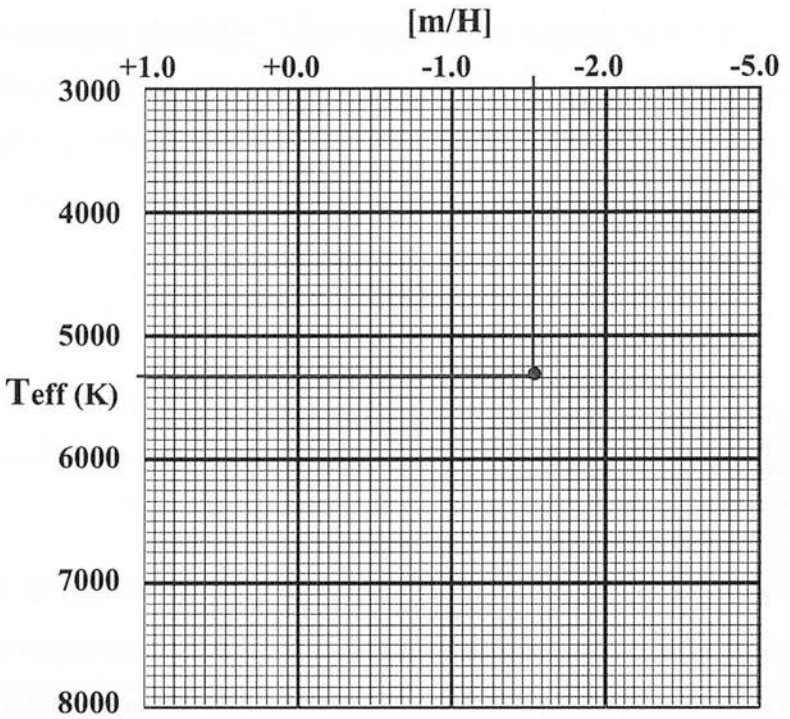


*Figure 4.23: The method of metallicity and temperature estimation by interpolating the four-colour parameter space over the metallicity-temperature model grids of Lenz et al. 1998.*

models — a very large metallicity spread which will inevitably introduce errors. Additionally, inaccuracies in the model atmospheres will lead to uncertainties in the derived metallicities, particularly for redder stars.

However, these systematic metallicity errors are unimportant in this application as only the *relative* metallicities of the sample subdwarfs are of interest. This is because the metallicities estimated are used in rejecting stars with metal content too high for them to be subdwarfs, and in adjusting the colour-magnitude relation to improve the accuracy of the photometric parallaxes (§4.4.3). Nowhere is the accurate absolute value of the metallicity of each star required.

Aside from the systematic offset, the derived metallicities and temperatures exhibit good internal accuracy and consistency. Figure 4.24 shows the correlation of effective temperature with $(r^* - i^*)$ colour, which is a good temperature indicator. The two-colour diagrams with model predictions overlaid also demonstrate the consistency of the metallicity estimates. The very small number of outliers in the metallicity-sensitive $(u^* - g^*, r^* - i^*)$ colour space in

Figure 4.22 shows that the four-colour interpolation in the temperature-metallicity model grids works effectively. There is also good consistency between the metallicity distributions for the SGS and NGS (Figure 4.25), with no systematic difference (whether intrinsic or not - see §4.4.4) between the stripes.

### 4.4.2 The metallicity-dependent colour magnitude relation

With a metallicity estimate for each candidate subdwarf, a metallicity-dependent colour-magnitude relation is used to provide a more reliable indication of each star's intrinsic luminosity. A median colour-magnitude relation $\widetilde{M_I}$ is derived by fitting a single cubic spline to the parallax subdwarfs of all metallicity (both sd and esd) from Gizis (1997) and Reid, van Wyk et al. (2001) described in §4.3.6. The median $(M_{I_C}, V - I_C)$ relation is shown in Figure 4.26.

The absolute magnitude $M_I$ of each star in the sample is then estimated by offsetting from this median magnitude by an amount proportional to the star's deviation from the sample median metallicity at that particular colour. The estimated absolute magnitude is given by:

$$M_I = \widetilde{M_I} + d[m/H]\, w \left.\frac{dM_I}{d[m/H]}\right|_{r^*-i^*}, \tag{4.15}$$

where

$$d[m/H] = [m/H]^* - [\widetilde{m/H}]_{r^*-i^*}, \tag{4.16}$$

is the metallicity offset of the star from the sample median at that colour, $w$ is a weighting function to allow for colour-dependent errors, and the derivative is the variation of absolute magnitude with metallicity derived from theoretical colour-magnitude relations.

Figure 4.27 shows the two-colour $(u^* - g^*, r^* - i^*)$ diagram for all candidate subdwarfs in the SGS and NGS. The larger spread in colour at redder wavelengths is evident, and is assumed to be solely due to larger colour errors and inaccuracies in the models at these colours. The implicit understanding in this assumption is that the actual metallicity spread of the sample is independent of colour, so in estimating the metallicities the weight function $w$ is used to correct for the greater observed colour spread at the red end. The intrinsic metallicity spread, $\sigma^{true}_{[m/H]}$,

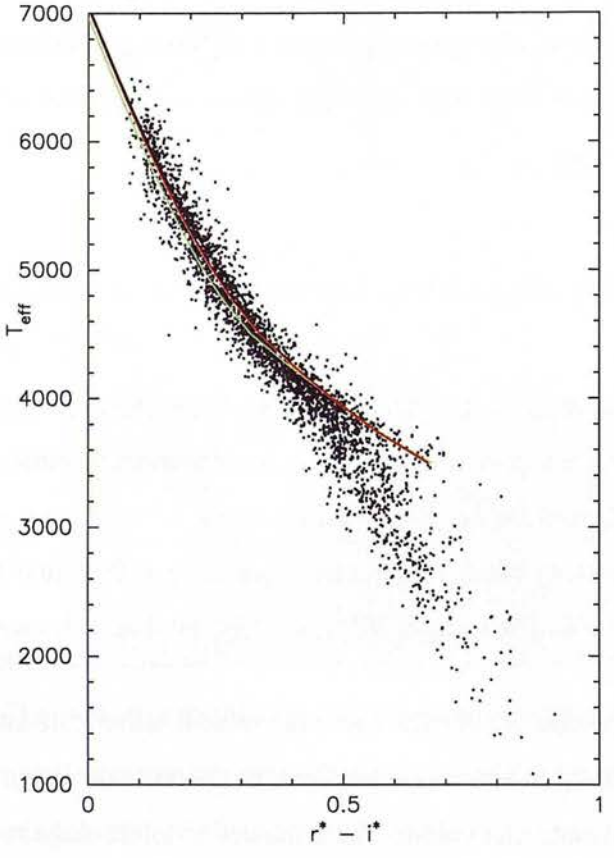


*Figure 4.24: The correlation between estimated effective temperature and* $(r^* - i^*)$*, with model predictions for [m/H]* $= -1.0, -2.0, -5.0$ *(in order of increasing temperature at* $r^* - i^* \sim 0.2$*) from Lenz et al. (1998). For the majority of stars (those with* $r^* - i^* \lesssim 0.4$*) there is close agreement with the models and good internal consistency of the metallicity and temperature estimates. The poor fit of the models for* $(r^* - i^*) \gtrsim 0.4$ *is likely to be mostly due to less accurate temperature interpolations over this range, arising from the larger colour spread and the fact that the [m/H]* $= -5.0$ *model does not extend to these redder wavelengths. However, since the majority of the sample lies blueward of* $(r^* - i^*) \approx 0.5$ *and the metallicities are not used in an absolute sense, the effect of these discrepancies will be limited.*

is taken to be the rms metallicity deviation from the median for $0.1 \leq (r^* - i^*) \leq 0.25$. At a given colour the rms of the metallicity difference from the median, $\sigma_{[m/H]}$, is calculated, and

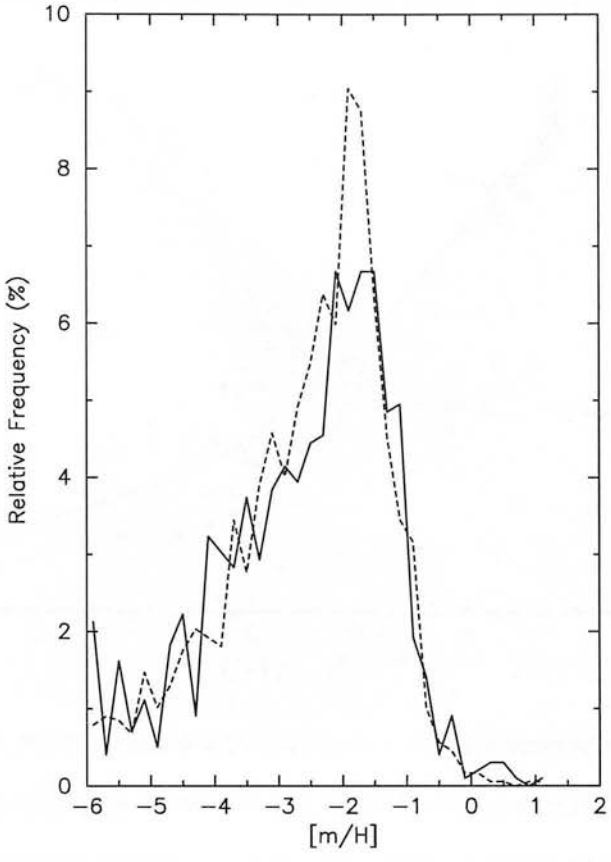


*Figure 4.25: The distributions of estimated metallicities for the SGS (solid line) and NGS (dashed line). Although the metallicities are systematically too low for the [Fe/H]$\sim -1.5$ expected for spheroid subdwarfs, there is good agreement between the samples and no systematic differences between the two. The median metallicities of [m/H] $= -2.5$ for the SGS and $-2.3$ for the NGS agree well within the expected errors.*

the weight function is defined as

$$w = \left( \frac{\sigma^{true}_{[m/H]}}{\sigma_{[m/H]}} \right)^2 \tag{4.17}$$

Note that if the larger colour spread at redder wavelengths is entirely due to errors, then to reflect the true scatter of absolute magnitude about the median colour-magnitude relation the weight function should be defined without the squared index in Equation 4.17, which has a

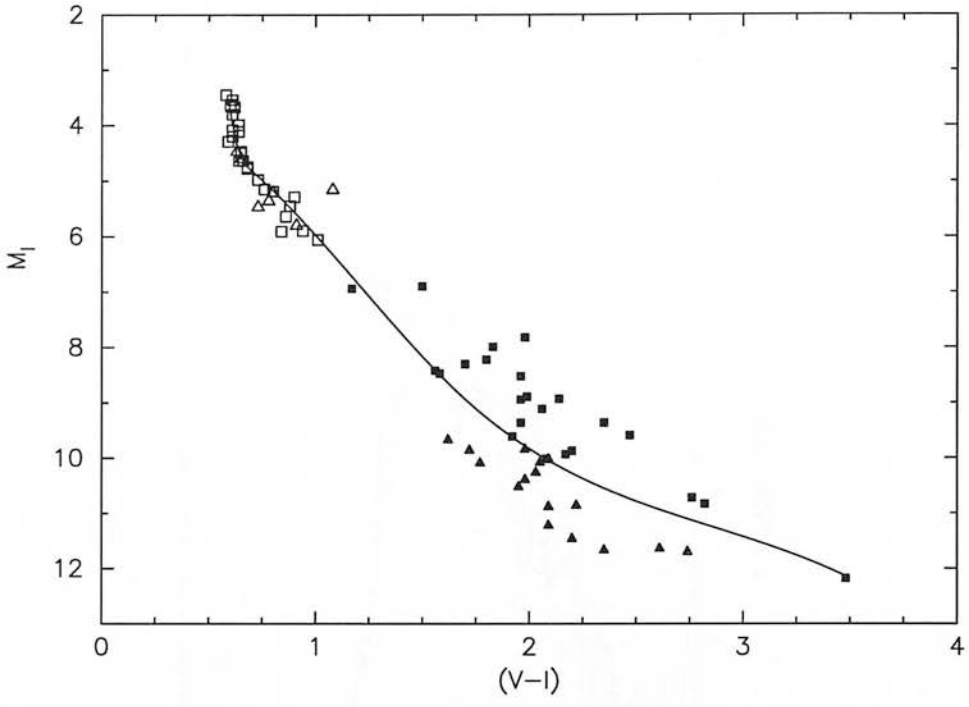


*Figure 4.26: The median colour-magnitude relation obtained by fitting a cubic spline to the parallax subdwarfs of all metallicities described in §4.3.6. Again, triangles denote extremes subdwarfs (esd) and squares represent subdwarfs (sd); filled symbols are those subdwarfs from Gizis (1997) and open symbols are from Reid, van Wyk et al. (2001).*

tendency to underestimate the correction for redder stars. However, it is included since without it stars close to the $(V - I_C \approx 1.6)$ inflection of the colour-magnitude relation (Figure 4.26) are accorded too large an absolute magnitude correction due to the steep $(M_I, [m/H])$ gradient there (Figure 4.29). The metallicity correction to the colour-magnitude relation is only approximate, and so the weight function defined here is designed to provide a similarly approximate modification to the correction, whilst erring on the side of caution in determining its size.

The derivative of absolute magnitude with respect to metallicity at each colour is derived from the theoretical colour-magnitude relations for stars of different metallicities provided by Baraffe et al. (1997) (Figure 4.28). The metallicity-absolute magnitude relation varies considerably with colour (Figure 4.29), but is approximately linear. The slope of this relation can therefore be assumed to a constant, which is estimated from the models for each star's colour to provide the last term in Equation 4.15. The models of Baraffe et al. (1997) and the median

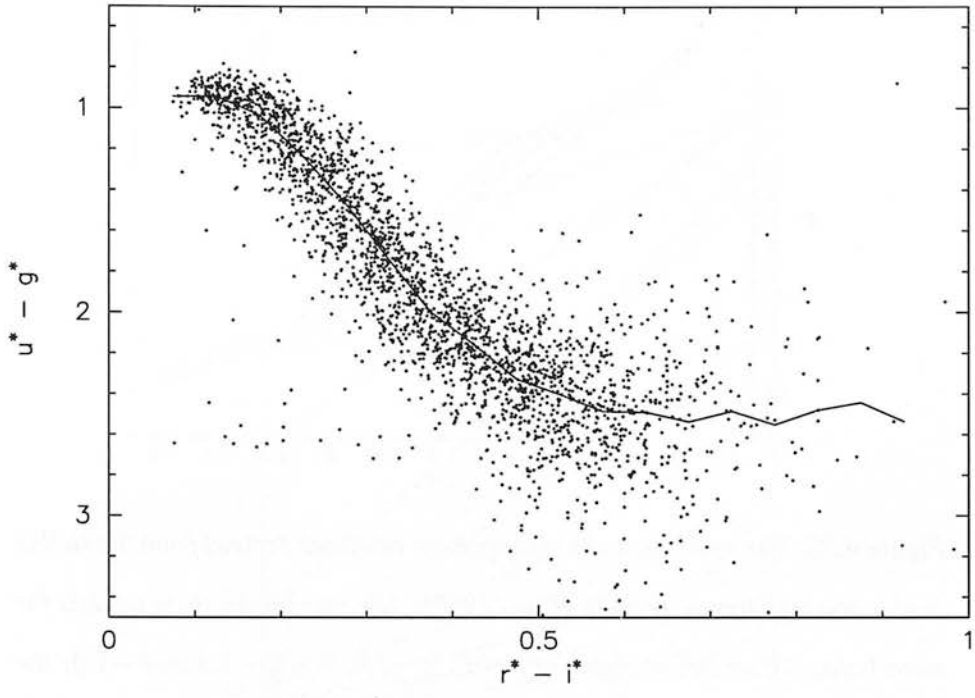


*Figure 4.27: The two-colour $(u^* - g^*, r^* - i^*)$ diagram for candidate subdwarfs in the SGS and NGS, with the median $(u^* - g^*)$ colour shown as a function of $(r^* - i^*)$ (solid line.) The larger colour spread at red wavelengths is clear and needs to be corrected for when estimating metallicities. This is achieved by using the weight function, $w$, to scale the larger metallicity spread at red colours to the assumed intrinsic spread, $\sigma^{true}_{[m/H]}$, which is defined as the rms deviation from the median metallicity for $0.1 \leq (r^* - i^*) \leq 0.25$.*

colour-magnitude relation of the parallax subdwarfs are given in the $(M_I, V - I)$ colour plane; conversion to $(M_{r^*}, r^* - i^*)$ is achieved using Equation 4.9.

It is stressed that this modification of the colour magnitude relation based upon estimated metallicity is only an approximation. It is only intended to adjust the predicted magnitude of each star according to its likely metallicity in the right direction and by a suitable amount. In light of this the adjustment of absolute magnitude from the median is restricted to a maximum of $\pm 1.5$ magnitudes, to prevent any stars being assigned inappropriate values. However, it can be seen from the sample estimated colour-magnitude diagram (Figure 4.30) that this method provides a far more realistic and accurate distribution of absolute magnitudes than a simple division of the colour-magnitude relation into two metallicity ranges.

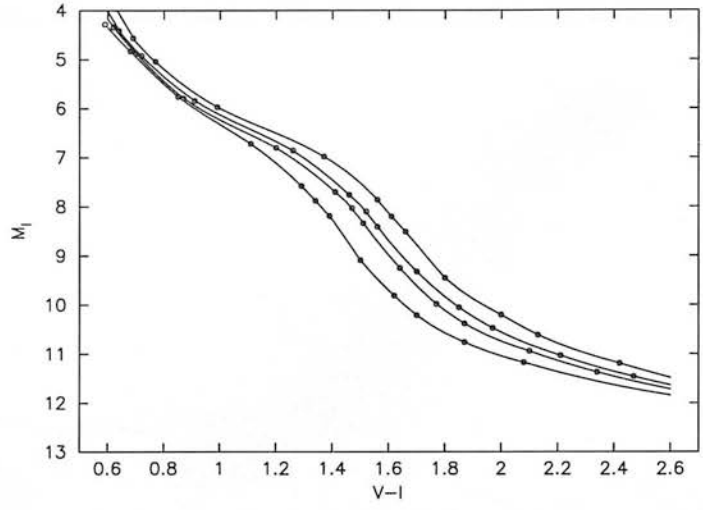


*Figure 4.28: The synthetic colour-magnitude relations derived from the stellar model atmospheres of Baraffe et al. (1997). The solid lines show models for metallicities (from left to right) of [m/H] = −2.0, −1.5, −1.3 and −1.0; the circles correspond to different values of stellar mass.*

### 4.4.3 Photometric parallaxes

With an estimated absolute magnitude for each star a distance can be derived, with an assumption of no reddening adopted due to the high latitude of the fields ($|b| \geq 37$ °). The distances sampled are in the range ∼260 pc to ∼2.8 kpc, and the distributions for the SGS and NGS are shown in Figure 4.31. The distribution of distances for each stripe are closely matched, although the SGS has comparatively fewer subdwarfs with estimated distances over 2 kpc. Given that the SGS and NGS samples have identical proper motion and similar magnitude limits and no apparent metallicity difference, it appears that this is due to a real effect of the sample distributions rather than systematic reasons (see §4.4.4.) With a non-uniform spheroid density decreasing with radius the distance distributions will differ, with proportionally fewer stars at larger distances expected towards the Galactic anticentre, and hence the SGS, than towards the higher-density regions of the Galactic centre where the NGS lies.

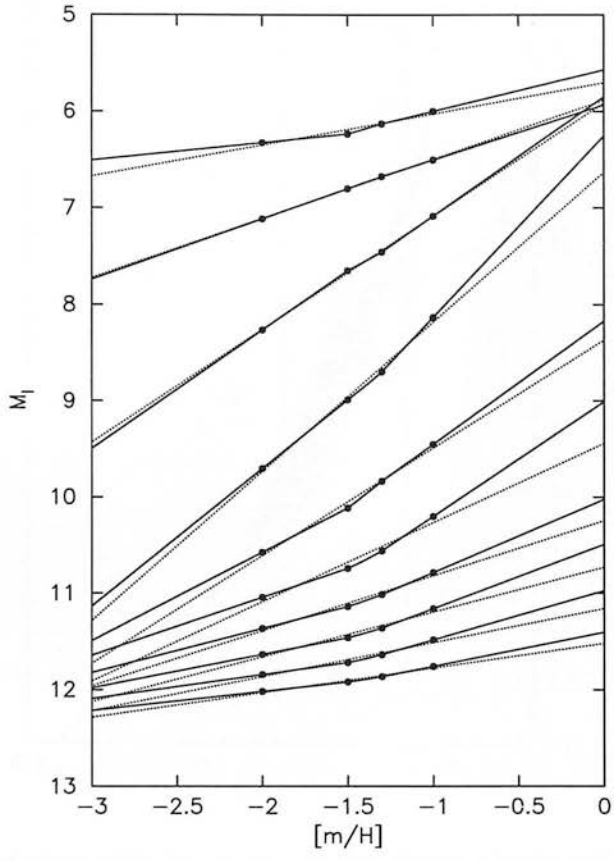


*Figure 4.29: The relations between absolute magnitude and metallicity as a function of colour from the models of Baraffe et al. (1997). The models shown are for $(V - I_C)$ from 1.0 (top) to 2.8 (bottom), in intervals of 0.2 mag.*

### 4.4.4 Tests for sample systematic errors

The luminosity functions derived from the two independent SGS and NGS samples provide not only an excellent probe of the spheroid density distribution, but also can be compared to ensure that the results are free from significant systematic errors - a source of concern with earlier studies (§2.3.2).

Prior to comparing the results from each stripe, however, steps must be taken to ensure that the two samples are in fact self-consistent and free from systematic effects. Inconsistency between the samples could arise from either a systematic disparity in the selection of each sample, or from an intrinsic difference in the constituent stars of each.

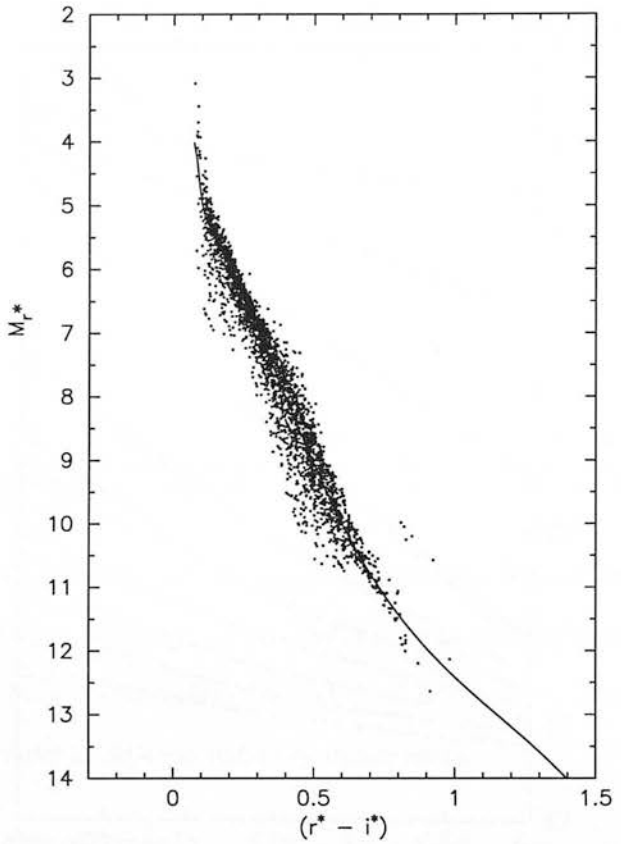


*Figure 4.30: Estimated absolute magnitudes for all subdwarfs in the SGS and NGS, derived from a median colour-magnitude relation fitted to calibrating subdwarfs (solid line) and offset according to the metallicity estimate of each star.*

**Sampling systematic errors**

Systematic errors arising from the sample selection are the most likely, with a whole range of possible causes such as a difference in astrometric or photometric accuracy between the stripes. However, any significant difference of this type can be tested for by investigating the completeness of each subdwarf sample. This is done in a somewhat crude way by comparing cumulative proper motion number counts: assuming a uniform stellar density and that proper motion and distance are inversely proportional ($\mu \propto d^{-1}$), a plot of log cumulative number count ($\Sigma N$) against $\log \mu$ should have a gradient of $-3$:

$$\Sigma N \propto V \propto d^3 \propto \mu^{-3}. \tag{4.18}$$

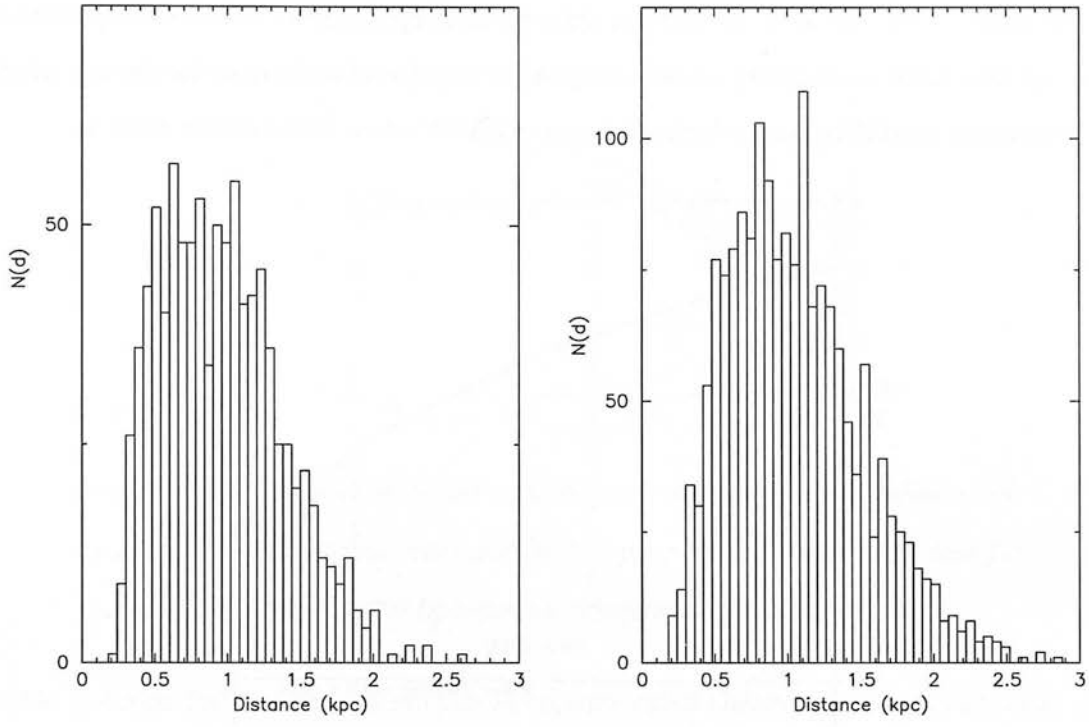


*Figure 4.31: The distributions of estimated distances for the SGS (left) and NGS (right).*

Figure 4.32 shows the histogram of cumulative proper motion counts for all paired stars in the NGS and SGS after the error mapper has been applied. A straight line is fitted to the points between the global proper motion limits for each stripe: $\mu_{\rm min}$ = 40.5 mas yr$^{-1}$ and $\mu_{\rm max}$ = 160 mas yr$^{-1}$. Both give a close fit to the expected gradient: $-2.92\pm$ 0.06 for the SGS and $-2.99\pm$ 0.06 for the NGS. Similar plots for just the candidate subdwarfs in each stripe are shown in Figure 4.33, where least-square linear fits to the counts have gradients of $-3.10$ for each stripe.

There is some evidence for incompleteness in the non-linearity of the histograms, especially for the subdwarf samples where proper motion errors lead to incompleteness towards the proper motion limits. This is particularly relevant to the higher proper motions, where the errors will be more dominant, and this explains the rapid tailing off of the distributions for $\log \mu \gtrsim 2.1$, caused by the imposition of the upper proper motion limit. However, the number counts for the population of stars from which the subdwarfs are selected demonstrate that it is complete for 40.5 mas yr$^{-1} \leq \mu \leq$ 160 mas yr$^{-1}$, and the good match of all of the histograms to the expected gradient of $-3$ indicate that there are no significant signs of incompleteness affecting

the samples. It must be also stressed that these are only approximate tests for completeness, and will have some unreliability introduced by the assumption of uniform stellar density, which is particularly invalid for stars at large distances that tend to have lower proper motions.

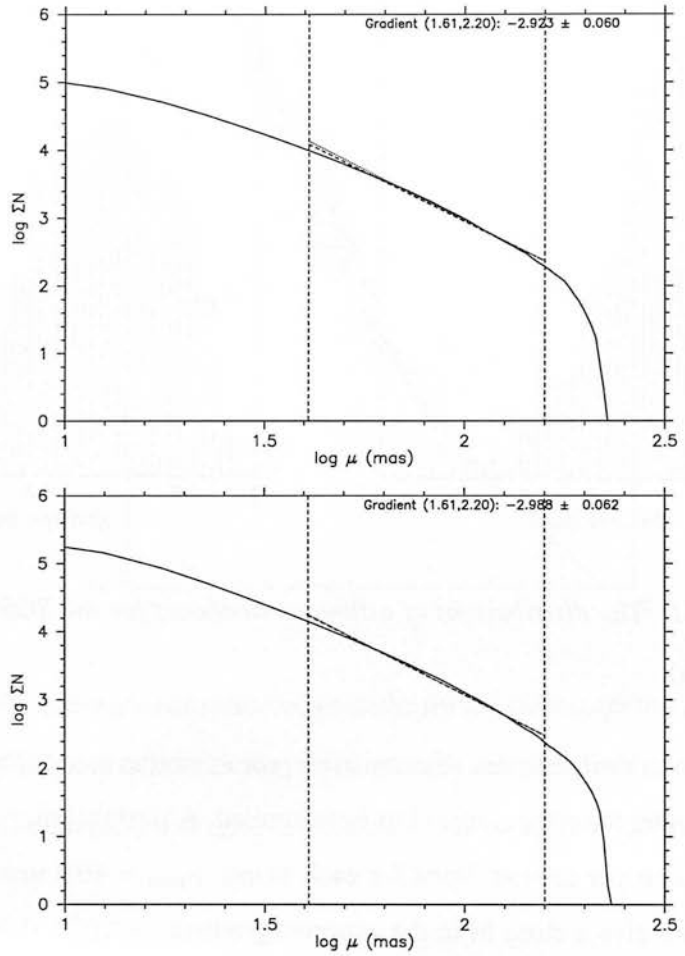


*Figure 4.32: Cumulative proper motion number counts for all stars in the SGS (top) and NGS (bottom). The straight line fits between the proper motion limits in each stripe are shown (dashed line), along with the expected line of gradient of* $-3.0$ *(dotted line). The logarithm of the proper motion limits* $\mu_{min} = 40.5$ *mas yr*$^{-1}$ *and* $\mu_{max} = 160$ *mas yr*$^{-1}$ *are shown as vertical dotted lines.*

**Metallicity differences**

An intrinsic difference between the samples that could have a significant effect on the results is a difference in median metallicity between the SGS and NGS. Although the radial metallicity gradient of the spheroid is thought to be small ( $\Delta[Fe/H]/\Delta r \approx -0.012$ dex kpc$^{-1}$

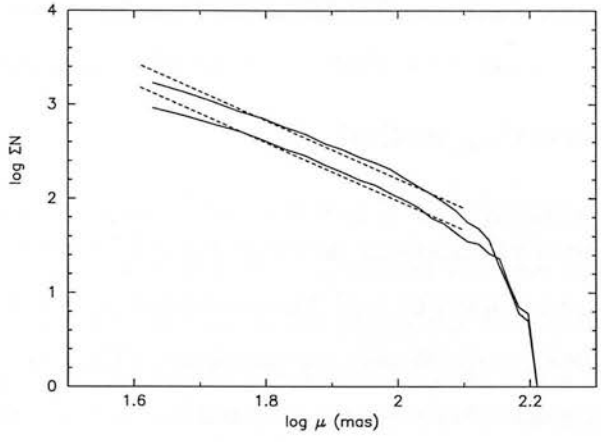


*Figure 4.33: Cumulative proper motion number counts for candidate subdwarfs in the SGS (lower line) and NGS (upper line). The straight line fits between* $1.6 \leq \log \mu \leq 2.1$ *(dashed lines) both have gradients of* $-3.1$

Bekki & Chiba 2001), with both samples in opposite radial Galactic directions this could nevertheless introduce a source of error. The assumption of a single colour-magnitude relation for both of the samples would mean that stars in the sample with the higher metallicity would have their absolute magnitudes overestimated, and hence their distances and contribution to the luminosity function would be underestimated. The derived luminosity function of the SGS and NGS would therefore be expected to differ, with the higher-metallicity sample exhibiting a luminosity function with a lower normalisation. This effect would be less pronounced with the photometric parallax relation defined in §4.4.3 that partially accounts for metallicity variations, but is an issue that should still be addressed.

However, my data display little evidence of metallicity gradient. The two-colour diagrams for the subdwarf sample in each stripe in Figure 4.22 show no systematic difference, and the estimated metallicity distribution and median metallicity of each (Figure 4.25) are very similar. It is therefore highly unlikely that there is any strong systematic metallicity difference between the samples.

These checks of sample consistency indicate that there are no large systematic differences between the samples arising from sampling errors or intrinsic variations. A further and final test of the sample completenesses can be ascertained following the luminosity function calculations from the value of $\langle V/V_{\rm max} \rangle$ (§4.6.3).

## 4.5 Methods: The luminosity function

### 4.5.1 The generalised $V_{max}$ method

With a final sample size of 918 candidate subdwarfs in the SGS and 1696 in the NGS, the luminosity function can be accurately derived. This is achieved using a modification of the $V_{max}$ method of Schmidt (1968), in which each star contributes $1/V_{max}$ to the luminosity function, where $V_{max}$ is the maximum volume that the star could have been detected in, given the proper motion and magnitude limits of the survey. By taking these limits into account this technique therefore implicitly corrects for any bias arising from the proper motion selection.

Schmidt's original $1/V_{max}$ method assumes that the sample is selected from a uniformly-distributed population. This certainly is not the case for my subdwarf sample; indeed, I intend to use it to determine the variation in halo density. I therefore adopt the "generalised $V_{max}$" method (Stobie, Ishida, & Peacock 1989, Tinney, Reid, & Mould 1993), which extends Schmidt's method to non-uniformly distributed samples. Given that each star in the survey can be detected to minimum and maximum distances $d_{min}, d_{max}$ in a field of solid angle $\Omega$, the luminosity function is defined as:

$$\Phi_{\rm sample} = \sum \frac{1}{\rm V'_{max}}, \tag{4.19}$$

$$V'_{max} = \Omega \int_{d_{min}}^{d_{max}} s^2 \frac{n(s)}{n_\odot}\, ds, \tag{4.20}$$

where $s$ is the heliocentric distance and $n(s)$ is the adopted halo density law (§4.5.3).

### 4.5.2 Proper motion and magnitude limits

The distance limits depend on the minimum and maximum proper motion and magnitudes in each field. The minimum proper motion limit employed is $\mu_{\rm min} = 40.5$ mas yr$^{-1}$ (§4.3.1). The maximum proper motion is theoretically determined by the maximum pairing radius of 10 arcsec, corresponding to $\mu_{\rm max} \approx 220$ mas yr$^{-1}$. However, the actual maximum is somewhat

smaller than this value due to systematic shifts in position affecting the pairing process; I therefore adopt a conservative $\mu_{\rm max} = 160$ mas yr$^{-1}$ from the cumulative proper motion number counts (Figure 4.32.)

Ascertaining the magnitude limits for each field is less straightforward as the data come from two quite different sources, and there is significant variation in the depth of the plate material. However, the fact that the datasets are paired and that the SDSS data probe much fainter ($r^* \sim 23$) than the POSS-I plates means that only the SDSS $r^*$ magnitudes need be considered.

The POSS-I plates reach incomplete levels at R $\sim$ 20, at which magnitude the SDSS data are certainly complete. Stars need to appear in both datasets to pass the pairing criteria, so the faint magnitude limit can be defined solely in terms of the much more accurate SDSS $r^*$ magnitude. A histogram of the logarithm of number counts against $r^*$ magnitude is plotted for all of the paired stars in each field, and an upper limit is conservatively defined from the magnitude at which $\log(N\,(r^*))$ departs from a steady increase (Figure 4.34.) The brighter limit is less crucial due to the smaller likelihood of subdwarfs having such magnitudes, but a limit of $r^* \sim$15 is applied to encompass the magnitude range that is likely to be complete as indicated by the histogram.

With proper motion limits $\mu_{\rm min}$, $\mu_{\rm max}$ and magnitude limits $r^*_{\rm min}$, $r^*_{\rm max}$ for each field, the limiting distances for a subdwarf of distance $d$ and magnitude $r^*$ are therefore defined as

$$d_{\rm min} = d\ \max\left[\frac{\mu}{\mu_{\rm max}}, 10^{0.2(r^*_{\rm min}-r^*)}\right], \tag{4.21}$$

$$d_{\rm max} = d\ \min\left[\frac{\mu}{\mu_{\rm min}}, 10^{0.2(r^*_{\rm max}-r^*)}\right]. \tag{4.22}$$

### 4.5.3 The spheroid density law

Recent studies of the structure of the Galactic inner spheroid have indicated that its density profile is flattened and follows a power law: an axial ratio of (c/a) $\approx$ 0.6 and $\rho(r) \sim r^{-3}$

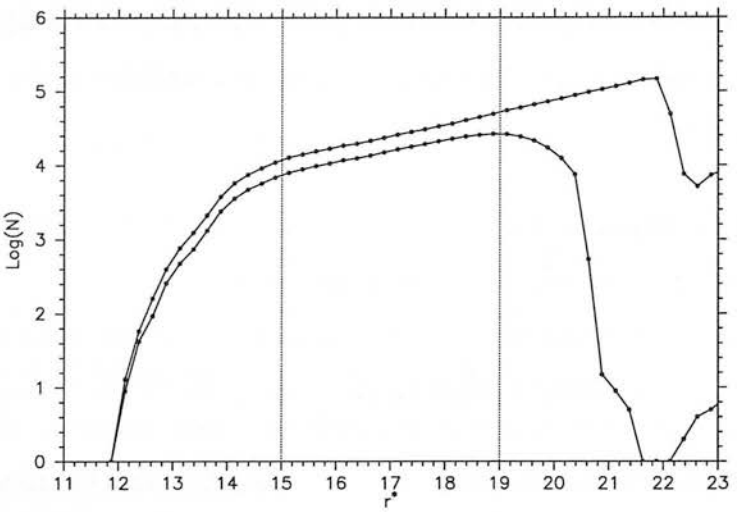


*Figure 4.34: The log number - magnitude plot for all unpaired (top) and paired (bottom) stars in the NGS. The approximate upper and lower $r^*$ magnitude limits for the fields in the NGS are shown. Although this shows the number counts for the whole NGS, this method is applied on a field-by-field basis to determine the magnitude limits for each field.*

(Gould et al. 1998, Sluis & Arnold 1998, Yanny et al. 2000, Ivezić et al. 2000, Chen et al. 2001, Siegel et al. 2002, Gould 2003). I therefore adopt a spheroid density law of the form

$$\frac{n}{n_\odot} = \left( \frac{r_c^2 + R_0^2}{r_c^2 + R^2 + z^2/q^2} \right)^\alpha , \tag{4.23}$$

where $n_\odot$ is the local spheroid density, $\alpha$ is the power law index and $q = (c/a)$ is the axial ratio. I assume $R_0$ = 8.0 kpc for the Sun's Galactocentric distance, and a core radius of $r_c$ = 1.0 kpc. Converting the Galactocentric cylindrical coordinates $R$ and $z$ in terms of heliocentric coordinates $(s, l, b)$, where $s$ is the distance from the Sun and $l$ and $b$ are Galactic latitude and longitude, gives:

$$\frac{n}{n_\odot} = \left( \frac{r_c^2 + R_0^2}{r_c^2 + R_0^2 + s^2 - 2sR_0 \cos l \cos b + s^2 \sin^2 b \frac{1-q^2}{q^2}} \right)^\alpha . \tag{4.24}$$

The two density law parameters $\alpha$ and $q$ are allowed to vary, and luminosity functions are derived for a range of values to find the $(\alpha, q)$ law which best matches the observations (see §4.5.8.) A significant benefit of this approach is that the density law variables $\alpha$ and $q$ can be fitted without having to make an assumption about the local spheroid density $n_\odot$.

SGS

| Field | $r^*_{max}$ | $\chi_h(\%)$ | $\chi_{td}(\%)$ |
|---|---|---|---|
| 0932 | 18.7 | 61.15 | 0.01 |
| 0363 | 19.5 | 62.56 | 0.01 |
| 1453 | 19.0 | 63.57 | 0.01 |
| 1283 | 19.2 | 64.16 | 0.02 |
| 0852 | 19.1 | 64.39 | 0.02 |
| 0362 | 19.2 | 64.27 | 0.02 |
| 1259 | 19.1 | 63.85 | 0.03 |
| 1196 | 19.1 | 63.13 | 0.03 |
| 0591 | 19.3 | 62.13 | 0.04 |
| 0319 | 19.2 | 60.85 | 0.04 |
| 0431 | 19.0 | 59.31 | 0.04 |
| 0834 | 18.9 | 57.50 | 0.04 |

NGS

| Field | $r^*_{max}$ | $\chi_h(\%)$ | $\chi_{td}(\%)$ |
|---|---|---|---|
| 0151 | 19.0 | 61.15 | 0.01 |
| 1402 | 19.2 | 62.56 | 0.01 |
| 1613 | 18.8 | 63.57 | 0.01 |
| 1440 | 19.1 | 64.16 | 0.02 |
| 1424 | 19.1 | 64.39 | 0.02 |
| 0465 | 19.0 | 64.27 | 0.02 |
| 1595 | 18.7 | 63.87 | 0.03 |
| 1578 | 18.9 | 63.13 | 0.03 |
| 1405 | 19.0 | 62.12 | 0.04 |
| 1401 | 19.2 | 60.85 | 0.04 |
| 0471 | 19.2 | 59.31 | 0.04 |
| 1400 | 19.0 | 57.50 | 0.04 |
| 1397 | 18.7 | 55.42 | 0.03 |
| 0467 | 19.3 | 53.26 | 0.03 |
| 0470 | 19.1 | 50.94 | 0.03 |
| 1318 | 18.8 | 48.62 | 0.03 |

*Table 4.7: Magnitude limits and spheroid and thick disc discovery fractions for fields in the SGS (left) and NGS (right). The minimum magnitude limit for all fields is $r^* = 15.0$ and the global proper motion limits are $\mu_{min} = 40.5$ mas yr$^{-1}$ and $\mu_{max} = 160$ mas yr$^{-1}$.*

### 4.5.4 Discovery fraction

Given distance limits and an assumed $(\alpha, q)$ density distribution, the sample luminosity function can be calculated. However, the tangential velocity cut-offs (§4.3.6) causes the sample to exclude a given fraction of halo stars, so this scaling needs to be taken into account in order to derive the true halo luminosity function from the sample.

The fraction $\chi_h$ of halo stars expected to have 200 km s$^{-1}$ $\leq V_T \leq$ 500 km s$^{-1}$ is calculated for each field using the tangential velocity calculations as described in §4.3.6. Using our adopted velocity ellipsoids, the spheroid discovery fraction $\chi_h$ varies between 0.58 and 0.64 in the SGS, and 0.49 and 0.64 in the NGS, and scales the halo luminosity function as

$$\Phi_{\rm h}^{\rm true} = \frac{1}{\chi_{\rm h}} \Phi_{\rm h}^{\rm sample}. \tag{4.25}$$

At this stage any possible contamination by thick disc stars can be considered. Assuming they are also included in the sample with $V_T \geq 200$ km s$^{-1}$, then the derived luminosity function will comprise a total for spheroid and thick disc members. The sample *spheroid* luminosity function can then be calculated from the *total* (spheroid plus thick disc) by

$$\Phi_{\rm h}^{\rm sample} = \lambda_{\rm h} \Phi_{\rm h+td}^{\rm sample}, \tag{4.26}$$

where $\lambda_h$ is the fraction of halo stars in the sample. This is given by

$$\lambda_h = \frac{1}{\frac{\chi_{td}}{\chi_h}\frac{n_{td}}{n_h} + 1}, \tag{4.27}$$

where $\chi_{td}$ and $\chi_h$ are the fractions of thick disc and halo stars with 200km s$^{-1}$ $\leq V_T \leq$ 500 km s$^{-1}$ and $n_{td}$ and $n_h$ are the local number densities of thick disc and halo stars. The discovery fractions $\chi_{td}$ and $\chi_h$ are known from the simulations described in §4.3.6, whilst the relative normalisation of thick disc to halo stars is taken from independent studies. Assuming a thick to thin disc density ratio of 1:10 (Reid et al. 1995, Chen et al. 2001, Siegel et al. 2002) and a combined disc to halo normalisation of 400:1 (Chabrier & Mera 1997, Holmberg & Flynn 2000), I adopt a thick disc to halo ratio of $n_{td}$:$n_h$ = 40:1. With this consideration of thick disc contamination, the true halo luminosity function is therefore derived from

$$\Phi_{\rm h}^{\rm true} = \frac{\lambda_{\rm h}}{\chi_{\rm h}} \Phi_{\rm h+td}^{\rm sample}. \tag{4.28}$$

However, with a tangential velocity cut-off of $V_T \geq 200$ km s$^{-1}$, this scaling for thick disc contamination has very little effect on the luminosity function. This normalisation gives a scaling factor of $0.97 \leq \lambda_h \leq 1.00$, so at worst the thick disc contamination has just a three percent effect on the normalisation of the luminosity function.

### 4.5.5 Luminosity function errors

In estimating the errors in the luminosity function I adopt the assumption of Poissonian errors (Felten 1976):

$$\sigma^2_{\Phi_{\rm sample}} = \sum \frac{1}{V^2_{max}} \tag{4.29}$$

Allowing for the discovery fraction and thick disc scaling:

$$\sigma^2_{\Phi_{\rm true}} = \left(\frac{\lambda_h}{\chi_h}\right)^2 \sigma^2_{\Phi_{\rm sample}} \tag{4.30}$$

### 4.5.6 Combining fields

Whilst the luminosity functions and densities for each field are derived separately to investigate the spheroid density profile, it is desirable to calculate a combined luminosity function for the fields in each stripe. Unfortunately the necessity of scaling to account for the spheroid discovery fraction and thick disc contamination on a field by field basis means that a total $1/V_{max}$ luminosity function cannot be calculated for the whole sample. However, a combined luminosity function for all of the fields in each stripe can be derived by combining the luminosity functions for each field with a simple weighted mean. The mean density and error for each magnitude bin are then given by

$$\overline{\log\Phi} = \frac{\sum \frac{\log\Phi}{\sigma^2_{\log\Phi}}}{\sum \frac{1}{\sigma^2_{\log\Phi}}}, \tag{4.31}$$

$$\sigma^2_{\overline{\log\Phi}} = \frac{1}{\sum \frac{1}{\sigma^2_{\log\Phi}}}, \tag{4.32}$$

where the summations are over the fields in each stripe.

### 4.5.7 Transforming $\Phi(M_{r*})$ to $\Phi(M_V)$

To facilitate comparison with published luminosity functions, it is necessary to convert the derived luminosity function from SDSS $r^*$ absolute magnitude to Johnson $V$. This is achieved using the transformation

$$\Phi\left(M_V\right) = \Phi\left(M_{r*}\right) \frac{dM_{r*}}{dM_V}. \tag{4.33}$$

The derivative is evaluated from

$$M_V = M_{r*} - (r^* - V) \tag{4.34}$$

$$= M_{r*} - (-0.889(r^* - i^*) - 0.040)\,, \tag{4.35}$$

from Equation 4.10. By varying $(r^* - i^*)$, $M_{r*}$ can be plotted against $M_V$, a spline fitted and the derivative evaluated (Figure 4.35). Hence $dM_{r*}/dM_V$ can be calculated for a given $M_{r*}$, and repeating this for each $M_{r*}$ bin in the luminosity function completes the transformation.

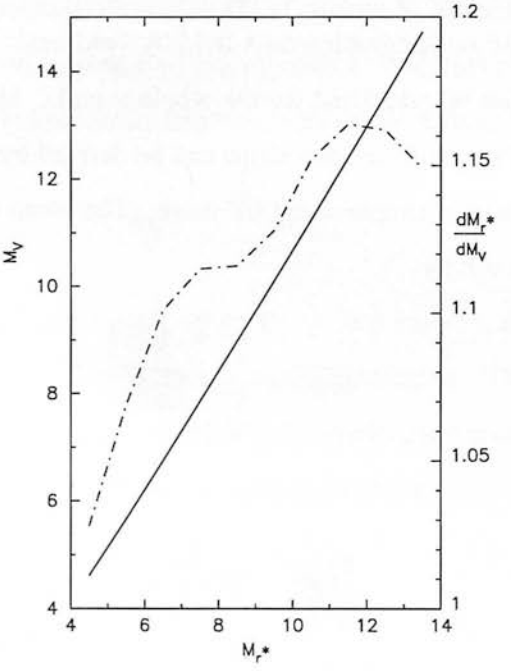


*Figure 4.35: The relations between $M_{r*}$ and $M_V$ (solid line) and $\frac{dM_{r*}}{dM_V}$ (dot-dashed line) derived from the two-colour relations. These are used to convert the derived luminosity function from SDSS $M_{r*}$ to Johnson $M_V$.*

### 4.5.8 Constraining the spheroid density profile

With a wide range of lines of sight, the SGS and NGS samples are ideally suited to constraining the density distribution of the spheroid. Indeed, a non-uniform density law has to be assumed in order to compare the luminosity functions of the different samples. Figure 4.36 shows the number densities (the luminosity function integrated over $5 \leq M_{r^*} \leq 10$) for each field plotted against Galactic longitude when derived using a conventional $V_{max}$ method under the assumption of uniform space density. It is clear from the similarity to the models that at the distances sampled the varying density of the spheroid has a strong effect and so has to be taken into account when deriving the luminosity function.

In order to constrain the density distribution a power law of the form given in Equation 4.24 is assumed, and subdwarf number densities are calculated for each field in the SGS and NGS for a range of power law indices and axial ratios. The power law index $\alpha$ is allowed to vary from $-2.0$ to $-4.4$ in steps of 0.05, and the axial ratio from 0.2 to 1.0 in intervals of 0.05.

The generalised $V_{max}$ method (§4.5.1) should ensure that the derived number densities are constant and independent of line of sight, so how well a $(\alpha, q)$ power law model fits the data is ascertained by measuring how close to a uniform value are the field number densities under the model. This goodness of fit is defined by a modified chi-square statistic

$$\chi^2 = \sum_{i=1}^{nf} \sum_{j=i}^{nf} \frac{(n_i - n_j)^2}{\sigma_i^2 + \sigma_j^2}, \tag{4.36}$$

where $n_i$ and $\sigma_i$ are the number density and its standard deviation for each of $nf$ fields. The best-fit $(\alpha, q)$ density model is therefore the model with the minimum value of $\chi^2$, and the likelihood of each model can be evaluated by comparing its statistic value with the minimum.

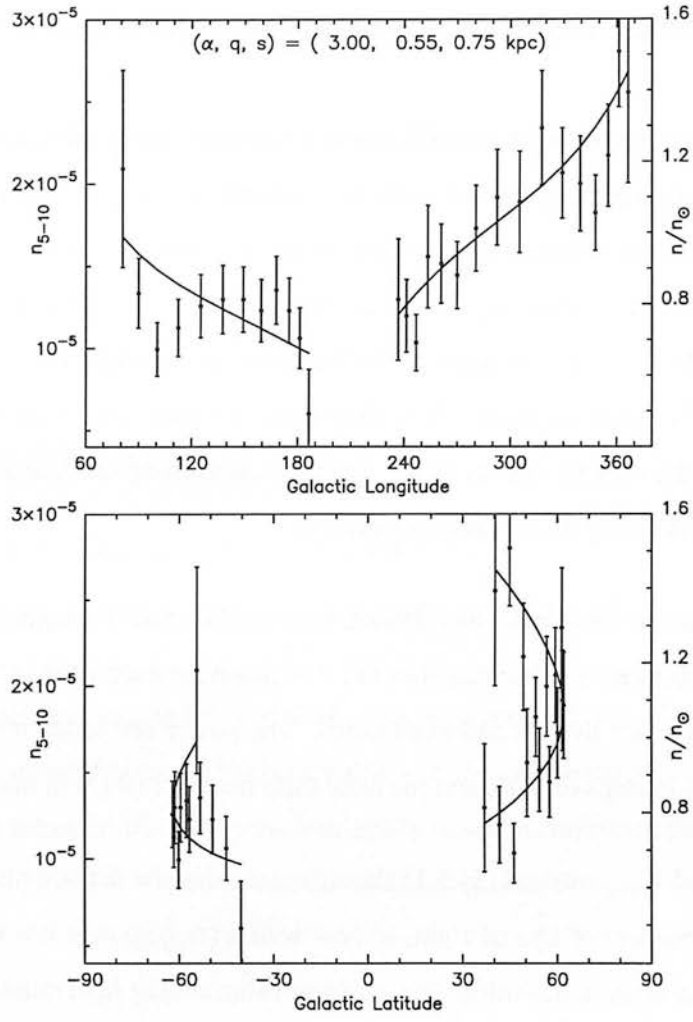


*Figure 4.36: The subdwarf number densities (points) in each field derived from a conventional $V_{max}$ method assuming uniform population density. The lines show the expected relative number densities at a distance of 0.75 kpc from a spheroid density power law with $(\alpha, q) = (-3.0, 0.55)$. Is is clear that the uniform density assumption is invalid for this sample and so a non-uniform distribution must be assumed in the calculation of the luminosity functions. Accordingly, these data can be used to constrain the form of the density profile, which is matched well by a power law of the form given in Equation 4.23.*

## 4.6 Results and discussion

### 4.6.1 Spheroid density profile

Figure 4.37 shows the results of fitting spheroid density models $(\alpha, q)$ to the combined SGS and NGS data, with contours of equal $\chi^2$ plotted. Although there is a slight degeneracy with

$q$, the best-fit power law index is $\alpha = -3.15 \pm 0.30$ for the range $0.55 \leq q \leq 0.85$, which is the value of the axial ratio derived from recent studies (Sluis & Arnold 1998, Gould et al. 1998, Robin, Reylé, & Crézé 2000, Chen et al. 2001, Siegel et al. 2002). This power law index is largely in agreement with the recent results of Gould et al. (1998) ($\alpha = -3.13 \pm 0.23$); Sluis & Arnold (1998) ($\alpha = -3.2 \pm 0.3$); Yanny et al. (2000) ($\alpha = -3.2 \pm 0.3$); Ivezić et al. (2000)($\alpha = -3$); Chen et al. (2001) ($\alpha = -2.55 \pm 0.3$); Siegel et al. (2002) ($\alpha = -2.75$) and Gould (2003) ($\alpha = -3.1 \pm 1.0$). This $r^{-3}$ distribution differs significantly from the $r^{-2}$ power law of the dark matter halo, providing further evidence for the theory that faint halo stars constitute only a negligible fraction of Galactic dark matter (Bahcall et al. 1994, Flynn et al. 1996, Chabrier & Mera 1997, Fields et al. 1998).

These results are only able to constrain $q \gtrsim 0.3$. Comparison of the limits of $q \approx 0.55 \pm 0.06$ set by Chen et al. (2001) with the SDSS EDR data, and inspection of Equation 4.24, shows that this is due to a combination of the much smaller distances and restricted range of Galactic latitude ($\Delta b \lesssim 30°$in each stripe) probed by this study. Small values of $s$ in Equation 4.24 cause the $q$ term to be negligible compared to the $r_c^2 + R_0^2$ terms, and a small variation in $b$ will lead to little sensitivity to different values of $q$. The low distances are a result of the relatively bright lower magnitude limit of $r^* \sim 19$ set by the POSS-I R plates, but using a wider range of Galactic coordinates (especially latitude) from future SDSS releases will help to overcome this degeneracy.

A similar problem afflicts independent analysis of the density distributions of the SGS and NGS. The smaller ranges of Galactic longitude and distances (Figure 4.31) sampled in the SGS and the decreased sensitivity to the density profile parameters in this direction means that neither $\alpha$ or $q$ can be adequately constrained for the SGS taken in isolation. The NGS alone does allow limits to be placed on $\alpha$ and $q$, and these agree well with the values derived for the joint SGS/NGS sample, albeit with larger errors.

The standard error of the $\alpha$ derived for the SGS and NGS was obtained from bootstrap resampling. One thousand bootstrap samples comprised of random selections of stars from the original with replacement (the same size as the actual sample) are analysed to find a best-fit $\alpha$ for each. The standard deviation of $\alpha$ for these bootstrap sample is an estimate of the standard error in the power law index.

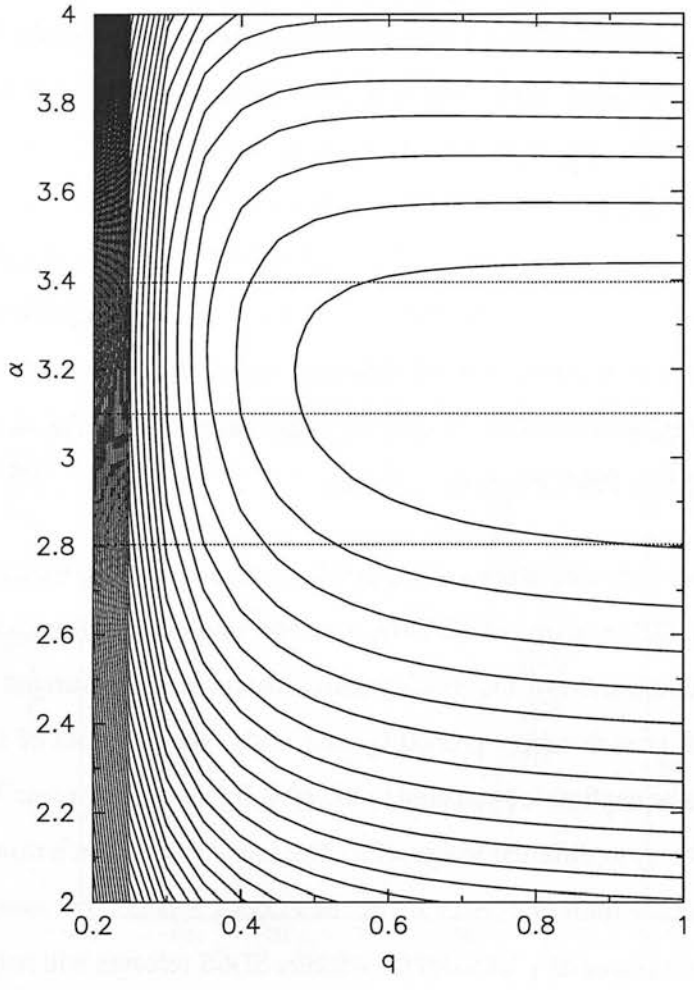


*Figure 4.37: Contours of equal $\chi^2$ constraining the spheroid density models $(\alpha, q)$. Although $q$ cannot be adequately constrained with these data, I find $\alpha = -3.15 \pm 0.30$. The dashed lines show the one standard error interval from the best-fit power law index. The standard error in $\alpha$ is calculated from bootstrap resampling.*

### 4.6.2 The subdwarf luminosity function

The combined luminosity functions of the SGS and NGS fields for the best-fit power law $\alpha = -3.15$ are shown in Figure 4.38 (the luminosity functions for my samples are insensitive to the value of $q$.) The results for each stripe are in excellent accordance with each other, with all but one magnitude bin agreeing within the $1\sigma$ error bars. For true $1\sigma$ errors $\sim$68% (5-6) bins would be expected to agree, suggesting that the errors here may be overestimated. If

so, this can be explained by considering that the given uncertainties in the luminosity function are derived from a Poissonian approximation: the uncertainty in a star's contribution to each bin is assumed to be equal to its contribution ($\sum 1/V_{max}$; Equation 4.19) and the errors of the stars in each bin are summed in quadrature (Equation 4.29). This assumption of Poissonian errors is only approximate, and is less reliable for small numbers of stars and when the values of $V_{max}$ are not similar (Tinney et al. 1993). In order to reflect more accurate uncertainties a full simulation incorporating the observational errors is necessary. Indeed, such determinations show that for bins with larger numbers of objects, where observational errors are less important, Possonian errors tend to overestimate the true inaccuracies (Méndez & Ruiz 2001), providing a possible explanation for the unexpectedly good agreement between the SGS and NGS luminosity functions found here. However, given the small size of the errors expected in these luminosity functions it is considered unnecessary to perform a complete error analysis, so instead the approximate analytically-derived Possion errors are used to give an indication of the expected accuracies of the luminosity functions. Even with the possibility that the errors shown are slightly overestimated, there is still very good agreement between the SGS and NGS luminosity functions, suggesting that there are no systematic spatial effects in the analysis of the two samples.

There is also good agreement with the kinematic studies of Gizis & Reid (1999), Dahn et al. (1995)/Casertano et al. (1990) and Gould (2003) (note that as in Figure 2.2 the Dahn et al. 1995 result has been scaled by 0.75 to reflect use of Casertano et al. 1990 kinematics.) This indicates that the correction of my sample to the solar neighbourhood data by an $r^{-3.15}$ power law is a good approximation, and that this distribution therefore well describes the inner halo out to 2.5kpc. The disagreement with the result of Gould et al. (1998) is pronounced, however, and this may be due to systematic errors affecting their sample: for example, Gizis & Reid (1999) postulated that the choice of local calibrating subdwarfs in Gould et al. (1998) could cause their luminosity function to be underestimated. Alternatively, there could be a real effect behind the discrepancy. The inability of the Gould et al. (1998) data to match the local luminosity functions when fitted with a $(\alpha, q) = (-3.13, 0.8)$ density power law indicates that this model does not accurately describe the spheroid. As I find that an $r^{-3.15}$ power law accurately fits these data out to 2.5kpc, this provides additional evidence that a difference in the axial ratios of the inner and outer spheroids (Sommer-Larsen & Zhen 1990) may be responsible

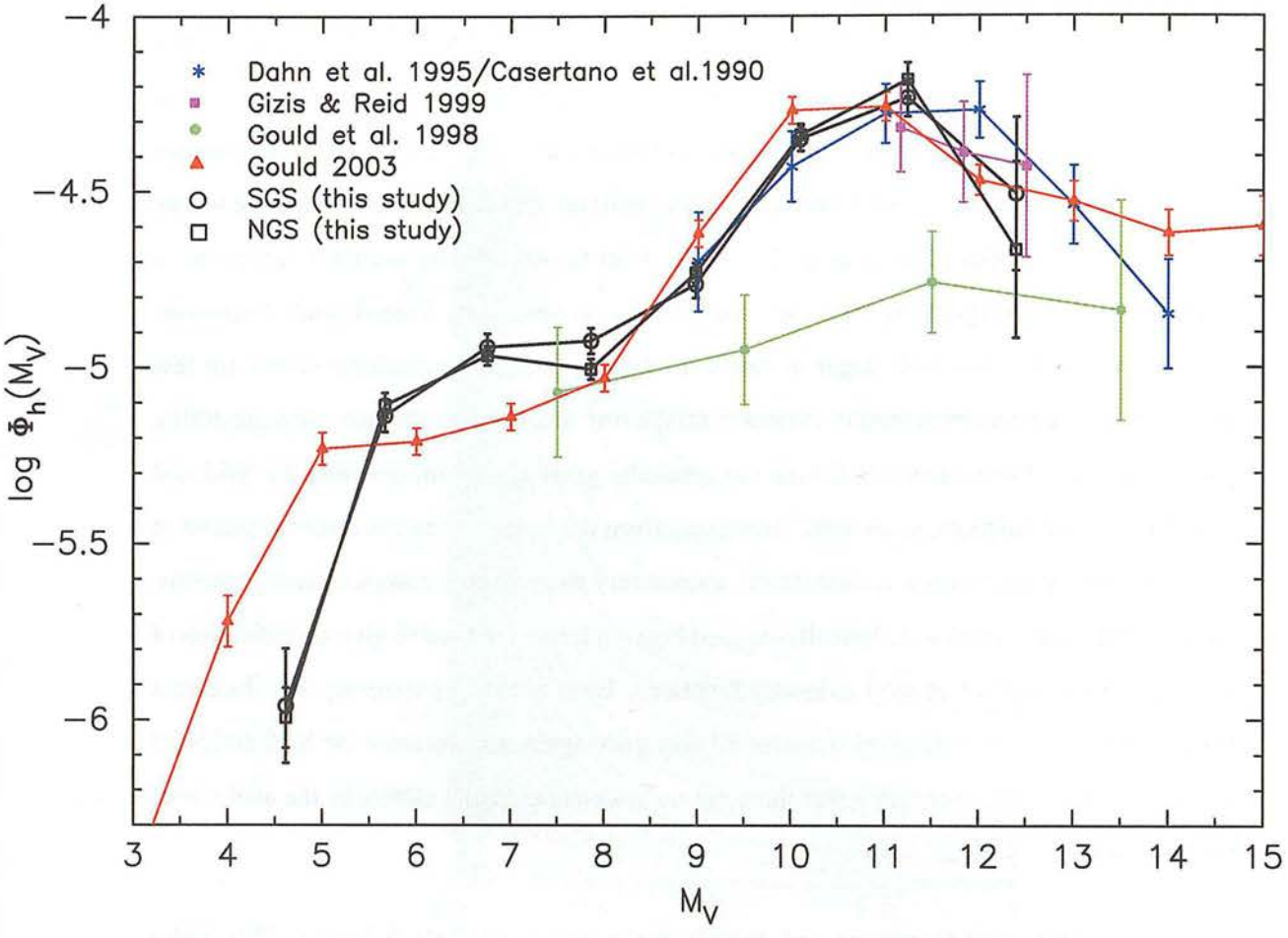


*Figure 4.38: The combined luminosity function for the SGS (solid line, open circles) and NGS (solid line, open squares) assuming the best-fit spheroid density power law of* $\alpha = -3.15$. *The SGS and NGS results are in excellent agreement with each other and agree well with the results of Dahn et al. (1995)/Casertano et al. (1990) (blue asterisks), Gizis & Reid (1999) (magenta filled squares) and Gould (2003) (red filled triangles), but not with the outer halo sample of Gould et al. (1998) (green filled circles), lending weight to the suggestion that a single power law cannot describe the density distributions of both the inner and outer spheroid. The small error bars of this study's luminosity function reflects the much greater size of the subdwarf sample; Gould (2003) claims a similar total sample size, although his is more likely to suffer from thick disc contamination.*

for the discrepancy of the Gould et al. (1998) result. With increasing evidence for a model of the Galaxy where the spheroid, bulge and disc populations form continuous distributions in

age, metallicity and kinematics (eg. Chiba & Yoshii 1998, Chiba & Beers 2000, Siegel et al. 2002), it is likely than the inadequacy of the discrete four-component model is behind the discrepancies seen here.

A further feature evident from Figure 4.38 is the precision of these results. That the error bars from my study are so small reflects the size of the sample, with only the Gould (2003) luminosity function exhibiting comparable errors. However, my subdwarf selection is far more rigorous than that of Gould (2003), who identified ~4500 subdwarfs simply by taking cuts by eye in the reduced proper motion plane and whose sample is therefore prone to thick disc contamination.

Figure 4.39 plots the luminosity functions for stars of different metallicities, with the samples divided into subdwarfs with metallicities either greater or less than the median of $[\widetilde{m/H}] \approx -2.4$. As in the study of Gizis & Reid (1999), I find that the very metal-poor subdwarfs extend to fainter absolute magnitudes and tend to have a higher space density than the more metal-rich ones.

### 4.6.3 The $\langle V/V_{\rm max} \rangle$ test

The overall completeness of the subdwarf samples can be estimated by using the $\langle V/V_{\rm max} \rangle$ test. For each star the ratio of the volume $V$ (corresponding to its distance $d$) to $V_{max}$ is calculated (Equation 4.37), and the mean of this quantity should be 0.5 for a complete survey evenly sampling the survey volume. The error in this mean is $1/\left(12N\right)^{\frac{1}{2}}$, where N is the number of stars in the sample.

$$\left\langle \frac{V}{V_{max}} \right\rangle = \left\langle \left( \frac{d}{d_{max}} \right)^3 \right\rangle \tag{4.37}$$

The values of $\langle V/V_{\rm max} \rangle$ for each field in the SGS and NGS are plotted against Galactic longitude in Figure 4.40. The SGS has a combined value of $\langle V/V_{\rm max} \rangle = 0.495 \pm 0.010$ and the NGS has $0.506 \pm 0.007$. Although this is not a rigorous test of completeness, especially for non-uniformly distributed samples, these results nevertheless provide evidence of no significant incompleteness affecting the samples.

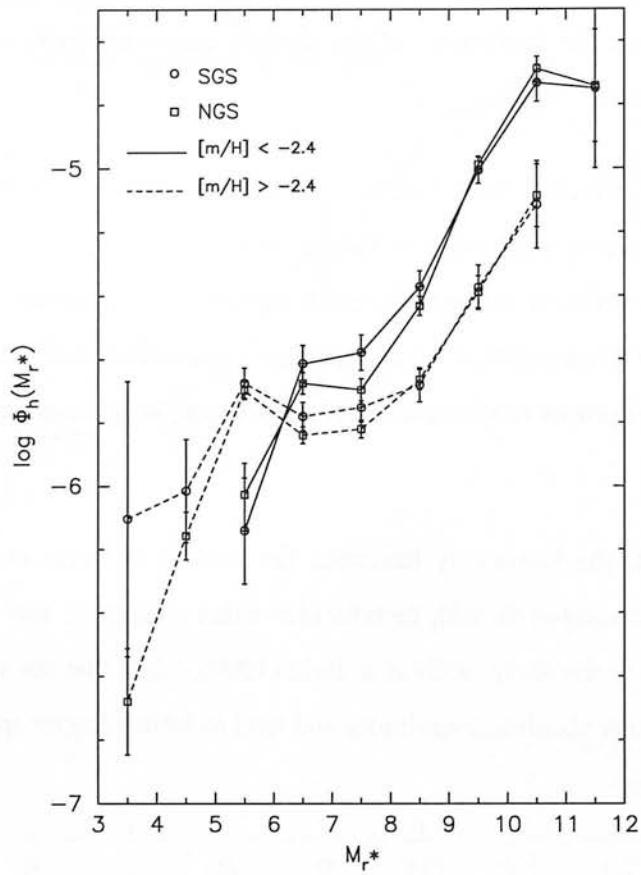


*Figure 4.39: The luminosity functions for stars with metallicities either greater (dashed line) or less than (solid line) the median metallicity of* $[m/H] \approx -2.4$ *in the SGS (circles) and NGS (squares). As in Gizis & Reid (1999), I find that more metal-poor subdwarfs have a higher space density.*

### 4.6.4 Summary

With these data I have demonstrated the effectiveness of the method of reduced proper motion at selecting spheroid stars, and have used it to obtain one of the largest samples of known halo subdwarfs. From this I derive the subdwarf luminosity functions to unprecedented accuracy in two diametrically opposite quadrants of the Galaxy. The large samples along different lines of sight in this study have enabled me to constrain the form of the spheroid density distribution out to 2.5kpc to a power law with an index of $\alpha = -3.15 \pm 0.3$. This is in accordance with other recent results (Gould et al. 1998, Sluis & Arnold 1998, Yanny et al. 2000, Ivezić et al. 2000, Chen et al. 2001, Siegel et al. 2002). I am unfortunately unable to adequately constrain

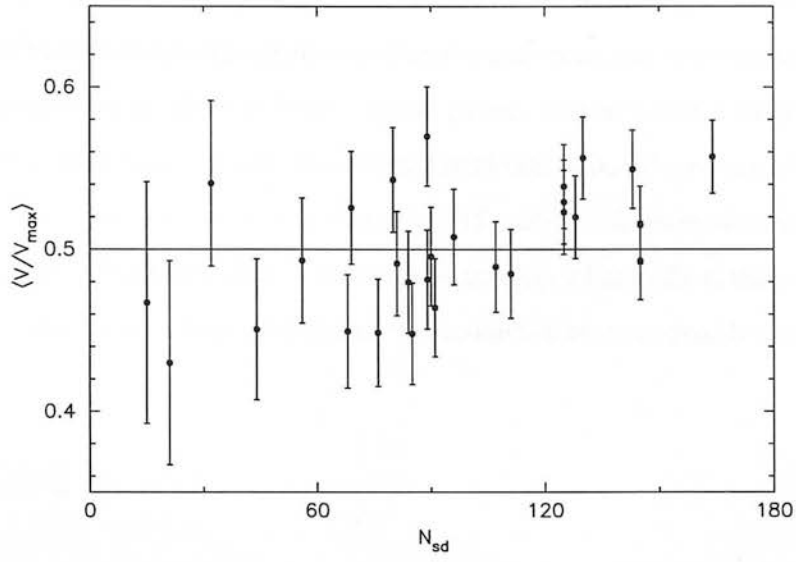


*Figure 4.40:* $\langle V/V_{\rm max}\rangle$ *for all fields in the SGS and NGS plotted against the number of candidate subdwarfs* ($N_{sd}$) *in each field. Although the expected value of* $\langle V/V_{\rm max}\rangle = 0.5$ *for a complete sample is only valid for uniformly-distributed stars, there is nevertheless no evidence for incompleteness in the samples.*

the spheroid flattening parameter $q$ with this study (I can only rule out a very flat halo), due to insufficient survey depth.

My luminosity functions agree well with other recent local derivations, so that with this result the solar neighbourhood subdwarf luminosity function is now well defined to $M_V \approx 12.5$. These data corrected by an $r^{-3.15}$ spheroid density distribution closely match the local luminosity functions, suggesting that this power law well describes the inner halo density profile. On the other hand, my result further confirms the discrepancy between the local luminosity functions and the outer halo luminosity function of Gould et al. (1998) corrected by an $r^{-3.1}$ power law. The Gould et al. (1998) sample is drawn from stars between ~2.5 kpc and ~40 kpc from the Sun, so their derived *local* luminosity function is strongly dependent on the density profile of the spheroid between the solar neighbourhood and the majority of their stars situated at distances of 10-20 kpc. A steeper radial profile would increase the inferred local density and would bring the normalisation of their luminosity function more into accordance with the local results. However, the shape of their luminosity function would also be likely to change, with

the brighter bins being inflated more than the faint ones, since more luminous stars are sampled to greater distances and so are more sensitive to changes in the assumed Galactic structure parameters. Thus whilst a steeper density profile would bring the normalisation of the Gould et al. (1998) luminosity function into better agreement with the local studies, the shape would be likely to become more discrepant. This provides additional evidence that either the Gould et al. (1998) result is affected by systematic errors, or that the inner and outer halo follow quite different density distributions and cannot be described by a simple power law.

# Chapter 5

# Summary

## 5.1 This study

Photographic astronomy has a distinguished record in Galactic astronomy, and in particular the study of stellar populations, as a means to elucidating the structure and evolution of the Galaxy. A large fraction of what we know about the Galaxy today has come from photographic data taken over the last half-century, resulting in important findings such as the discovery of the thick disc (Gilmore & Reid 1983) and one of the first clear detections of spheroid kinematic substructure (Majewski 1992). More recently photographic plates have been used to find further evidence of these halo streams (Ibata et al. 2001b), and to provide evidence for a previously-unknown population of cool white dwarfs in the halo (Oppenheimer et al. 2001).

However, the proliferation of CCD astronomy in the last decade has borne witness to the limitations of photographic data. The photometry attainable from photographic plates is as much as an order of magnitude less accurate than that achievable with CCDs, and effects such as photometric-dependent astrometric errors present significant problems in analysing the positions and motions of objects. I have demonstrated in this thesis how these factors limit the effectiveness of photographic material in the study of local spheroid stars. The large samples of subdwarfs necessary to provide a better understanding of the stellar halo population are not obtainable with astrometric plates, which, whilst yielding the necessary positional and proper

motion accuracy, do not have sufficient depth and photometric precision. Factors such as these, combined with large CCD mosaics that have overcome the previous restrictive narrow fields of view, have caused CCDs to replace photographic plates as the observational medium of choice.

Despite this, there is still significant scope for the continued use of photographic plate material. Huge catalogues of digitised plate data such as the SuperCOSMOS Sky Survey, the APM Catalogue and the Digitised Sky Survey provide all-sky coverage with which to study many diverse areas of both Galactic and extragalactic astronomy (eg. see Hambly et al. 2001a for examples.) These datasets are also important in their use as input coordinate catalogues for recent spectroscopic surveys as the 2dF Galaxy Redshift Survey (Colless et al. 2001).

The advent of wide-field CCD surveys such as the SDSS could be expected to diminish the usefulness of the large-scale photographic studies, but, as shown in this thesis, these two types of dataset provide excellent foils for each other. This is particularly true for the study of celestial motions, since whilst CCDs undoubted offer greater depth and photometric precision, they are unable to match the huge resources of historic data present in the photographic catalogues. Combining the faint magnitude limits and highly accurate photometry of the CCD data with the long time baselines of the photographic plates creates a powerful dataset with which to identify and study stellar populations in our Galaxy. Thus, whilst the majority of the new CCD programmes were designed with extragalactic studies as the principal motivation, I have provided a further example of their suitability for Galactic astronomy.

## 5.2 Future work

*Larger volumes*

There are many lines of research which can be pursued to continue this study, and several steps taken to refine the present analyses. An obvious extension that can be easily applied is to extend the study to larger volumes, which with the methods employed here will enable stronger constraints to be placed on the density law of the spheroid. Adding the SIRTF First Look field from the SDSS EDR will immediately increase the sample size by $\sim$18%, and will provide additional lines of sight, important for determining power law index. The subsequent SDSS data releases will significantly increase the scientific return of this work. With the next

release in mid 2003 some 15% of the SDSS photometry will be available, increasing to ~40% by January 2004. This represents a huge increase over the 4% available from the EDR, and will mean that tens of thousands of subdwarfs will be found with the methods described in this thesis. These will yield even more accurate estimates of the subdwarf luminosity function and will provide much tighter constraints on the spheroid density law through the increase in sample size and lines of sight. In addition to the density power law fitted here and by other studies (see §4.5.3), alternatives such as de Vaucouleurs $r^{1/4}$ models (eg Bahcall & Soneira 1981) can be tested against the data.

*Follow-up spectroscopy*

A further development of this study that is already under way is to obtain spectra of the candidate subdwarfs. Confirmation of their spectral type is important for determining the accuracy of the reduced proper motion selection methods, and for ascertaining the true level of thick disc contamination in the samples. In addition, radial velocities will also enable the sample to be probed for evidence of spheroid kinematic substructure (§2.3.4). Spectra of several hundred subdwarf candidates have already been obtained using the 6dF multi-fibre spectrograph on the UKST at AAO.

*Binarity correction*

In addition to expanding the study to use extra data, additional steps can be taken to improve the methods of the analyses. At present no correction has been made to the data to allow for binarity, but the sample is likely to include a large number of multiple systems: whilst no published figures exist for the binarity fraction of halo subdwarfs, the proportion for M-dwarfs is typically $\gtrsim$30% (Reid & Gizis 1997). The effect of unseen companions on the luminosity function is uncertain, as is seen in discussions over the discrepancy between the Galactic disc nearby and photometric luminosity functions. Kroupa (1995) suggests that missing binaries in photometric surveys could cause the luminosity function to be underestimated by a factor of 2-3, whereas Reid & Gizis (1997) argue that it is much less, with the number of companions missed balanced by the number accidentally included through Malmquist-type biases arising from photometric parallax estimates. There are hence indications that unseen multiple systems may not have an pronounced effect on the subdwarf luminosity function as derived in this study, but it is nevertheless an aspect which deserves closer attention.

*Photometric parallaxes*

The photometric parallaxes used in the derivation of the luminosity function are also a likely source of error — possibly more than any other contributing factor. The large spread in metallicities for subdwarfs results in a large variation of absolute magnitude for a given colour, and these can lead to significant errors in the luminosity function, both through the use of the derived distance in the $V_{max}$ method, and through a star being assigned to an incorrect magnitude bin. The main obstacles in obtaining improved photometric parallaxes are deficiencies in the colour-magnitude relations, caused by either the lack of calibrating subdwarfs with accurate trigonometric parallaxes and a range of well-defined metallicities in the empirical case, or inadequacies in model atmosphere approximations in the theoretical colour-magnitude relations. I have provided some compensation for these difficulties through the use of a colour-magnitude relation that is dependent on the subdwarf metallicity estimate (§4.4.2), although this is only a limited measure, and additional uncertainties in the conversion between SDSS and Johnson/Cousins photometry contribute to any errors in the derived $M_V$ luminosity function. This latter problem can be remedied with more calibrations from SDSS observations, and subsequent releases of larger trigonometric parallax datasets (such as from the USNO programme) and improved model atmospheres should all help to improve the metal-poor colour-magnitude relations.

*Subdwarf mass function*

An important progression of this work is to convert the luminosity functions into an accurate subdwarf mass function by use of a mass-magnitude relation. As described in §2.3.1, the shape and form of the mass function has many important ramifications, from estimating stellar and substellar dark matter contributions to constraining star formation and evolution theories. However, there are several difficulties in assuming a mass-luminosity relation for metal-poor stars (see §2.3.3 and eg. Chabrier 2003), so this aspect in particular will require careful consideration.

*White dwarfs*

In addition to the clear subdwarf component, large numbers of white dwarfs appear in the reduced proper motion diagrams from the SDSS/SSS data of Chapter 4. There is therefore significant scope to derive the luminosity functions of both the spheroid and disc white dwarfs, with the size of the potential samples from these data likely to lead to a large improvements over

existing estimates (Liebert, Dahn, & Monet 1988, Bergeron, Ruiz, & Leggett 1997, Méndez & Ruiz 2001). In addition, the accurate SDSS photometry can be employed in the search for white dwarfs in otherwise crowded areas of the reduced proper motion diagram, using model grid colour interpolations similar to those described in §4.4.1. This could form the basis for a survey of rare helium white dwarfs, with a better comprehension of these objects and the white dwarf luminosity functions contributing to an enhanced understanding of stellar evolution, the age of the Galactic disc and the chemical evolution and star formation history of the Galaxy.

## 5.3 Galactic structure and evolution

Whilst this thesis has been able to make few immediate conclusions about the structure of the Galactic spheroid, there is a huge potential for the expansion of this work into extended and related studies of the history of the Galaxy. These results present arguably the most accurate derivation of the subdwarf luminosity function to date, and provide further evidence for the dual nature of the spheroid, yet they also can be seen as a starting point for future analyses. I have shown that photographic astronomy still has important applications in the study of stellar populations, and with the coupling to CCD survey data have demonstrated how it can be used to great effect to obtain large and relatively pure samples of stars from the spheroid.

Large subdwarf samples identified in this manner will help to resolve some of the outstanding galaxy formation and structure issues outlined in Chapter 1. Using large numbers of subdwarfs with accurate proper motions and radial velocities, the inner spheroid can be searched for kinematic substructure — the fossil remnants of the Galaxy's early history which are central to understanding its formation and evolution. The larger samples will also yield a more accurate probe of the density distribution of the spheroid, and subsequent evidence for spatial substructure, or gradients or breaks in number density, metallicity or kinematics which could provide vital clues in understanding how this oldest part of the Galaxy formed. Only large stellar population studies such as these can fully test the validity of the current model of the Galaxy comprising of four discrete components.

Future astrometric satellites such as Gaia (Gilmore et al. 1998), FAME (Horner et al. 1999) and SIM (Shao 2001, NASA 2002) will provide answers to many aspects of the formation of

our Galaxy, but results from these missions are not expected for some six to ten years. In the absence of these studies, larger samples of stars with accurate proper motions and distances are required to investigate the nature of the Galaxy's stellar populations. The use of wide-field photographic and CCD data and the proper motion selection methods described in this thesis provide an ideal and timely opportunity with which to accurate probe the Galaxy's stellar components and its current structure. Combined with observations of young galaxies at high redshifts, these analyses can finally help to resolve the outstanding puzzles of galaxy and structure formation in the Universe.

# Bibliography


Afonso C., Albert J. N., Andersen J., et al., 2003, A&A, 400, 951

Alcock C., Allsman R. A., Alves D. R., et al., 2000, ApJ, 542, 281

Alexander D. R., Brocato E., Cassisi S., Castellani V., Ciacio F., d'Innocenti S., 1997, A&A, 317, 90

Allen C., Schuster W. J., Poveda A., 1991, A&A, 244, 280

van Altena W. F., Lee J. T., Hoffleit E. D., 1995, New Haven, CT: Yale University Observatory, 4th ed.

Axer M., Fuhrmann K., Gehren T., 1994, A&A, 291, 895

Axer M., Fuhrmann K., Gehren T., 1995, A&A, 300, 751

Bahcall J. N., Casertano S., 1986, ApJ, 308, 347

Bahcall J. N., Soneira R. M., 1981, ApJS, 47, 357

Bahcall J. N., Flynn C., Gould A., Kirhakos S., 1994, ApJ, 435, L51

Baraffe I., Chabrier G., Allard F., Hauschildt P. H., 1995, ApJ, 446, L35

Baraffe I., Chabrier G., Allard F., Hauschildt P. H., 1997, A&A, 327, 1054

Baraffe I., Chabrier G., Allard F., Hauschildt P. H., 1998, A&A, 337, 403

Barnes, 1996, in ASP Conf. Ser. 92 The Formation of the Halo: Inside and Out, ed. H. L. Morrison and A. Sarajedini (San Fransisco: ASP)

Beard S. M., MacGillivray H. T., Thanisch P. F., 1990, MNRAS, 247, 311

Beers T. C., Sommer-Larsen J., 1995, ApJS, 96, 175

Bekki K., Chiba M., 2001, ApJ, 558, 666

van den Bergh, S., 1993, ApJ, 441, 178

van den Bergh, S., 1994, AJ, 108, 2145

van den Bergh, S., 1995, AJ, 110, 1171

Bergeron P., Ruiz M. T., Leggett S. K., 1997, ApJS, 108, 339

Binney J., Merrifield M., Galactic Astronomy, Princeton University Press, New Jersey

Bullock J. S., Kravtsov A. V., Weinberg D. H., 2001, ApJ, 548, 33

Bunclark P. S., Irwin M. J., 1983, in: Proceedings of the Symposium on Statistical Methods in Astronomy, ESA SP-201, ed. E. J. Rolfe (ESA Scientific & Technical Publications Branch, Noordwijk), 195

Burkert A., Yoshii Y., 1996, MNRAS, 282, 1349

Carney B. W., 1999, in The Third Stromlo Symposium: The Galactic Halo, ASP Conf. Ser., eds B. K. Gibson, T. S. Axelrod, M. E. Putman (San Francisco: ASP), p.230

Carney B. W., Aguilar L., Latham D. W., Laird J. B., 1990, AJ, 99, 201

Carney B. W., Laird J. B., Latham D. W., Aguilar L. A., 1996, AJ, 112, 668

Casertano S., Ratnatunga K. U., Bahcall J. N., 1990, ApJ, 357, 435

Chabrier G., 2001, ApJ, 554, 1274

Chabrier G., 2003, PASP, 115, 763

Chabrier G., Baraffe I., 2000, ARA&A, 38, 337

Chabrier G., Mera D., 1997, A&A, 328, 83

Charlot S., Silk J., 1995, ApJ, 445, 124

Chen B., 1997, ApJ, 491, 181

Chen B., 1999, A&A, 344, 494

Chen B., Stoughton C., Smith J. A., et al., 2001, ApJ, 553, 184

Chiba M., Beers T. C., 2000, AJ, 119, 2843

Chiba M., Yoshii Y., 1998, AJ, 115, 168

Chiu L.-T. G., 1980, ApJS, 44, 31

Colless M. et al., The 2dF Galaxy Redshift Survey, http://www.mso.anu.edu.au/2dFGRS/

Cooke J. A., Reid I. N., 2000, MNRAS, 318, 1206

Cox A. N., 2000, Allen's astrophysical quantities, 4th ed. Publisher: New York: AIP Press; Springer, 2000. Editedy by Arthur N. Cox. ISBN: 0387987460,

D'Antona F., Mazzitelli I., 1996, ApJ, 456, 329

Dahn C. C., Liebert J., Harris H. C., Guetter H. H., 1995, The Bottom of the Main Sequence - and Beyond, 239, ed C. G. Tinney. Springer-Verlag Berlin Heidelberg New York.

Davenhall A. C., "Programmer's Note for XYTORADEC", ftp://ftp.roe.ac.uk/pub/scos/xytoradec.ps

Dawson P. C., 1990, Journal of the Royal Astronomical Society of Canada, 84, 175

Dehnen W., 1998, AJ, 115, 2384

Digby A. P., Hambly N. C., Cooke J. A., Reid I. N., Cannon R. D., 2003, MNRAS, in press, pre-print (astro-ph/0304056)

Dinescu D. I., Majewski S. R., Girard T. M., et al., 2002, ApJ, 575, L67

Dohm-Palmer R. C., Helmi A., Morrison H., et al., 2001, ApJ, 555, L37

Doinidis S., Beers T. C., 1989, ApJ, 340, L57

Eggen O. J., 1979, ApJS, 39, 89

Eggen O. J., 1983, ApJS, 51, 183

Eggen O. J., Lynden-Bell D., Sandage A. R., 1962, ApJ, 136, 748 (ELS)

Eichhorn H. K., Russell J., 1976, MNRAS, 174, 679

Evans D. W., 1998, PhD thesis, Cambridge University

Evans D. W., 1992, MNRAS, 255, 521

Evans D. W., Irwin M., 1995, MNRAS, 277, 820

Evans N. W., Invited Review for "IDM 2002: The 4th International Workshop on the Identification of Dark Matter", eds N. Spooner, V. Kudryavtsev (World Scientific), preprint (astro-ph/0211302)

*Explanatory Supplement to the Astronomical Almanac*, 1992, US Naval Observatory (Univer-

sity Science Books, California)

Felten J. E., 1976, ApJ, 207, 700

Fields B. D., Freese K., Graff D. S., 1998, New Astronomy, 3, 347

Flynn C., Gould A., Bahcall J. N., 1996, ApJ, 466, L55

Freese K., Fields B. D., Graff D. S., 2001, Identification of Dark Matter, 213

Fry A. M., Morrison H. L., Harding P., Boroson T. A., 1999, AJ, 118, 1209

Fuhrmann K., 1998, A&A, 338, 161

Fukugita M., Ichikawa T., Gunn J. E., Doi M., Shimasaku K., Schneider D. P., 1996, AJ, 111, 1748

Fulbright J. P., 2000, AJ, 120, 1841

Gibson B. K., Flynn C., 2001, Science, Technical Comment to Oppenheimer et al. (2001)

Gibson B. K., Mould J. R., 1997, ApJ, 482, 98

Gilmore G., Reid N., 1983, MNRAS, 202, 1025

Gilmore G. F., Perryman M. A., Lindegren L., et al., 1998, Proc. SPIE, 3350, 541

Gilmore G., Wyse R. F. G., Norris J. E., 2002, ApJ, 574, L39

Gizis J. E., 1997, AJ, 113, 806

Gizis J. E., Reid I. N., 1999, AJ, 117, 508

Goldman B., Afonso C., Alard C., et al., 2002, A&A, 389, L69

Gould A., Salim S., 2002, ApJ, in press, preprint(astro-ph/0204217)

Gould A., Flynn C., Bahcall J. N., 1998, ApJ, 503, 798

Gould A., 2003, ApJ, 583, 765

Graff D. S., Freese K., 1996a, ApJ, 456, L49

Graff D. S., Freese K., 1996b, ApJ, 467, L65

Gratton R. G., Carretta E., Matteucci F., Sneden C., 2000, A&A, 358, 671

Green R. M., 1985, *Spherical Astronomy*, Cambridge University Press, 1985

Hambly N. C., 1998, http://www.roe.ac.uk/cosmos/manuals/photometry.ps.gz

Hambly N. C., Smartt S. J., Hodgkin S. T., 1997, ApJ, 489, L157

Hambly N. C., MacGillivray H. T., Read M. A., et al., 2001a, MNRAS, 326, 1279

Hambly N. C., Irwin M. J., MacGillivray H. T., 2001b, MNRAS, 326, 1295

Hambly N. C., Davenhall A. C., Irwin M. J., MacGillivray H. T., 2001c, MNRAS, 326, 1315

Hansen B. M. S., 1999, ApJ, 520, 680

Hansen B. M. S., 2001, ApJ, 558, L39

Hanson R. B., 1979, MNRAS, 186, 875

Hanson R. B., 1983, IAU Colloq. 76: Nearby Stars and the Stellar Luminosity Function, 51

Hanson R. B., 1989, BAAS, 21, 1107

Harding P., Morrison H. L., Olszewski E. W., Arabadjis J., Mateo M., Dohm-Palmer R. C., Freeman K. C., Norris J. E., 2001, AJ, 122, 1397

Hartmann K., Gehren T., 1988, A&A, 199, 269

Hawley S. L., Gizis J. E., Reid I. N., 1996, AJ, 112, 2799

Helmi A., White S. D. M., 1999, MNRAS, 307, 495

Helmi A., de Zeeuw P.T., 2000, MNRAS, 319, 657

Helmi A., White S.D.M., de Zeeuw P.T., Zhao H.S., 1999, Nature, 402, 53

Høg E., Fabricius C., Makarov V. V., et al., 2000, A&A, 355, L27

Holmberg J., Flynn C., 2000, MNRAS, 313, 209

Horner S. D., Germain M. E., Greene T. P., et al., 1999, Bulletin of the American Astronomical Society, 31, 1504

Ibata R. A., Lewis G. F., 1998, ApJ, 500, 575

Ibata R. A., Gilmore G., Irwin M. J., 1994, Nature, 370, 194

Ibata R. A., Wyse R. F. G., Gilmore G., Irwin M. J., Suntzeff N. B., 1997, AJ, 113, 634

Ibata R. A., Richer H. B., Gilliland R. L., Scott D., 1999, ApJ, 524, L95

Ibata R., Irwin M., Bienaymé O., Scholz R., Guibert J., 2000, ApJ, 532, L41

Ibata R., Irwin M., Lewis G. F., Stolte A., 2001a, ApJ, 547, L133

Ibata R., Lewis G. F., Irwin M., Totten E., Quinn T., 2001b, ApJ, 551, 294

Isobe S., 1974, A&A, 36, 333

Ivezić Z., Goldston J., Finlator K., et al., 2000, AJ, 120, 963

Jenkins A., 1992, MNRAS, 257, 620

Johnston K. V., Spergel D. N., Hernquist L., 1995, ApJ, 451, 598

Johnston K. V., Majewski S. R., Siegel M. H., Reid I. N., Kunkel W. E., 1999, AJ, 118, 1719

Kinman T. D., Pier J. R., Suntzeff N. B., Harmer D. L., Valdes F., Hanson R. B., Klemola A. R., Kraft R. P., 1996, AJ, 111, 1164

Knox R. A., Hawkins M. R. S., Hambly N. C., 1999, MNRAS, 306, 736

Koopmans L. V. E., Blandford R. D., 2002, MNRAS, in press, preprint(astro-ph/0107358)

Kroupa P., 1995, ApJ, 453, 358

Kroupa P., 2001, MNRAS, 322, 231

Kroupa P., 2002, Science, 295, 82

Kundu A., Majewski S. R., Rhee J., et al., 2002, ApJ, 576, L125

Kurucz R., 1993, ATLAS9 Stellar Atmosphere Programs and 2 km/s grid. Kurucz CD-ROM No. 13. Cambridge, Mass.: Smithsonian Astrophysical Observatory, 1993., 13

Laird J. B., Carney B. W., Rupen M. P., Latham D. W., 1988, AJ, 96, 1908

Landolt A. U., 1992, AJ, 104, 340

Larson R. B., 1969, MNRAS, 145, 405

Larson R. B., 1976, MNRAS, 176, 31

Lasker B. M., Sturch C. R., Lopez C., et al., 1988, ApJS, 68, 1

Lasserre T., Afonso C., Albert J. N., et al., 2000, A&A, 355, L39

Layden A. C., 1995, AJ, 110, 2288

Layden A. C., Sarajedini A., 2000, AJ, 119, 1760

Layden A. C., Hanson R. B., Hawley S. L., Klemola A. R., Hanley C. J., 1996, AJ, 112, 2110

Lee J. W., Carney B. W., 1999, AJ, 118, 1373

Lee Y., Demarque P., Zinn R., 1994, ApJ, 423, 248

Leggett S. K., 1992, ApJS, 82, 351

Lenz D. D., Newberg J., Rosner R., Richards G. T., Stoughton C., 1998, ApJS, 119, 121

Liebert J., Dahn C. C., Monet D. G., 1988, ApJ, 332, 891

Lutz T. E., Kelker D. H., 1973, PASP, 85, 573

Luyten W. J., 1925, ApJ, 62, 8

Luyten, W. J. 1979, LHS Catalogue, Minneapolis: University of Minnesota, 1979, 2nd ed

Luyten W. J., 1980, NLTT Catalogue, Minneapolis: University of Minnesota

Lynden-Bell D., Lynden-Bell R. M., 1995, MNRAS, 275, 429

Majewski S. R., 1992, ApJS, 78, 87

Majewski S. R., 1993, ARA&A, 31, 575

Majewski S. R., Siegel M. H., 2002, ApJ, 569, 432

Majewski S. R., Munn J. A., Hawley S. L., 1994, ApJ, 427, L37

Majewski S. R., Munn J. A., Hawley S. L., 1996, ApJ, 459, L73

Majewski S. R., Siegel M. H., Kunkel W. E., Reid I. N., Johnston K. V., Thompson I. B., Landolt A. U., Palma C., 1999, AJ, 118, 1709

Malkov O., Zinnecker H., 2001, MNRAS, 321, 149

Martínez-Delgado D., Aparicio A., Gómez-Flechoso M. Á., Carrera R., 2001, ApJ, 549, L199

Mateo M., Olszewski E. W., Morrison H. L., 1998, ApJ, 508, L55

May A., Binney J., 1986, MNRAS, 221, 857

Méndez R. A., 2002, A&A, 395, 779

Méndez R. A., Ruiz M. T., 2001, ApJ, 547, 252

Méndez R. A., Platais I., Girard T. M., Kozhurina-Platais V., van Altena W. F., 1999, ApJ, 524, L39

Méndez R. A., Plaitais I., Girard T. M., Kozhurina-Platais V., van Altena W. F., 2000, AJ, 119, 813

Menzies J. W., Cousins A. W. J., Banfield R. M., Laing J. D., 1989, South African Astronomical Observatory Circular, 13, 1

Monet D. G., Dahn C. C., Vrba F. J., Harris H. C., Pier J. R., Luginbuhl C. B., Ables H. D., 1992, AJ, 103, 638

Monet D. G., 1996, AAS Meeting, 188, 54.04

Monet D. G., 1998, AAS Meeting, 193, 120.03

Moore B., Ghigna S., Governato F., Lake G., Quinn T., Stadel J., Tozzi P., 1999, ApJ, 524, L19

Morrison H. L., Flynn C., Freeman K. C., 1990, AJ, 100, 1191

Morrison H. L., Boroson T. A., Harding P., 1994, AJ, 108, 1191

Morrison H. L., Miller E. D., Harding P., Stinebring D. R., Boroson T. A., 1997, AJ, 113, 2061

Morrison H. L., Mateo M., Olszewski E. W., Harding P., Dohm-Palmer R. C., Freeman K. C., Norris J. E., Morita M., 2000, AJ, 119, 2254

Murray C. A., 1983, Vectorial Astrometry, Adam Hilger, Bristol, UK

Murray C. A., 1986, MNRAS, 223, 649

Murray C. A., Corben P. M., 1979, MNRAS, 187, 723

Murray C. A., Tucker R. H., Clements E. D., 1971, Royal Observatory Bulletin, No. 162, Appendix I and II

Murray C. A., Argyle R. W., Corben P. M., 1986, MNRAS, 223, 629

NASA, 2002, http://planetquest.jpl.nasa.gov/SIM/sim_index.html

Nelson C. A., Cook K. H., Axelrod T. S., Mould J. R., Alcock C., 2002, ApJ, 573, 644

Newberg H. J., Yanny B., Rockosi C., et al., 2002, ApJ, 569, 245

Nissen P. E., Schuster W. J., 1991, A&A, 251, 457

Norris J. E., 1986, ApJS, 61, 667

Norris J. E., 1994, ApJ, 431, 645

Norris J. E., Ryan S. G., 1989, ApJ, 340, 739

Oppenheimer B. R., Hambly N. C., Digby A. P., Hodgkin S. T., Saumon D., 2001, Science, 292, 698

Perryman, M. A. C. & ESA 1997, The Hipparcos and Tycho catalogues. Astrometric and photometric star catalogues derived from the ESA Hipparcos Space Astrometry Mission, Publisher: Noordwijk, Netherlands: ESA Publications Division, 1997, Series: ESA SP Series vol no: 1200

Perryman M. A. C., Lindegren L., Kovalevsky J., et al., 1997, A&A, 323, L49

Piotto G., Zoccali M., 1999, A&A, 345, 485

Preston G. W., Shectman S. A., Beers T. C., 1991a, ApJ, 375, 121

Preston G. W., Shectman S. A., Beers T. C., 1991b, ApJS, 76, 1001

Preston G. W., Beers T. C., Shectman S. A., 1994, AJ, 108, 538

Prochaska J. X., Naumov S. O., Carney B. W., McWilliam A., Wolfe A. M., 2000, AJ, 120, 2513

Quinn P. J., Hernquist L., Fullagar D. P., 1993, ApJ, 403,74

Reid N., 1984, MNRAS, 206, 1

Reid N., 1990, MNRAS, 247, 70

Reid I. N., 1997a, AJ, 114, 161

Reid I. N., 1997b, in ASP Conf. Ser. Vol. 127, Proper Motions and Galactic Astronomy, ed. Humpreys R. M., The Astronomical Society of the Pacific, San Francisco, p.63

Reid N., 1998, AJ, 115, 204

Reid I. N., Gizis J. E., 1997, AJ, 113, 2246

Reid N., Hawley S. L., 2000, New light on dark stars : red dwarfs, low mass stars, brown dwarfs / Neill Reid and Suzanne L. Hawley. New York : Springer, 2000. (Springer-Praxis series in astronomy and astrophysics)

Reid N., Murray C. A., 1992, AJ, 103, 514

Reid I. N., Hawley S. L., Gizis J. E., 1995, AJ, 110, 1838

Reid I. N., Sahu K. C., Hawley S. L., 2001, ApJ, 559, 942

Reid I. N., van Wyk F., Marang F., Roberts G., Kilkenny D., Mahoney S., 2001, MNRAS, 325, 931

Reylé C., Robin A. C., Crézé M., 2001, A&A, 378, L53

Richer H. B., Fahlman G. G., 1992, Nature, 358, 383

Richer H. B., Harris W. E., Fahlman G. G., et al., 1996, ApJ, 463, 602

Richer H. B., 2002, Mem. Soc. Astron. It., 73, 372

Robin A. C., Reylé C., Crézé M., 2000, A&A, 359, 103

Rodgers A. W., Roberts W. H., 1993, AJ, 106, 1839

Rodgers A. W., Harding P., Sadler E., 1981, ApJ, 244, 912

Rong J., 1997, ChA&A, 21, 127

Rosenberg A., Saviane I., Piotto G., Aparicio A., 1999, AJ, 118, 230

Röser, S., 1996, in IAU Sump. 172, Dynamics, Ephemerides and Astrometry of the Solar System, ed. S. Ferraz-Mello, B. Morando, & J. E., Arlot (Dordrecth: Kluwer), 481

Saio H., Yoshii Y., 1979, PASP, 91, 553

Salim S., Gould A., 2002a, ApJ, 575, L83

Salim S., Gould A., 2002b, ApJ, submitted, preprint(astro-ph/0206318)

Sandage A. R., 1990, J.R.ASC, 84, 70

Sandquist E. L., Bolte M., Stetson P. B., Hesser J. E., 1996, ApJ, 470, 910

Santiago B. X., Elson R. A. W., Gilmore G. F., 1996, MNRAS, 281, 1363

Sarajedini A., Chaboyer B., Demarque P., 1997, PASP, 109, 1321

Schmidt M., 1968, ApJ, 151, 393

Schmidt M., 1975, ApJ, 202, 22

Schneider D. P., Richards G. T., Fan X., et al., 2002, AJ, 123, 567

Schuster W. J., Nissen P. E., 1989, A&A, 222, 69

Schuster W. J., Parrao L., Contreras Martinez M. E., 1993, A&A Supp, 97, 951

Searle L., 1977, In The Evolution of Galaxies and Stellar Populations, ed. B. M. Tinsley, R. B. Larson, p219. New Haven, Yale University Press.

Searle L., Zinn R., 1978, ApJ, 225, 357 (SZ)

Sellwood J. A., Nelson R. W., Tremaine S., 1998, ApJ, 506, 590

Shao M., 2001, American Astronomical Society Meeting, 198, 5121

Siegel M. H., Majewski S. R., Reid I. N., Thompson I. B., 2002, ApJ, 578, 151

Silk J., Wyse R. F. G., 1993, Phys. Rep., 231, 295

Sluis A. P. N., Arnold R. A., 1998, MNRAS, 297, 732

Smith J. A., Tucker D. L., Kent S., et al., 2002, AJ, 123, 2121

Sneden C., Kraft R. P., Prosser C. F., Langer G. E., 1992, AJ, 104, 2121

Sommer-Larsen J., Christensen P. R., 1989, MNRAS, 239, 441

Sommer-Larsen J., Zhen C., 1990, MNRAS, 242, 10

Sommer-Larsen J., 1991, MNRAS, 249, 368

Sommer-Larsen J., Flynn C., Christensen P. R., 1994, MNRAS, 271, 94

Sommer-Larsen J., Beers T. C., Flynn C., Wilhelm R., Christensen P. R., 1997, ApJ, 481, 775

Spaenhauer A., 1989, Contrib. Van Vleck Obs, 9, 45

Stobie R. S., 1986, Pattern Recognition Letters, 4, 317

Stobie R. S., Ishida K., Peacock J. A., 1989, MNRAS, 238, 709

Stoughton C., Lupton R. H., Bernardi M., et al., 2002, AJ, 123, 485

Taff L. G., Lattanzi M. G., Bucciarelli B., Daou D., 1992, ASSL Vol. 174: Digitised Optical Sky Surveys, 185

Tinney C. G., Reid I. N., Mould J. R., 1993, ApJ, 414, 254

Tinsley B. M., Larson R. B., 1979, MNRAS, 186, 503

Toomre A., 1977, In The Evolution of Galaxies and Stellar Populations, ed. B. M. Tinsley, R. B. Larson, p219. New Haven, Yale University Press.

Toth G., Ostriker J. P., 1992, ApJ, 389, 5

Velazquez H., White S. D. M., 1999, MNRAS, 304, 254

Veron-Cetty M. P., Veron P., 2001, A&A, 374, 92

Walker I. R., Hihos J. C., Hernquist L., 1996, ApJ, 460, 121

White S. D. M., 1996, in Schaeffer R., Silk J., Spiro M., Zinn-Justin J., eds, Cosmology and Large Scale Structure, Les Houches, Session LX. Elsevier, Amsterdam, p.349

Wilhelm R. J., 1995, Ph.D. Thesis, Michigan State University

Wilhelm R., Beers T. C., Kriessler J. R., Pier J. R., Sommer-Larsen J., Layden A. C., 1996, ASP Conf. Ser. 92: Formation of the Galactic Halo...Inside and Out, 171

Wyse R. F. G., Gilmore, G., 1992, AJ, 104, 144

Yanny B., Newberg H. J., Kent S., et al., 2000, ApJ, 540, 825

Zaritsky D., Olszewski E. W., Schommer R. A., Peterson R. C., Aaronson M., 1989, ApJ, 345, 759

Zepf S. E., Ashman K. M., 1993, MNRAS, 264, 611

Zinn R., 1996, ASP Conf. Ser. 92: Formation of the Galactic Halo...Inside and Out, 211

# Appendix A

# SuperCOSMOS Measures

The SuperCOSMOS plate measuring machine, based at the Royal Observatory Edinburgh, is a fast, high-precision microdensitometer able to scan Schmidt plates at $10\mu m$ (0.67 arcsec) resolution with high positional accuracy. It superseded COSMOS in 1993, which provided $16\mu m$/ 1.1 arcsec resolution, which was in a turn the successor of GALAXY, the original plate-measuring machines used in Murray's precursor studies to this one (Murray & Corben 1979). Since much of the work in this thesis relies on digitised data from SuperCOSMOS, the measuring and parameterisation processes of the machine are presented here as a summary of the SuperCOSMOS Sky Survey documentation (Hambly et al. 2001a,b,c).

## A.1 Plate processing

### A.1.1 Scanning and digitisation

The 0.67 arcsec SuperCOSMOS pixels are scanned in 32768 grey levels with "lanes" of 1152 pixels scanned simultaneously and combined to build up the complete plate image. The pixel values are given in terms of transmission units, $T$, which are related to the density $D$ and

intensity $I$ on the log-linear part of the photographic curve by

$$\log_{10} \frac{1}{T} \propto D \propto \gamma \log_{10} I \tag{A.1}$$

The scanning of a single Schmidt plate, producing ~2 Gbyte of data, takes about 2 hours. The digitised data are then run through "image analysis mode" (IAM) software, which detects images and parameterises the data. Upon request (as with this current study) the complete pixel data is supplied to the user, for producing images of small areas of the plate.

### A.1.2 Transmission to intensity calibration

In order to facilitate image detection the transmission values of images must be transformed to intensity units. This is traditionally achieved by using the calibrating step-wedges on the corner of Schmidt plates to determine the characteristic curve gradient $\gamma$ from the measured transmission of the intensity spots. However, problems arise with this method from non-uniform emulsion sensitivity across the plate, variations in the intensity spot illumination, and in diffracted light from the clearer areas surrounding the step wedges affecting the measured light levels from dense spots. For this reason an assumed gradient of $\gamma = 2$ is adopted, measured from calibrating plates and shown to be appropriately accurate from comparison of the resulting instrumental magnitude scale with CCD data.

### A.1.3 Sky level estimation

Sky value estimates are needed at every point of the plate for image detection. These are obtained by filtering the raw median sky values with a weighted median filter which smooths the sky values on a scale length of ~2 arcmin.

### A.1.4 Thresholding

Images are detected by applying a threshold at a constant multiple of the sky noise above the local sky estimate. The threshold for any part of the plate is defined by

$$I_{\rm thresh} = \frac{100 + {\rm PCUT}}{100} I_{\rm sky} \tag{A.2}$$

with $I_{\rm sky}$ the local sky estimate from bilinear interpolation of the filtered sky map, and the percentage cut given by

$${\rm PCUT} = 100 \times 2.3 \frac{\sigma_{\rm sky_0}}{I_{\rm sky_0}} \tag{A.3}$$

The sky background in a $10\times10$ arcmin region at the plate centre is $I_{\rm sky_0}$, and the sky noise in this area is estimated from

$$\sigma_{\rm sky_0} = 1.48 \times {\rm MAD(sky_0)} \tag{A.4}$$

where $\rm MAD(sky_0)$ is the median of the absolute deviations about the sky background estimate $\rm I_{sky_0}$, and the factor of 1.48 scales the MAD estimate to a Gaussian sigma. The percentage cut is typically 7% for survey plates.

This thresholding method is chosen to cope with the fact that vignetting causes the sky and noise levels to vary over the plate. A zero point sky intensity value for the transmission-to-intensity calibration is adopted such that the threshold, in terms of multiples of sigma above the sky background, is constant over the plate irrespective of sky variations.

### A.1.5 Image detection

Once the set of pixels above the threshold have been determined across the plate, the SuperCOSMOS image analysis mode uses 8-fold nearest-neighbour pixel connectivity to identify images, with the criterion applied that images must contain at least 8 connected pixels. Multiple objects are detected by the procedure described in Beard, MacGillivray, & Thanisch (1990): each object is rethresholded at up to 16 intensity levels above than the original threshold in or-

der to generate contour information in log(intensity) space, and a connectivity algorithm is applied to pixels above the threshold to determine if an object has split into more than one part.

The spatial extent of an object is determined by its "areal profiles", which are used for object profile analysis and classification. The image is rethresholded at 8 levels with intensities of $0.5\sigma$, $1\sigma$, $2\sigma$ etc above the threshold intensity $I_{\rm thresh}$ given by

$$I_{\rm APn} = I_{\rm thresh} + 2^{n-2}\sigma_{\rm sky0}\ ,\ n = 1, 2, ... 8 \tag{A.5}$$

### A.1.6 Image parameterisation

Following detection the objects are parameterised for both unit- and intensity-weighted parameters as described in Stobie (1986). The resulting 32 4-byte parameters for each image are stored in the IAM (image analysis mode) file for that plate, and are listed in Table A.1.

- COSMAG (parameter 9): this is the isophotal SuperCOSMOS magnitude derived from intensity values in the $n$ image pixels as:

$$\text{COSMAG} = [-2.5\log_{10}\sum_{i=1}^{n}(I_i - I_{\rm sky})] \times 10^3 \quad \text{(millimags)} \tag{A.6}$$

- BLEND (parameter 29): images are deblended using the method of Beard et al. (1990) described in §A.1.5, and the results are indicated with this parameter. A value of $-n$ means the image is the parent of $n$ child images, whereas $+n$ denotes the $n^{\rm th}$ child of a parent image.

- QUALITY (parameter 30): an 32-bit integer flag used to flag conditions occurring during the image analysis that could affect the image integrity. More severe conditions are indicated by setting increasingly severe bits in the quality flag, which are described in Table A.2. Two of the flags are set during post-processing (§A.2): a flag if the region is affected (or likely to be) by labels or step wedges, and another if the object is close to a bright star and could therefore be a spurious detection due to diffraction spikes (see §A.1.6).

| No. | Name | Description | Units | Comments |
|---|---|---|---|---|
| 1 | RA | Celestial Right Ascension | $10^{-8}$ radians | see § A.2.1 |
| 2 | DEC | Celestial Declination | $10^{-8}$ radians | see § A.2.1 |
| 3 | XMIN | Left extent | 0.01 micron | |
| 4 | XMAX | Right extent | 0.01 micron | |
| 5 | YMIN | Bottom extent | 0.01 micron | |
| 6 | YMAX | Top extent | 0.01 micron | |
| 7 | AREA | Total area | Pixels | |
| 8 | IPEAK | Peak intensity | Intensity | |
| 9 | COSMAG | Isophotal magnitude | Millimag | Equation A.6 |
| 10 | ISKY | Sky intensity at (XCEN_I,YCEN_I) | Intensity | $I_{\mathrm{SKY}}$, see §A.1.4 |
| 11 | XCEN_I | Intensity weighted X centroid | 0.01 micron | |
| 12 | YCEN_I | Intensity weighted Y centroid | 0.01 micron | |
| 13 | A_U | Unweighted semi-major axis | 0.01 micron | |
| 14 | B_U | Unweighted semi-minor axis | 0.01 micron | |
| 15 | THETA_U | Unweighted orientation | Degrees | |
| 16 | A_I | Weighted semi-major axis | 0.01 micron | |
| 17 | B_I | Weighted semi-minor axis | 0.01 micron | |
| 18 | THETA_I | Weighted orientation | Degrees | |
| 19 | CLASS | Classification flag | | see § A.2.2 |
| 20 | P_A | Celestial position angle | Degrees | see § A.2.1 |
| 21 | AP(1) | Area above areal profile level 1 | Pixels | Equation A.5 |
| 22 | AP(2) | Area above areal profile level 2 | Pixels | |
| 23 | AP(3) | Area above areal profile level 3 | Pixels | |
| 24 | AP(4) | Area above areal profile level 4 | Pixels | |
| 25 | AP(5) | Area above areal profile level 5 | Pixels | |
| 26 | AP(6) | Area above areal profile level 6 | Pixels | |
| 27 | AP(7) | Area above areal profile level 7 | Pixels | |
| 28 | AP(8) | Area above areal profile level 8 | Pixels | |
| 29 | BLEND | Deblending flag | | see text |
| 30 | QUALITY | Quality flag | | see text |
| 31 | N(0,1) | Profile classification statistic | $\sigma \times 1000$ | see § A.2.2 |
| 32 | PRFMAG | Profile magnitude | Millimag | see § A.2.2 |

*Table A.1: The 32 parameter Image Analysis Mode SuperCOSMOS parameters for each image. Note that parameters 1, 2, 19, 20, 31, 32 and some bits of parameter 30 are determined during the second stage of processing.*

## A.2 Post-processing

Following the plate processing, tasks are performed to provide astrometry, further quality information and object classifications.

| Event | Bit set | Increment | Severity | Comments |
|---|---|---|---|---|
| Orientation calculation failed | 0 | 1 | Information | Image perfectly straight |
| Ellipticity calculation failed | 1 | 2 | Information | Image perfectly round |
| Image too multiple for deblending | 2 | 4 | Warning | Image split into too many fragments |
| Bright image | 4 | 16 | Information | Image has pixels brighter than highest areal profile level (as defined by $n = 8$ in Equation A.5) |
| Large image | 6 | 64 | Warning | Image has area greater than maximum specified for deblending |
| Possible bad image | 7 | 128 | Warning | Image is in region likely to be affected by step wedge or label (post-processing information) |
| Image near very bright star | 10 | 1024 | Warning | Image may be spurious due to bright star (post-processing information) |
| Image touches boundary | 16 | 65536 | Severe defect | Image may be partially missing |

*Table A.2: Determination of the quality flag (IAM parameter 30)*

### A.2.1 Astrometric solution

To convert between the measured $(x, y)$ reference frame and celestial coordinates, the SuperCOSMOS astrometric software (XYTORADEC; Davenhall (2000)) uses reference stars from the Tycho-2 catalogue spread across each plate. The method used is a slight adaptation of the standard tangent plane reduction for converting measured positions to coordinates, in that the exact plate centre is not assumed *a priori* and is allowed to vary in the fit. The technique proceeds as follows:

*(i)* The celestial coordinates of the telescope pointing are established

*(ii)* The reference star coordinates are converted to apparent coordinates by correcting for aberration and refraction (§C.3.5)

*(iii)* Tangent plane (or standard) coordinates $(\xi, \eta)$ are calculated for each reference star about the tangent point

*(iv)* Cubic distortion arising from the deformation of the photographic plates in the curved Schmidt plate-holder is compensated for by scaling each standard coordinate such that

$$\xi' = \frac{r}{\tan r}\xi \ , \ \eta' = \frac{r}{\tan r}\eta \ , \ \text{where } r = \frac{(\xi^2 + \eta^2)^{\frac{1}{2}}}{\tan(\xi^2 + \eta^2)^{\frac{1}{2}}} \tag{A.7}$$

*(v)* The next stage is to remove position-dependent astrometric errors which create well-known "swirl patterns" on Schmidt plates (Taff et al. 1992) of systematic distortions between measured plate positions and the expected tangent plane coordinates. Large scale "swirl patterns" are then removed by applying a mean distortion map, created by averaging the positional residuals on a grid over a large number of plates from the appropriate survey (see Hambly et al. (2001c) for details.) A grid size of 10 arcminute is used since this is adequate to map the expected ~30 arcminute scale non-linear distortions. The mean correction at the location of each reference star is then obtained by bilinearly interpolating in the grid, and the corrections are added to the standard coordinates.

*(vi)* The standard coordinates $(\xi, \eta)$ are then fit to the measured positions $(x, y)$ by a linear six-coefficient least-squares fit to derive a global transformation for the plate. This plate model is given as a relation between the estimated tangent plane coordinates of the reference stars $(\xi_e, \eta_e)$ and their measured plate coordinates $(x_m, y_m)$

$$\begin{aligned} \xi_e &\approx a_1 + a_2 x_m + a_3 y_m \\ \eta_e &\approx b_1 + b_2 x_m + b_3 y_m \end{aligned} \tag{A.8}$$

The coefficients $a_i, b_i$ are found by a least-squares adjustment of the estimated positions $(\xi_e, \eta_e)$ and the *predicted* positions $(\xi_p, \eta_p)$ from the current plate model.

*(vii)* With the plate model determined from the reference stars, the measured positions of programme stars can then be converted to standard coordinates. These standard coordinates are then corrected for geometrical distortion in the same way as for the reference stars (see *(v)*), before being converted from apparent to true coordinates by allowing for aberration and refraction, and then deprojected from tangent plane to celestial coordinates (see eg. Murray 1983 Equation 8.2.3).

### A.2.2 Image classification

Image classification is achieved using a two-stage process originally developed for APM data. The first stage employs conventional methods using parameters such as surface brightness and shape, before the second level traces the stellar locus in multidimensional parameter space to quantify the similarity of each object to a star of comparable intensity. The advantages of

this scheme are the ability to generate a 'linearised profile magnitude' scale and to incorporate prior knowledge of the expected fraction of each type of image class, as well as producing a 'stellarness' index for each object (given as a normalised Gaussian distribution) in addition to the more usual discrete classification.

**Stage 1 of image classification**

The first stage makes use of magnitude, surface brightness, peak brightness and isophotal area plots in order to automatically trace the stellar locus. Images with clear noise-like properties, such as high ellipticity, or with areal profile slopes inconsistent with real objects are discarded, and the stellar locus and its spread are found by converting each scatter plot into a $128 \times 128$ two-dimensional map and finding the mode of the counts and scatter about the mode in each magnitude or peak slice. For faint magnitudes the centre of gravity of the distribution is used instead of the mode.

The scatter plots used are isophotal area against magnitude, weighted area against magnitude and weighted area against peak brightness, and are shown in Figure A.1. The stellar locus boundary is defined as being $2\sigma$ away from the mode where well-defined, or from the centre of gravity at faint magnitudes, and the first plot of isophotal area against magnitude is used to define a stellar/noise boundary (upper line) above which objects are considered to be noise and not used in the other plots.

The scatter plots are used to determine the distance (in each direction and sigma-normalised) of each object from the stellar locii in each: anything above the stellar locus boundary ($2\sigma$ from the mode) and with sensible ellipticity and areal profile slope values is considered stellar. At this stage each image has IAM parameter 19 overwritten according to its preliminary classification: 1 = non-stellar, 2 = stellar, 3 = unclassifiable, 4 = noise.

**Stage 2 of image classification**

The preliminary stellar/non-stellar classifications from the first stage can be used to derive the position and spread in the stellar locus for any image shape parameter. The population median

serves to defined the locus as a function of magnitude and the median of the absolute deviations from the median (MAD) scaled by 1.48 gives an estimate of the scatter.

Next the stellar point spread function (PSF) for the plate is determined iteratively and a linear profile magnitude scale is obtained. The areal profile measures are used with the assumption that all stars should have the same image profile shape irrespective of magnitude, following the methods of Bunclark & Irwin (1983) to determine a typical stellar profile and a linear transformation function between isophotal and profile magnitude.

Next the intensity-normalised slope of the sigma-weighted difference between the image's radial profile and the plate's stellar PSF is combined additively with the sigma-weighted second moments and the sigma-weighted peak intensity to provide a single scalar measure of an object's 'stellarness'. Objects previously classified as stellar are then used, as a function of magnitude, to create a N(0,1) index for the stellar sequence. This index is averaged over the plate to remove zero point variations arising from field effects. An example of this index and the derived stellar locus are shown in Figure A.2.

In order to differentiate between star and galaxy images a Bayesian scheme is used, with the quantity

$$\frac{p(s|d)}{p(g|d)} = \frac{p(s)p(d|s)}{p(g)p(d|g)} \begin{array}{ll} > 1 & \text{for stars} \\ < 1 & \text{for galaxies} \end{array} \tag{A.9}$$

where $p(s)$ and $p(g)$ are the respective prior probabilities of finding a star or galaxy, $p(s|d), p(g|d)$ are the posterior probabilities of an image being a star or galaxy, and $p(d|s), p(d|g)$ are the likelihoods of observing the image descriptors for stars and galaxies. The exact details of this calculation are described in Hambly et al. (2001b).

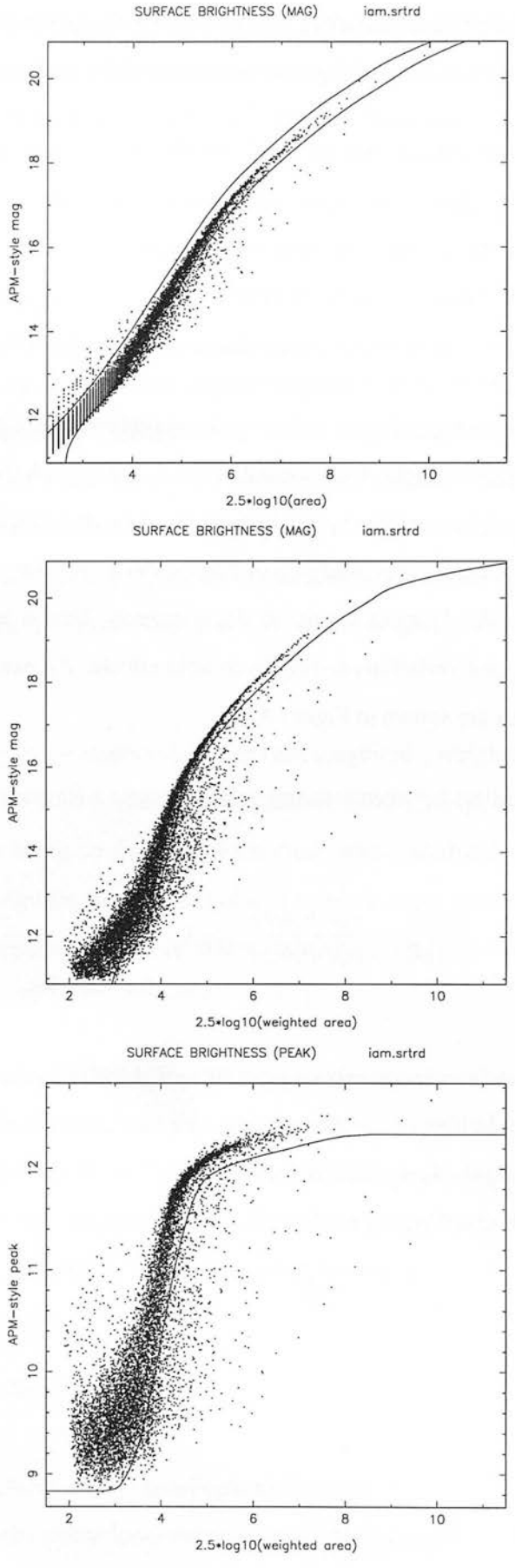


*Figure A.1: The scatter plots used to define the stellar locus (solid line) during the first stage of image classification. The upper line in the top plot is the stellar/noise boundary above which objects are classified as noise and not*

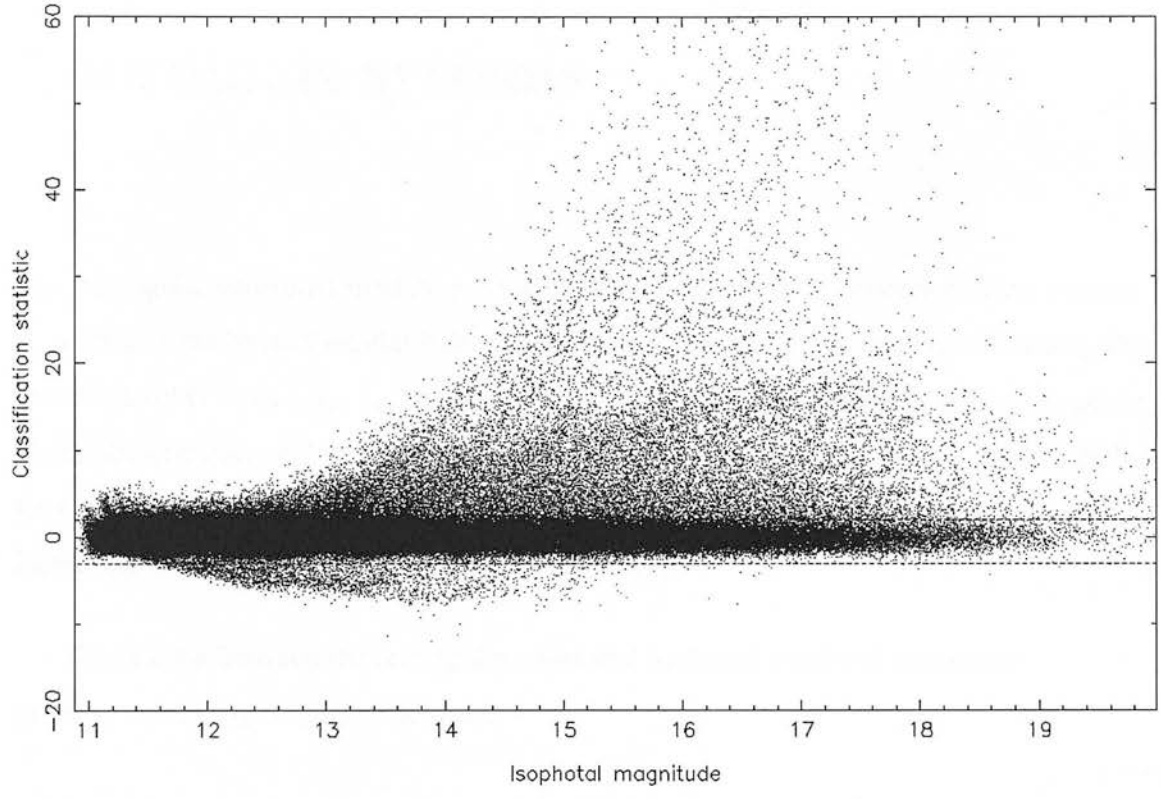


*Figure A.2: The stellar index for a typical plate, indicating the residuals of the areal profile of each image when compared with an average stellar profile. The boundaries show the $+2\sigma$ locus for star/galaxy and $-3\sigma$ for star/noise.*

# Appendix B

# Coordinate systems

The rectangular equatorial triad $\mathrm{N} = (\mathbf{l}\ \mathbf{m}\ \mathbf{n})$ is formed by $\mathbf{l}$ in the direction of the equinox $\gamma$, $\mathbf{n}$ towards the North Celestial Pole, and $\mathbf{m}$ completing the right-handed set. Similarly, the Galactic triad $\mathrm{G} = (\mathbf{x}_\mathrm{G}\ \mathbf{y}_\mathrm{G}\ \mathbf{z}_\mathrm{G})$ has $\mathbf{x}_\mathrm{G}$ towards the Galactic centre, $\mathbf{z}_\mathrm{G}$ in the direction of the North Galactic Pole, and $\mathbf{y}_\mathrm{G}$ orthogonal to both. The normal triad $\mathbf{R} = (\mathbf{p}\ \mathbf{q}\ \mathbf{r})$ has $\mathbf{r}$ radially from the observer to a source, with $\mathbf{p}$ and $\mathbf{q}$ in the plane normal to $\mathbf{r}$: $\mathbf{p}$ parallel to the equator, increasing towards the east, and $\mathbf{q}$ positive to the north.

The relation between the rectangular equatorial triad and equatorial coordinates $(\alpha, \delta)$ is given by expressing the unit vector $\mathbf{r}$ as:

$$\mathbf{r} = \mathrm{N} \begin{pmatrix} \cos\delta\cos\alpha \\ \cos\delta\sin\alpha \\ \sin\delta \end{pmatrix} \tag{B.1}$$

and the relation between the rectangular equatorial and normal triads is:

$$\mathbf{R} = \mathrm{N} \begin{pmatrix} -\sin\alpha & -\sin\delta\cos\alpha & \cos\delta\cos\alpha \\ \cos\alpha & -\sin\delta\sin\alpha & \cos\delta\sin\alpha \\ 0 & \cos\delta & \sin\delta \end{pmatrix} \tag{B.2}$$

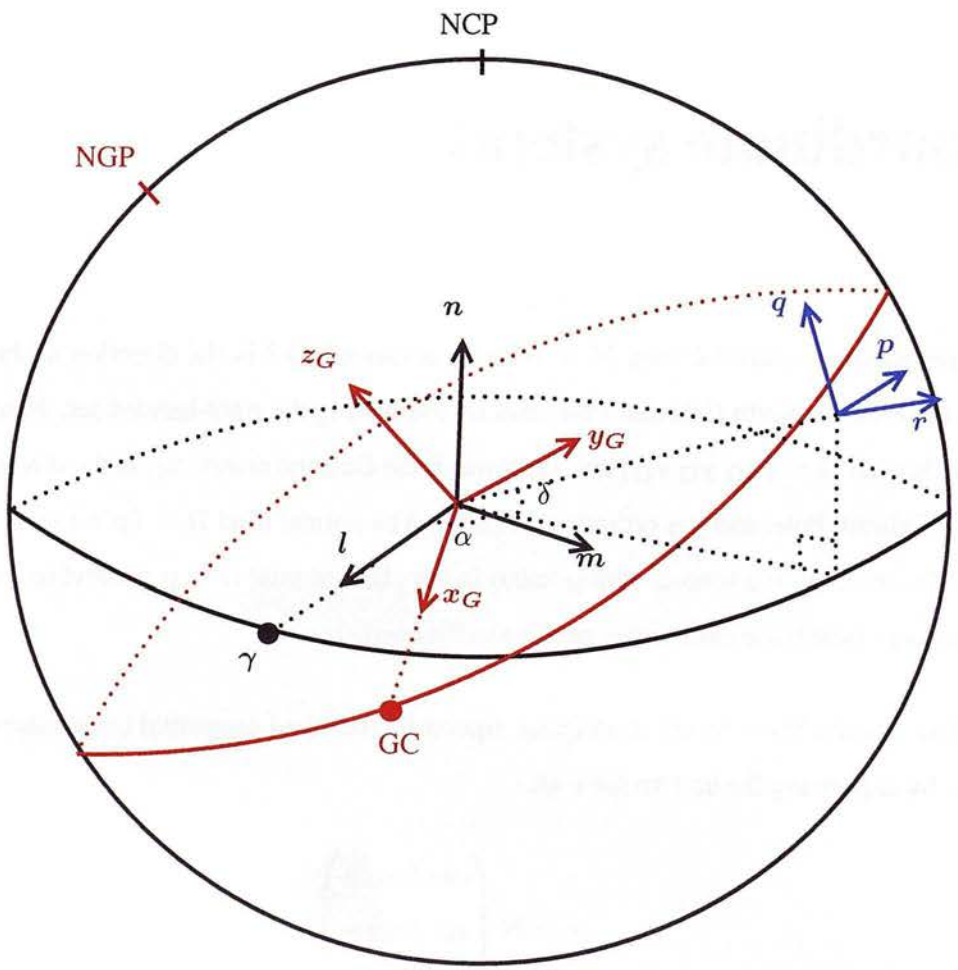


*Figure B.1: Coordinate systems used in these Appendices and described in the text above.*

# Appendix C

# Tangent plane reduction

## C.1 Gnomic Projection

The projection of the sky onto the tangent plane (ie. a photographic plate) is known as *central* or *gnomic* projection. Figure C.1 shows the configuration, where $\hat{\mathbf{w}}$ is the unit vector in the tangential direction from the centre of projection, O, to the tangent point on the plate, W, and S is the image on the plate of a star in the direction $\mathbf{x}$.

## C.2 Astrometric plate reduction problem

### C.2.1 Definition of the problem

A star has measured plate coordinates given by $(x, y)$ and standard coordinates $(\xi, \eta)$. For relatively narrow fields and long-focus telescopes such as Schmidts, it is sufficiently accurate to assume that the tangent point of the plate is at the centre, thus coinciding with the origin of the plate measures. Then the unit vector direction from the centre of projection to the origin of measurement, $\hat{\mathbf{h}}$, is assumed to be identical to $\mathbf{w}$ in Figure C.1. Thus if $\mathbf{f}$ and $\mathbf{g}$ are vectors in the plane of the plate in the directions of measurement (and need not be orthogonal) and $\mathbf{u}$, $\mathbf{v}$

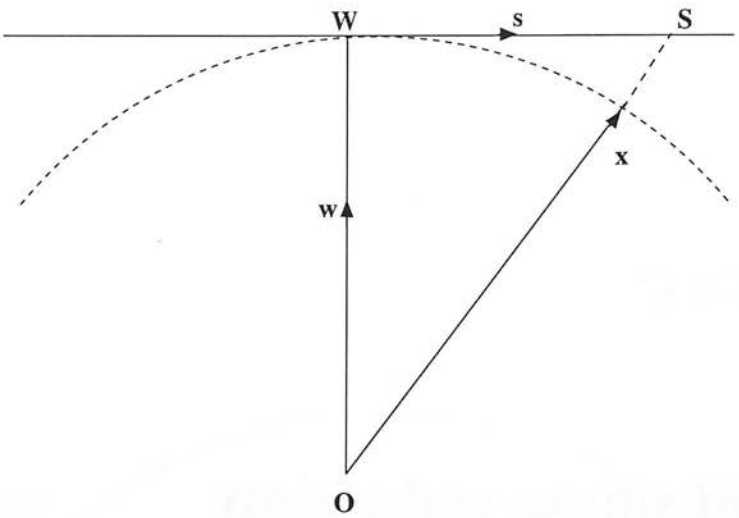


*Figure C.1: Tangent plane coordinates describing the projection of the sky onto the image plane. The centre of projection is O and the direction to the tangent point in the image plane, W, is given by the vector* **w**. *A star in the direction* **x** *has an image S on the plate, which has position vector* **s** *in the plate coordinate system.*

and $\mathbf{w}$ are standard coordinates, the position vector of a star can be written

$$\mathbf{x} = \mathbf{X} \begin{pmatrix} x \\ y \\ 1 \end{pmatrix} = \mathbf{N} \begin{pmatrix} x_l \\ x_m \\ x_n \end{pmatrix} = \mathbf{W} \begin{pmatrix} \xi \\ \eta \\ 1 \end{pmatrix} \tag{C.1}$$

relative to (i) the measurement triad $\mathbf{X} = (\mathbf{f}\ \mathbf{g}\ \mathbf{h})$

(ii) the equatorial triad $\mathbf{N} = (\mathbf{l}\ \mathbf{m}\ \mathbf{n})$

and (ii) the standard coordinate triad $\mathbf{W} = (\mathbf{u}\ \mathbf{v}\ \mathbf{w})$.

The star's position vector can therefore be expressed

$$\mathbf{x} = x\mathbf{f} + y\mathbf{g} + \mathbf{h} = \xi\mathbf{u} + \eta\mathbf{v} + \mathbf{w} \tag{C.2}$$

The problem is to calculate the standard coordinates $(\xi, \eta)$ from the measured coordinates

$(x, y)$ for each star on every plate. This is done by first transforming to the equatorial triad N:

$$\begin{pmatrix} x_l \\ x_m \\ x_n \end{pmatrix} = \mathrm{N}^{\mathrm{T}}\mathrm{X} \begin{pmatrix} x \\ y \\ 1 \end{pmatrix} \tag{C.3}$$

and then to the standard coordinate triad W:

$$\begin{pmatrix} \xi \\ \eta \\ 1 \end{pmatrix} = \mathrm{W}^{\mathrm{T}}\mathrm{N} \begin{pmatrix} x_l \\ x_m \\ x_n \end{pmatrix} \tag{C.4}$$

The tensor $\mathrm{N}^{\mathrm{T}}\mathrm{X}$ for transforming from measured to equatorial components is derived from the reference stars on a plate by plate basis. The direction cosines of the reference stars relative to the equatorial triad N are matched to their plate measurements, leading to a set of normal equations which can be solved to give the components of $\mathrm{N}^{\mathrm{T}}\mathrm{X}$ (§C.2.3).

Once the plate solution has been obtained from the reference stars, the measured coordinates of the programme stars on each plate are transformed to equatorial coordinates. Corrections are made for space motion, aberration and refraction to convert the observed to true directions for each star, and finally the conversion from equatorial to standard coordinates is achieved by pre-multiplication by

$$\mathrm{W}^{\mathrm{T}}\mathrm{N} = \begin{pmatrix} -\sin\alpha_W & \cos\alpha_W & 0 \\ -\sin\delta_W\cos\alpha_W & -\sin\delta_W\sin\alpha_W & \cos\delta_W \\ \cos\delta_W\cos\alpha_W & \cos\delta_W\sin\alpha_W & \sin\alpha_W \end{pmatrix} \tag{C.5}$$

where $(\alpha_W, \delta_W)$ are the right ascension and declination of the tangential direction w referred to the normal triad (Murray 1983, equation 8.2.3). The calculations described in §C.2 are applied through Fortran code written by Andrew Murray.

### C.2.2 Forming the normal equations from the reference stars

If $\hat{\mathbf{r}}$ is the unit vector describing the apparent topocentric direction to a reference star with measured direction $\hat{\mathbf{x}}$, then the star's observational equation can be written

$$\hat{\mathbf{r}} - \hat{\mathbf{x}} = \boldsymbol{v} \tag{C.6}$$

where $\boldsymbol{v}$ is a vector residual.

The problem is to determine the equatorial components of the vectors $\mathbf{f}, \mathbf{g}$ and $\hat{\mathbf{h}}$ by minimising the sum of the square of the residuals, $\sum \boldsymbol{v}^2$, subject to certain constraints. The assumption that the origin of plate measurement coincides with the tangent point imposes the constraints $\mathbf{f}.\hat{\mathbf{h}} = \mathbf{g}.\hat{\mathbf{h}} = 0$, and since $\hat{\mathbf{h}}$ is a unit vector then $\hat{\mathbf{h}}.\hat{\mathbf{h}} = 1$. So the normal equations are derived by minimising the function

$$E = \sum \boldsymbol{v}^2 + 2\alpha \mathbf{f}.\hat{\mathbf{h}} + 2\beta \mathbf{g}.\hat{\mathbf{h}} + \gamma(\hat{\mathbf{h}}.\hat{\mathbf{h}} - 1) \tag{C.7}$$

where $\alpha$, $\beta$ and $\gamma$ are Langrangian multipliers. It is hence necessary to solve

$$\mathrm{dE} = \frac{\partial \mathrm{E}}{\partial \mathbf{f}}\mathrm{d}\mathbf{f} + \frac{\partial \mathrm{E}}{\partial \mathbf{g}}\mathrm{d}\mathbf{g} + \frac{\partial \mathrm{E}}{\partial \hat{\mathbf{h}}}\mathrm{d}\hat{\mathbf{h}} = 0 \tag{C.8}$$

$$\begin{aligned}
\text{Now} \qquad & \boldsymbol{v}^2 = \boldsymbol{v}.\boldsymbol{v} = 2(1 - \hat{\mathbf{r}}.\hat{\mathbf{x}}) \\
\Longrightarrow \quad & 2\boldsymbol{v}.d\boldsymbol{v} = -2\hat{\mathbf{r}}.d\hat{\mathbf{x}} = -2\hat{\mathbf{r}}.(I - \hat{\mathbf{x}}.\hat{\mathbf{x}})\tfrac{dx}{|x|} \\
\text{since} \quad & \mathrm{d}\hat{\mathbf{x}} = \mathrm{d}\tfrac{\mathrm{x}}{|\mathrm{x}|} = \mathrm{d}\tfrac{\mathrm{x}}{(\mathrm{x}.\mathrm{x})^{\frac{1}{2}}} = (\mathrm{I} - \hat{\mathbf{x}}.\hat{\mathbf{x}})\tfrac{\mathrm{dx}}{|\mathrm{x}|}
\end{aligned}$$

But $|\boldsymbol{v}| \sim 1'' \approx 5 \times 10^{-6}$ rad, so $\hat{\mathbf{r}}.\hat{\mathbf{x}} \approx 1$. Hence

$$\boldsymbol{v}.\mathrm{d}\boldsymbol{v} \approx -\boldsymbol{v}.\frac{\mathrm{dx}}{|\mathrm{x}|}$$

$$\Longrightarrow \mathrm{d}(\sum \boldsymbol{v}^2) = -2\sum \boldsymbol{v}.\frac{\mathrm{dx}}{|\mathrm{x}|} \tag{C.9}$$

So the minimisation of E with constraints is given by

$$\mathrm{dE} = \mathrm{d}(\sum \upsilon^2) + 2\alpha(\hat{\mathbf{h}}.\mathrm{d}\mathbf{f} + \mathbf{f}.\mathrm{d}\hat{\mathbf{h}}) + 2\beta(\hat{\mathbf{h}}.\mathrm{d}\mathbf{g} + \mathbf{g}.\mathrm{d}\hat{\mathbf{h}}) + 2\gamma\hat{\mathbf{h}}.\mathrm{d}\hat{\mathbf{h}} \tag{C.10}$$

Given Equation C.9 and that $\mathrm{dx} = x\mathrm{d}\mathbf{f} + y\mathrm{dg} + \mathrm{d}\hat{\mathbf{h}}$, then Equation C.10 reduces to

$$\begin{aligned}\mathrm{dE} = (-2\sum \frac{\mathrm{x}}{|\mathrm{x}|}\upsilon. + 2\alpha\hat{\mathbf{h}}.)\mathrm{df} + (-2\sum \frac{\mathrm{y}}{|\mathrm{x}|}\upsilon. + 2\beta\hat{\mathbf{h}}.)\mathrm{dg} + \\ (-2\sum \frac{\upsilon}{|\mathrm{x}|}. + 2\alpha\mathbf{f}. + 2\beta\hat{\mathbf{h}}. + 2\gamma\hat{\mathbf{h}}.)\mathrm{d}\hat{\mathbf{h}} = 0\end{aligned} \tag{C.11}$$

Equating the coefficients of $\mathrm{d}\mathbf{f}$, $\mathrm{dg}$ and $\mathrm{d}\hat{\mathbf{h}}$ with zero gives

$$\begin{aligned}\sum \frac{\mathrm{x}}{|\mathrm{x}|}\upsilon - \alpha\hat{\mathbf{h}} = 0 \\ \sum \frac{y}{|\mathrm{x}|}\upsilon - \beta\hat{\mathbf{h}} = 0 \\ \sum \frac{\upsilon}{|\mathrm{x}|} - \alpha\mathbf{f} - \beta\mathbf{g} - \gamma\hat{\mathbf{h}} = 0\end{aligned} \tag{C.12}$$

Scalarly multiplying Equations C.12 by $\hat{\mathbf{h}}$ and using $\hat{\mathbf{h}}.\mathbf{f} = \hat{\mathbf{h}}.\mathbf{g} = 1 - \hat{\mathbf{h}}.\hat{\mathbf{h}} = 0$ with $\upsilon.\hat{\mathbf{h}} = \mathbf{r}.\hat{\mathbf{h}} - |\mathrm{x}|^{-1}$ from Equation C.6 gives expressions for the Langrangian multipliers:

$$\begin{aligned}\alpha = \sum \frac{x(\mathbf{r}.\hat{\mathbf{h}})}{|\mathrm{x}|} - \sum \frac{x}{|\mathrm{x}|^2} \\ \beta = \sum \frac{y(\mathbf{r}.\hat{\mathbf{h}})}{|\mathrm{x}|} - \sum \frac{y}{|\mathrm{x}|^2} \\ \gamma = \sum \frac{(\mathbf{r}.\hat{\mathbf{h}})}{|\mathrm{x}|} - \sum \frac{1}{|\mathrm{x}|^2}\end{aligned} \tag{C.13}$$

Finally, by substituting these expressions for $\alpha, \beta$ and $\gamma$ into Equation C.12 and using $\upsilon = \mathbf{r} - \hat{\mathbf{x}} = \mathbf{r} - (x\mathbf{f} - y\mathbf{g} - \hat{\mathbf{h}})/|\mathrm{x}|$, the normal equations can be written in matrix form:

$$\begin{pmatrix} \sum \frac{x^2}{|\mathrm{x}|} & \sum \frac{xy}{|\mathrm{x}|^2} & \sum \frac{x(\mathbf{r}.\hat{\mathbf{h}})}{|\mathrm{x}|} \\ \sum \frac{xy}{|\mathrm{x}|} & \sum \frac{y^2}{|\mathrm{x}|^2} & \sum \frac{y(\mathbf{r}.\hat{\mathbf{h}})}{|\mathrm{x}|} \\ \sum \frac{x(\mathbf{r}.\hat{\mathbf{h}})}{|\mathrm{x}|} & \sum \frac{y(\mathbf{r}.\hat{\mathbf{h}})}{|\mathrm{x}|^2} & \sum \frac{(\mathbf{r}.\hat{\mathbf{h}})}{|\mathrm{x}|} \end{pmatrix} \begin{pmatrix} \mathbf{f} \\ \mathbf{g} \\ \hat{\mathbf{h}} \end{pmatrix} = \begin{pmatrix} \sum \frac{x}{|\mathrm{x}|} \\ \sum \frac{y}{|\mathrm{x}|} \\ \sum \frac{1}{|\mathrm{x}|} \end{pmatrix} \mathbf{r} \tag{C.14}$$

### C.2.3 Solving the normal equations

Since x is a function of $\mathbf{f}, \mathbf{g}$ and $\hat{\mathbf{h}}$, Equations C.14 are non-linear in these vectors, and so an iterative solution is necessary. Now

$$|\mathbf{x}| = (\mathbf{x}.\mathbf{x})^{\frac{1}{2}} = (1 + x^2\mathbf{f}^2 + 2xy\mathbf{f}.\mathbf{g} + y^2\mathbf{g}^2) \tag{C.15}$$

and from scalarly multiplying Equation C.6 with $\hat{\mathbf{h}}$

$$\mathbf{r}.\hat{\mathbf{h}} = \frac{1}{|\mathbf{x}|} + \boldsymbol{\upsilon}.\hat{\mathbf{h}} \tag{C.16}$$

If $(x, y)$ are given in units of an adopted focal length value then the lengths of $\mathbf{f}$ and $\mathbf{g}$ will be approximately unity. But $\mathbf{f}^2 \approx \mathbf{g}^2 \approx 1$ and $\mathbf{f}.\mathbf{g} \approx 0$, and $\boldsymbol{\upsilon}.\hat{\mathbf{h}} \approx 0$ since $|\boldsymbol{\upsilon}| << 1$ and $\boldsymbol{\upsilon}$ is approximately perpendicular to $\hat{\mathbf{h}}$. So then

$$\begin{aligned} \mathbf{r}.\hat{\mathbf{h}} &\approx \frac{1}{|\mathbf{x}|} \\ |\mathbf{x}| &\approx (1 + x^2 + y^2)^{\frac{1}{2}} \end{aligned} \tag{C.17}$$

This first approximation to $|\mathbf{x}|$ is used to solve Equations C.14 for $\mathbf{f}, \mathbf{g}$ and $\hat{\mathbf{h}}$. The resulting estimates for $|\mathbf{x}|$ and $\mathbf{r}.\hat{\mathbf{h}}$ are then used in the next iteration, and this procedure is repeated until $\mathbf{f}, \mathbf{g}$ and $\hat{\mathbf{h}}$ are found to sufficient precision. Hence the components of $\mathbf{f}$ and $\mathbf{g}$ and the direction cosines of $\hat{\mathbf{h}}$ relative to the equatorial triad are obtained:

$$\mathbf{X} = (\mathbf{f}\ \mathbf{g}\ \hat{\mathbf{h}}) = \mathbf{N} \begin{pmatrix} f_1 & g_1 & \frac{h_1}{|h|} \\ f_2 & g_2 & \frac{h_2}{|h|} \\ f_3 & g_3 & \frac{h_3}{|h|} \end{pmatrix} \tag{C.18}$$

and these provide the tensor required to transform between the measured plate coordinates and equatorial coordinates (Equation C.3):

$$\mathbf{N}^{\mathrm{T}}\mathbf{X} = \begin{pmatrix} f_1 & g_1 & \frac{h_1}{|h|} \\ f_2 & g_2 & \frac{h_2}{|h|} \\ f_3 & g_3 & \frac{h_3}{|h|} \end{pmatrix} \tag{C.19}$$

## C.3 Calculating apparent topocentric directions to reference stars

In order to derive the transformation from measured plate coordinates to observed tangent plane coordinates, it is necessary to obtain the apparent topocentric directions for the reference stars, $\mathbf{r}$. This requires converting the heliocentric catalogued positions of the astrometric reference stars to the topocentric observed positions with the following steps:

*(1)* Derive heliocentric directions to the reference stars from the catalogued positions.

*(2)* Convert to true geocentric coordinates at the plate epoch by allowing for space motions (proper motion and parallax) and annual aberration.

*(3)* Convert to apparent topocentric coordinates by correcting for diurnal aberration and then atmospheric refraction.

### C.3.1 True geocentric directions at epoch

If $\alpha$, $\delta$, $r$ are the equatorial coordinates of a reference star at epoch T, then its direction with respect to the equatorial triad N is

$$\mathbf{r} = \mathrm{N}r \begin{pmatrix} \cos\delta\cos\alpha \\ \cos\delta\sin\alpha \\ \sin\delta \end{pmatrix} \tag{C.20}$$

At epoch $\mathrm{T}+\Delta\mathrm{T}$ the star has position $\mathbf{r}_0 = \mathbf{r} + \Delta T\dot{\mathbf{r}}$ where $\dot{\mathbf{r}}$ is the derivative wrt time. Hence

$$\mathbf{r}_0 = \begin{pmatrix} -\cos\delta\sin\alpha & -\sin\delta\cos\alpha & \cos\delta\cos\alpha \\ \cos\delta\cos\alpha & -\sin\delta\sin\alpha & \cos\delta\sin\alpha \\ 0 & \cos\delta & \sin\delta \end{pmatrix} \begin{pmatrix} 15r\mu_\alpha \\ r\mu_\delta \\ 2\dot{r} \end{pmatrix} \tag{C.21}$$

If the star has parallax $\omega$ radians then the true geocentric direction at epoch is given by

$$\mathbf{r}_1 = \frac{\mathbf{r}_0 - \omega\mathbf{e}}{|\mathbf{r}_0 - \omega\mathbf{e}|} \tag{C.22}$$

where $\mathbf{e}$ is the heliocentric coordinate vector of the Earth in AU.

### C.3.2 Direction of Zenith

The direction of the zenith referred to the true equator and mean equinox of date is

$$\mathbf{z} = \begin{pmatrix} \cos\phi\cos t \\ \cos\phi\sin t \\ \sin\phi \end{pmatrix} \tag{C.23}$$

where $\phi$ is the astronomical latitude and $t$ is the local mean sidereal time (Murray 1983, p89).

### C.3.3 Aberration

#### Diurnal aberration

Also with respect to the true equator and mean equinox of date, the observer's geocentric velocity, which leads to *diurnal aberration*, is given in terms of the speed of light by

$$\frac{\mathbf{v}_d}{c} = \begin{pmatrix} -v\sin t \\ v\cos t \\ 0 \end{pmatrix} \tag{C.24}$$

where

$$v = \frac{2\pi}{86400}\frac{a}{c}\rho\cos\phi' \tag{C.25}$$

with $a$ the Earth's equatorial radius, $\rho$ and $\phi'$ the observer's geocentric distance and latitude and $c$ the speed of light.

**Annual and total aberration**

The Earth's orbital motion around the Sun results in *annual aberration*. The heliocentric velocity of the Earth is given by (Murray 1983§1.4)

$$\frac{\mathbf{v}_a}{c} = \kappa(\mathbf{h} \wedge \mathbf{u} + e\mathbf{g}) \tag{C.26}$$

where $\mathbf{u}$ is the heliocentric unit vector to the Earth, $\mathbf{g}$ is the unit vector along the minor axis of the Earth's elliptical orbit (orbital eccentricity $e$), and $\mathbf{h}$ is the unit vector normal to the orbital plane. The constant of aberration, $\kappa$, is expressed as

$$\kappa = \frac{na}{c}(1 - e^2)^{-\frac{1}{2}} \approx 20''.495519 \tag{C.27}$$

where $n$ is the mean angular rate of motion and $a$ is the semi-major axis.

The total heliocentric velocity of the observer in units of the speed of light is then given by $\mathbf{v}/c = \mathbf{v}_d/c + \mathbf{v}_a/c$, allowing for the effects of diurnal and annual aberration, and for the heliocentric velocity effect of the eccentricity of the Earth's orbit. If $\mathbf{r}_1$ is the geocentric direction of a star after correction for space motion (Equation C.22), then the apparent, unrefracted direction after taking aberration into account is

$$\mathbf{r}_2 = \frac{\mathbf{r}_1 + \mathbf{v}}{|\mathbf{r}_1 + \mathbf{v}|} \tag{C.28}$$

### C.3.4 Precession and nutation

Precession and nutation describe the motion of the Earth's pole on the celestial sphere due to the forces acting on the Earth affecting its orbit and spin. Precession accounts for the long-term, or secular, components, whilst nutation allows for the short-term, periodic oscillations. *Luni-solar precession* describes the gravitational forces of the Sun and Moon on the Earth's equatorial bulge, giving rise to motion of the celestial equator, whereas the (much smaller) perturbations of the Earth's orbit due to the influence of the other planets is given by *planetary precession*, which causes motion of the ecliptic plane. Nutation describes the periodic motion of the Earth's true pole about its mean position, divided into its displacement parallel to the ecliptic (the

*nutation in longitude*, $\Delta\psi$) and perpendicular to the ecliptic (the *nutation in obliquity*, $\Delta\varepsilon$). Figure C.2 shows these components.

Precession and nutation cause the position of the equator and the equinox, and hence the dependent equatorial coordinate system, to change with time. The *mean* equinox or equator of date describe the positions allowing for precession; the *true* equinox or equator also account for nutation, providing instantaneous locations. The *mean equator or equinox of epoch* are the positions of the equator or equinox at a given fixed epoch, $\varepsilon_0 = t_0$, whereas the *mean equator or equinox of date* give the positions at date $\varepsilon = t$.

Prior to use in deriving topocentric direction cosines to the reference stars, the zenith direction vector $\mathbf{z}$ and the observer's geocentric velocity $\mathbf{v}_d$ must be corrected for precession and nutation. The values of $\mathbf{z}$ and $\mathbf{v}_d$ defined above are referred to the true equator and mean equinox of date; these are transformed first to the mean equator of date of the standard star observations and then to the mean equinox and equator of fixed epoch 2000.0.

**Nutation**

The conversion from true equator to mean equator of date is achieved by pre-multiplying $\mathbf{z}$ and $\mathbf{v}_d$ by $\mathrm{N}^{\mathrm{T}}$, the transpose of the nutation tensor N. This is given in simple form by the *Explanatory Supplement* (1992, p120):

$$\mathrm{N} = \begin{pmatrix} 1 & -\Delta\psi\cos\varepsilon & -\Delta\psi\sin\varepsilon \\ \Delta\psi\cos\varepsilon & 1 & -\Delta\varepsilon \\ \Delta\psi\sin\varepsilon & \Delta\varepsilon & 1 \end{pmatrix} \tag{C.29}$$

where $\Delta\psi$ is the longitudinal component of nutation and $\Delta\varepsilon$ is the obliquity of the ecliptic (Figure C.2). The values of $\Delta\psi$ and $\Delta\varepsilon$ are obtained from the *Explanatory Supplement* (1992, §3.2)

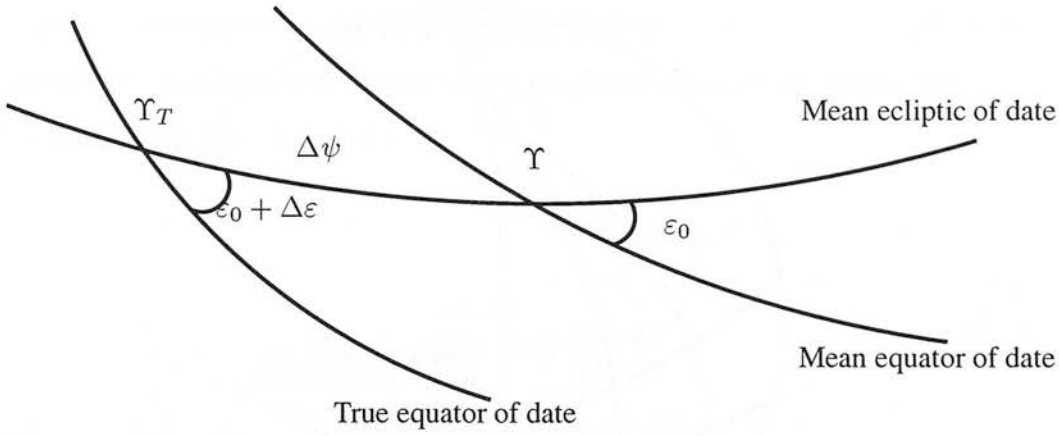


*Figure C.2: The mean and true equators and equinoxes ($\Upsilon$ and $\Upsilon_T$ respectively) of date, and the two components of nutation: the nutation in longitude, $\Delta\psi$, and the nutation in obliquity, $\Delta\varepsilon$.*

**Precession**

Precession is accounted for by converting $\mathbf{z}$ and $\mathbf{v}_d$ from the mean equinox and equator of the standard catalogue observations date to the mean equinox and equator of fixed epoch 2000.0 through pre-multiplication by the transpose of the precession tensor $\mathbf{P}$ (*Explanatory Supplement* 1992, p103).

$$\mathbf{P} = \begin{pmatrix} \cos z_A \cos\theta_A \cos\zeta_A - \sin z_A \sin\zeta_A & \cos z_A \cos\theta_A \sin\zeta_A - \sin z_A \cos\zeta_A & -\cos z_A \sin\theta_A \\ \sin z_A \cos\theta_A \cos\zeta_A + \cos z_A \sin\zeta_A & -\sin z_A \cos\theta_A \sin\zeta_A + \cos z_A \cos\zeta_A & -\sin z_A \sin\theta_A \\ \sin\theta_A \cos\zeta_A & -\sin\theta_A \sin\zeta_A & \cos\theta_A \end{pmatrix}$$

The values of $\varepsilon_0$, $\Delta\varepsilon$ and $\Delta\psi$ are taken from *Explanatory Supplement* (1992) and are described in Figure C.3 in terms of the pole of equator and equinox at the fixed epoch ($P_0$, $\Upsilon$) and the pole and equinox of date ($P$, $\Upsilon$).

### C.3.5 Refraction

If $\theta$ is the apparent zenith distance of a star, then the refraction is approximated by

$$\Delta\theta = a\tan\theta + b\tan^3\theta \qquad \text{(C.30)}$$

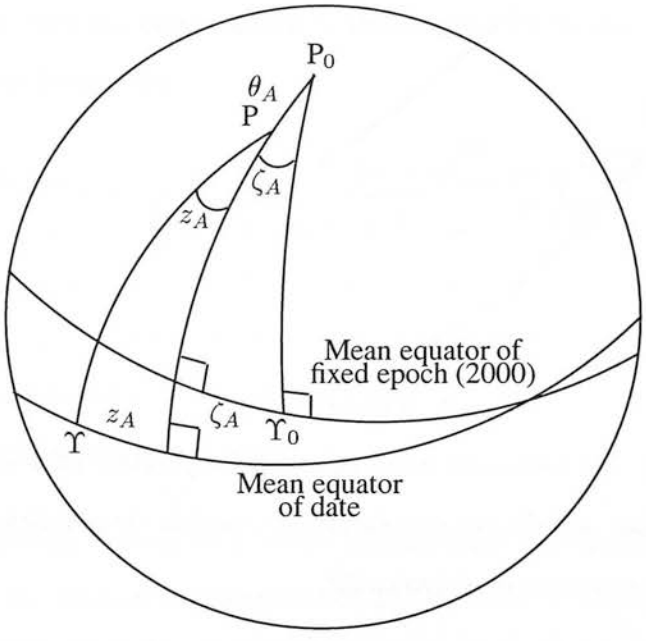


*Figure C.3: The precession angles $\zeta_A$, $z_A$ and $\theta_A$, describing the motion due to precession of the pole $P_0$ and equinox $\Upsilon_0$ at fixed epoch to the pole $P$ and equinox $\Upsilon$ at a given date.*

The coefficients $a$ and $b$ are calculated from the refractivity of the air at exposure, given the current temperature, atmospheric pressure and humidity at the time, with the air mass and star colour. (Murray 1983, §7). The value of $(\theta + \Delta\theta)$ is known for each observation, so $\Delta\theta$ is first obtained from an iterative calculation of Equation C.30.

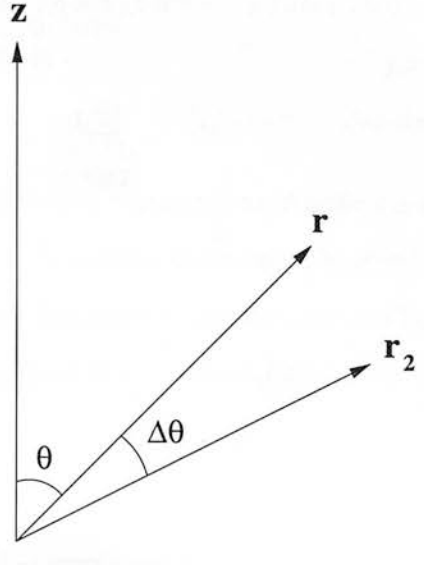


*Figure C.4: Calculating the effect of refraction*

The refracted direction of the star, $\mathbf{r}$, is calculated from the direction of the zenith, $\mathbf{z}$, and the apparent unrefracted direction for space motion and aberration, $\mathbf{r}_2$, both of which have been derived by the methods described above.

From Figure C.4

$$\mathbf{r}_2 \wedge \mathbf{r} = \frac{\sin \Delta\theta}{\sin(\theta + \Delta\theta)} (\mathbf{r}_2 \wedge \mathbf{z}) \tag{C.31}$$

The vector product of Equation C.31 with $\mathbf{r}_2$ gives

$$(\mathbf{r}_2.\mathbf{r})\mathbf{r}_2 - \mathbf{r} = \frac{\sin(\Delta\theta)}{\sin(\theta + \Delta\theta)} [(\mathbf{r}_2.\mathbf{z})\mathbf{r}_2 - \mathbf{z}] \tag{C.32}$$

Using $\zeta = \frac{\sin(\Delta\theta)}{\tan(\theta+\Delta\theta)}$ and the fact that $\cos(\Delta\theta + \theta) = \mathbf{r}_2.\mathbf{z}$, the apparent refracted direction to the star is found by

$$\mathbf{r} = (\cos \Delta\theta - \zeta)\mathbf{r}_2 + \frac{\zeta}{\mathbf{r}_2.\mathbf{z}} z \tag{C.33}$$

## C.4 Calculating standard coordinate of programme stars

Once a plate solution has been derived from the reference stars, the equatorial coordinates of all of the programme stars on each plate can be derived from the measured coordinates $(x, y)$ by Equation C.3. These equatorial coordinates must be scaled to take account of Schmidt telescope projection to allow for the fact that the plates are constrained to the form of the Schmidt focal surface (a sphere with radius equal to the focal length) during exposure. From Figure C.1, if $\mathbf{s}$ is the tangential coordinate vector of the image of a star with direction $\mathbf{x}$ relative to the tangential direction $\mathbf{w}$, then

$$\tan\theta = |\mathbf{t}|, \sin\theta = |\mathbf{w} \wedge \mathbf{x}|, \cos\theta = \mathbf{w}.\mathbf{x} \tag{C.34}$$

When the plate is restored to its original flat shape after exposure the first approximation of the vector OS is therefore

$$\mathbf{x} + \Delta\mathbf{x} = \frac{\theta}{\tan\theta}\mathbf{x} \tag{C.35}$$

where

$$\Delta\mathbf{x} \approx -\frac{1}{3}|\mathbf{x}|^2\mathbf{x} \tag{C.36}$$

for a cubic radial distortion. The derived equatorial coordinates are therefore scaled by $\tan\theta/\theta$ to account for Schmidt projection.

The coordinates referred to the equatorial triad thus derived are observed values - ie. apparent topocentric coordinates. It is necessary to convert these to true geocentric values by correcting for refraction and then aberration with the inverse of the procedure used for the reference stars. From Figure C.4

$$\mathbf{r}_2 \wedge \mathbf{r} = \frac{\sin\Delta\theta}{\sin\theta}(\mathbf{r} \wedge \mathbf{z}) \tag{C.37}$$

Multiplying vectorially by $\mathbf{r}$

$$\mathbf{r}_2 - (\mathbf{r}.\mathbf{r}_2) = \frac{\sin\Delta\theta}{\sin\theta}\left[(\mathbf{r}.\mathbf{z})', \mathbf{r} - \mathbf{z}\right] \tag{C.38}$$

where $\Delta\theta$ is calculated from Equation C.30 given that $\theta$ is known from $\mathbf{r}.\mathbf{z} = \cos\theta$. Writing

$$\zeta' = \frac{\sin\Delta\theta}{\tan\theta} \tag{C.39}$$

then the direction corrected for refraction is given by

$$\mathbf{r}_2 = (\cos\Delta\theta + \zeta')\,\mathbf{r} - \frac{\zeta'}{\mathbf{r}.\mathbf{z}}\,\mathbf{z} \tag{C.40}$$

The true geocentric direction cosines of the programme stars allowing for aberration are then

found from

$$\mathbf{r}_1 = \frac{\mathbf{r}_2 - \mathbf{V}}{|\mathbf{r}_2 - \mathbf{V}|} \tag{C.41}$$

The coordinates of each star are then transformed from the equatorial triad to the standard coordinate triad on a plate by plate basis by means of Equation C.4. The mean standard coordinates $(\xi_0, \eta_0)$ taken over all plates are calculated from these coordinates, and the coordinates of each programme star on every plate can be analysed for proper motions and parallaxes using the central overlap method (Appendix D).

# Appendix D

# The central overlap method

## D.1 The conditional equations

The astrometric problem of determining positions, proper motions and parallaxes for the programme stars is expressed as a set of conditional equations which connect the measurements of each star on a plate series with the corresponding star and plate constants. For overlapping fields as in this project, the solutions are obtained by means of the variation of the "central overlap method", originally devised by Eichhorn & Russell (1976). This technique calculates linear plate constants (zero point, scale and orientation) for each plate and star constants (position, proper motion and parallax) for each star in a single least-squares solution, using measures of stars on all plates to improve the accuracy of the derived plate constants. The method was used in the study of Murray & Corben (1979), Murray et al. (1986), Murray (1986) and is described in Murray (1983), from which this summary is derived.

### D.1.1 Star constants

If a star has mean standard coordinates $(\xi_0, \eta_0)$ at epoch 2000.0 and coordinates $(\xi_0 + \Delta\xi, \eta_0 + \Delta\eta)$ at epoch $T_j$, then the change in coordinates can be expressed as

$$\begin{aligned} \xi_j - \xi_0 &= \Delta\xi_j + \mu_\xi T_j + P_{\xi j}\pi \\ \eta_j - \eta_0 &= \Delta\eta_j + \mu_\eta T_j + P_{\eta j}\pi \end{aligned} \tag{D.1}$$

where $\mu_\xi$ and $\mu_\eta$ are the star's proper motion components, $\pi$ is the parallax, and $P_{\xi j}$, $P_{\eta j}$ are *parallax factors*, assumed to be constant across the plate. There are thus five star constants per star which cause the star's position to vary from plate to plate: two coordinate corrections at epoch, two proper motion components, and parallax.

### D.1.2 Plate constants

The position of a star from plate to plate will also vary due to differences in the plate model for each. A six-constant linear model is used, with terms for zero-point, scale and orientation corrections. The difference between the mean standard coordinates and those at epoch $T_j$ arising from the plate model variations is therefore given by

$$\begin{aligned} \xi_j - \xi_0 &= a_{1j} + a_{2j}\xi_0 + a_{3j}\eta_0 \\ \eta_j - \eta_0 &= b_{1j} + b_{2j}\xi_0 + b_{3j}\eta_0 \end{aligned} \tag{D.2}$$

where $a_{\gamma j}, b\gamma j(\gamma = 1, 3)$ are the plate constants for the plate $j$. Since the scale and orientation plate constants are small in each coordinate, use is made of $a_{2j}\xi_j \approx a_{2j}\xi_0$ and $b_{2j}\xi_j \approx b_{2j}\xi_0$ (etc.) Systematic errors will arise from inaccuracies in the adopted mean positions and proper motions and in the measured positions of the reference stars, and these will be a function of plate position and epoch. However, if the same set of reference stars is used for all plates then these systematic effects will be linear functions of coordinates and epoch, and it is therefore appropriate to use a linear plate model.

### D.1.3 Conditional equations

Assuming that the variation of stellar positions between plates is due to the star and plate constants described above, then the total coordinate differences from the mean that are to be adjusted in the solution are

$$\begin{aligned} \xi_j - \xi_0 &= \Delta\xi_j + \mu_\xi T_j + P_{\xi j}\pi + a_{1j} + a_{2j}\xi_0 + a_{3j}\eta_0 \\ \eta_j - \eta_0 &= \Delta\eta_j + \mu_\eta T_j + P_{\eta j}\pi + b_{1j} + b_{2j}\xi_0 + b_{3j}\eta_0 \end{aligned} \tag{D.3}$$

The conditional equations for the measurement of star $i$ on plate $j$ are therefore

$$\mathbf{F}_{ij} = \begin{pmatrix} \Delta\xi_{ij} + \mu_{\xi i}T_j + P_{\xi ij}\pi + a_{1j} + a_{2j}\xi_{i0} + a_{3j}\eta_{i0} - (\xi_{ij} - \xi_{i0}) \\ \Delta\eta_{ij} + \mu_{\eta i}T_j + P_{\eta ij}\pi + b_{1j} + b_{2j}\xi_{i0} + b_{3j}\eta_{i0} - (\eta_{ij} - \eta_{i0}) \end{pmatrix} = 0 \tag{D.4}$$

The star and plate constants are derived from these set of equations corresponding to the measures over a series of plates by means of a least-squares method.

## D.2 Constraints on the solution

With no *a priori* information about the star constants, the normal equation matrix in Equation D.4 is singular, and so constraint equations have to be imposed in order to derive an unique solution. These constraints are arbitrary, but in the present solution for position, proper motion and parallax, fifteen constraint equations are required. In order to ensure that the constraint equations do not introduce errors into the derived plate constants, the constraints are only applied to stars with non-extreme values of proper motion and parallax, which are termed "constraint stars". These are selected on the basis of photometric properties, such that stars between specified magnitude and colour limits are defined as constraint stars.

For the constraint equations the example of Murray & Corben (1979) is followed, by stipulating that the sum of star constants over all "constraint" stars is zero, and that there is no correlation between any star constant and either coordinate. Thus the 15 constraint equations

are

$$\sum_i \begin{pmatrix} 1 \\ \xi_{i0} \\ \eta_{i0} \end{pmatrix} (\Delta\xi_{i0}\ \Delta\eta_{i0}\ \mu_{\xi i}\ \mu_{\eta i}\ \pi_i) = 0 \tag{D.5}$$

where the summation is over the constraint stars only.

## D.3 The general least-squares method

Let $\mathbf{x}_0$ denote the matrix of $n$ coordinate measures, and $\mathbf{a}$ and $\mathbf{c}$ the arrays of star and plates constants respectively; the conditional equations in Equation D.4 can then be expressed

$$\mathbf{F}(\mathbf{x}_0 + \boldsymbol{\upsilon}, \mathbf{a}, \mathbf{c}) = 0 \tag{D.6}$$

where $\boldsymbol{\upsilon}$ is an $n \times 1$ matrix of residuals. The constraint equations in Equation D.5 are written

$$\mathbf{G}(\mathbf{a}, \mathbf{c}) = 0 \tag{D.7}$$

To solve these conditional equations and constraints it is necessary to minimise

$$E = \boldsymbol{\upsilon}^{\mathrm{T}}\mathbf{S}^{-1}\boldsymbol{\upsilon} - 2\boldsymbol{\lambda}^{\mathrm{T}}\mathbf{F} - 2\boldsymbol{\mu}^{\mathrm{T}}\mathbf{G} \tag{D.8}$$

with $\boldsymbol{\lambda}$ and $\boldsymbol{\mu}$ matrices of Lagrangian multipliers and $\mathbf{S}$ the covariance matrix describing the errors in the coordinate measures $\mathbf{x}_0$. Differentiating $E$ and equating the coefficients of $\mathrm{d}\boldsymbol{\upsilon}$, $\mathrm{d}\mathbf{a}$ and $\mathrm{d}\mathbf{c}$ to zero before transposing gives:

$$\boldsymbol{\upsilon}^{\mathrm{T}}\mathbf{S} - \boldsymbol{\lambda}^{\mathrm{T}}\frac{\partial\mathbf{F}}{\partial\mathbf{x}_0^{\mathrm{T}}} = 0 \Rightarrow \mathbf{S}^{\mathrm{T}}\boldsymbol{\upsilon} - \frac{\partial\mathbf{F}^{\mathrm{T}}}{\partial\mathbf{x}_0}\boldsymbol{\lambda} = 0 \tag{D.9}$$

$$\boldsymbol{\lambda}^{\mathrm{T}}\frac{\partial\mathbf{F}}{\partial\mathbf{a}^{\mathrm{T}}} + \boldsymbol{\mu}^{\mathrm{T}}\frac{\partial\mathbf{G}}{\partial\mathbf{a}^{\mathrm{T}}} = 0 \Rightarrow \frac{\partial\mathbf{F}^{\mathrm{T}}}{\partial\mathbf{a}}\boldsymbol{\lambda} + \frac{\partial\mathbf{G}^{\mathrm{T}}}{\partial\mathbf{a}}\boldsymbol{\mu} = 0 \tag{D.10}$$

$$\boldsymbol{\lambda}^{\mathrm{T}}\frac{\partial\mathbf{F}}{\partial\mathbf{c}^{\mathrm{T}}} + \boldsymbol{\mu}^{\mathrm{T}}\frac{\partial\mathbf{G}}{\partial\mathbf{c}^{\mathrm{T}}} = 0 \Rightarrow \frac{\partial\mathbf{F}^{\mathrm{T}}}{\partial\mathbf{c}}\boldsymbol{\lambda} + \frac{\partial\mathbf{G}^{\mathrm{T}}}{\partial\mathbf{c}}\boldsymbol{\mu} = 0 \tag{D.11}$$

Now if $\mathbf{a} = \mathbf{a}_0 + \Delta\mathbf{a}$ and $\mathbf{c} = \mathbf{c}_0 + \Delta\mathbf{c}$ where $\mathbf{a}_0$, $\mathbf{c}_0$ are estimated values, then to first order

Equations D.6 and D.7 expand to

$$\begin{aligned}\mathbf{F}(\mathbf{x}_0+\boldsymbol{\upsilon},\mathbf{a}_0+\Delta\mathbf{a},\mathbf{c}_0+\Delta\mathbf{c})&=\mathbf{F}(\mathbf{x}_0,\mathbf{a}_0,\mathbf{c}_0)+\frac{\partial F}{\partial\mathbf{x}_0^{\mathrm{T}}}\boldsymbol{\upsilon}+\frac{\partial\mathbf{F}}{\partial\mathbf{a}_0^{\mathrm{T}}}\Delta\mathbf{a}+\frac{\partial\mathbf{F}}{\partial\mathbf{c}_0^{\mathrm{T}}}\Delta\mathbf{c}=0\\ \mathbf{G}(\mathbf{a}_0+\Delta\mathbf{a},\mathbf{c}_0+\Delta\mathbf{c})&=\mathbf{G}(\mathbf{a}_0,\mathbf{c}_0)+\frac{\partial\mathbf{G}}{\partial\mathbf{a}_0^{\mathrm{T}}}\Delta\mathbf{a}+\frac{\partial\mathbf{G}}{\partial\mathbf{c}_0^{\mathrm{T}}}\Delta\mathbf{c}=0\end{aligned}\tag{D.12}$$

Then with

$$\boldsymbol{\upsilon}=\mathbf{S}\frac{\partial\mathbf{F}^{\mathrm{T}}}{\partial\mathbf{x}_0}\boldsymbol{\lambda}\tag{D.13}$$

from Equation D.9 and using

$$\mathbf{K}=\frac{\partial\mathbf{F}}{\partial\mathbf{x}_0^{\mathrm{T}}}\mathbf{S}\frac{\partial\mathbf{F}^{\mathrm{T}}}{\partial\mathbf{x}_0}\tag{D.14}$$

Equations D.10-D.12 can be combined into a single matrix equation

$$\begin{pmatrix}\mathbf{K}&\frac{\partial\mathbf{F}}{\partial\mathbf{a}_0^{\mathrm{T}}}&\frac{\partial\mathbf{F}}{\partial\mathbf{c}_0^{\mathrm{T}}}&0\\ \frac{\partial\mathbf{F}^{\mathrm{T}}}{\partial\mathbf{a}_0}&0&0&\frac{\partial\mathbf{G}^{\mathrm{T}}}{\partial\mathbf{a}_0}\\ \frac{\partial\mathbf{F}^{\mathrm{T}}}{\partial\mathbf{a}_0}&0&0&\frac{\partial\mathbf{G}^{\mathrm{T}}}{\partial\mathbf{c}_0}\\ 0&\frac{\partial\mathbf{G}}{\partial\mathbf{a}_0^{\mathrm{T}}}&\frac{\partial\mathbf{G}}{\partial\mathbf{c}_0^{\mathrm{T}}}&0\end{pmatrix}\begin{pmatrix}\boldsymbol{\lambda}\\ \Delta\mathbf{a}\\ \Delta\mathbf{c}\\ \boldsymbol{\mu}\end{pmatrix}=\begin{pmatrix}-\mathbf{F}_0\\ 0\\ 0\\ -\mathbf{G}_0\end{pmatrix}\tag{D.15}$$

where derivatives are evaluated at $(\mathbf{x}_0,\mathbf{a}_0,\mathbf{c}_0)$ and $\mathbf{F}_0=\mathbf{F}(\mathbf{x}_0,\mathbf{a}_0,\mathbf{c}_0)$ and $\mathbf{G}_0=\mathbf{G}(\mathbf{x}_0,\mathbf{a}_0,\mathbf{c}_0)$. Now $\mathbf{K}$ is always invertible, so $\boldsymbol{\lambda}$ can be eliminated from Equations D.15 by the transforms ($r_i$ denote rows)

$$\begin{aligned}r_2'&=\frac{\partial\mathbf{F}^{\mathrm{T}}}{\partial\mathbf{a}_0}\mathbf{K}^{-1}r_1-r_2\\ r_3'&=\frac{\partial\mathbf{F}^{\mathrm{T}}}{\partial\mathbf{c}_0}\mathbf{K}^{-1}r_1-r_3\\ r_4'&=-r_4\end{aligned}$$

to give the reduced normal equations

$$\begin{pmatrix}\frac{\partial\mathbf{F}^{\mathrm{T}}}{\partial\mathbf{a}_0}\mathbf{K}^{-1}\frac{\partial\mathbf{F}^{\mathrm{T}}}{\partial\mathbf{a}_0^{\mathrm{T}}}&\frac{\partial\mathbf{F}^{\mathrm{T}}}{\partial\mathbf{a}_0}\mathbf{K}^{-1}\frac{\partial\mathbf{F}}{\partial\mathbf{c}_0^{\mathrm{T}}}&-\frac{\partial\mathbf{G}^{\mathrm{T}}}{\partial\mathbf{a}_0}\\ \frac{\partial\mathbf{F}^{\mathrm{T}}}{\partial\mathbf{c}_0}\mathbf{K}^{-1}\frac{\partial\mathbf{F}^{\mathrm{T}}}{\partial\mathbf{a}_0^{\mathrm{T}}}&\frac{\partial\mathbf{F}^{\mathrm{T}}}{\partial\mathbf{c}_0}\mathbf{K}^{-1}\frac{\partial\mathbf{F}}{\partial\mathbf{c}_0^{\mathrm{T}}}&-\frac{\partial\mathbf{G}^{\mathrm{T}}}{\partial\mathbf{c}_0}\\ -\frac{\partial\mathbf{G}}{\partial\mathbf{a}_0^{\mathrm{T}}}&-\frac{\partial\mathbf{G}}{\partial\mathbf{c}_0^{\mathrm{T}}}&0\end{pmatrix}\begin{pmatrix}\Delta\mathbf{a}\\ \Delta\mathbf{c}\\ \boldsymbol{\mu}\end{pmatrix}=\begin{pmatrix}-\frac{\partial\mathbf{F}^{\mathrm{T}}}{\partial\mathbf{a}_0}\mathbf{K}^{-1}\mathbf{F}_0\\ -\frac{\partial\mathbf{F}^{\mathrm{T}}}{\partial\mathbf{c}_0}\mathbf{K}^{-1}\mathbf{F}_0\\ \mathbf{G}_0\end{pmatrix}\tag{D.16}$$

Simplifying:

$$\begin{pmatrix} \mathbf{A} & \mathbf{D} & -\mathbf{G}_a^{\mathrm{T}} \\ \mathbf{D}^{\mathrm{T}} & \mathbf{C} & -\mathbf{G}_c^{\mathrm{T}} \\ -\mathbf{G}_a & -\mathbf{G}_c & 0 \end{pmatrix} \begin{pmatrix} \Delta\mathbf{a} \\ \Delta\mathbf{c} \\ \mu \end{pmatrix} = \begin{pmatrix} -\mathbf{H}_{a0} \\ -\mathbf{H}_{c0} \\ \mathbf{G}_0 \end{pmatrix} \tag{D.17}$$

where $\mathbf{A}$ is a $k \times k$ diagonal matrix for $k$ star constants, $\mathbf{D}$ is such that its rows and columns correspond to star and plate constants respectively, and $\mathbf{C}$ is a diagonal matrix.

## D.4 The central overlap least squares solution

### D.4.1 Forming the normal equations

Determining the reduced normal equations and solving for position, proper motion and parallax by the central overlap method is a special case of the generalised least-squares method (§D.3). In this instance the normal equations are given by Equation D.4, and the star and plate constant matrices are written as

$$\begin{aligned} \Delta\mathbf{a}^{\mathrm{T}} &= \begin{pmatrix} \Delta\mathbf{a}_1^{\mathrm{T}} & \Delta\mathbf{a}_2^{\mathrm{T}} & \ldots \end{pmatrix} \\ \Delta\mathbf{c}^{\mathrm{T}} &= \begin{pmatrix} \Delta\mathbf{c}_1^{\mathrm{T}} & \Delta\mathbf{c}_2^{\mathrm{T}} & \ldots \end{pmatrix} \end{aligned} \tag{D.18}$$

where

$$\Delta\mathbf{a}_i^{\mathrm{T}} = \begin{pmatrix} \Delta\xi_{i0} & \Delta\eta_{i0} & \mu_{\xi i} & \mu_{\eta i} & \pi_i \end{pmatrix} \text{ for star } i \tag{D.19}$$

$$\Delta\mathbf{c}_i^{\mathrm{T}} = \begin{pmatrix} a_{1j} & a_{2j} & a_{3j} & b_{1j} & b_{2j} & b_{3j} \end{pmatrix} \text{ for plate } j \tag{D.20}$$

From Equation D.4

$$\frac{\partial\mathbf{F}_{ij}}{\partial\mathbf{a}_i^{\mathrm{T}}} = \begin{pmatrix} 1 & 0 & T_j & 0 & P_{\xi ij} \\ 0 & 1 & 0 & T_j & P_{\eta ij} \end{pmatrix} \tag{D.21}$$

$$\frac{\partial\mathbf{F}_{ij}}{\partial\mathbf{c}_j^{\mathrm{T}}} = \begin{pmatrix} 1 & \xi_{i0} & \eta_{i0} & 0 & 0 & 0 \\ 0 & 0 & 0 & 1 & \xi_{i0} & \eta_{i0} \end{pmatrix} \tag{D.22}$$

and

$$\mathbf{F}_{ij0} = -\begin{pmatrix} \xi_{ij} - \xi_{i0} \\ \eta_{ij} - \eta_{i0} \end{pmatrix} \tag{D.23}$$

If the variance of measurement of star $i$ on plate $j$ is assumed to be the same in both coordinates and equal to $w_{ij}^{-1}$, then from Equations D.16 and D.17

$$\begin{aligned} \mathbf{A}_{ii} &= \sum_j w_{ij} \frac{\partial \mathbf{F}_{ij}^{\mathrm{T}}}{\partial \mathbf{a}_i} \frac{\partial \mathbf{F}_{ij}}{\partial \mathbf{a}_i^{\mathrm{T}}} \\ \mathbf{C}_{jj} &= \sum_i w_{ij} \frac{\partial \mathbf{F}_{ij}^{\mathrm{T}}}{\partial \mathbf{c}_j} \frac{\partial \mathbf{F}_{ij}}{\partial \mathbf{c}_j^{\mathrm{T}}} \\ \mathbf{D}_{ij} &= w_{ij} \frac{\partial \mathbf{F}_{ij}^{\mathrm{T}}}{\partial \mathbf{a}_i} \frac{\partial \mathbf{F}_{ij}}{\partial \mathbf{c}_j^{\mathrm{T}}} \\ \mathbf{H}_{a0} &= \sum_j w_{ij} \frac{\partial \mathbf{F}_{ij}^{\mathrm{T}}}{\partial \mathbf{a}_i} \mathbf{F}_{ij0} \\ \mathbf{H}_{c0} &= \sum_i w_{ij} \frac{\partial \mathbf{F}_{ij}^{\mathrm{T}}}{\partial \mathbf{c}_j} \mathbf{F}_{ij0} \end{aligned} \tag{D.24}$$

(no summation convention.)

### D.4.2 Solving the normal equations

The normal equations given by Equations D.16 and D.24 are solved by first eliminating the star constants $\Delta\mathbf{a}$ from Equation D.16 to give

$$\begin{pmatrix} \mathbf{C} - \mathbf{D}^{\mathrm{T}}\mathbf{A}^{-1}\mathbf{D} & -\mathbf{G}_c^{\mathrm{T}} + \mathbf{D}^{\mathrm{T}}\mathbf{A}^{-1}\mathbf{G}_a^{\mathrm{T}} \\ -\mathbf{G}_c + \mathbf{G}_a\mathbf{A}^{-1}\mathbf{D} & -\mathbf{G}_a\mathbf{A}^{-1}\mathbf{G}_a^{\mathrm{T}} \end{pmatrix} \begin{pmatrix} \Delta\mathbf{c} \\ \boldsymbol{\mu} \end{pmatrix} = \begin{pmatrix} -\mathbf{H}_{c0} + \mathbf{D}^{\mathrm{T}}\mathbf{A}^{-1}\mathbf{H}_{a0} \\ \mathbf{G}_0 - \mathbf{G}_a\mathbf{A}^{-1}\mathbf{H}_{a0} \end{pmatrix} \tag{D.25}$$

from which the plate constants $\Delta\mathbf{c}$ and the Lagrangian multipliers $\boldsymbol{\mu}$ are obtained. The star constants are then obtained by back-substitution: multiplying the first equation of Equation D.17 by $\mathbf{A}^{-1}$ gives

$$\Delta\mathbf{a} = \mathbf{A}^{-1}(-\mathbf{H}_{a0} - \mathbf{D}\Delta\mathbf{c} + \mathbf{G}_a^{\mathrm{T}}\boldsymbol{\mu}) \tag{D.26}$$

where $\mathbf{A}^{-1}$ is a diagonal matrix with $(\mathbf{A}^{-1})_{ij} = (\mathbf{A}_{ij})^{-1}$.

The central overlap solution provides the five star constants of two proper motion components, parallax, and two coordinate corrections to the mean standard coordinates calculated in the tangent plane reduction (Appendix C). The tangent plane coordinates at equinox J2000.0 are then derived and converted to the equatorial reference frame to provide a celestial position for each star.

# Appendix E

# Tangential velocity distributions

## E.1 Theoretical $V_T$ distributions

The transverse velocity distributions are derived from the velocity ellipsoids and the solar motion following the method of Murray (1983, p285) and Evans (1988).

With a population of stars whose peculiar velocities can be described by a single velocity ellipsoid, the peculiar velocity $\boldsymbol{v}$ of a given star can be described by a deviation from the mean of a residual velocity $\boldsymbol{\eta}$:

$$\boldsymbol{v} = \bar{\boldsymbol{v}} + \boldsymbol{\eta} \tag{E.1}$$

It is assumed that the residual velocities $\boldsymbol{\eta}$ take the form of a Schwarzchild velocity distribution

$$F(\boldsymbol{\eta}) = \frac{1}{(2\pi)^{\frac{3}{2}}|\boldsymbol{\Sigma}|^{\frac{1}{2}}} e^{-\frac{1}{2}\boldsymbol{\eta}^{\mathrm{T}}\boldsymbol{\Sigma}^{-1}\boldsymbol{\eta}} \tag{E.2}$$

where $\boldsymbol{\Sigma}$ is the covariance tensor of peculiar velocities and $^{\mathrm{T}}$ denotes vector transpose. With $\mathbf{T}$ the triad of unit vectors along the axes of the velocity ellipsoid and $\sigma_i$ the dispersions along

these axes, $\Sigma$ is given by

$$\Sigma = \mathbf{T} \begin{bmatrix} \sigma_1^2 & 0 & 0 \\ 0 & \sigma_2^2 & 0 \\ 0 & 0 & \sigma_3^2 \end{bmatrix} \mathbf{T}^{\mathrm{T}} \tag{E.3}$$

With the assumptions that there is no vertex deviation and the tensor orientation is independent of distance, $\Sigma$ can be expressed in terms of the right-handed Galactic coordinate velocity triad $\mathbf{G}$ (Appendix B), where $\hat{\boldsymbol{u}}$, $\hat{\boldsymbol{v}}$ and $\hat{\boldsymbol{w}}$ are velocities in the directions of the Galactic centre, rotation and north pole respectively.

$$\Sigma = \mathbf{G} \begin{bmatrix} \sigma_u^2 & 0 & 0 \\ 0 & \sigma_v^2 & 0 \\ 0 & 0 & \sigma_w^2 \end{bmatrix} \mathbf{G}^{\mathrm{T}} \tag{E.4}$$

Expressing $\eta$ and $\Sigma$ in terms of the normal triad $\mathbf{R}$ (Appendix B), with $\mathbf{p}$, $\mathbf{q}$ and $\mathbf{r}$ in the directions of increasing right ascension, declination and distance respectively:

$$\eta = \mathbf{R} \begin{bmatrix} \eta_p \\ \eta_q \\ \eta_r \end{bmatrix} \tag{E.5}$$

$$\Sigma = \mathbf{R} \begin{bmatrix} C_{pp} & C_{pq} & C_{rp} \\ C_{pq} & C_{qq} & C_{qr} \\ C_{rp} & C_{qr} & C_{rr} \end{bmatrix} \mathbf{R}^{\mathrm{T}}, \quad \Sigma^{-1} = \mathbf{R} \begin{bmatrix} c_{pp} & c_{pq} & c_{rp} \\ c_{pq} & c_{qq} & c_{qr} \\ c_{rp} & c_{qr} & c_{rr} \end{bmatrix} \mathbf{R}^{\mathrm{T}} \tag{E.6}$$

The tensors $\Sigma$ and $\Sigma^{-1}$ are symmetric in the equatorial triad and the determinant $|\Sigma|$ is invariant under any transform, so that

$$|\Sigma| = \sigma_u^2 \sigma_v^2 \sigma_w^2 \tag{E.7}$$

Projecting $F_\eta$ onto the tangent plane by integrating over $\eta_r$ gives:

$$F_{pq} = \int_\infty^\infty F(\boldsymbol{\eta})\,\mathrm{d}\eta_r \tag{E.8}$$

$$= \frac{1}{2\pi|\boldsymbol{\Sigma}|^{\frac{1}{2}}c_{rr}^{\frac{1}{2}}} e^{-\frac{1}{2c_{rr}|\boldsymbol{\Sigma}|}\left(C_{qq}\eta_p^2+C_{pp}\eta_q^2-2C_{pq}\eta_p\eta_q\right)} \tag{E.9}$$

The observed velocity of a star can be expressed by $\boldsymbol{v} = \boldsymbol{\eta} - \boldsymbol{v}_\odot$, where $\boldsymbol{v}_\odot$ is the solar motion. If $\boldsymbol{v}$ is expressed in terms of a tangential velocity $V_T$, a radial velocity $V_r$, and a position angle $\theta$, then

$$\eta_p = V_T \sin\theta + v_{\odot p} \tag{E.10}$$

$$\eta_q = V_T \cos\theta + v_{\odot q} \tag{E.11}$$

Transforming $F_{pq}$ using this parameterisation and integrating over $\theta$ gives the $V_T$ distribution, then a further transformation gives the $5\log V_T$ distribution:

$$\psi(V_T) = V_T \int_0^{2\pi} F_{pq}\,\mathrm{d}\theta \tag{E.12}$$

$$\psi(5\log V_T) = \frac{V_T^2}{5\log e}\int_0^{2\pi} F_{pq}\,\mathrm{d}\theta \tag{E.13}$$

In determining $F_{pq}$ the following parameters are all required, expressed in normal coordinates: *(i)* the components $C_{pp}$, $C_{qq}$ and $C_{pq}$ of the tensor $\boldsymbol{\Sigma}$ ; *(ii)* the element $c_{rr}$ of $\boldsymbol{\Sigma}$ ; and *(iii)* the solar motion components $v_{\odot p}$ and $v_{\odot q}$.

*(i)* The components $C_{ij}$ of $\boldsymbol{\Sigma}$ are found from

$$\begin{pmatrix} C_{pp} & C_{pq} & C_{rp} \\ C_{pq} & C_{qq} & C_{qr} \\ C_{rp} & C_{qr} & C_{rr} \end{pmatrix} = \mathbf{R}^{\mathrm{T}}\mathbf{G} \begin{pmatrix} \sigma_u^2 & 0 & 0 \\ 0 & \sigma_v^2 & 0 \\ 0 & 0 & \sigma_w^2 \end{pmatrix} \mathbf{G}^{\mathrm{T}}\mathbf{R} \tag{E.14}$$

where

$$\mathbf{G}^{\mathrm{T}}\mathbf{R} = \left(\mathbf{R}^{\mathrm{T}}\mathbf{G}\right)^{-1} = (\mathbf{G}^{\mathrm{T}}\mathbf{N})(\mathbf{N}^{\mathrm{T}}\mathbf{R}) \tag{E.15}$$

and the equatorial triad $\mathbf{N} = (\boldsymbol{l}\,\boldsymbol{m}\,\boldsymbol{n})$ has components $\boldsymbol{l}$ towards the equinox, $\boldsymbol{n}$ towards the north celestial pole and $\boldsymbol{m}$ orthogonal to both (Murray 1983, p85). The conversion from equatorial to Galactic coordinates is given by (Green 1985, p355):

$$\mathbf{G}^{\mathrm{T}}\mathrm{N} = \begin{pmatrix} -0.054876 & -0.873437 & -0.483835 \\ 0.494109 & -0.444830 & 0.746982 \\ 0.867666 & -0.198076 & 0.455984 \end{pmatrix} \tag{E.16}$$

for NGP coordinates $\alpha_G = 12^h51^m$, $\delta_G = 27°\ 7.7'$ and a position angle of the Galactic centre (longitude of the NCP) $\theta$ = 122.932° (Binney & Merrifield 1998, p31). The transformation from the normal to equatorial coordinate system is given by (Murray 1983, p116):

$$\mathrm{N}^{\mathrm{T}}\mathbf{R} = \begin{pmatrix} -\sin\alpha & -\sin\delta\cos\alpha & \cos\delta\cos\alpha \\ \cos\alpha & -\sin\delta\sin\alpha & \cos\delta\sin\alpha \\ 0 & \cos\delta & \sin\delta \end{pmatrix} \tag{E.17}$$

*(ii)* The element $c_r$ of $\boldsymbol{\Sigma}^{-1}$ is found by inverting the tensor $C_{ij}$. From Equation E.6:

$$\boldsymbol{\Sigma}^{-1} = (\boldsymbol{R}\boldsymbol{C}\boldsymbol{R}^{\mathrm{T}})^{-1} = \boldsymbol{R}\boldsymbol{C}^{-1}\boldsymbol{R}^{\mathrm{T}} = \boldsymbol{R}\boldsymbol{c}\boldsymbol{R}^{\mathrm{T}}$$

$$\Longrightarrow c_{rr} = \frac{\left(C_{pp}C_{qq} - C_{pq}^2\right)}{\sigma_u^2\sigma_v^2\sigma_w^2} \tag{E.18}$$

*(iii)* The components of the solar motion are converted from Galactic to normal coordinates by:

$$\begin{pmatrix} v_{\odot p} \\ v_{\odot q} \\ v_{\odot r} \end{pmatrix} = \left(\boldsymbol{R}^{\mathrm{T}}\boldsymbol{G}\right) \begin{pmatrix} U_\odot \\ V_\odot \\ W_\odot \end{pmatrix} \tag{E.19}$$

where $(\boldsymbol{R}^{\mathrm{T}}\boldsymbol{G})$ is given by Equations E.15 - E.17.

Figures 4.12 and 4.13 show the $\Psi V_T$ and $\Psi(5\log V_T)$ distributions for the spheroid and discs for field 0363 in the SGS, calculated from Equations E.12 and E.13.

## E.2 Monte Carlo simulations

As an alternative to the analytical results (§E.1), Monte Carlo simulations were also used to verify the form of the tangential velocity distributions.

A sample of $5 \times 10^6$ stars was generated each with Galactocentric velocities $(U, V, W)$ randomly selected from each of the Gaussian velocity distributions given in Table 4.3. The velocity vector $\boldsymbol{v} = (U, V, W)$ can be expressed in terms of a radial velocity component $v_r$ and tangential velocity vector $\boldsymbol{v_T}$

$$\boldsymbol{v} = v_r\boldsymbol{s} + \boldsymbol{v_T} \tag{E.20}$$

where $\boldsymbol{s}$ is the unit vector giving the heliocentric direction to the star. In terms of Galactic coordinates, $\boldsymbol{s}$ is given by (Murray 1983, p274):

$$\boldsymbol{s_G} = \begin{pmatrix} \cos l \cos b \\ \sin l \cos b \\ \sin b \end{pmatrix} \tag{E.21}$$

So with a Galactocentric velocity $(U, V, W)$ for each star and a given field direction $(l, b)$, the radial and tangential components of its observed velocity can be calculated. It is assumed that all the stars in each field lie along a single line of sight (ie. they all have the same $(l, b)$), since the fields are relatively narrow. For each Monte Carlo-generated star, the velocity components are found from

$$v_r = \boldsymbol{v}.\boldsymbol{s_G} \tag{E.22}$$

and

$$\boldsymbol{v_T} = \boldsymbol{s_G} \times (\boldsymbol{v} \times \boldsymbol{s_G}) \tag{E.23}$$

The values of $|\boldsymbol{v_T}|$ and $5 \log |\boldsymbol{v_T}|$ for each star and hence the tangential velocity distributions can then be derived. Figures 4.14 and 4.15 show the Monte Carlo tangential velocity distribution in the direction of field 0363 in the SGS.